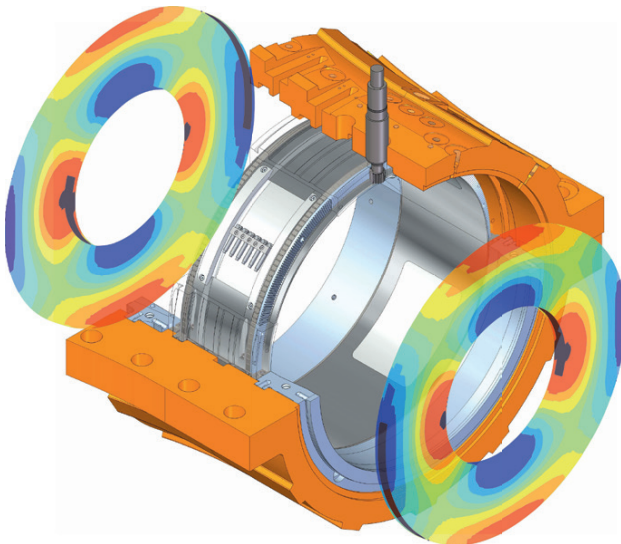Juan David Laguna

On the Sensitivity of the Radial Mode Analysis (RMA) for the Experimental Evaluation of Sound Propagation in a Low-Pressure Turbine
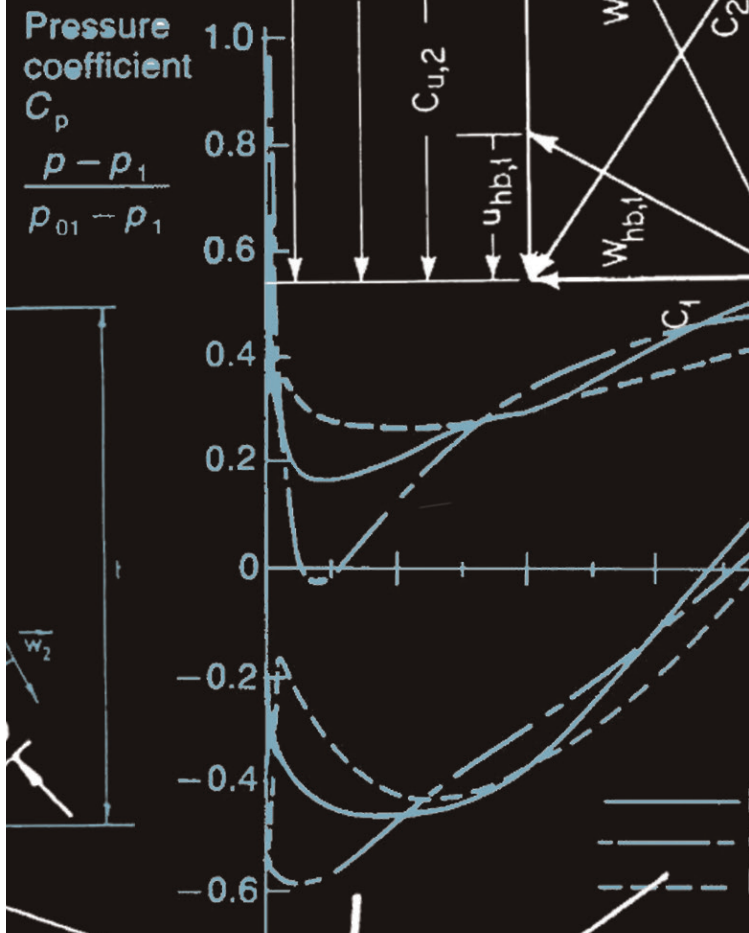
Institut für Turbomaschinen
und Fluid-Dynamik

On the Sensitivity of the Radial Mode Analysis (RMA) for the Experimental Evaluation of Sound Propagation in a Low-Pressure Turbine

von
Juan David Laguna Trujillo, M. Sc
geboren am 8. Januar 1985
in Bogotá, Kolumbien

2015

Vorsitzender: Prof. Dr.-Ing. Ludger Overmeyer
1. Referent: Prof. Dr.-Ing. Jörg Seume
2. Referent: Prof. Ph.D. Stéphane Moreau

Tag der mündlichen Prüfung: 17. Dezember 2015

Abstract

The aeronautical industry is nowadays confronted with an important increase in the volume of passengers and transported freight. While this tendency encourages the industry expansion as well as further technology development associated with this branch, it brings along serious concerns related to the accomplishment of the stringent noise standards dictated by the governing authorities. This situation is especially critical for citizens living close to airports, as they are increasingly affected by the noise exposure. This problematic can be addressed by the development of innovative quiet and low-emission aircraft propulsion solutions. The development of such propulsion units demands however a deep understanding of the sound transport mechanisms taking place in real turbomachinery. Accordingly, the Institute of **T**urbomachinery and **F**luid-**D**ynamics (TFD) studies the sound propagation through a low-pressure turbine with the purpose of developing quieter aircraft engines. Sound propagation is thus quantified by means of known established evaluation methods, one of these being the **R**adial **M**ode **A**nalysis (RMA).

The current work focuses on three central topics. In the first place, the RMA is implemented for the quantification of the associated acoustical mode amplitudes. The implementation of the RMA is achieved by means of a turbine-integrated rotating measurement unit. The development process associated with the abovementioned measuring device constitutes the second central topic. Thirdly, the RMA is optimized with respect to the quality of its output for a single operating point ($\dot{m} = 5$ kg s^{-1}, $\Omega = 3500$ min^{-1}). To this end, a sensitivity analysis of the parameters which influence the overall error associated to the RMA is performed. The analysis concentrates on the effect of two data acquisition parameters: the number of triggered rotor revolutions and the circumferential spacing of microphones.

The results of the present RMA exhibit an acoustical modal structure composed of the modes $m_{[1,0]}$ and $m_{[2,2]}$ propagating at $f_{\mathrm{BPF}} = 1750$ Hz and at $f_{2\mathrm{BPF}} = 3500$ Hz, respectively. Regarding the selected data acquisition parameters, these do have an influence on the output of the RMA. An increase of the circumferential angular spacing (more azimuthal measurement positions) results in a decrease of the relative error associated to the circumferential mode amplitudes. In this way, a sufficient number of circumferential measurement positions assures a low relative error of the circumferential mode amplitude. This is only true if the number of triggered revolutions is high enough. The sensitivity analysis shows that only a sufficiently high number of triggered revolutions ensures satisfactory results independent of the circumferential mode order. As such, a realistic measurement setting for future experiments should be performed with maximal circumferential resolution ($\Delta\varphi = 1°$) and at least $N = 50$ triggered revolutions. In this way, relative errors below 10% should be expected.

Zusammenfassung

Die Luftfahrtindustrie wird heutzutage mit zunehmenden Passagierzahlen und steigendem Volumen zu transportierender Fracht konfrontiert. Während diese Tendenz eine formschlüssige Industrieexpansion sowie weitere verbundenen Technologieentwicklungen fördert, führt sie unmittelbar zu Emissionsanstiegen. Dabei sind insbesondere die Lärmemissionen in der Umgebung von Flughäfen eine große Belastung für Mensch und Umwelt. Die Entwicklung leiser und emissionsarmer Flugantriebe könnte zur Beseitigung dieser Problematik führen. Die Entwicklung solcher Flugantriebe erfordert jedoch ein tiefes Verständnis der in realen Turbinen wirkenden Schalltransportmechanismen. Dazu werden am TFD experimentelle Untersuchungen zur Schallausbreitung in Niederdruckturbinen durchgeführt. Ziel ist es, durch die Optimierung und Weiterentwicklung bereits existierender Mess- und Auswertungsmethoden sowie durch das Anpassen geeigneter akustischer Messtechnik, solche Untersuchungen zu ermöglichen. Die Quantifizierung des sich im Turbinenkanal ausbreitenden Schallfelds erfolgt mittels eines empirischen Analyseverfahrens, der **R**adial**m**oden**a**nalyse (RMA).

Die vorliegende Arbeit konzentriert sich auf drei zentrale Themen. Zunächst wird die RMA zugleich mit der notwendigen akustischen Messtechnik implementiert, um Rückschlüsse auf die dominanten Schallfeldanteile ziehen zu können. Dies erfordert die Entwicklung einer drehbaren Messeinheit, die in den Turbinenkanal integriert werden kann. Der auf die Messeinheit zugeschnittene Entwicklungsprozess stellt den zweiten Schwerpunkt dieser Arbeit dar. Schließlich ist eine Optimierung der RMA vorgesehen. Dazu wird die Sensitivität der RMA auf zwei Datenaufnahme-Parameter analysiert, die die Qualität und den Gesamtfehler der Messmethode beeinflussen. Diese Parameter sind die Anzahl getriggerter Umdrehungen und der Abstand bzw. die Auflösung der Umfangsmesspositionen. Die durchgeführte Sensitivitätsanalyse der gemessenen experimentellen Daten dient dazu, eine optimale Kombination für die jeweilige Messsituation bestimmen zu können.

Die Ergebnisse der RMA weisen in diesem Fall auf ein akustisches Feld hin, das aus den sich ausbreitenden Moden $m_{[1,0]}$ und $m_{[2,2]}$ zusammengesetzt ist. Das akustische Feld breitet sich bei den tonalen Frequenzen $f_{\mathrm{BPF}} = 1750$ Hz und $f_{\mathrm{2BPF}} = 3500$ Hz. Die ausgewählte Datenerfassungsparameter spielen eine entscheidende Rolle in Bezug auf die Ergebnisse der RMA. Eine Erhöhung der Auflösung der Umfangsmesspositionen führt zu einer Reduzierung des relativen Fehlers der modalen Umfangssamplituden. Dazu gewährleistet eine ausreichende Anzahl von Umfangsmesspositionen einen niedrigen relativen Fehler. Dies gilt nur, wenn die Anzahl der getriggerten Umdrehungen hoch genug ist. Basiert auf die zuvor gewonnenen Erkenntnisse, ein realistischer Messaufbau für zukünftige Versuche mittels der RMA sollte mit einer maximalen Umfangsauflösung ($\Delta\varphi = 1°$) und mindestens 50 getriggerte Umdrehungen durchgeführt werden.

Danksagung

Contents

Contents

List of Figures

List of Tables

List of Tables

Nomenclature

Latin nomenclature

Symbol	Unit	Meaning	Definition
A_i	Pa	Sound pressure amplitude	Sec. 2.3.1
A_m	Pa	Circumferential mode amplitude	Eq. 3.2
$A_{mn}^{\pm}$	Pa	Radial mode amplitude	Eq. 3.11
a	m/s	Speed of sound	Eq. 2.12
B	—	Number of rotor blades	
B_i	Pa	Sound pressure amplitude	Sec. 2.3.1
c	—	Condition number	Sec. 3.2
c	m/s	Absolute flow velocity	Sec. 5.2
c_r	mm	Cord length of the rotor blades	
c_s	mm	Cord length of the stator vanes	
c_u	m/s	Circumferential component of c	
c_x	m/s	Axial component of c	
f	1/s = Hz	Sound field frequency	
f_{BPF}	1/s = Hz	Blade-passing frequency	Sec. 2.4.1
$f_{\text{Cut-On}}$	1/s = Hz	Cut-On frequency	Eq. 2.65
f_l	1/s = Hz	Lower limit frequency	
f_n	1/s = Hz	Shaft rotary frequency	Sec. 5.5.2
f_s	1/s = Hz	Sampling frequency	
f_{st}	1/s = Hz	Frequency IGV interaction	Sec. 5.5.2
f_u	1/s = Hz	Upper limit frequency	
He	—	Helmholtz number	kR
h	—	Harmonic multiple of the f_{BPF}	
h	mm	Turbine channel height	
K	Pa	Bulk modulus	
k	1/m	Wave number	$\frac{\omega}{a} = \frac{2\pi f}{a}$
$k_{mn}^{\pm}$	1/m	Axial wave number	Eq. 2.59 and 2.64
L_p	dB	Sound pressure level	
l	—	Integer index	Eq. 3.5

Nomenclature

M		Number of measurement microphones	
$\mathbf{M}$	–	Eigenvalue matrix	Eq. 3.10
Ma	–	Mach number	$\frac{u}{a}$
Ma_x	–	Mach number in axial direction	
Ma_φ	–	Mach number in circumferential direction	
m	–	Circumferential mode order	Eq. 2.67
m_{TS}	–	Maximum azimuthal mode order	Sec. 4.2.1
$\dot{m}$	kg/s	Mass flow rate	
N	–	Number of data samples	
N	–	Number of rotor-triggered revolutions	
N_x	–	Number of axial measuring positions	Sec. 3.2
N_φ	–	Number of azimuthal measuring positions	Sec. 3.2
N_Ω	–	Number of averaged rotor revolutions	Sec. 5.4.2
n	–	Radial mode order	Sec. 2.3.4
n_F	–	Digital filter order	
n_{TSmax}	–	Maximum propagating radial mode order	Sec. 4.2.1
P	Pa	Total pressure	
p	Pa	Pressure	Eq. 2.3
p'_{mn}	Pa	Sound pressure distribution	Eq. 2.63
p_0	Pa	Steady mean pressure	
p_c	Pa	Circumferential sound pressure	Sec. 3.2
p'	Pa	Unsteady sound pressure	
Q_{mn}		Amplitude factor	Eq. 2.51
R_i	m	Inner duct radius	
R_o	m	Outer duct radius	
r	m	Radial coordinate	
s	–	Integral multiple	
s_{mn}	–	n-th eigenvalue	Eq. 2.42
T	K	Total temperature	
T	s	Signal period	Sec. 2.4.1
t	s	Time	
t_i	–	Specific time instant	
$\mathbf{U}$		Orthogonal matrix	
u	m/s	Axial velocity component	
u'_r	m/s	Radial particle velocity	
V	–	Number of stator vanes	
$\mathbf{V}$		Orthogonal transposed matrix	

$\mathbf{v}$	m/s	Velocity vector	Eq. 2.5
$\mathbf{v}'$	m/s	Acoustic velocity vector	
$\mathbf{W}$		Singular value matrix	
w_j	–	Singular value	Sec. 3.2
x, y, z	m	Cartesian coordinates	
x_j^i	–	Sample data of a time series	Sec. 5.4.2
y		General unsteady signal	Eq. 5.3
$\varnothing_{TO}$	mm	Turbine casing outer diameter	
$\varnothing_{TR}$	mm	Turbine rotor diameter	

Greek symbols

Symbol	Unit	Meaning	Definition
α	1/m	Constant term	Eq. 2.58
α	Degrees	Stator vane incidence angle	Sec. 5.2
β	1/m	Radial wave number	Eq. 2.24
β	Degrees	Rotor blade exit angle	Sec. 5.2
γ	Degrees	Absolute flow velocity vector angle	Sec. 5.2
Δ	–	Difference	
λ	W/mK	Thermal conductivity	
μ	Pa s	Dynamic viscosity	
ν	1/m	Constant term	Eq. 2.28
π	–	Turbine pressure ratio	
ρ	kg/m^3	Fluid density	Eq. 2.4
ρ'	kg/m^3	Sound density	
σ	–	Hub-to-tip ratio	$\frac{R_i}{R_o}$
φ	°	Circumferential coordinate	
Ω	rad/s	Rotor angular velocity	
Ω_m	rad/s	m-lobe angular velocity	Eq. 2.68
ω	rad/s	Sound waves angular frequency	

Subscripts

Symbol	Meaning
$(.)_0$	Steady mean value
$(.)_{amb}$	Ambient condition of a physical quantity
$(.)_{avg}$	Average value of a physical quantity
$(.)_c$	Computed quantity
$(.)_{\text{Cut-On}}$	Propagating acoustical mode
$(.)_{nom}$	Nominal physical quantity
$(.)_p$	Periodically varying signal component
$(.)_{rel}$	Normalized physical quantity
$(.)_s$	Simulated quantity
$(.)_{tot-in}$	Total temperature and pressure at the turbine inlet
$(.)_{tot-out}$	Total temperature and pressure at the turbine outlet
$(.)_{var}$	Variable quantity
$(.)_x$	Axial direction
$(.)_\varphi$	Circumferential direction

Superscripts

Symbol	Meaning
$(.)^+$	Downstream sound propagation (in the flow direction)
$(.)^-$	Upstream sound propagation (against the flow direction)
$(.)'$	Unsteady perturbation

Mathematical symbols

Symbol	Meaning
∇	Nabla operator
∇^2	Laplace operator

Mathematical functions

Symbol	Meaning
$f(s)$	General solution of the Bessel differential equation, Eq. 2.33
$f(x)$	Harmonic function describing the axial sound pressure distribution
$g(r)$	General Bessel function describing the radial sound pressure distribution
$h(\varphi)$	Harmonic function describing the circumferential sound pressure distribution
J_m	Bessel function m-*th* order
J'_m	Derivative of the Bessel function m-*th* order
U_m^σ	Temporal function for the determination of the eigenvalues $s_{[mn]}$
Y_m	Neumann function m-*th* order
Y'_m	Derivative of the Neumann function m-*th* order

Acronyms

Abbreviation	Meaning
ANC	**A**ctive **N**oise **C**ontrol
BNF	**B**ürger**n**ahes **F**lugzeug
BPF	**B**lade-**P**assing **F**requency
DIN	**D**eutsches **I**nstitut für **N**ormung
DLR	**D**eutsches Zentrum für **L**uft- und **R**aumfahrt
EGV	**E**xit **G**uide **V**anes
FFT	**F**ast **F**ourier **T**ransformation
FIR	**F**inite **I**mpulse **R**esponse Filter
ICAO	**I**nternational **C**ivil **A**viation **O**rganization
IGV	**I**nlet **G**uide **V**anes
LPT	**L**ow-**P**ressure **T**urbine
LUH	**L**eibniz **U**niversität **H**annover
ODE	**O**rdinary **D**ifferential **E**quation
PDE	**P**artial **D**ifferential **E**quation
PLEA	**P**hase-**L**ocked **E**nsemble **A**verage
PNL	**P**erceived **N**oise **L**evel

RMA	**R**adial **M**ode **A**nalysis
RMS	**R**oot **M**ean **S**quare
SK	**S**chrauben**k**ompressor
SPL	**S**ound **P**ressure **L**evel
SVD	**S**ingular **V**alue **D**ecomposition
SNR	**S**ignal-to-**N**oise **R**atio
TDMS	**T**echnical **D**ata **M**anagement **S**treaming
TFD	Institut für **T**urbomaschinen und **F**luid-**D**ynamik

1 Introduction

The first commercial jet flight took place in the early 1950s (Mensen 2003). In May 1952, the British de Havilland Comet jet airliner departed from London flying to Johannesburg as its final destination. This historical milestone was a result of many technological advances that had taken place over several decades, including the development of flight aerodynamics, propulsion, and navigation systems. Despite these advancements, the early Comet was involved in a series of accidents as a result of fuselage structural problems, severely damaging both the company's image and the machine's reputation. This prevented the commercial flight industry to quickly rely on jet propelled aircrafts. Despite this fact, in October 1958, the Pan Am jet passenger airliner Boeing 707, equipped with four JT3D Pratt & Whittney turbojet engines, took flight and proved over the years, to be highly reliable with respect to operation and maintenance (Price 1967). Consequently, the commercial feasibility of jet transport was finally confirmed.

The growing popularity of jet transport initiated by the introduction of the Boeing 707 turbojet was, however, accompanied by numerous complaints about noise emissions from residents in neighborhoods around airport areas (Galloway and Von Gierke 1966, Beranek 1969). Particularly in the United States, many airports were confronted with legal actions from those communities even before the corresponding permissions to begin jet aircraft operations were granted. In 1968, a report regarding the aircraft noise problem was presented by the Aeronautics and Space Engineering Board (ASEB 1968), an american governmental agency established in 1967 with the task of introducing appropriate aerospace policies and programs. Within this report, the increase in noise levels with the introduction of each successive new aircraft generation was documented. A series of quantitative results was obtained in terms of the maximum perceived noise levels (PNL)[1] for a Douglas DC-3 propeller-driven airplane (year of introduction into airline service, 1936) and a Boeing 707-120. The measured PNL of both airplanes showed a difference of 31 PNdB and 21 PNdB during take-off and approach, respectively. These figures strengthened the argument that commercial jets exceeded the usual noise levels emitted by other types of aircrafts (propeller-driven and piston-powered machines). At the same time, they justified the rejection of communities close to airports to the introduction of the new type of jet transport.

The negative community reaction to the new jet transport era was and still is supported by several medical and psychological studies which describe the effects of noise on human beings. Those effects include cardiovascular disease, disruption of rest and sleep, changes in auditory threshold, tinnitus, irritation, general mental distress and losses in

---

[1] Scale reflecting the human annoyance to emitted aircraft noise at different frequencies (Smith 1989, Kryter 1960). The perceived noise level is expressed in units of PNdB.

work capacities, among others (Cohen 1969, Jansen 1969, Franssen et al. 2004, WHO 2011). In order to reduce or at least prevent the adverse effects of noise on exposed populations, a series of noise goals and guidelines were recommended during the years following the introduction of the turbojet engine (ASEB 1968, EPA 1971). Some of these recommendations regarding the improvement of environmental performance of aircrafts have materialized through the standards, policies and guidance material prepared by the ICAO (**I**nternational **C**ivil **A**viation **O**rganization) over the past forty years. Specific noise certification standards aimed at reducing noise at the source are given in Annex 16 (ICAO 2008). They intend to ensure that the most recent noise reduction technology is incorporated into aircraft design. The incorporated noise reduction technology should allow normal everyday operation and guarantee a proven quantitative noise reduction around airports (ICAO 2008).

The quantitative noise reduction mandated by the aforementioned legal regulations has been achieved over the last few decades through the introduction of various airplane noise-reducing features. These include, among others, the increase of the engine bypass ratio, defined as the ratio of the mass flow through the fan to the air volume flowing through the core engine (Wilson and Korakianitis 1998). Higher bypass ratios contribute to lower jet exhaust velocities, thus generating reduced jet noise levels while maintaining the same level of thrust (Martens 2002). Further noise reduction solutions comprise the use of acoustical linings, (Bräuling 2009) core serrated nozzle designs which are better known as Chevron nozzles (Bartlett et al. 2004, Reed et al. 2006), and active noise control (ANC) mechanisms (Tapken et al. 2001, Enghardt et al. 2009).

Public concern is expected to grow with the projected increase of general aircraft traffic in the years to come. This in spite of the technological achievements developed by the aeronautical industry and the research community to meet the stringent noise standards derived from noise certification processes. New aircraft will be put into service as well as more departures and landings are expected, with an associated increase in the volume of passengers and freight (Airbus 2013, Boeing 2013). The number of passengers on commercial flights, for example, has been growing at an almost constant annual rate of 6% over the past four decades. This trend will continue - at lower levels - but still close to 5% annually (Airbus 2013). This aggravates the general aircraft noise problem, as residents close to airports are to be increasingly and more frequently exposed to it.

The research cluster "Bürgernahes Flugzeug" (BNF - citizen-friendly airplane) was launched in July 2009 with the aim of addressing this problem. This joint research initiative of the Braunschweig University of Technology (TU Braunschweig), the German Aerospace Center (DLR–**D**eutsches Zentrum für **L**uft- und **R**aumfahrt), and the **L**eibniz **U**niversität **H**annover (LUH), aims at developing the basic technology required to materialize the future of inter-European air transportation (Hummel 2012). This future is based on the vision of providing people with efficient point-to-point connections from small airports close to cities, while considerably reducing the negative impacts on citizens caused by noise and emissions. In order to accomplish this vision, the research cluster focuses its efforts on the development of new aircraft design concepts such as lightweight airframe designs, innovative flight system technologies, and new quiet and low-emission propulsion solutions (Bartelt and Seume 2011).

Regarding the latter of the aforementioned concepts, the Institute of **T**urbomachinery and **F**luid-**D**ynamics (TFD) at the LUH experimentally investigates the sound propagation through a **L**ow-**P**ressure **T**urbine (LPT) with the aim of developing quieter aircraft engines (Bartelt et al. 2013). However, the development of such alternatives requires a detailed study and consequent understanding of the sound transport mechanisms taking place within such a complex system. In order to attain this understanding, a series of experimental measurements focused on the in-duct sound propagation are conducted on a model air turbine, by applying appropriate sound field decomposition techniques. In this way, the spatio-temporal structure of the acoustic field propagating within the turbine can be identified. Therefore, the following objectives and the associated tasks can be established for the current thesis:

- *Implementation, optimization and further development of already existing acoustical measurement and analysis methods suitable for sound propagation in axial turbomachinery.* In this respect, a series of acoustical field decomposition techniques denominated as direct methods (Holste 1995) have proven to be suitable for sound propagation analysis in axial turbomachinery. Among the already existing methods, the **R**adial **M**ode **A**nalysis (RMA) is considered for implementation in this work. The RMA is a well-established evaluation technique developed by the DLR (Holste and Neise 1992) to quantify the sound transmission of the discrete tonal noise components present in turbomachinery and propagating at the **B**lade-**P**assing **F**requency (f_{BPF}). The method resolves the sound field as a superposition of acoustical modes, i.e., space and time varying sound pressure patterns. In this way, a complete representation of the turbine in-duct sound field can be established. Complementary to the further development of the RMA, the implementation of the appropriate acoustic instrumentation required for such studies is envisaged as well.

- *Detailed measurement concept for sound transport measurement in high resolution.* The implementation of the RMA for the intended sound propagation studies requires the development of a measurement unit, integrated into the model air turbine flow channel. As a result, a rotating measurement unit equipped with condenser microphones is proposed as test carrier for the detection of the in-duct propagating acoustical structure.

- *Sensitivity study of the already existing analysis methods for turbomachinery acoustical studies.* A potential for improvement related to the quality of the results derived from the RMA was identified, suggesting the possibility to optimize this existing method. This conclusion derives from the fact that recent studies related to the RMA focus mainly on this aspect rather than on technical implementation details. Numerical studies carried out by Tapken and Enghardt (2006) and Tapken et al. (2008) pointed out the dependence of the RMA output on operating, data acquisition and sensor-related parameters. Despite of the relevance of the results from these investigations, there have been no experimental studies of the influence of such variables on the outcome of the RMA so far.

1 Introduction

Based on the latter item, the present research examines the influence of selected data acquisition parameters on the RMA output. This study is based on sound pressure measurements performed by the aforementioned instrumented rotating-ring system designed for this purpose. The measurement variables taken into account are: (1) the circumferential spacing of the measuring positions, and (2) the number of rotor-triggered revolutions. Both parameters are varied accordingly, allowing to analyze the impact of the performed variations on the output of a measurable quantity, namely, on the sound pressure amplitude of the circumferential modes. Measurements are done under realistic turbine-related conditions including swirling flow, typical operating temperatures and pressures and a single-stage blade configuration.

This approach is useful for several purposes. First, it provides a sensitivity analysis to determine the impact of data acquisition parameters on in-duct acoustical measurements. This is meaningful for planning and implementation of an experimental measurement campaign, which ensures minimal uncertainty in the obtained results. Additionally, an order of magnitude of the expected measurement error from the RMA can be established, allowing a careful experimental design as well as a detailed selection of proper measurement parameters. Finally, this knowledge can be used to define optimum ranges for the data acquisition parameters previously listed.

Having established the scope and main objectives of the present research work and following this introduction, Chapter 2 lays out the theoretical principles related to in-duct and axial turbomachinery sound propagation. A review of several measurement techniques developed during the last four decades for the study of sound propagation in ducts and in axial turbomachinery is presented in Chapter 3. The theoretical aspects and practical application of the RMA are emphasized. Additionally, studies related to its sensitivity to operating and measurement variables are presented as well. Chapter 4 is concerned with the TFD low-pressure multistage air tubine test rig. In the context of this chapter, the experimental setup is presented along with the instrumented rotating-ring used for the in-duct acoustical analysis. The results derived from the RMA for a single-stage turbine configuration and for a selected operating point are presented and discussed in Chapter 5. The propagating acoustical modes are identified and subsequently the circumferential and radial amplitudes corresponding to the aforementioned modes are determined. Chapter 6 presents and discusses the results derived from the sensitivity analysis along with the validation of a simulation routine previously developed to predict the influence of varying measurement and operating parameters on the output of the RMA. This validation is carried out by comparison with the experimental results previously obtained from the turbine measurements. The present document is finalized by presenting the conclusions derived from the performed work along with a series of suggestions for further work.

2 Theoretical Principles of the Sound Propagation in Turbomachines

As stated in the introduction of the present document, the focus of the current research is to determine the influence of data acquisition parameters on the output of the **R**adial **M**ode **A**nalysis (RMA). However, an adequate interpretation of the experimental results derived from the RMA demands a good understanding of the underlying principles of sound propagation within axial turbomachines. As a consequence, within the scope of this chapter, several fundamental topics related to sound propagation are discussed. The chapter starts with the derivation of the acoustic wave equation. This is followed by a discussion of particular cases involving its application and solution for cylindrical geometries. In this respect, special attention is paid to sound propagation in circular and annular geometries, as in general, turbomachinery flow passages feature both cross-sections. Finally, tonal and broadband noise along with rotor-stator interaction and turbomachinery specific sound field structures are presented.

2.1 Mathematical model of the acoustic wave propagation

Among the broad range of disciplines of classical mechanics, aeroacoustics deal with sound generated aerodynamically, either by turbulent fluid motion or by aerodynamic forces interacting with surfaces (Beranek 1969, Delfs 2011). Within the physical properties most frequently occurring in fluid mechanics, those directly related to viscous and inertial effects contribute to pressure fluctuations within the flow field. Viscous effects are reflected on the elasticity of the fluid, quantified by the bulk modulus K, a measure of the fluid reaction to compression. Additionally, inertial effects are quantified by the mass of the air molecules and its resistance to be displaced from their rest position. Because of these two properties, pressure disturbances take place once air molecules are put into motion as a result of aerodynamic forces (aeroacoustics) or externally applied forces or motion (classical acoustics). Those fluctuations are transmitted to the surrounding medium, i.e., to the adjacent air molecules and propagate as sound waves away from the excitation source.

The sound propagation process is therefore caused by the small perturbations in the flow about a mean reference value. The physical processes taking place can be described by the acoustic wave equation, which is in turn derived from the classical conservation equations of the fluid mechanics. In this respect, and considering that aeroacoustics are related to sound propagation through fluids with low dynamic viscosity ($\mu = 2{\cdot}10^{-5}$ Pa s) and thermal conductivity ($\lambda = 2.4 \cdot 10^{-2}$ W m^{-1} K^{-1}), both effects can be neglected (Goldstein 1976), thus allowing the quantification of the flow fluctuations by means of the continuity (cf. Eq. 2.1) and Euler equations (cf. Eq. 2.2) in vector notation:

$$\frac{\partial \rho}{\partial t} + \nabla \cdot (\rho \mathbf{v}) = 0 \tag{2.1}$$

$$\rho \left(\frac{\partial \mathbf{v}}{\partial t} + (\mathbf{v} \cdot \nabla) \mathbf{v} \right) + \nabla p = 0 \tag{2.2}$$

The variable ρ represents the fluid density, $\mathbf{v}$ is the velocity vector of the fluid and p its pressure. Both expressions are defined for the Cartesian spatial coordinate system (x, y, z) (cf. Fig. 2.1).
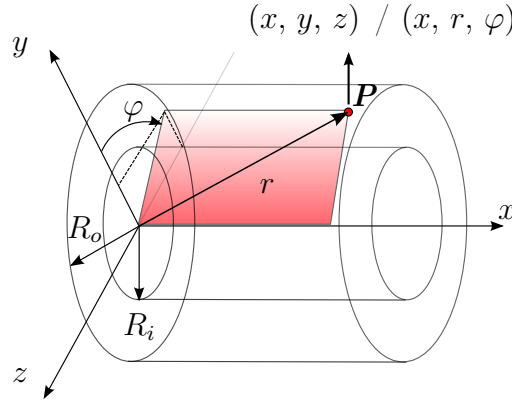
Figure 2.1: Representation of a point P in a concentric duct in Cartesian and cylindrical coordinates

Following the wave equation derivation approach of Ehrenfried (2004), both conservation equations (Eqs. 2.1 and 2.2) are first linearized. This requires the distinction of the intrinsic flow field magnitudes from those exclusively related to the acoustic phenomena. This is done by replacing all flow variables $(p, \rho, \mathbf{v})$ present in the conservation equations by a small unsteady perturbation $(p', \rho', \mathbf{v}')$ superposed to steady mean values $(p_0, \rho_0, \mathbf{v}_0)$:

$$p = p_0 + p' \tag{2.3}$$

$$\rho = \rho_0 + \rho' \tag{2.4}$$

$$\mathbf{v} = \mathbf{v}_0 + \mathbf{v}' \tag{2.5}$$

In this way, all flow variables are constituted by a mean steady value plus a small and unsteady perturbation. For the velocity decomposition (cf. Eq. 2.5), it will be first

assumed that the fluid is in rest ($\mathbf{v}_0 = \mathbf{0}$). This assumption is however not realistic when considering turbine flow. As a way to overcome this limitation, the results of this section are complemented with the representation of the acoustic wave equation under the assumption of uniform flow in Sec. 2.3. The expressions including the mean values of the variables superposed by the unsteady fluctuations are accordingly substituted in the conservation equations (Eqs. 2.1 and 2.2). Products between unsteady fluctuations are considered to be very small and are therefore neglected, resulting in the expressions:

$$\frac{\partial \rho'}{\partial t} + \rho_0 \nabla \cdot \mathbf{v}' = 0 \tag{2.6}$$

$$\rho_0 \frac{\partial \mathbf{v}'}{\partial t} + \nabla p' = 0 \tag{2.7}$$

The set of resulting equations describe the small fluctuations of a steady inviscid mean flow in terms of the flow variables pressure, density, and velocity. In this respect, and in order to establish a single expression for the fluctuating sound pressure p', the time derivative of Eq. 2.6 is determined accompanied by the calculation of the divergence of Eq. 2.7. This procedure results in the following equations:

$$\frac{\partial^2 \rho'}{\partial t^2} + \rho_0 \nabla \cdot \left(\frac{\partial \mathbf{v}'}{\partial t} \right) = 0 \tag{2.8}$$

$$\rho_0 \nabla \cdot \left(\frac{\partial \mathbf{v}'}{\partial t} \right) + \nabla \cdot (\nabla p') = 0 \tag{2.9}$$

Both equations are subtracted, giving rise to the expression:

$$\frac{\partial^2 \rho'}{\partial t^2} - \nabla^2 p' = 0 \tag{2.10}$$

with ∇^2 representing the Laplace operator. To account only for the acoustical phenomena within the inviscid flow field, a separate equation for the pressure perturbation has to be established. This is necessary, since Eq. 2.10 still comprises two fluctuating flow variables. A single dependent variable differential equation is established by setting a mathematical relationship between density and pressure. This is accomplished with a Taylor series expansion, in which the fluctuating pressure as a function of density is represented as an infinite sum of terms, calculated from the function's derivative at an specific point:

$$p(\rho) = p_0 + p' = p_0 + \left. \frac{\partial p}{\partial \rho} \right|_{\rho_0} \rho' + \left. \frac{\partial^2 p}{\partial \rho^2} \right|_{\rho_0} \frac{\rho'^2}{2} + \dots \tag{2.11}$$

Higher order terms are dropped, resulting in a relationship between two state variables and the speed of sound, which is defined according to Spurk and Aksel (2010) as:

$$a^2 = \left(\frac{\partial \rho}{\partial p} \right)^{-1} \tag{2.12}$$

In this way, the resulting expression turns out to be the fluid equation of state for an isentropic gas, in which the pressure varies only with the fluid density:

$$p' = a^2 \rho' \tag{2.13}$$

The acoustic wave equation is finally established by inserting Eq. 2.13 in the previously linearized pressure-density relationship (cf. Eq. 2.10):

$$\frac{1}{a^2} \frac{\partial^2 p'}{\partial t^2} - \nabla^2 p' = 0 \tag{2.14}$$

The acoustic wave equation describes the sound propagation in a geometry defined by the Cartesian coordinate system (x, y, z), in which no air flow is present.

2.2 Acoustic wave equation in cylindrical coordinates

The linearized acoustic wave equation represents the starting point of any analysis related to sound propagation. Its importance lies in mathematically defining the time and space variation of sound pressure. As such, an analytical solution of the acoustic wave equation leads to a clear representation of the distribution and time history of the sound pressure within defined spatial boundaries. Those boundaries are chosen to be a straight, hard-walled concentric cylindrical duct, as represented in Fig. 2.1. These geometrical attributes resemble the flow channel of an axial turbine. In the sections to follow, the mathematical background of the sound propagation within cylindrical geometries is presented and discussed previous to the introduction of the RMA. As previously indicated, the sound propagation within axial turbomachinery is modeled by assuming a cylindrical, hard-walled geometry. In order to adapt the sound propagation domain to the existing mathematical model, an expression for the linearized acoustic wave equation (cf. Eq. 2.14) in cylindrical coordinates (x, r, φ) has to be established. For this purpose, two operators are introduced, the gradient (∇), and Laplacian (∇^2) operators:

$$\nabla = \left(\frac{\partial}{\partial r}, \frac{1}{r} \frac{\partial}{\partial \varphi}, \frac{\partial}{\partial x} \right)^T \tag{2.15}$$

$$\nabla^2 = \frac{1}{r} \left(r \frac{\partial}{\partial r} \right) + \frac{1}{r^2} \frac{\partial}{\partial \varphi^2} + \frac{\partial}{\partial x^2} \tag{2.16}$$

The substitution of the Laplace operator (cf. Eq. 2.16) in Eq. 2.14 results in an expression for the linearized wave equation in cylindrical coordinates, under the assumption of no in-duct air flow:

$$\frac{1}{a^2} \frac{\partial^2 p'}{\partial t^2} - \frac{\partial^2 p'}{\partial x^2} - \frac{1}{r} \frac{\partial}{\partial r} \left(r \frac{\partial p'}{\partial r} \right) - \frac{1}{r^2} \frac{\partial^2 p'}{\partial \varphi^2} = 0 \tag{2.17}$$

A uniform air flow condition within the cylindrical duct may be accounted for the mathematical model under the following simplifications and assumptions:

1. The air flow possesses a single axial mean velocity component $\mathbf{v} = (u, 0, 0)$, constant everywhere.

2. The flow velocity is assumed to be subsonic, i.e., $\mathrm{Ma}_x \ll 1$ ($\mathrm{Ma}_x = u/a$, Mach number defined in axial direction).

3. No gradients of the speed of sound are considered to occur over the in-duct cross section, i.e., the speed of sound a is constant.

4. Wall friction effects are neglected, i.e., no boundary layer effects are considered.

The incorporation of the previously listed assumptions in the mathematical model requires the substitution of the time derivative in Eq. 2.17 with the material derivative, expressed for the fluctuating sound pressure p':

$$\frac{Dp'}{Dt} = \frac{\partial p'}{\partial t} + (\mathbf{v} \cdot \nabla) p' \tag{2.18}$$

Thus, the linearized wave equation in cylindrical coordinates under the assumption of uniform axial flow and in terms of the axial Mach number is:

$$\frac{1}{a^2} \frac{\partial^2 p'}{\partial t^2} + \frac{2\mathrm{Ma}_x}{a} \frac{\partial^2 p'}{\partial x \partial t} - \left(1 - \mathrm{Ma}_x^2\right) \frac{\partial^2 p'}{\partial x^2} - \frac{1}{r} \frac{\partial}{\partial r} \left(r \frac{\partial p'}{\partial r}\right) - \frac{1}{r^2} \frac{\partial^2 p'}{\partial \varphi^2} = 0 \tag{2.19}$$

2.3 Solution of the acoustic wave equation for uniform flow

A solution for the wave equation of the form

$$p'(x, r, \varphi, t) = f(x)g(r)h(\varphi)\mathrm{e}^{i\omega t} \tag{2.20}$$

is proposed. The solution approach is based on the method of separation of variables, in which for each variable an independent function is determined. According to the separation approach, all terms depending on the space coordinates (x, r, φ) have to be individually isolated on one side of Eq. 2.20. In order to guarantee the validity of the undertaken approach, both sides of the modified equation have to be constant. In this way, a single partial differential equation (PDE) can be transformed into three ordinary differential equations (ODE) with corresponding boundary conditions.

Starting with the circumferential variable φ, a close examination of Eq. 2.20 reveals that after multiplying the whole expression with r^2, the φ-only dependent term can be moved to the right and set to be equal to a constant ν. This is possible due to the fact that the function $h(\varphi)$ is independent of r and x, as previously pointed out. Accordingly, the ordinary differential equation for the function $h(\varphi)$ is:

$$\frac{1}{h(\varphi)} \frac{d^2 h(\varphi)}{d\varphi^2} = -\nu^2 \tag{2.21}$$

A similar procedure is performed for the x-only dependent terms, resulting in an ordinary differential equation for $f(x)$ of the form:

$$\left(1 - \text{Ma}_x^2\right) \frac{1}{f(x)} \frac{d^2 f(x)}{dx^2} - 2ik\text{Ma}_x \frac{1}{f(x)} \frac{df(x)}{dx} = -\alpha^2 \tag{2.22}$$

in which k represents the wave number, defined as the ratio of the angular frequency to the speed of sound, $k = \omega/a$. For the remaining variable r, a direct derivation of an independent function for $g(r)$ is not possible, since two terms of the partial differential equation depend on r. To overcome this situation, $g(r)$ is written in terms of the unknown constants ν and α. After reorganizing, the ODE for $g(r)$ is expressed as

$$r^2 \frac{1}{g(r)} \frac{d^2 g(r)}{dr^2} + \frac{1}{g(r)} \frac{dg(r)}{dr} + r^2 \beta^2 - \nu^2 = -\alpha^2 \tag{2.23}$$

with β^2, the radial wave number (Nijboer 2001), defined as

$$\beta^2 = k^2 + \alpha^2 \tag{2.24}$$

In this way, the governing equations for the space coordinates x, r, and φ and their respective functions $f(x)$, $g(r)$, and $h(\varphi)$ are defined. The solution for each ordinary differential equation is separately covered in the sections to follow.

2.3.1 Circumferential sound pressure distribution

A proposed solution for the ODE for φ (Eq. 2.21) is a function of the form $\text{e}^{\pm i\nu\varphi}$, specifically:

$$h(\varphi) = A_1 \text{e}^{-i\nu\varphi} + B_1 \text{e}^{i\nu\varphi} \tag{2.25}$$

Since the solution for the circumferential pressure distribution has to be valid for a cylindrical axisymmetric geometry, it is reasonable to consider the establishment of a periodic boundary condition. This boundary condition guarantees the periodicity of the circumferential sound field and is expressed in terms of the following equations:

$$h(\varphi) = h(\varphi + 2\pi) \tag{2.26}$$

$$\frac{h(\varphi)}{d\varphi} = \frac{h(\varphi + 2\pi)}{d\varphi} \tag{2.27}$$

Both boundary conditions can only be fulfilled if the solution is a periodic function with an arbitrary integral number of periods ν around the physical domain circumference.

In the related literature (Carolus 2013, Ehrenfried 2004), the constant ν is denoted by m and referred to as circumferential mode order. It defines the number of sound pressure periods taking place in the circumferential direction and is mathematically expressed as:

$$\nu = m \in \mathbb{N} \tag{2.28}$$

Equation 2.25 stands for the circumferential sound propagation in counterclockwise or positive direction (first term) and clockwise or negative direction (second term). The inclusion of negative integrals for the circumferential mode order simplifies Eq. 2.25 to:

$$h(\varphi) = A_1 \mathrm{e}^{-im\varphi} \tag{2.29}$$

2.3.2 Radial sound pressure distribution

The function $g(r)$ mathematically describes the sound propagation in radial direction. It is determined by first rearranging Eq. 2.23 to

$$r^2 \frac{d^2 g(r)}{dr^2} + r \frac{dg(r)}{dr} + (r^2 \beta^2 - \nu^2)g(r) = 0 \tag{2.30}$$

with the substitutions

$$s = \beta r \tag{2.31}$$

and $\nu = m$ (cf. Eq. 2.28). Equation 2.30 resembles a Bessel differential equation, found in the literature as (Abramowitz and Stegun 2007):

$$s^2 \frac{d^2 f(s)}{dr^2} + s \frac{df(s)}{dr} + (s^2 - m^2)f(s) = 0 \tag{2.32}$$

The general solution of the Bessel differential equation is

$$f(s) = A_2 J_m(s) + B_2 Y_m(s) \tag{2.33}$$

where J_m and Y_m are the ordinary Bessel and Neumann functions, respectively. The order of each function is given by m. A_2 and B_2 are unknown constants. The first four Bessel functions J_0, J_1, J_2, and J_3 as well as the first four Neumann functions Y_0, Y_1, Y_2, and Y_3 are sketched in Figs. 2.2 and 2.3, respectively. It can be noticed that J_0 resembles a damped cosine function, whereas higher order Bessel functions are similar to damped sine functions. Neumann functions present a comparable harmonic damping behavior, but in contrast to the Bessel functions, they exhibit a singularity at the origin ($s = 0$). The general solution $f(s)$ can be adapted to the initially given ODE, Eq. 2.30 using the above established substitution, Eq. 2.31. The result is summarized as follows

$$g(r) = A_2 J_m(\beta r) + B_2 Y_m(\beta r) \tag{2.34}$$

and given in terms of the constant β. The determination of the unknown constants β, A_2, and B_2 requires the establishment of appropriate boundary conditions and the distinction of two geometrical cases. The considered geometries are a cylindrical duct of radius R_o and an annular duct, also of external radius R_o, with a co-axially integrated inner cylindrical body of radius R_i. Both cases are discussed separately (cf. Fig. 2.1).
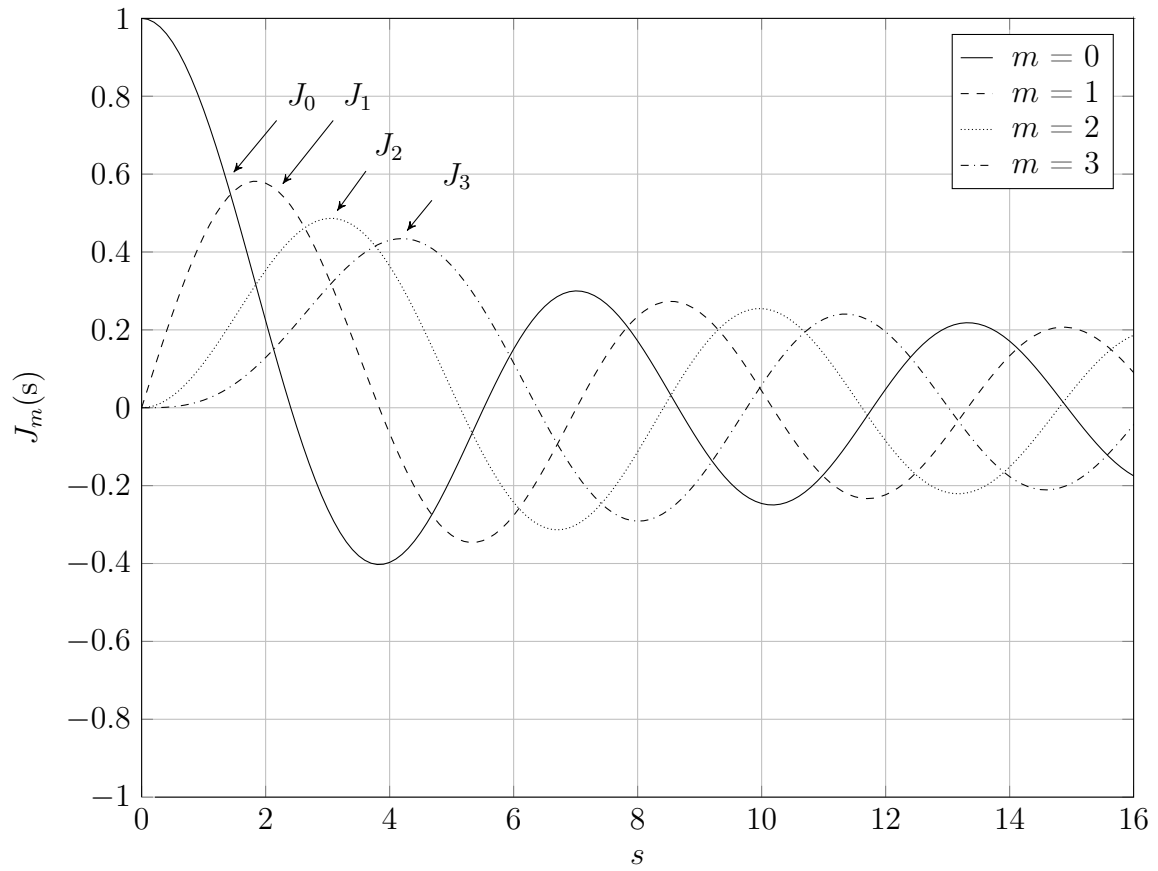
Figure 2.2: Bessel function J_m plot for integer orders $m = 0, 1, 2,$ and 3
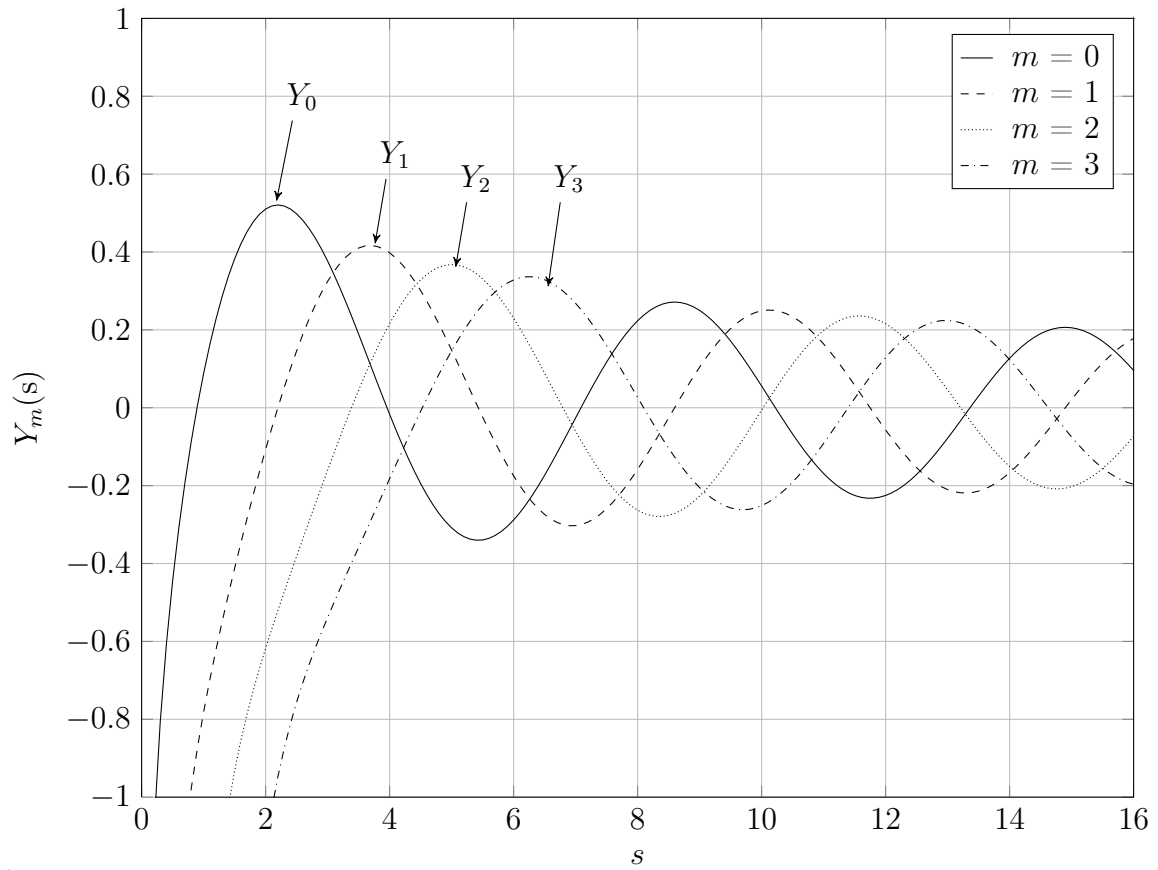
Figure 2.3: Bessel function Y_m plot for integer orders $m = 0, 1, 2,$ and 3

Circular cross-section

Since the duct surface is assumed to be rigid, the particle velocity in radial direction u'_r (cf. Fig. 2.1) should vanish at the duct wall. This is mathematically expressed as:

$$u'_r(R_o) = 0 \tag{2.35}$$

As a consequence, the sound pressure gradient normal to the wall takes a value of zero,

$$\frac{\partial p'}{\partial r}\Big|_{r=R_o} = 0 \tag{2.36}$$

resulting in the boundary condition:

$$\frac{dg(R_o)}{dr} = 0 \tag{2.37}$$

A further boundary condition has to be established, as two unknowns have to be determined. However, the second boundary condition cannot be directly deduced from geometrical considerations, but instead is set by examining the Neumann function waveform (cf. Fig. 2.3). At $s = 0$, the Neumann function presents a singularity, i.e., the function is discontinuous at its origin. This means, in a formal sense, that a solution at $r = 0$, in which $B_2 \neq 0$ (cf. Eq. 2.34), would lead to a nonphysical solution, as a result of the singularity at this location. Considering this, for the case of a cylindrical duct, the Neumann function is assumed to vanish, resulting in a value of zero for the constant B_2. Applying this derived result, the function $R(r)$ is reduced solely to the Bessel function

$$g(r) = A_2 J_m(\beta r) \tag{2.38}$$

Based on this result, the derivative of $g(r)$ represents the second and last boundary condition required for the determination of the unknown constants:

$$J'_m(\beta r)\big|_{r=R_o} = 0 \tag{2.39}$$

As shown in Fig. 2.4, the derivative of the Bessel function J_m oscillates about zero. This fact is a direct consequence of the infinite local extrema present in the Bessel function J_m. As a result of this, an infinite number of β-values which fulfill the boundary condition in Eq. 2.39 can be chosen. For future reference, the derivatives of the Bessel and Neumann functions are defined by the following identities as a function of the radial wave number β, renamed as $\beta_{[mn]}$, according to Abramowitz and Stegun (2007):

$$J'_m(\beta_{[mn]}r) = \frac{1}{2}[J_{m-1}(\beta_{[mn]}r) - J_{m+1}(\beta_{[mn]}r)] \tag{2.40}$$

$$Y'_m(\beta_{[mn]}r) = \frac{1}{2}[Y_{m-1}(\beta_{[mn]}r) - Y_{m+1}(\beta_{[mn]}r)] \tag{2.41}$$
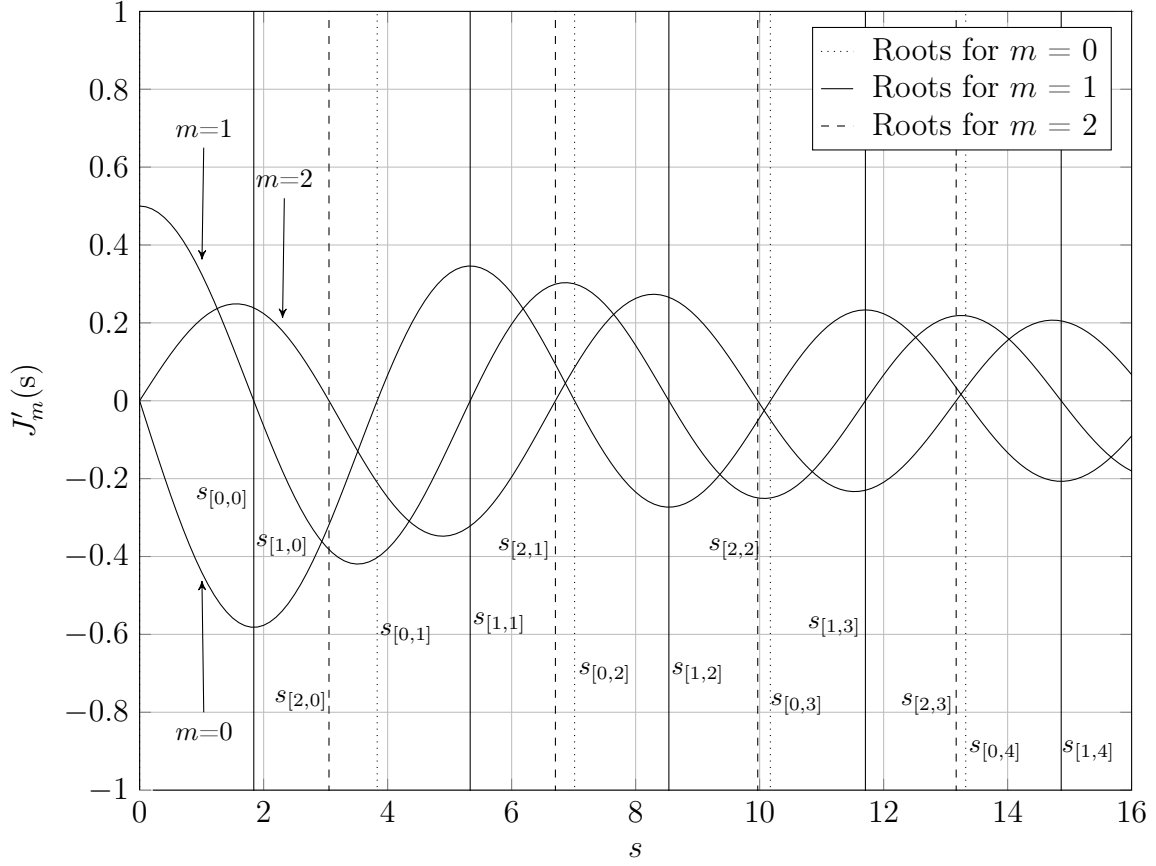
Figure 2.4: Bessel function derivative J'_m for the integer orders $m = 0$, 1, and 2

The positions of the local extrema are arranged according to their order of appearance along the s-axis (cf. Fig. 2.4). These positions are consecutively numbered with an integer $n = 0...\infty$. Accordingly, the local n-th extrema of the m-th order Bessel function is identified by the variable $s_{[mn]}$, the eigenvalues of the radial sound pressure function $g(r)$, defined analog to Eq. 2.31 as

$$s_{[mn]} = \beta_{[mn]}r \tag{2.42}$$

In this way, the solution to the ODE describing the radial behavior of the sound pressure is complete, except for the amplitude A_2, which is simply regarded as a scaling factor.

Annular cross-section

An annular-duct geometry resembles the flow channel of an axial turbomachine. The annular duct is formed by two coaxial cylinders, an external and an internal one with radius R_o and R_i, respectively (cf. Fig. 2.1). In this particular case, two Neumann boundary conditions arise based on the magnitude of the particle velocity u'_r:

$$u'_r(R_o) = 0, \qquad u'_r(R_i) = 0 \tag{2.43}$$

Analogous to the hollow cylinder case, the sound pressure gradient in radial direction is zero at the outer and inner duct wall:

$$\frac{dg(r)}{dr}\Big|_{r=R_o} = 0, \qquad \frac{dg(r)}{dr}\Big|_{r=R_i} = 0 \tag{2.44}$$

As opposed to the previously discussed geometry, the solution of the ODE for $g(r)$ comprises a Bessel function of the first kind as well as a Neumann function, also known as Bessel function of the second kind:

$$g(r) = A_2 J_m(\beta_{[mn]}r) + B_2 Y_m(\beta_{[mn]}r) \tag{2.45}$$

Alternatively, $g(r)$ can be written in terms of an amplitude factor $Q_{[mn]}$, defined as the ratio of the constant B_2 to A_2, $Q_{[mn]} = B_2/A_2$, resulting in the expression:

$$\frac{1}{A_2}g(r) = J_m(\beta_{[mn]}r) + Q_{[mn]}Y_m(\beta_{[mn]}r) \tag{2.46}$$

The determination of the constant $\beta_{[mn]}$ and the amplitude factor $Q_{[mn]}$ is performed by first replacing Eq. 2.46 in Eq. 2.44. This results in the expressions:

$$\frac{d}{dr}\left[J_m(\beta_{[mn]}r) + Q_{[mn]}Y_m(\beta_{[mn]}r)\right]\Big|_{r=R_o} = 0 \tag{2.47}$$

$$\frac{d}{dr}\left[J_m(\beta_{[mn]}r) + Q_{[mn]}Y_m(\beta_{[mn]}r)]\right]\Big|_{r=R_i} = 0 \tag{2.48}$$

which are equivalent to:

$$J'_m(\beta_{[mn]}R_o) + Q_{[mn]}Y'_m(\beta_{[mn]}R_o) = 0 \tag{2.49}$$

$$J'_m(\beta_{[mn]}R_i) + Q_{[mn]}Y'_m(\beta_{[mn]}R_i) = 0 \tag{2.50}$$

Equations 2.49 and 2.50 represent a system of equations with two unknowns, $\beta_{[mn]}$ and $Q_{[mn]}$. The determination of both constants is accomplished by first eliminating $Q_{[mn]}$ from Eq. 2.49:

$$Q_{[mn]} = -\frac{J'_m(\beta_{[mn]}R_o)}{Y'_m(\beta_{[mn]}R_o)} \tag{2.51}$$

The substitution of the right side of this expression into Eq. 2.50 results in:

$$J'_m(\beta_{[mn]}R_i)Y'_m(\beta_{[mn]}R_o) - J'_m(\beta_{[mn]}R_o)Y'_m(\beta_{[mn]}R_i) = 0 \tag{2.52}$$

The derivatives of the Bessel and Neumann functions in Eq. 2.52 are afterwards substituted by the expressions in Eqs. 2.40 and 2.41, resulting in two general equations, one for the amplitude factor $Q_{[mn]}$ and a second one for the determination of the constant $\beta_{[mn]}$ and the corresponding eigenvalues $s_{[mn]}$:

$$Q_{[mn]} = \frac{J_{m+1}(s_{[mn]}) - J_{m-1}(s_{[mn]})}{Y_{m-1}(s_{[mn]}) - Y_{m+1}(s_{[mn]})} \tag{2.53}$$

15

$$0 = [J_{m-1}(s_{[mn]}\sigma) - J_{m+1}(s_{[mn]}\sigma)][Y_{m-1}(s_{[mn]}) - Y_{m+1}(s_{[mn]})]$$
$$- [J_{m-1}(s_{[mn]}) - J_{m+1}(s_{[mn]})][Y_{m-1}(s_{[mn]}\sigma) - Y_{m+1}(s_{[mn]}\sigma)]$$

(2.54)

The variable σ in Eq. 2.54 is the hub-to-tip ratio, defined as the ratio of the duct inner to outer radius ($\sigma = R_i/R_o$). The procedure to determine $\beta_{[mn]}$ and $s_{[mn]}$ is analogous to that performed for the cylindrical geometry. To clarify this procedure, the right side of Eq. 2.54 is equated to the variable $U_m^\sigma(s_{[mn]})$ instead of being set equal to zero:

$$U_m^\sigma(s_{[mn]}) = [J_{m-1}(s_{[mn]}\sigma) - J_{m+1}(s_{[mn]}\sigma)][Y_{m-1}(s_{[mn]}) - Y_{m+1}(s_{[mn]})]$$
$$- [J_{m-1}(s_{[mn]}) - J_{m+1}(s_{[mn]})][Y_{m-1}(s_{[mn]}\sigma) - Y_{m+1}(s_{[mn]}\sigma)]$$

(2.55)

The function $U_m^\sigma(s_{[mn]})$ is plotted for $m = 1$ and $\sigma = 0.5$ (hub-to-tip ratio), as shown in Fig. 2.5. The function has an infinite number of roots. These represent the eigenvalues $s_{[mn]}$ required for the determination of the radial wave number $\beta_{[mn]}$.
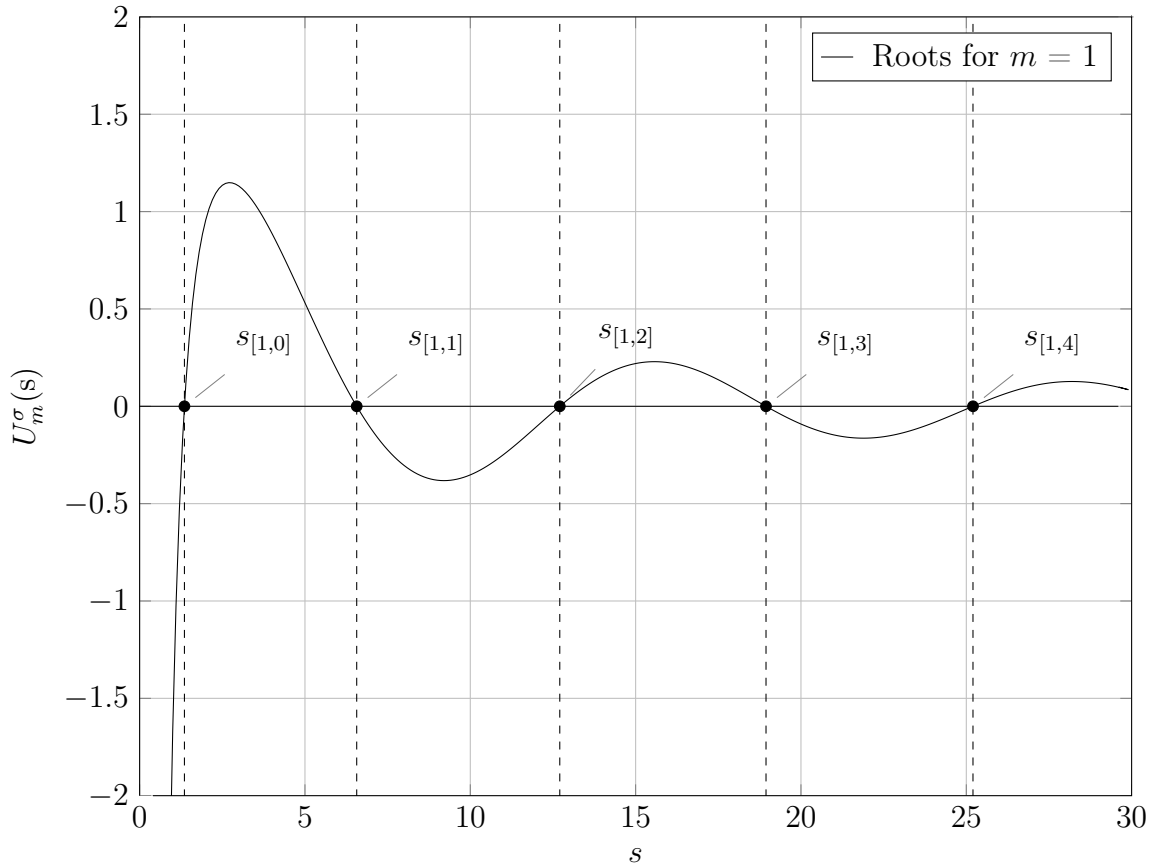
Figure 2.5: Waveform of the function $U_m^\sigma(s)$ for the integer order $m = 1$ and hub-to-tip ratio $\sigma = 0.5$
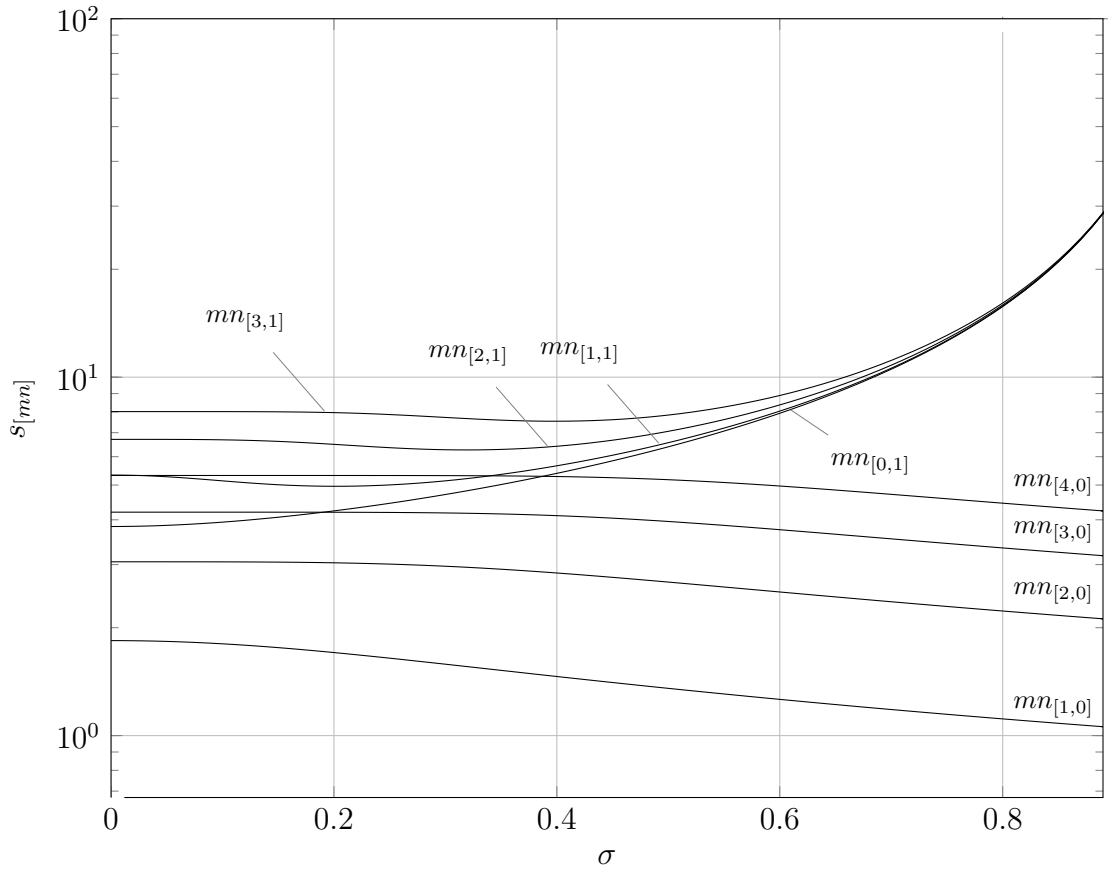
Figure 2.6: Eigenvalues for modes (m, n) as a function of the hub-to-tip ratio σ
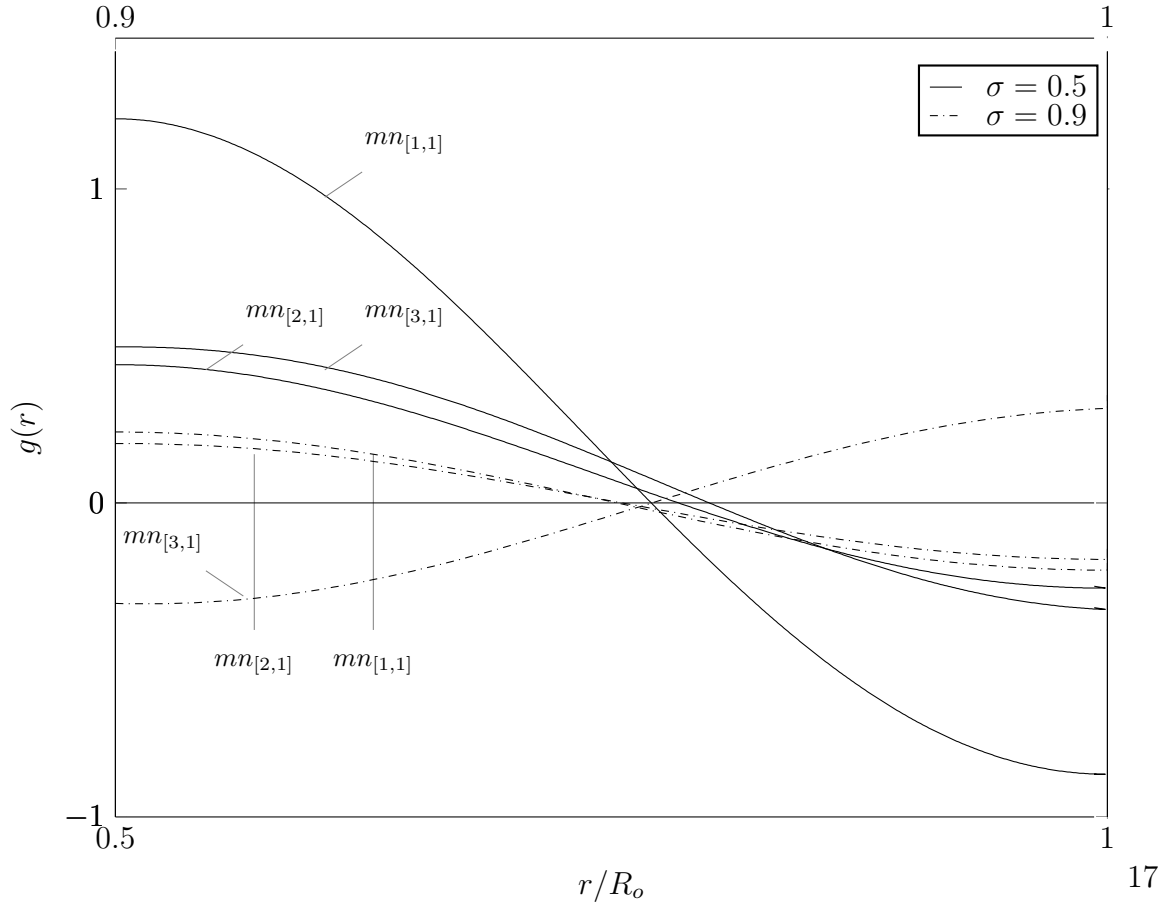
Figure 2.7: Radial sound pressure profile for selected modes and σ

Additionally, Fig. 2.6 shows several eigenvalues for chosen mode combinations m and n as well as for $\sigma = 0...0.9$. It can be noticed that a change in σ for low order mode combinations moderately affects the magnitude of the related eigenvalues, whereas for higher order modes, a pronounced increase of the eigenvalue's magnitude is perceived for a change in σ. Figure 2.6 is complemented by the representation of selected radial pressure profiles for the specific mode combinations and the hub-to-tip ratios $\sigma = 0.5$ and 0.75, as shown in Fig. 2.7.

2.3.3 Axial sound pressure distribution

The proposed solution for the ODE representing the analytical sound pressure distribution in axial direction (cf. Eq. 2.22) takes the form:

$$f(x) = A_3 e^{i\lambda^+ x} + B_3 e^{i\lambda^- x} \tag{2.56}$$

Before establishing the complete solution to the axial function $f(x)$, the value of the constant λ in Eq. 2.25 is first determined. This is done by replacing Eq. 2.25 into Eq. 2.22, leading to the expression

$$\lambda^2 - \frac{k \mathrm{Ma}_x}{1 - \mathrm{Ma}_x^2}\lambda - k^2 - \frac{\alpha_{[mn]}^2}{1 - \mathrm{Ma}_x^2} = 0 \tag{2.57}$$

with α replaced by $\alpha_{[mn]}$ and defined as

$$\alpha_{[mn]}^2 = k^2 - \beta_{[mn]}^2 \tag{2.58}$$

after reorganizing Eq. 2.24. As reported by Hanson (1973), Zorumski and Lester (1974), Schiffer (1976) and Hanson (1994), among others, the constant λ is known as axial wave number. This constant will be denoted by $k_{[mn]}$ to highlight its dependence on the mode orders m and n as well as to avoid confusion with the plane wave number k. The quadratic expression presented in Eq. 2.57 is solved for λ, i.e., for $k_{[mn]}$, resulting in two analytical expressions for the axial wave number

$$k_{[mn]}^{\pm} = \frac{k\mathrm{Ma}_x \pm \sqrt{k^2 - (1 - \mathrm{Ma}_x^2)\beta_{[mn]}^2}}{1 - \mathrm{Ma}_x^2} \tag{2.59}$$

with $k_{[mn]}^+$ and $k_{[mn]}^-$ representing the downstream (i.e., in the same direction of the flow) and the upstream axial wave numbers, respectively. This equation is relevant from the point of view of the expected in-duct sound pressure field, since it analytically predicts the axial propagation of specific mode combinations. Before proceeding to the discussion related to the general propagating sound field structure, the general expression for the sound pressure distribution in axial direction is rewritten in terms of the axial wave number:

$$f(x) = A_3 e^{ik_{[mn]}^+ x} + B_3 e^{ik_{[mn]}^- x} \tag{2.60}$$

As previously indicated, the prediction of the in-duct propagating acoustical structure is based on the numerical value of $k_{[mn]}$. Further details related to this structure and its relation to the axial wave number under the influence of turbine-related conditions including swirling flow are discussed in Sec. 2.3.5, following the presentation of the general in-duct sound pressure distribution.

2.3.4 General in-duct sound pressure distribution

With the functions $f(x)$, $g(r)$, and $h(\varphi)$ entirely established, each one is subsequently replaced in the proposed general solution for the acoustic wave equation (cf. Eq. 2.20). This leads to the general analytical expression for the in-duct pressure distribution for a single frequency component ω:

$$p'_{[mn]}(x, r, \varphi, t) = \left(A_3 e^{ik^+_{[mn]}x} + B_3 e^{ik^-_{[mn]}x} \right) g(r) A_1 e^{-im\varphi} e^{i\omega t} \tag{2.61}$$

Equation 2.62 presents a compact version of the previously stated equation, in which the constants A_1, A_3, and B_3 have been summarized in the constants $A^+_{[mn]}$ and $A^-_{[mn]}$:

$$p'_{[mn]}(x, r, \varphi, t) = \left(A^+_{[mn]} e^{ik^+_{[mn]}x} + A^-_{[mn]} e^{ik^-_{[mn]}x} \right) g(r) e^{-im\varphi} e^{i\omega t} \tag{2.62}$$

Considering that the acoustic field prevailing inside a turbomachine is composed of several superimposed space and time dependent sound pressure waves, a complete field representation arises as a result of the addition of individual solutions. In this way, the in-duct pressure distribution is characterized by the general expression

$$p'_{[mn]}(x, r, \varphi, t) = \sum_{m=-\infty}^{\infty} \sum_{n=0}^{\infty} \left(A^+_{[mn]} e^{ik^+_{[mn]}x} + A^-_{[mn]} e^{ik^-_{[mn]}x} \right) g(r) e^{-im\varphi} e^{i\omega t} \tag{2.63}$$

where $p'_{[mn]}$ is the sound pressure and $A^+_{[mn]}$ and $A^-_{[mn]}$ are the complex radial mode amplitudes. As stated before $k^\pm_{[mn]}$ represent the axial wave number. Both parameters are characterized by a $(+)$ and a $(-)$ sign. Both symbols account for the axial propagation direction of the sound waves, which takes place both downstream and upstream of the machine flow channel (cf. Fig. 2.8). Further variables include the angular frequency ω and the time t. The radial dependent term $g(r)$, representing the radial mode shapes, i.e., the sound pressure distribution in radial direction with associated eigenvalues $s_{[mn]}$, is the solution of the general m-*th* order Bessel differential equation (cf. Eq. 2.45).
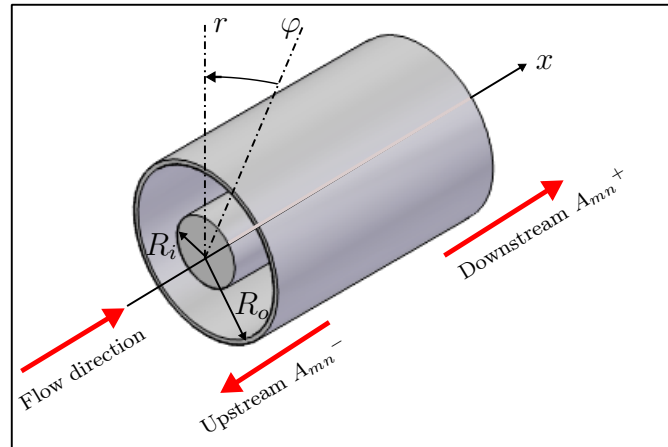
Figure 2.8: Direction of propagation of the radial modes in an annular duct geometry

The general analytical solution represents the sound field generated by an infinite number of acoustical modes (m, n). Each mode combination (m, n) constitutes two sound pressure waves with a common angular frequency ω and respective radial amplitudes $A^+_{[mn]}$ and $A^-_{[mn]}$. Both waves can propagate in axial direction but in opposite senses. While propagating, they rotate and displace radially as well. The ordered pair (m, n) defines a specific acoustical mode. The index m (cf. Eq. 2.28) defines the number of sound pressure cycles taking place in the circumferential direction. The index n, the radial mode order, gives an indication of the sound pressure nodes (zero pressure zones) present along the radial direction.

The general analytical solution (cf. Eq. 2.63) describes in a compact way the three-dimensional and time dependent acoustical modal structure within a duct. This description is carried out through the decomposition of the complex sound field in three elementary harmonic functions, each assigned to a specific space coordinate. Thus, a complete definition of the in-duct sound field requires the specification of a few parameters, including the circumferential mode order m and the associated eigenvalues and axial wave number for a single frequency or even for several frequencies, which implies the superposition of each analyzed component. In order to illustrate the previous statement, the modal structure of a selected mode $mn_{[2,1]}$ is represented schematically in Fig. 2.9.
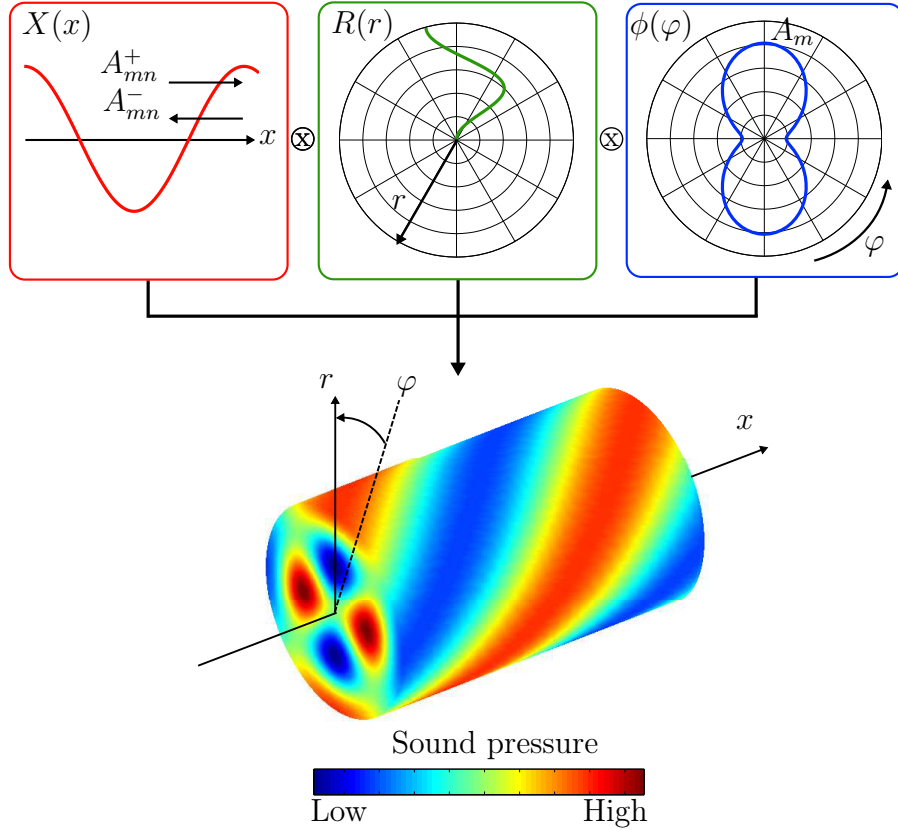
Figure 2.9: Schematic representation of an in-duct $mn_{[2,1]}$ acoustical mode

A circumferential sound pressure pattern corresponding to the azimuthal mode order $m = 2$ and representing the function $h(\varphi)$ can be recognized. The pressure pattern rotates about the x-axis with the frequency ω, featuring an overall quantity of two maximum and two minimum peaks. Beside the circumferential wave form of the sound pressure, the radial modal structure represented by the function $g(r)$ is plotted. For this particular case, a single zero-crossing along the duct radius is identified, which corresponds to the magnitude of the radial mode order, in this case, $n = 1$. In axial direction, a single wave propagating upstream is shown for a particular radial and circumferential position as well as for an specific instant of time. This information is complemented by the three-dimensional pattern shown at the bottom of Fig. 2.9 corresponding as well to the analyzed mode $mn_{[2,1]}$ for the time $t = 0$. For this time instant, a set of spiral waves with varying color patterns representing positive and negative sound pressure magnitudes can be recognized.

With the aim of complementing the previously presented diagram, a cross-sectional representation of the same mode for the time instant $t = 0$ and $x = 0$ is shown in Fig. 2.10. The diagram originates from the product of circumferential and radial sound pressure wave forms varying between $\varphi = 0°...360°$ and $r/R = 0...1$. In order to clarify the rotating character of the sound pressure, the cross-sectional representation of the chosen mode is shown as a sequence of diagrams for several instants of time in Fig. 2.11.
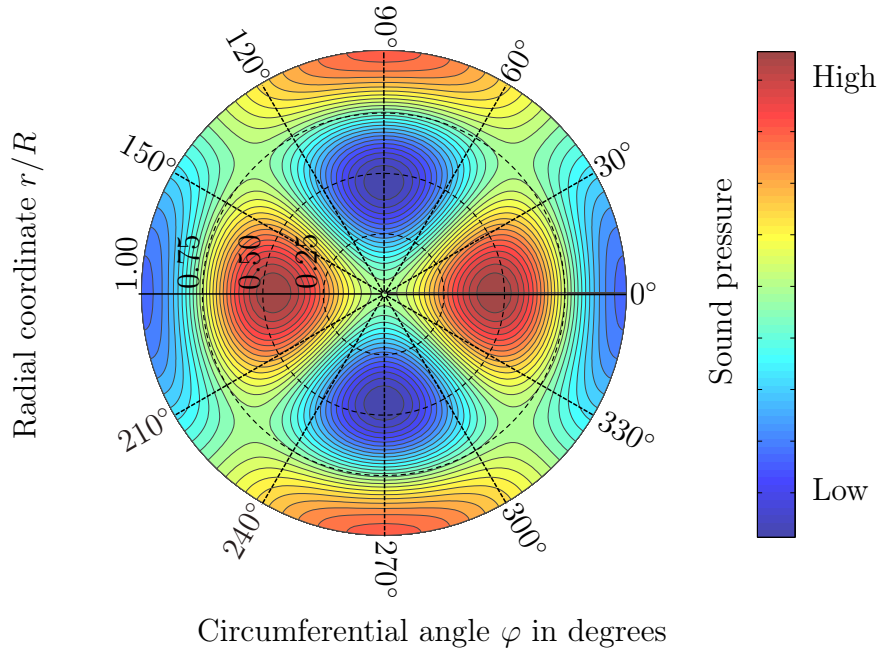
Figure 2.10: Cross-sectional representation mode $mn_{[2,1]}$ acoustical mode for $x = 0$ and $t = 0$

$t = 0.0$ s $\qquad$ $t = 0.25$ s $\qquad$ $t = 0.50$ s $\qquad$ $t = 0.75$ s $\qquad$ $t = 1.0$ s

Sound pressure

Low $\qquad$ High

◯ Reference (rotating) point
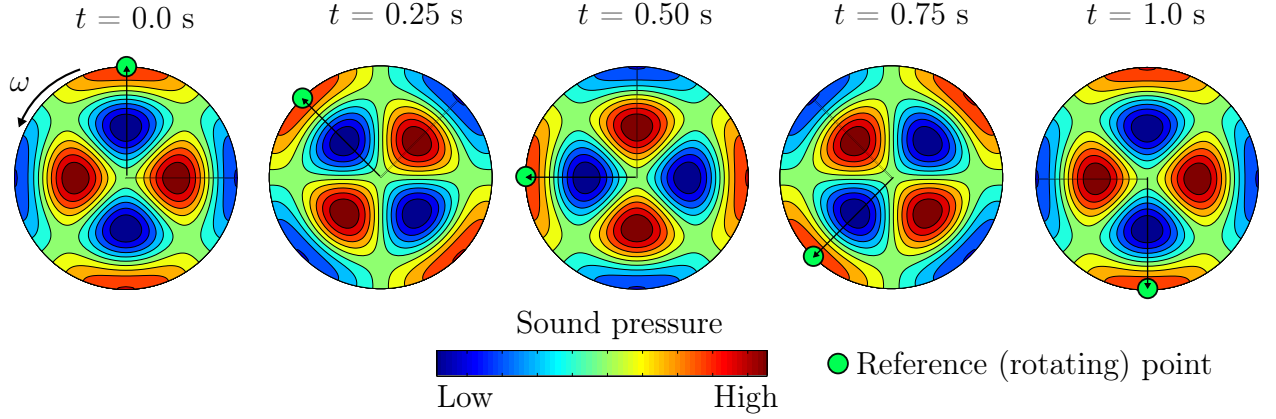
Figure 2.11: Rotating acoustical mode $mn_{[2,1]}$ for selected time instants t and $x = 0$

2.3.5 Propagating modal structure

Knowing beforehand the space variation of the in-duct sound pressure, the current section deals with analytical aspects related to the propagation of such field. In respect thereof, theoretically, an infinite number of acoustical modes constitute the sound field within a cylindrical or annular geometry. However, flow and geometrically related conditions allow the propagation of only a certain quantity of them. The modes constituting the propagating sound field are quantified by the axial wave number $k_{[mn]}^{\pm}$. In this respect, according to Taddei et al. (2009), the accuracy of the sound field decomposition - which is in turn associated with the resulting propagating structure - improves once the dominating in-duct real flow field is adequately modeled. This modeling demands however the consideration of flow non-uniformities, e.g., swirling flow, which prevent the derivation of analytical functions for the axial wave number as that previously derived in Sec. 2.3.3 (cf. Eq. 2.59).

As a consequence, several analytical approximations as well as numerical approaches have been proposed to account for the effect of such non-uniformities in the in-duct acoustical structure (Salant 1967, Lohmann 1977, Golubev and Atassi 1996, Kousen 1999). In respect thereof, Bartelt (2014) conducted a detailed examination and comparison of the validity of several analytical approximations to the axial wave number under consideration of uniform and swirling flow. The considered approximations model the swirling flow in terms of solid body rotation, by which the tangential velocity linearly varies with the radial distance from the duct center line. Among the approximations to the axial wave number $k_{[mn]}^{\pm}$ analyzed by Bartelt (2014), those developed by Kousen (1996) and Nijboer (2001) featured a good agreement with swirling flows results of $k_{[mn]}^{\pm}$ available in the open literature. As a result, the approximation developed by Kousen (1996) is used throughout this work as mode propagating model for the identification of the resulting in-duct acoustical field. The mathematical model is expressed as follows:

$$k_{[mn]}^{\pm} = \frac{\mathrm{Ma}_x}{\mathrm{Ma}_x^2 - 1} \cdot \left(k - m\frac{\mathrm{Ma}_\varphi}{R_o} \right) \mp \frac{1}{\mathrm{Ma}_x^2 - 1} \sqrt{\left(k - m\frac{\mathrm{Ma}_\varphi}{R_o} \right)^2 + (\mathrm{Ma}_x^2 - 1) \cdot \left(\frac{s_{[mn]}}{R_o} \right)^2}$$

$$(2.64)$$

where Ma_φ is the circumferential Mach number and $s_{[mn]}$ the eigenvalues of the radial sound pressure. The latter are not a function of the swirl, represented in terms of the circumferential Mach number, but rather only of the mode orders and the hub-to-tip ratio. A real axial wave number results in a cyclic propagation of the sound pressure in x-direction. This is made evident once $k^+_{[mn]}$ or $k^-_{[mn]}$ are incorporated into the exponential terms $A_3\mathrm{e}^{ik^+_{[mn]}x}$ and $B_3\mathrm{e}^{ik^-_{[mn]}x}$ of $f(x)$ (cf. Eq. 2.60). A complex axial wave number gives rise to a pure real exponent, resulting in an exponential decay or growth of the traveling acoustic wave depending on the sign of the imaginary term. A positive imaginary term represents an evanescent mode; a negative one stands for an amplifying mode. The latter is discarded as non-physical (Golubev and Atassi 1996). Finally, a value of zero in the square root term of Eq. 2.64 derives in a limiting situation, leading to the definition of the Cut-On frequency

$$f_{\text{Cut-On}} = \frac{a}{2\pi R_o} \cdot (m\mathrm{Ma}_\varphi + s_{[mn]}\sqrt{1 - \mathrm{Ma}_x^2}) \tag{2.65}$$

at which a mode (m, n) is first able to propagate. Should $2\pi f_{\text{Cut-On}}$ be greater than the angular frequency ω of a particular mode, then it will contribute to the in-duct acoustical field. Figure 2.12 complements the information regarding the axial wave number variation based on changing flow conditions. The real and imaginary parts of the downstream axial wave number $k^+_{[mn]}$ are shown for a fixed $k = 10$, $\sigma = 0.5$, circumferential mode orders varying between $m = 0, 1, 2, ..., 30$, and a single radial mode order, $n = 1$. The considered flow conditions include no flow, uniform flow with $\mathrm{Ma}_x = 0.3$ and positive and negative swirling flow with $\mathrm{Ma}_x = 0.3$, $\mathrm{Ma}_\varphi = 0.2$. The no flow and uniform flow conditions exhibit similar symmetrical patterns, except for a left shift in $Re(k^+_{[mn]})$, which is reflected in the propagation of more modes. Additionally, modes rotating in the direction of the swirling flow ($-\diamond-$) cut on earlier, i.e., at a lower frequency than that required for modes rotating in the opposite direction ($-*-$). Hence, swirling flow influences the propagating properties of the sound pressure field within an annular geometry.
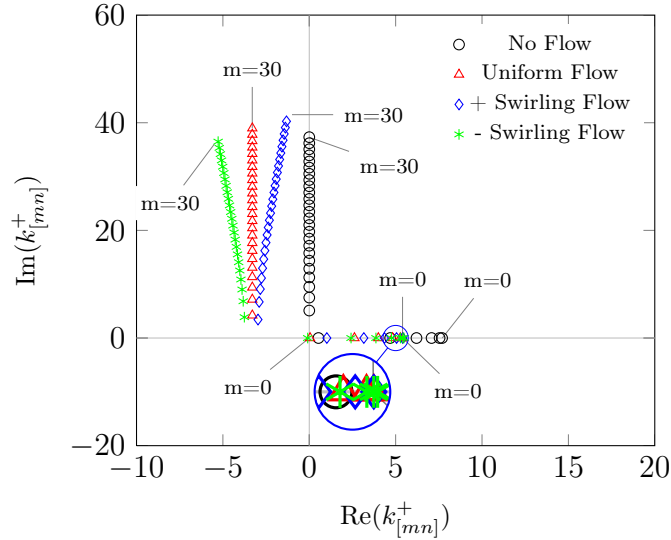
Figure 2.12: Downstream axial wave numbers $k^+_{[mn]}$

2.4 Sound propagation in turbomachinery

Having before analyzed the spatial and temporal variation of the in-duct sound pressure along with its propagation properties, this section gives an insight of the specific sound propagation mechanisms in turbomachinery. In this respect, in turbomachinery-related flows, not every acoustical mode is able to propagate. Sound fields described by the general solution to the wave equation (cf. Eq. 2.63) are excited by an acoustic source, i.e., the rotating and stationary blading in the specific case of turbomachinery (Schiffer 1976, Költzsch 1984). As such, issues related to the in-duct acoustic excitation mechanisms and the resulting noise spectral characteristics are shortly discussed in this section. Additionally addressed issues include potential blading interactions and their influence on the propagating sound field structure within the machine.

2.4.1 Acoustic excitation mechanisms in turbomachinery

The acoustic output of axial flow machines is characterized by a typical frequency spectrum composed of broadband noise resulting from laminar and turbulent boundary layer shedding and discrete noise components generated by impulsive blade loading (Wright 1975). Responsible for the broadband noise are also the mean wake distortions of the flow (Mongenau et al. 1993). A representative noise frequency spectrum from an axial turbomachine exhibits discrete frequency peaks rising above low amplitude broadband noise distributed over a wide range of frequencies (cf. Fig. 2.13). Although the current research is concerned with the turbine noise having components that are multiples of the blade-passing frequency, rather than broadband noise, both noise sources are discussed separately in the following sections. Accordingly, emphasis is set on the tonal noise, since it is the dominant source when treating turbine sound propagation (Smith 1989).
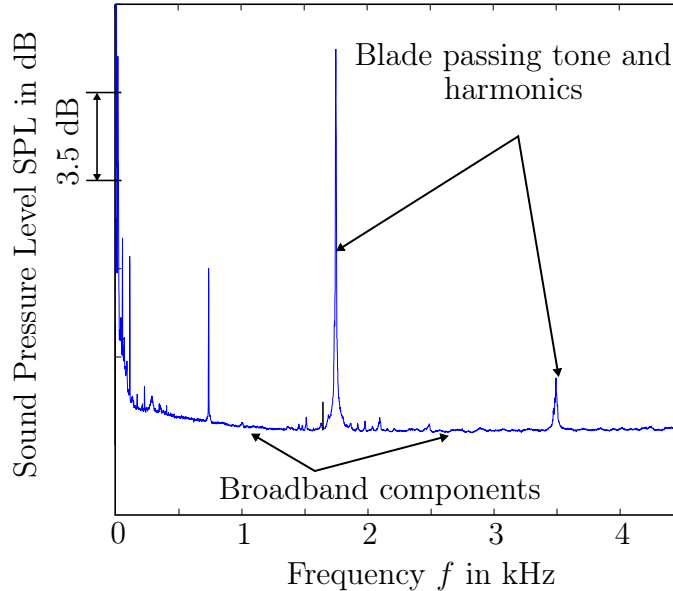
Figure 2.13: Typical frequency spectrum of an axial turbomachine (TFD air turbine, $\dot{m} = 5$ kg s^{-1}, $\Omega = 3500$ min^{-1})

Broadband turbine noise

Broadband noise is of aerodynamic origin (Tyler and Sofrin 1962). It is a consequence of the pressure fluctuations associated with the turbulent flow past a blade surface, resulting in generation and subsequent propagation of sound of random nature. Turbulent flow is induced once air flow is disturbed by a solid surface. Consequently, elements such as the machine inner duct wall and the rotating and stationary turbine stages turn out to be sources of turbulence generation. In this way, in each turbine stage, broadband noise arises as the result of two mechanisms. The first mechanism leading to broadband noise generation is the rotor blade tip interaction with the inner duct wall turbulent boundary layer. In this process, turbulence levels tend to be high provided that the blade tip-speed is a maximum (Smith 1989). A further broadband noise inducing process arises due to the interaction of the turbulent wake shed by the rotor with the the stator (Lowis and Joseph 2006). As concluding remark, several measurement techniques have been developed during the last years to allow the quantification of broadband noise, including inverse methods (Lowis and Joseph 2006) and decomposition of broadband acoustical modes based on the spectral cross correlation techniques (Enghardt et al. 2007).

Tonal turbine noise

The source of discrete tones in axial turbomachinery are the cyclic pressure field and wake interactions between rotating and stationary stages (Smith 1989). Both processes take place once rotating blades and stationary obstructions, including stator stages, support struts and inlet guide vanes interact (Yardley 1974). Each discrete tone is associated with a specific frequency, the blade-passing frequency (f_{BPF}), defined as the product of the number of blades in a row and the rotor angular speed (Peake and Parry 2012). Fig. 2.14 ilustrates the concept of the f_{BPF} for a four-bladed rotor turning at $\Omega = 120$ min^{-1}.
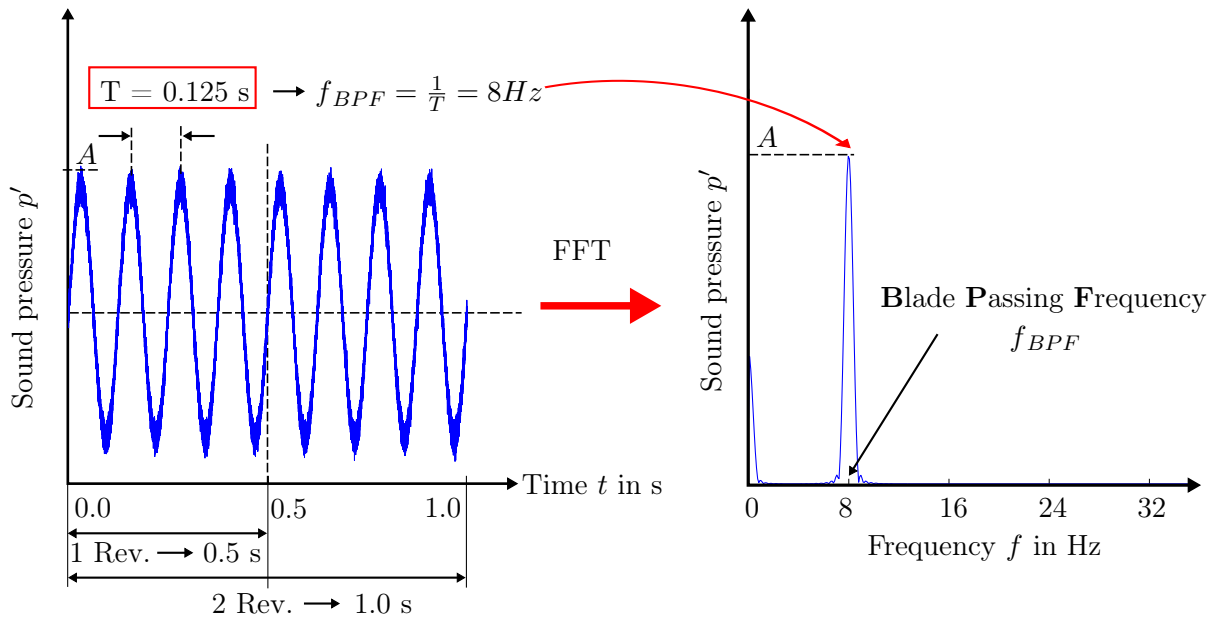
Figure 2.14: Example of a frequency spectrum of an axial turbomachine

The pressure patterns resulting from the previously mentioned interactions lead to rotating lobe-shaped pressure distributions, the so-called spinning modes. The spinning modes propagating within axial turbomachinery are predominantly produced by two acoustic sources, a single rotor (i.e., fan) or a rotor-stator configuration. For the case of a single rotor, the pressure field is constituted by the superposition of circumferential pressure patterns turning with rotor rotational speed Ω. Each circumferential pressure pattern is represented by a number of lobes proportional to an integer multiple or harmonic $h = 0,1,2,...$ and the number of rotor blades B.

$$m = hB \tag{2.66}$$

Thus, the number of lobes associated with each rotating pressure pattern corresponds to the circumferential mode order m. In this case, only one circumferential mode is excited for the fundamental f_{BPF} as well as for each corresponding harmonic component. However, this is not the case for the rotor-stator interaction, in which for each single frequency a wide variety of spinning modes are produced. The rotor-stator interaction noise at f_{BPF} and associated harmonics is in contrast generated by several superposed sound pressure patterns, i.e., acoustical modes, each pattern having a specific number of lobes and a defined rotational speed. The specific modes produced as a result of the rotor-stator interaction are defined by the following model proposed by Tyler and Sofrin (1962):

$$m = hB + sV \tag{2.67}$$

In addition to the variables of the rotor-alone configuration, V denotes the number of stator vanes and s is an integer ($s = ...,-2,-1,0,1,2,...$). The Tyler and Sofrin relation implies that for a particular harmonic of the f_{BPF}, the sound pressure field is determined by the successive values of m, generated as an index s, which ranges over all positive and negative integers. This circumstance is equivalent to adding and subtracting multiples of the number of vanes from the product hB. Additionally, each m-lobe circumferential pattern rotates at a different speed, defined as:

$$\Omega_m = hB\Omega/m \tag{2.68}$$

This rotational speed guarantees the generation of h times f_{BPF}, as not every circumferential mode is turning with the rotor angular velocity. A positive value of m represents a mode turning in the same direction as the rotor, whereas a negative m corresponds to a rotation in the opposite sense. A simple case of an eight-bladed rotor (B=8) and a six vane-stator (V=6) is considered in order to illustrate in diagrammatic form the sound pressure field resulting from the rotor-stator interaction (cf. Fig. 2.15). Consequently, the rotor-stator interactions are highlighted once the rotor turns in counterclockwise direction. Equation 2.67 predicts the occurrence of a $m = 2$ circumferential pressure pattern (for the fundamental of the f_{BPF}, $h = 1$ and $s = $ -1), rotating at 4 times the shaft speed (cf. Eq. 2.68). Once the rotor goes past a stator vane, two interaction pulses occur simultaneously, suggesting the appearance of a two-lobed sound pressure pattern. The successive intermediate positions of the rotor shaft in Fig. 2.15 evidence the difference in angular speed between the rotor and the rotating mode. As seen, the circumferential mode shifts one complete revolution during just a quarter turn of the rotor shaft.
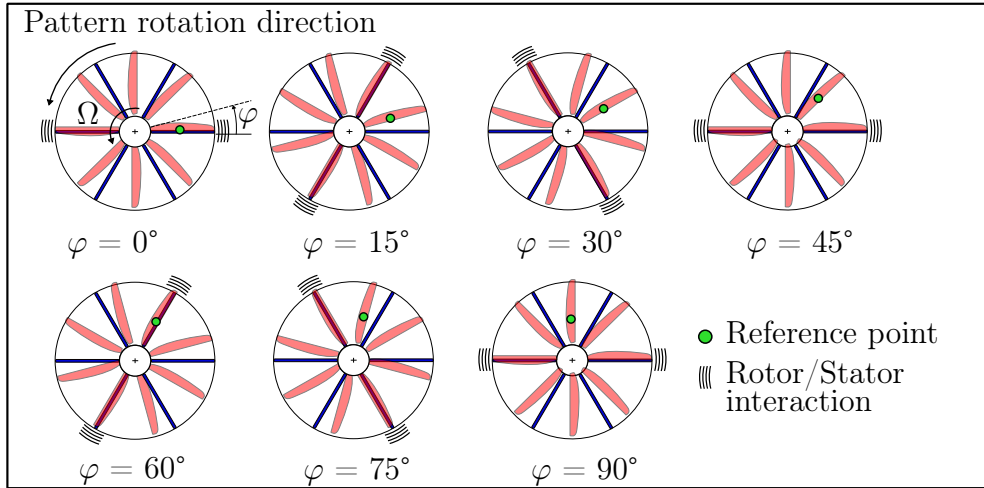
Figure 2.15: Tone generation by rotor-stator interaction

For multi-stage turbine configurations, the frequency spectrum contains additional discrete tones resulting from the interactions between the flow wakes and the successive rotor and stator stages of the machine. This is exemplified by the specific case of a two-stage turbine, which is schematically shown in Fig. 2.16 along with the denominations R and S for the rotor and stator stages, respectively. Furthermore, a frequency spectrum showing the fundamental blade-passing harmonics and intermediate frequencies resulting from the interactions S1-R1, S1-R1-S2 and S2-R2 is shown. In order to account for the additional interactions, the Tyler and Sofrin relationship can be extended to n-th rotor and stator stages provided that all stages turn at the same rotational speed. A general expression for the circumferential mode order m is therefore given by:

$$m = \sum_i h_i B_i + \sum_j s_j V_j \qquad (2.69)$$

where hB has been replaced by $h_i B_i$ and sV by $s_j V_j$.
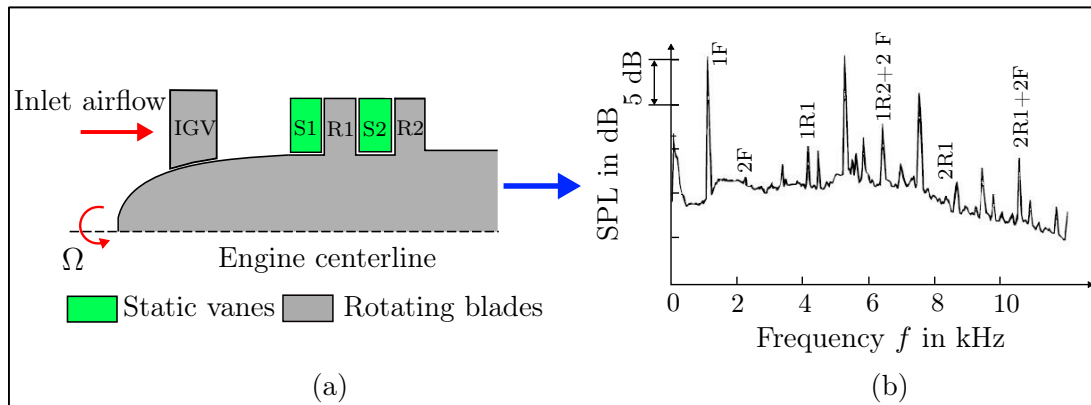
Figure 2.16: Schematic representation of a two-stage turbine (a), and spectrum with intermediate frequencies resulting from additional stage interactions (b), adapted from Smith (1989)

2.5 Concluding remarks

The set of theoretical foundations covered in the present chapter are considered to be a basis for the material to follow. The foundation of the experimental methods for the study of the propagating field within axial turbomachinery lies on the general solution of the acoustic wave equation along with the concepts associated with the acoustical spinning modes. Important aspects related to the sound propagation in cylindrical geometries include:

1. The acoustic field prevailing inside a turbomachine can be represented by superimposed space and time dependent sound pressure waves, known as acoustical modes.

2. From a mathematical point of view, an acoustical mode is an individual solution to the homogeneous acoustic wave equation in cylindrical coordinates satisfying specific boundary conditions. The superposition of individual solutions, i.e., acoustical modes, results in a clear representation of the propagating sound pressure field structure in a turbomachine.

3. Each acoustical mode is uniquely defined by an ordered index combination m and n, representing a circumferential and a radial mode order, respectively. The index m defines the number of sound pressure cycles taking place in azimuthal direction, while n stands for the total of sound pressure nodes along the radial direction.

4. Although an infinite number of acoustical modes can be generated within an axial rotating machine (being the acoustical source the moving blading), only a limited quantity of them propagate. The Cut-On frequency $f_{\text{Cut-On}}$ defines the excitation frequency at which a specific mode combination (m, n) is able to propagate according to the dominating flow conditions in the machine and its geometry.

5. Specific circumferential modes are produced as a result of rotor-stator interaction in turbomachinery. The circumferential mode order can be predicted by means of a mathematical relationship developed by Tyler and Sofrin (c.f. Sec. 2.4.1).

Having discussed the previously mentioned topics in the context of this chapter, available in-duct measuring and analysis methods for the the experimental determination of the acoustical structure within axial turbomachinery are considered in the following chapter. Accordingly, emphasis is set specifically on the **R**adial **M**ode **A**nalysis (RMA) evaluation technique and specially on the effect of relevant measurement parameters on its output.

3 Experimental sound propagation by the Radial Mode Analysis (RMA)

As stated in the previous chapter, the sound field propagating within a duct, i.e., an axial turbomachine, can be expressed as a sum of acoustical modes. Each mode represents an analytical solution of the acoustic wave equation which satisfies given boundary conditions. The quantification of the acoustical structure is carried out by means of in-duct modal analysis, a set of measurement techniques developed to deduce the amplitude of each tonal component from sound pressure measurements performed inside the turbomachine flow channel.

Among the existing in-duct measurement techniques, the **R**adial **M**ode **A**nalysis (RMA) has established itself as a well-known evaluation method to experimentally study the sound transmission of the discrete tonal noise components present in turbomachinery (Holste and Neise 1997). As such, this chapter describes this analytical method by first presenting some historical background regarding the development of related experimental in-duct measurement techniques. This is followed by the theoretical background of the RMA and concluded with some remarks concerning the practical application of the method to the TFD model air turbine. Special emphasis is set though in the involved data acquisition parameters and the quantification of the RMA output sensitivity to variations in these parameters.

3.1 Literature survey of modal analysis techniques

For more than fifty years, research efforts in the context of aeroengine noise have focused on understanding sound propagation phenomena as well as on developing appropriate measurement methods, techniques and approaches to quantify it. In the early 60s, special effort was taken to understand the generation, transmission and radiation of noise from axial turbomachinery. Pioneer work in this aspect was accomplished by Tyler and Sofrin (1962) and exposed in a detailed publication on axial compressor noise studies. The authors analytically clarified these processes and experimentally demonstrated the spinning nature of the in-duct sound pressure structure. Over the years to follow, several experimental techniques for the acoustical field decomposition and mode separation were developed. Special attention was payed to the quantification of the amplitude of the dominant acoustical modes propagating at specific frequencies within axial turbomachinery.

For instance, an early attempt to demonstrate the cut-off phenomenon and the space and time variation of a selected mode was performed by Morfey (1964). Accordingly, a selected mode was excited by a siren coupled with a cylindrical duct with no steady flow. In this way, the theoretical Cut-Off frequency of the mode was identified by varying the siren frequency until observing a sudden variation in its sound pressure. Additionally, the radial sound pressure profile in the duct was measured and afterwards compared to a theoretical curve for the chosen mode, resulting in close agreement.

Mugridge (1969) and Bolleter and Crocker (1971) went a step further by implementing a so-called indirect analysis procedure, specifically, a space-time correlation technique between two transducers to determine the amplitude and phase of the propagating spinning modes in a fan test-rig. In contrast to Bolleter and Crocker (1971), who made use of condenser microphones to implement the measuring method, Mugridge (1969) used hot-wire anemometers for the same purpose. The execution of the measuring technique required the installation of transducers at different positions. One transducer was placed at a reference fixed position, the second one was arbitrarily displaced to a selected in-duct position.

The recorded signals were subsequently multiplied and used to generate a cross-spectral matrix (Rossing 2007). With this done, a mathematical model based on the general solution of the homogeneous acoustic equation (cf. Eq. 2.14) was formulated for the incident and reflected propagating modes. This procedure resulted in a large number of cross products with associated amplitude factors, representing the modal amplitudes. A similar approach was undertaken by Schiffer (1976), who additionally considered flow effects such as uncorrelated boundary layer alternating pressure and flow noise. Both effects were suppressed with a narrow band filter before performing the cross-correlation of the sound pressure signals, leaving only the tonal propagating noise components and thus avoiding the influence of broadband noise components.

Parallel to Mugridge's (1969) work, and despite not directly related to mode decomposition, Mason (1969) gave advice on the effect of fluid flow on the Cut-Off frequencies of propagating acoustical modes. Several Cut-Off frequencies were detected by evaluating the duct pressure spectra of a complex acoustical field generated by a loudspeaker. From the performed measurements, it was established, that the Cut-Off frequency for the excited modes decreased with increasing flow speed (cf. Sec. 2.3.5).

Returning to the cross-correlation method for in-duct modal analysis, similar work based on acoustic signal correlation for sound power computation was performed some years later by Salikuddin and Ramakrishnan (1987) and Michalke (1989, 1990). Salikuddin and Ramakrishnan (1987) determined the acoustic power for incident, reflected, and transmitted fields for cylindrical and annular geometries. In addition, Michalke (1989, 1990) extended the method by determining the sound power spectrum by separating the influence of the flow field from the developed models and results.

Besides cross-correlation techniques, acoustical modal decomposition was alternatively carried out by other researchers by using microphone arrays flush mounted to the duct wall, techniques commonly referred to as direct in-duct analysis methods (Holste 1995).

In the context of this procedure and with the recorded data, the sound pressure pattern is separated into circumferential and radial acoustical modes. As depicted before, early attempts to identify acoustical modes by performing such modal breakdown were carried out by Tyler and Sofrin (1962). A microphone was placed in the inlet of an axial compressor and was then circumferentially displaced along a constant radius arc in the direction of the shaft rotation. An instantaneous sound pressure signal was displayed every time the rotor passed by a trigger. Once the microphone was displaced, it was noticed that the sound pressure signal arrived later, indicating a pressure pattern gradually rotating. This fact suggested a circumferential mode coupled to the rotor angular velocity. The performed analysis had a qualitative nature, as no sound pressure level or amplitude was directly measured.

Based on the same principle, Moore (1972) quantified the amplitude of rotating circumferential modes by performing a series of measurements on a four-bladed ducted ventilator. Similarly, a microphone was circumferentially traversed and the recorded signal was triggered once per shaft revolution. Each recorded signal was analyzed with a **F**ast **F**ourier **T**ransformation (FFT), allowing the quantification of the signal amplitude and phase variation with frequency. Afterwards, the sound pressure and the phase angle variation in the azimuthal direction were reconstructed. This was accomplished by analyzing the magnitude of the signal amplitude and phase for the f_{BPF} or one of its harmonic components from each position previously traversed by the microphone. Finally, a spatial FFT was performed over the reconstructed circumferential sound pressure signal, enabling the quantification of the azimuthal mode amplitudes.

An extension to include the amplitude of the radial modes was also undertaken and presented in a later publication by Moore (1979). In what the author denoted radial transform, three different methods were investigated and later validated with experimental data from an axial fan. According to Moore (1979), it is possible to determine the magnitude of $A^{\pm}_{[mn]}$ by integration, matrix inversion and least squares fitting. All three methods were based on the previous knowledge of the magnitude of the circumferential mode amplitudes, which are in turn a function of the unknown radial mode amplitudes $A^{\pm}_{[mn]}$ (cf. Eq. 2.63).

Following the findings of Moore (1979), a series of experiments in the early 90s were performed to examine the dominant sound generation mechanisms of tonal noise components in complex turbomachinery. Acoustical measurements were initially carried out by Holste and Neise (1992) in a novel counter rotating prop-fan designed by the company MTU Aero Engines (Schimming 2003). The conducted measurement routine for modal decomposition was referred to as **R**adial **M**ode **A**nalysis (RMA) and comprised similar implementation steps as those applied by Moore (1972) during his research. By installing radial microphone rakes, a spatial frequency analysis of the sound pressure signals was first performed followed by matrix-inversion and least square fit algorithms for the determination of the radial mode amplitudes. The measured propagating modes in the work of Holste and Neise (1992) resulted from the rotor-stator and rotor-support struts interaction, an extension to the research of Moore (1979), which considered solely rotor alone generated modes.

The RMA was further implemented for acoustic measurements in the outlet duct of a three-stage low pressure axial turbine. Measurements were carried out by MTU Aero Engines in cooperation with the Institute of Propulsion Technology, a research institute appointed to the DLR (Enghardt et al. 2001, Neise and Enghardt 2003). The study concentrated its efforts on determining the influence of several exit guide vane (EGV) designs on the acoustic structure in the turbine outlet. Additionally, the total radiated sound power was quantified for selected acoustical mode combinations. The effect of multiple stator and rotor interactions due to the multi-stage turbine configuration was taken into account by extending the Tyler and Sofrin's rotor-stator interaction mathematical relationship by Enghardt et al. (1999). This mathematical expression involves multiples of the rotor and stator blades and vanes (cf. Eq. 2.69).

Improvements to the RMA technique were introduced by Rademaker et al. (2001) in the context of the RESOUND project in a Rolls-Royce model fan rig (Fisher and Self 2002). The improvements were related to the development of an optimized circumferential array consisting of 100 unsteady pressure transducers able to decompose up to 180 circumferential mode orders m. Meanwhile, Sijtsma and Zillmann (2007) proposed four different techniques for circumferential mode detection when using circular microphone arrays. The proposed processing techniques for mode detection included conventional rms-averaging (RMS), diagonal removal (DR), cross-correlation with a reference channel (CC) and Principal Component Analysis (PC). Further details concerning each analytical approach is found in Sijtsma and Zillmann (2007).

Recent studies related to the RMA concentrate, however, on the quality of the analysis results rather than on its technical application, which, as previously mentioned, has been carried out for more than 20 years. Related to this fact and based on an optimization study, Tapken and Enghardt (2006) stated that the quality of the RMA output strongly depends on the arrangement of the measurement transducers and the flow parameters. On the one hand, the latter influences only the propagating characteristics of the induct sound field. On the other hand, regarding the sensor arrangement, and based on a generalized simulation approach, Tapken and Enghardt (2006) found that significant discrepancies arise when implementing wall-flush sensors rather than radial sensor rakes. In this respect, wall-flush arrangements are adequate for decomposing low order modes, while radial sensor rakes detect higher order modes more efficiently.

More recently, Tapken et al. (2008) studied the influence of microphone related characteristics including the sensor signal-to-noise ratio (SNR), the mode detection sensitivity to microphone mal-positioning and failure when installed in an array. These parameters were investigated by generating a synthetic sound field comprising selected acoustical mode combinations and superimposed noise. High SNR values varying between 10 and 20 dB, yielded appropriate results for the modal decomposition as the signal background noise remained below the original signal level. In contrast, lower SNR values resulted in background noise almost matching the original measured signal level. Moreover, mal-positioned microphones shifted in the radial direction relative to a reference coordinate system led to signal phase shift, resulting in varying acoustical mode amplitudes after the RMA implementation when compared to a reference case without mal-positioning.

Regarding the omission of data points as a result of microphone mal-functioning, Tapken et al. (2008) found that the failure of up to eight transducers is reflected on an underprediction of the studied mode amplitude in the order of magnitude of 1.5 dB. The predicted amplitude increased as more microphones failed, reaching differences as high as 12.5 dB with respect to a reference modal amplitude.

Complementing this study, Tapken et al. (2011) extended the RMA sensitivity analysis with tolerances in sensor rake installation, considering additional sensor displacement in the axial and circumferential directions. The undertaken approach was similar to the one developed by Tapken et al. (2008), namely, the study of systematic errors derived from the RMA algorithm by generating a synthetic sound field. The obtained results indicated that axial and circumferential misalignment led to significant mode amplitude deviations when compared to a reference amplitude, specially for low order modes. Although mode amplitude differences resulted from radial microphone misalignment, it turned out that these were not as high as those produced by axial and azimuthal mal-positioning.

Additional sensitivity studies of the RMA were performed by Laguna et al. (2013a,b). These studies concentrated on examining the influence of selected data acquisition parameters on the RMA output based also on a numerical simulation. The considered parameters taken into account were the microphone SNR, the circumferential spacing of microphone measuring positions, the number of recorded triggered revolutions, and a time trigger delay. The numerical simulation was performed under the consideration of realistic turbine-related conditions (Laguna et al. 2013a) and swirling flow (Laguna et al. 2013b). Regarding the influence of the SNR, similar results to those found by Tapken et al. (2008) were attained. SNR values above 30 dB led to relatively low discrepancies in the acoustical mode amplitude, normally around 1%. In contrast, SNR values below 10 dB resulted in differences above 10%. Enough circumferential measurement positions assured acceptable results provided that the microphone SNR was high enough. For low SNR transducers (below 10 dB) the acoustical mode amplitude errors were above 10% even for circumferential resolutions as high as 1°. Meanwhile, a sufficient number of triggered revolutions (>10) guaranteed optimal output acoustical modal amplitudes independently of the mode order. Finally, a time delay represented a noticeable error source, considering that delays in the order of magnitude of 1 ms resulted in amplitude errors of more than 5%.

From the consulted literature related to the sensitivity of the RMA to data acquisition parameters and installation tolerances, it is clear that no experimental studies have been performed to assess the influence of such parameters on real turbomachinery. Consequently, the current work goes a step forward by examining the impact of two specific data acquisition parameters on the output of the RMA on a multi-stage low pressure turbine. As mentioned in the Introduction (cf. Chapter 1), the studied parameters are the measurement circumferential resolution and the number of triggered revolutions. This is accomplished by a rotating ring equipped with condenser microphones and installed within the turbine flow channel. Details of the measurement device are extensively discussed in Chapter 4 along with the derived results (Chapters 5 and 6). Before proceeding to the discussion of the previously mentioned aspects, the theoretical background of the RMA is presented in the sections to follow.

3.2 Theoretical Background of the RMA

The application of the RMA requires the previous prediction of the expected acoustical propagating structure inside the turbine. Therefore, once the propagating mode combinations (m, n) are analytically determined (cf. Sec. 2.3.5), the complete description of the sound field still requires the magnitude of the radial mode amplitudes $A^{\pm}_{[mn]}$ (cf. Eq. 2.62). Before proceeding, Eq. 2.63, which analytically represents the sound pressure field within a cylindrical duct, can be summed up over all circumferential modes and rewritten as follows:

$$p'_{[mn]}(x, r, \varphi, t) = \sum_{m=-\infty}^{\infty} A_m(x, r) \mathrm{e}^{-im\varphi} \mathrm{e}^{i\omega t} \tag{3.1}$$

The combined terms presented in Eq. 3.1 correspond to the amplitude A_m, known as the circumferential mode amplitude. This amplitude results from the addition of the downstream and upstream radial mode amplitudes $A^+_{[mn]}$ and $A^-_{[mn]}$ multiplied with the eigenvalues derived from the Bessel function $g(r)$:

$$A_m(x, r) = \sum_{n=0}^{\infty} \left(A^+_{[mn]} \mathrm{e}^{ik^+_{[mn]}x} + A^-_{[mn]} \mathrm{e}^{ik^-_{[mn]}x} \right) g(r) \tag{3.2}$$

The goal of the RMA is to determine these amplitudes. This process is performed in two steps. The first one, an experimental one, requires the measurement of the sound pressure with condenser microphones located at several axial and circumferential positions, denoted by N_x and N_φ, respectively. This microphone arrangement allows the determination of the instantaneous sound pressure distribution at specific axial positions. The RMA requires rotor-synchronized sound pressure measurements as input, as the synchronization provides a common data acquisition starting point for each microphone recording a signal. The measured data is subsequently used to reconstruct at specific times the instantaneous circumferential pressure distribution. This fact is clarified once Eq. 3.1 is analyzed and respectively restated for an instant of time $t = 0$:

$$p'_{[mn]}(x, r, \varphi, t = 0) = \sum_{m=-\infty}^{\infty} A_m(x, r) \mathrm{e}^{-im\varphi} \tag{3.3}$$

Equation 3.3 indicates that the circumferential pressure distribution can be expressed in terms of a series of coefficients A_m. This mathematical expression resembles a time signal given in terms of a series of harmonic or Fourier coefficients. As such, the desired circumferential amplitudes can be directly determined from an spatial Fourier Transformation performed with respect to the circumferential coordinate φ:

$$A_m(x, r) = \frac{1}{2\varphi} \int_0^\varphi p'_{[mn]}(r, \varphi, x) \mathrm{e}^{-im\varphi} d\varphi \tag{3.4}$$

However, as the recorded values from the sound pressure measurement are discrete and not continuous, Eq. 3.4 has to be replaced by a discrete formulation of the spatial Fourier Transformation.

The discrete version of the spatial Fourier Transformation is referenced to a fixed radial position R (the duct wall) and for varying axial positions x_i. The mathematical expression finally takes the form:

$$A_m(x_i, R) = \frac{1}{N_\varphi} \sum_{l=0}^{N_\varphi - 1} p_c(x_i, R, \varphi_l) \, e^{-im\varphi_l} \tag{3.5}$$

Here, p_c is the reconstructed circumferential sound pressure at the coordinate (x_i, R, φ_l), with the index l varying up to N_φ-1, the total number of circumferential measuring points. By means of the spatial FFT, the circumferential signal p_c can be decomposed in its harmonic components.

The amplitude of the harmonics constituents of the original space signal represents the circumferential mode amplitudes A_m for a particular f_{BPF} or one of its harmonics. The resolution of the spatial FFT is 1 ($m = 1$) and the highest quantifiable mode order m is restricted by the number of circumferential measuring positions and given by Nyquist-Shannon sampling theorem:

$$m \leq N_\varphi / 2 \tag{3.6}$$

Once the mode amplitudes A_m are known, the radial-mode amplitudes $A_{[mn]}^\pm$ can be determined. The proposed instrumentation arrangement with axially and circumferentially positioned microphones allows the determination of the amplitude A_m of x_i circumferential modes of the same order m, one specific mode per axial position. As a consequence, a linear system of equations is set up based on Eq. 3.2 and expressed as:

$$\vec{A_m} = M \vec{A_{[mn]}} \tag{3.7}$$

Each row comprises a mathematical expression relating A_m with $A_{[mn]}$ for a specific axial measuring position x_i at a constant duct radius R. Based on this fact, Eq. 3.7 can be rewritten as:

$$\begin{pmatrix} A_m(x_0, R) \\ A_m(x_1, R) \\ \vdots \\ A_m(x_{n-1}, R) \\ A_m(x_{n-1}, R) \end{pmatrix} = M \begin{pmatrix} A_{[m0]}^+ \\ A_{[m0]}^- \\ \vdots \\ A_{[mn]}^+ \\ A_{[mn]}^- \end{pmatrix} \tag{3.8}$$

A solution for $A_{[mn]}^\pm$ is established by inverting the eigenvalue matrix **M**. This matrix has a dimension (i x n), with i representing the number of axial measurement positions and n the number of analyzed radial mode orders for a specific circumferential mode order m. The eigenvalue matrix elements are a function of known flow, acoustical and geometrical parameters. The eigenvalue matrix is defined for a configuration of axially positioned microphones at a constant radius as follows, with the Bessel function $g(r)$ (cf. Eq. 2.46) written in terms of the eigenvalues $s_{[mn]}$

$$g(r) = g(r)_{[mn]} = g_{[mn]}\left(s_{[mn]} \cdot \frac{r}{R}\right) \tag{3.9}$$

resulting in:

$$
M = \begin{pmatrix}
g_{[m0]} \cdot \mathrm{e}^{ik^+_{[m0]}x_0} & g_{[m0]} \cdot \mathrm{e}^{ik^-_{[m0]}x_0} & \cdots & g_{[mn]} \cdot \mathrm{e}^{ik^+_{[mn]}x_0} & g_{[mn]} \cdot \mathrm{e}^{ik^-_{[mn]}x_0} \\
\vdots & \vdots & \ddots & \vdots & \vdots \\
g_{[m0]} \cdot \mathrm{e}^{ik^+_{[m0]}x_i} & g_{[m0]} \cdot \mathrm{e}^{ik^-_{[m0]}x_i} & \cdots & g_{[mn]} \cdot \mathrm{e}^{ik^+_{[mn]}x_i} & g_{[mn]} \cdot \mathrm{e}^{ik^-_{[mn]}x_i}
\end{pmatrix} \tag{3.10}
$$

Only a limited number of radial mode orders n can be decomposed. In this way, radial mode orders up to $n = N_x \backslash 2$ (considering upstream and downstream propagating modes) or $n = N_x - 1$ (including only downstream modes or upstream modes) can be resolved. Radial orders exceeding the specified limits lead to an undetermined linear system of equations (cf. Eq. 3.2).

The final step of the implementation of the RMA consists of finding a solution for the radial mode amplitudes $A^\pm_{[mn]}$ by inversion of the eigenvalue matrix. Before proceeding and for clarity, a diagram schematically showing the Radial Mode Analysis implementation is presented in Fig. 3.1 below.
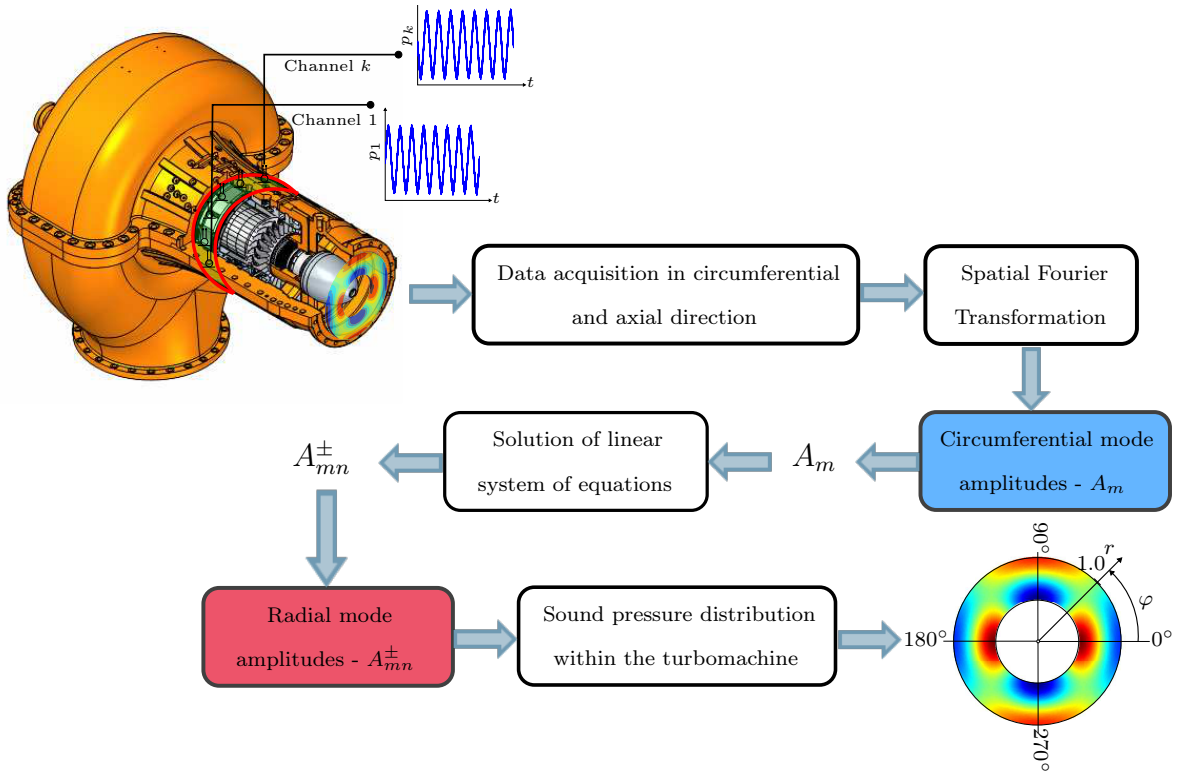
Figure 3.1: Radial Mode Analysis (RMA) schematic representation

In order to determine the radial mode amplitude vector $\vec{A}_{mn}$, the system of equations 3.7 is reorganized and solved by inverting the eigenvalue matrix $\mathbf{M}$ as follows:

$$
\vec{A}_{[mn]} = M^{-1}\vec{A}_m \tag{3.11}
$$

The solution of the resulting system of equations highly depends on the stability of the matrix equation (cf. Eq. 3.8). In that regard, the solution of the mentioned system of equations is strongly influenced by physical and geometrical variables present in the eigenvalue matrix. These variables include stationary flow parameters (axial and circumferential Mach-numbers Ma_x and Ma_φ, respectively), duct hub-to-tip ratio σ and microphone positioning (Tapken and Enghardt 2006). The influence of the solution procedure through matrix inversion on the output amplitudes $A_{[mn]}^{\pm}$ can be quantified by the **S**ingular **V**alue **D**ecomposition (SVD) (Nelson and Yoon 2000, Yoon and Nelson 2000, Lowis and Joseph 2006).

The SVD method is based on a theorem of linear algebra which establishes that any matrix $\mathbf{M}$ of size i x n can be written as the product

$$\mathbf{M} = \mathbf{U} \cdot \mathbf{W} \cdot \mathbf{V}^T \tag{3.12}$$

consisting of a column-orthogonal matrix $\mathbf{U}$ of the same size of $\mathbf{M}$, a diagonal matrix $\mathbf{W}$ of size $(n$ x $n)$ with a series of positive or zero values known as singular values w_j and a orthogonal transposed matrix $\mathbf{V}$ of the same size of $\mathbf{W}$. The inverse of the eigenvalue matrix $\mathbf{M}$ is defined as

$$\mathbf{M}^{-1} = \mathbf{V} \cdot \mathbf{W}^{-1} \cdot \mathbf{U}^T \tag{3.13}$$

leading to the determination of the unknown radial mode amplitudes $A_{[mn]}^{\pm}$

$$\vec{A_{[mn]}} = \mathbf{M}^{-1} \cdot \vec{A_m} = \left[\mathbf{V} \cdot \mathbf{W}^{-1} \cdot \mathbf{U}^T \right] \cdot \vec{A_m} \tag{3.14}$$

The stability of the matrix equation is closely related to the magnitude of the singular values w_j, initially present in the square diagonal matrix $\mathbf{W}$. As such, a measure of the error resulting from the matrix inversion can be established in terms of the condition number c, defined as the ratio of the largest to the smallest singular value. A condition number equal to unity leads to a well-conditioned system of equations (Press et al. 2007). This would result in relative amplitude perturbations of the input data propagating exactly equal to relative amplitude variations of the output data. In other words, an input amplitude 1% error would lead to a maximum output amplitude error of the same order of magnitude (Tapken and Enghardt 2006). However, if the condition number is far from unity then the problem is ill-conditioned and its solution cannot be trusted if any change were to be made, since a minimum variation in the input would result in a significant increase in the output value. A condition number analysis by means of the SVD was performed in the context of this work to optimize the microphone axial spacing. Several simulations were performed for selected modes based on real operating parameters of the TFD model air turbine. Further details are given in Ioannou (2012).

3.3 Implementation of the RMA in the TFD low-pressure air turbine

Having established the theoretical background of the RMA, this section shortly exposes the required procedures for the practical application of this method to the TFD model air turbine. In general, the following steps must be performed to decompose the propagating acoustical structure within the considered test facility:

1. The expected propagating acoustical structure for a particular excitation frequency has to be determined based on the machine geometrical and flow parameters.

2. Knowing beforehand the expected dominating tonal acoustical structure, the sound pressure distribution on the turbine wall is measured at several circumferential positions. This is performed with a rotating unit equipped with microphones and placed in the low-pressure turbine flow channel (cf. Chapter 4 and Laguna et al. (2012)).

3. The recorded data is synchronized and subsequently referenced to a common rotor specific position. Afterwards, the circumferential pressure distribution is reconstructed for a specific instant of time.

4. A discrete spatial Fast Fourier Transform is performed over the sound pressure circumferential distribution yielding the azimuthal mode amplitudes A_m of the analyzed sound field at the f_{BPF} or one of its harmonics.

5. The radial mode amplitudes $A^{\pm}_{[mn]}$ are determined by grouping together the radial and axial terms of the general solution to the homogeneous acoustic wave (cf. Eq. 2.63). This results in a linear system of equations set for one specific circumferential mode order m including the previously established azimuthal mode amplitudes A_m for different axial positions.

6. Once the radial mode amplitudes $A^{\pm}_{[mn]}$ are known, the in-duct propagating structure composed of several superimposed modes can be reconstructed for specific excitation frequencies

3.4 Concluding remarks

The literature survey conducted in the context of this chapter indicated that acoustical modal analysis techniques developed up to date fall into two categories. The first category is represented by the indirect analysis methods. This group comprises various correlation techniques. The second group, the direct methods, includes the application of a spatial FFT and the solution of a linear system of equations, basic procedures for the performance of the RMA. Regarding the RMA, the literature review evidenced its successful application to axial turbomachinery for tonal noise propagation studies, but exposed as well the lack of satisfactory experimental evidence related to the effect of relevant measurement parameters on its output. Based on this fact, it can be concluded that:

1. An accurate study of sound propagation in full-scale axial turbomachinery requires the performance of experimental measurements. However, full test-rig testing is time as well as resource consuming. As a consequence, a careful selection of appropriate measurement parameters to ensure minimum uncertainty in the output of the in-duct analysis methods is required.

2. Related to this fact, comparatively little work has been undertaken to identify the effect of relevant measurement parameters on the RMA output. As such, the influence of selected data acquisition parameters on the RMA output has to be studied in order to define a minimal measurement uncertainty after application of the RMA to sound propagation studies in turbomachinery.

Having pointed out some of the most relevant measurement techniques employed for the characterization of turbine noise within the scope of this chapter, the experimental setup for the application of the RMA to a low-pressure turbine is discussed in the following chapter. This is done before proceeding to the results derived from the study of the sensitivity of the RMA to specific data acquisition parameters, material to be covered in Chapter 5 and 6.

4 Experimental Setup

Having already discussed the theoretical foundations related to sound propagation and acoustical field decomposition in turbomachinery, the experimental set-up for the sound pressure measurements and therefore, for the application of the RMA are discussed in the current chapter. As such, this chapter gives an overview of the TFD air turbine test stand as well as details related to the experimental setup and instrumentation employed during the acoustic measurements. In respect thereof, the model air turbine test rig is described, accompanied by additional technical information, and operating aspects. Following this, the turbine-integrated rotating-ring measuring unit is presented. Technical requirements and limitations associated with the design and construction of the rotating-ring are also provided. The chapter is concluded with the presentation of technical and installation details of the used instrumentation followed by information related to the system rotation control and data acquisition.

4.1 TFD Multistage air low-pressure turbine

4.1.1 General test facility description

The axial low-pressure turbine test rig at the TFD is chosen as test facility for the sound propagation experiments. The test bench consists itself of a test carrier comprising a pressure-retaining outer cast iron housing with an inner diameter $\varnothing_{TO}$ of 500 mm at the inlet (Herzog et al. 2005, Henke et al. 2012). Within this external casing, different inner housing and rotor shaft configurations can be accommodated as shown in Fig. 4.1. This flexible design allows the adjustment of several blading set-ups, including one, two, four and seven-stage configurations (Zehner 1980). Only the single-stage configuration is considered for the performed acoustical measurements.
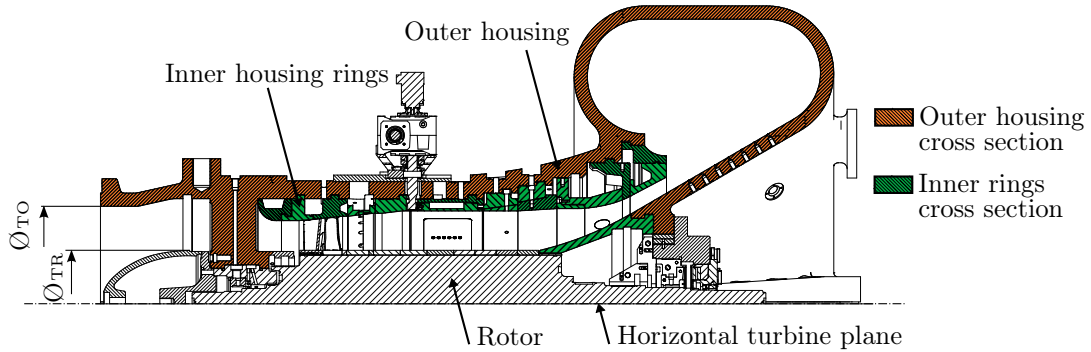
Figure 4.1: Sectional view of the turbine test rig for the single-stage configuration

The stage has $V=29$ stationary vanes and $B=30$ rotating blades attached to a rotor shaft with a diameter $\varnothing_{TR}$ of 270 mm. The chord length of the stator vanes is $c_s = 35.50$ mm, whereas that of the rotor blades amounts to $c_r = 36.50$ mm. Both chord lengths are measured at the blade mid-span (Evers 1985). The test facility is complemented by the coupling of the turbine with a clutch and a torque metering shaft to a spur-gear transmission. The transmission is coupled with a pendulum machine, which operates as a motor or a generator, being able to brake or drive the turbine shaft according to the machine operating point (Binner 2011). Simultaneously, the pendulum machine regulates the turbine rotational speed. In this way, the rotational speed can be adjusted independent of the mass flow rate. The general test stand including all main functional components is shown in Fig. 4.2.
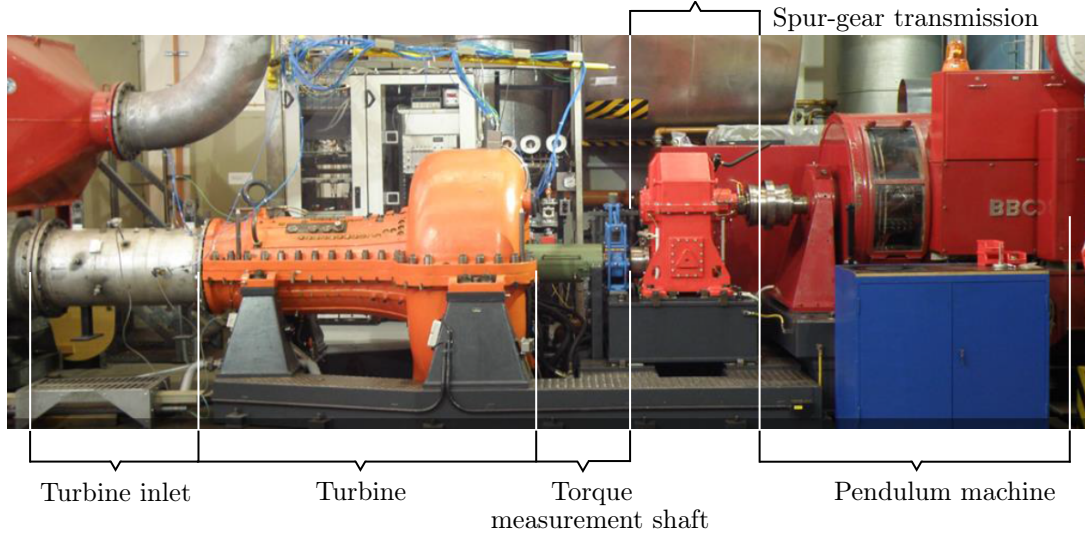
Figure 4.2: TFD multistage low-pressure turbine test stand

4.1.2 Test facility air supply

The test rig is powered by the air provided by three screw-type compressors able to deliver a maximum mass flow rate of 11 kg/s with an associated pressure ratio π of 3.2 (Binner and Seume 2014). Before being compressed, atmospheric air is filtered and immediately after, distributed into the screw compressors (SK31, SK40, and SK50, cf. Fig. 4.3). According to the required mass flow and inlet pressure, the compressors can be operated in parallel or partly in series. A process flow diagram for the test facility air supply is shown in Fig. 4.3. As seen in the diagram, the test stand is operated in open loop, i.e., the air, after being first compressed before entering the turbine and subsequently expanded when leaving it, is released back to the atmosphere right after being acoustically damped. Two bypass valves, a manually operated and a motor-driven one, labeled 1.11 and 1.12 in the process diagram, respectively, are used to adjust the mass flow. Both valves are put into operation for mass flow rates above $\dot{m} = 0.8$ kg s^{-1}. Lower mass flows are adjusted with the turbine inlet valve 1.31, while keeping fully open one of the bypass valves. Referring again to Fig. 4.3, a venturi nozzle can be identified. The mass flow magnitude is determined by means of this device, which is located 8.7 m ahead of the turbine inlet and calibrated according to the DIN EN ISO 5167-4 norm.
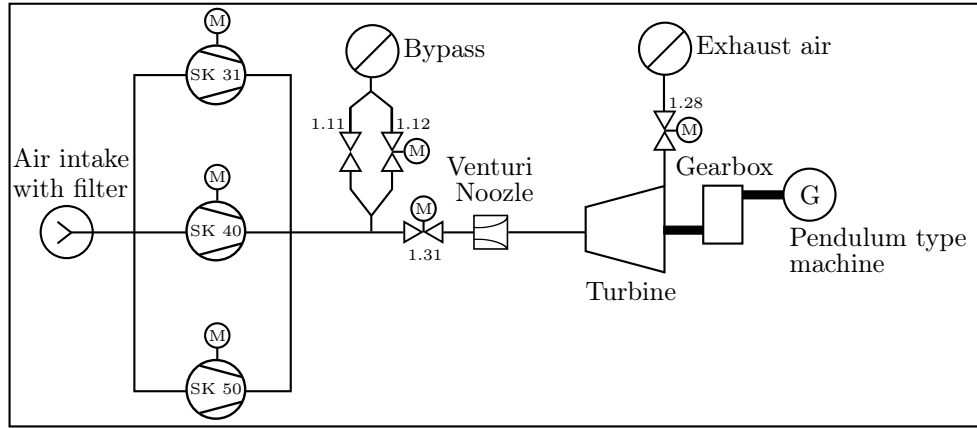
Figure 4.3: Air supply process diagram of the low-pressure turbine test facility

The venturi nozzle itself is placed within a 18 m long straight pipe connecting the turbine inlet valve 1.31 and the turbine inlet. This pipe ensures a homogeneous, axial and fully developed flow (Herzog et al. 2005). The nominal operating parameters for the turbine single-stage configuration according to Zehner (1980) are presented in Tab. 4.1.

Table 4.1: Nominal operating parameters of the TFD single-stage LPT

Parameter	Maximum value
Mass flow rate	7.8 kg s^{-1}
Pressure ratio	1.3
Outlet temperature	$52°C$
Rotational speed	7500 min^{-1}

4.2 Measuring technique development for turbine aeroacoustical studies

Having already presented the general operating aspects of the air turbine, the present section addresses more specific considerations related to the aeroacoustic experiments performed in the framework of this research. Among those aspects, topics related to the development of a measuring system to carry out the planned measurements are discussed. Special importance is given to the initial requirements, encountered limitations, design concept, construction and implementation of the aforementioned system for the determination of the sound propagation within the air turbine. Complementing this, the sensors and data acquisition systems implemented in the measuring set-up are presented.

4.2.1 Microphone ring development

Concept, idea and justification

The quantification of the sound propagation within axial turbomachinery requires the experimental determination of the spinning acoustical modes. As already stated in Chapter 2, sound is an alternating physical quantity, whose magnitude varies in axial, radial, and circumferential direction as well as in time. As a result, the measurement of such structure demands the installation of microphones in the machine geometry at circumferential and radial, or alternatively, at circumferential and axial positions. This microphone positioning allows the in-duct acoustical propagation determination by means of the Radial Mode Analysis (RMA). As such, a considerable quantity of microphones is required for the measurement itself and for the later data evaluation with the RMA.

This fact highlights the necessity to develop a measurement concept able to comply with the required task. A first alternative is the installation of microphones directly on the turbine outer casing. Regarding this point, there is a number of limitations that makes this possibility impractical. The first restriction is related to machining issues, as a prohibitive quantity of holes would have to be drilled in the turbine housing for the placement of the microphones. To put this affirmation into context, an example involving the propagating acoustical mode structure for the nominal operating point of the one-stage air turbine is presented (30 blades/29 vanes). Assuming uniform axial flow (no swirl), a constant rotational speed of 3500 min^{-1} and a mass flow of 5.0 kg s^{-1}, the expected acoustical structure is shown in Fig. 4.4.
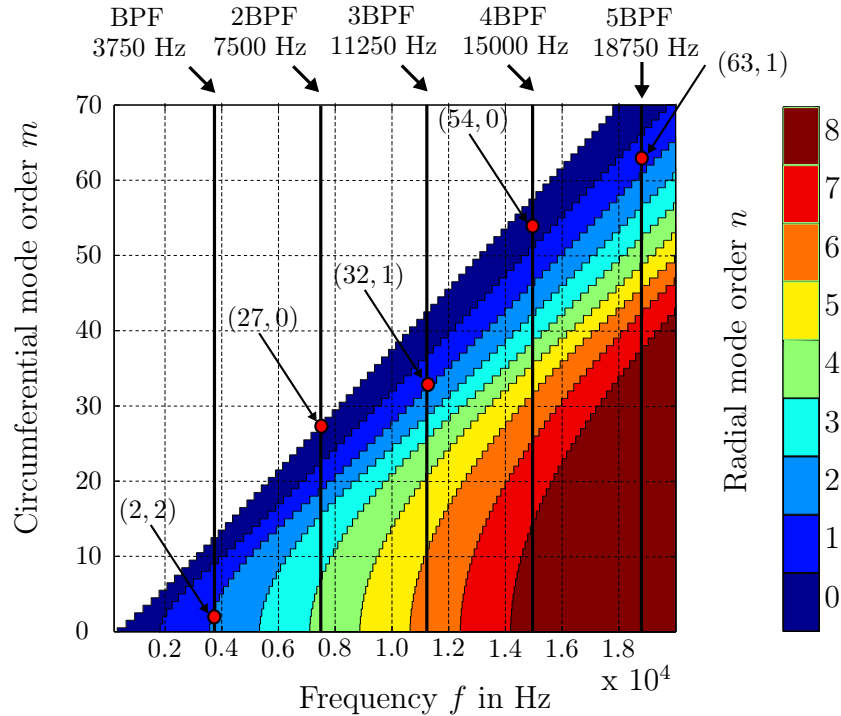
Figure 4.4: Expected propagating acoustical modes upstream of the turbine blading

Table 4.2: Required circumferential and axial measuring positions

Frequency	Maximum mode order m	Maximum mode order n	Azimuthal meas. pos. m_{TS}[1]	Radial meas. pos. n_{TSmax}[2]
f_{BPF}	1	2	2	6
f_{2BPF}	27	0	54	2
f_{3BPF}	32	1	64	4
f_{4BPF}	54	0	108	2
f_{5BPF}	63	1	126	4

A summary of the dominant modes and the required number of measuring positions is provided in Tab. 4.2. Regarding the required sensor measurement positions and as previously indicated in Chapter 3, the identification of circumferential modes demands at least twice the number of microphones as the mode m order. Radial modes require as much axial or radial positioned microphones as the mode order n in order to be identified, in case upstream and downstream wave propagation is being considered. As implied by both Fig. 4.4 and Tab. 4.2, the required number of measuring sensors to be positioned around and along the turbine casing would be excessively high.

The required quantity of measuring sensors varies according to the operating condition of the turbine as well as with the flow field within it. In respect thereof, a further example of the resulting propagating acoustical structure within the LPT with a different operating point is presented (the single-stage configuration with 30 blades/29 vanes is maintained). Assuming uniform axial flow with Ma_x=0.1 and swirling flow with Ma_φ=-0.13, a constant rotational speed of 3500 min^{-1}, a mass flow of 5.0 kg s^{-1} and an inlet total temperature of 50° C, the expected acoustical structure including co-rotating as well as counter-rotating modes (negative m) is shown in Fig. 4.5. A summary of the dominant modes and the required number of measuring positions is as well provided in Tab. 4.3. This summary is presented for both cases, co-rotating and counter-rotating acoustical modes. The dominant acoustical modes and the required instrumentation for the counter-rotating case are bold-highlighted in Tab. 4.3. As seen on Fig. 4.5, only low order acoustical modes are capable of propagating compared with the aforementioned case. In contrast to this, a circumferential high-order mode is first identified at a high multiple of the blade-passing frequency, namely at f_{5BPF}. Noticeable is also the appearance of a single counter-rotating acoustical mode, this as well at a high harmonic multiple of the f_{BPF}. It can be inferred from both presented examples, that the selected operating point of the LTP along with the in-duct flow conditions greatly influence the propagating acoustical structure. As such, and returning to the required measurement concept, the implemented system should be able to record the in-duct sound pressure, this for several operating conditions and for low as well as for high-order modes.

---

[1]Maximum azimuthal mode order m predicted with the Tyler and Sofrin relationship, cf. Eq. 2.67.
[2]Maximum propagating radial mode order n.

Table 4.3: Required circumferential and axial measuring positions for the resulting acoustical structure considering counter-rotating and co-rotating modes (positive and negative m, respectively)

Frequency	Maximum mode order m	Maximum mode order n	Azimuthal measuring positions m_{TS}	Radial measuring positions n_{TSmax}
f_{BPF}	1	0	2	2
f_{2BPF}	2	2	4	6
f_{3BPF}	3	2	6	6
f_{4BPF}	4	3	8	8
f_{5BPF}	34 **(-24)**	0	68 **(48)**	2
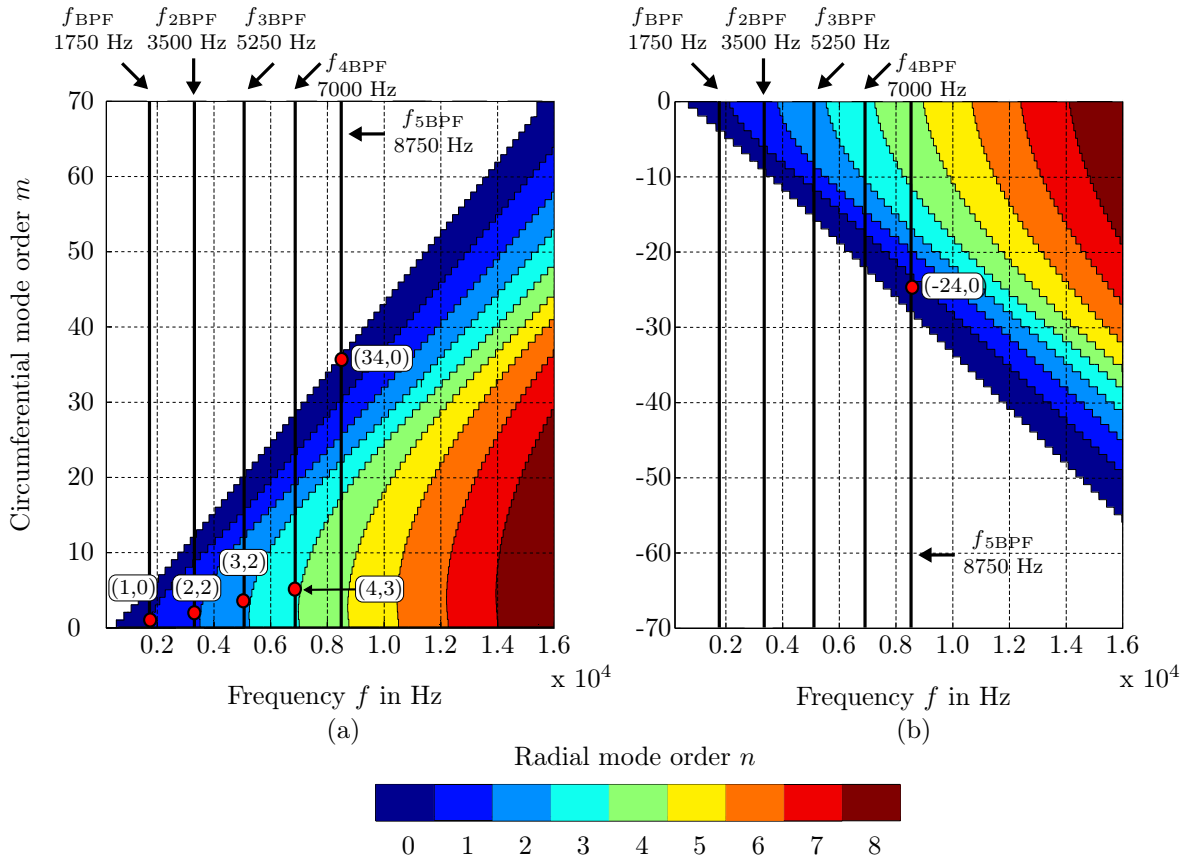
Figure 4.5: Expected propagating acoustical modes upstream of the turbine blades, operating point $\dot{m} = 5$ kg s^{-1}, $\Omega = 3500$ min^{-1}, counter-rotating modes (a), and (b) co-rotating modes

Besides the aforementioned restraints, additional ones associated with manufacturing issues are identified. The surface irregularities found in the turbine housing would require further machining, as the surface should be first smooth down to assure a properly placement of the microphones. Furthermore, along its geometry, the thickness of the outer cast iron housing constantly varies (cf. Fig. 4.1). As a consequence, this cross sectional variation would imply the manufacturing of additional microphone holder adapters with different lengths depending on the sensor axial position. Added to these technical matters, the outer casing disposes of numerous holes and external grooves for the positioning of pneumatic probes and traversing probe mechanisms. The distribution of this elements over the turbine casing hampers also the installation of the sensors, since no free position can be found.

Based on the arguments exposed before, the proposal of installing fixed microphones in the turbine outer casing is discarded. An alternative to overcome this limitation is the development of a rotating measurement unit instrumented with microphones and integrated within the turbine flow channel (cf. (Laguna et al. 2012)). The measuring unit should allow the detection of a sufficient amount of circumferential and radial modes by complying with the following items:

1. Since the turbine inner flow channel is constituted by different ring segments mounted in the turbine housing, the measurement unit should also be designed as an annular element. It is therefore useful to conceive the system in such a way, that it replaces an already existing ring segment and fits between available inner housing components.

2. The system must be integrated into the already existing one and two-stage blading configurations avoiding mechanical modification of the machine housing. This implies, that existing components of the air turbine should be as far as possible not modified.

3. The flow field within the turbine flow channel should not be altered by the carrier system.

4. The measurement unit must be rotated with an external adjustment mechanism during turbine operation.

5. The predicted acoustical propagating modes should be detected with a minimum number of spatially distributed microphones.

Bearing in mind the previous technical restrictions, a preliminary conception of the carrier system - from now on referred as microphone ring - is presented in the next section, followed by the involved development and construction process.

Microphone ring development and design

An important aspect defining the further development process of the microphone ring is related to the air turbine type of construction, one more likely to be found in the design of heavy duty gas turbines (Henke et al. 2012). As shown earlier, the air turbine test rig is divided by an horizontal plane, resulting in two split housing structures, a lower, ground-fixed outer casing section and an upper, removable section (cf. Fig. 4.1). Each section is equipped with inner half ring segments, secured against rotation by means of fastening screws. However, unlike the previously mentioned structures, the rotor is manufactured as a single steel component. This implies that the whole lower turbine section has to be first assembled before the rotor shaft can be positioned in the flow channel. In accordance with this and for reasons of installation and assembly, the microphone ring must be designed and subsequently manufactured in two half segments. With the general design concept for the microphone ring being stipulated, a location for its integration inside the air turbine has to be defined. Based on technical reasons to be exposed below, the microphone ring is located in the turbine cylindrical channel section approx. four chord lengths downstream of the blades for the single-stage blade configuration (cf. Fig. 4.6). Alternative placement locations for the ring were discarded, as being found impractical for its installation.
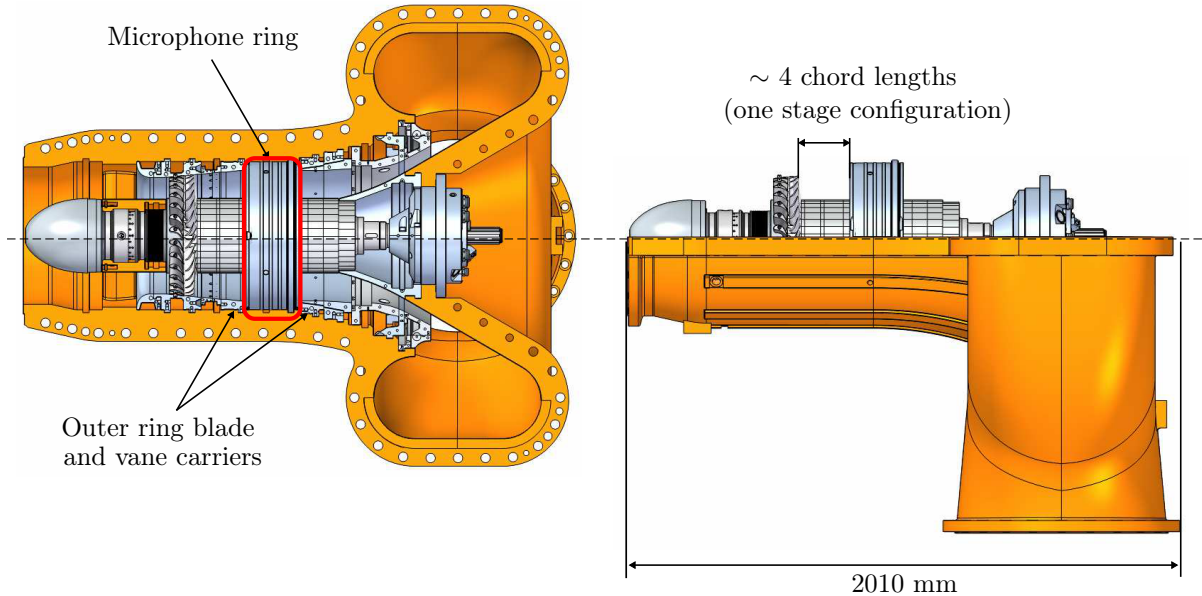
Figure 4.6: Microphone ring position within the air turbine flow channel

For instance, the turbine inlet continuously decreasing cross section as well as the inlet guide vanes, hinder the location of the cylindrical geometry of the microphone ring at that position. A similar situation is experienced at the diffusor section, that rather than exhibiting a decreasing cross section, broadens its geometry along the turbine axial direction. The final mounting position of the microphone ring demands the replacement of merely a ring segment and requires only minor mechanical modification of the turbine outer housing for the instrumentation cable leading-out (cf. Fig. 4.6). Each half section of the designed microphone ring is constituted by an internal half annular segment with a radius of 238 mm coupled to an external ring, as illustrated by Fig. 4.7(a).

The external ring is fixed to the turbine housing, while the internal ring is free to rotate within the flow channel. In order to ensure this free rotation, flat rolling bearings are used. The needle roller bearings are placed within two parallel rectangular grooves milled around the inner ring sides (cf. Fig. 4.7(a), Detail A). As required, the ring can be rotated during turbine operation by a external system located outside the turbine flow channel. The rotation is accomplished by a transmission mechanism constituted by a bevel gear wheel fastened to the inner ring front side and a drive shaft guided through the turbine housing to the outside (Trenke 2012). The internal ring is in turn equipped with four interchangeable aluminum carrier plates, allowing the installation of acoustic instrumentation. Additional to the schematic test set-up of Fig. 4.7(a), the actual microphone ring is shown in Fig. 4.7(b) accompanied by a detailed view of the carrier plate equipped with measurement microphones (cf. Fig. 4.7(c)).
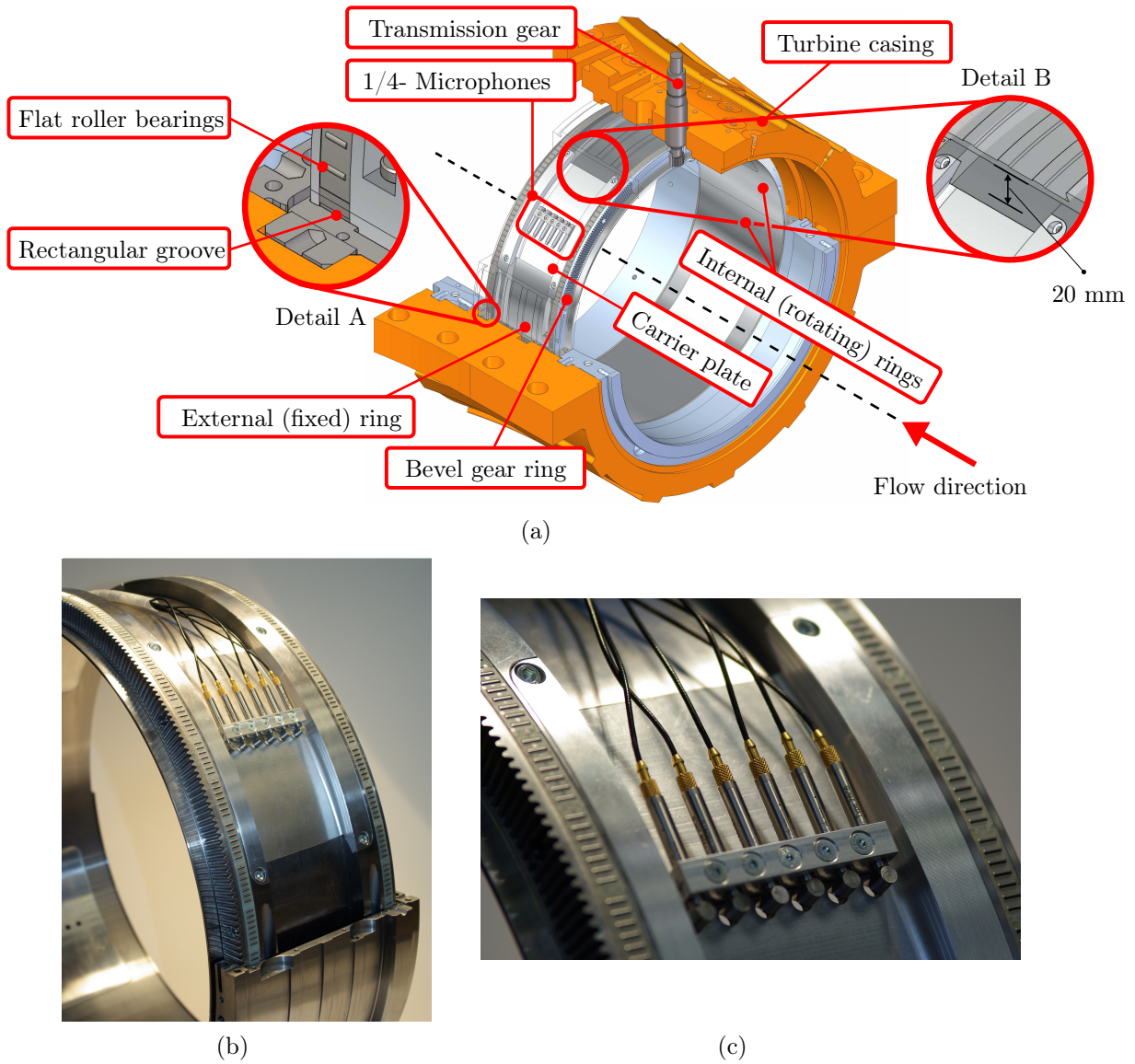
Figure 4.7: Microphone ring, (a) schematic microphone ring set-up, (b) actual assembled set-up, and (c) detailed view of the instrumented carrier plate

The installation and operation of the microphone ring within the turbine flow passage results in a series of complex technical requirements. Among them are included the design of the external transmission mechanism and the selection and integration of the implemented microphones. Each one of the listed items will be separately discussed, beginning with the implementation of the measurement microphones.

Measurement microphones implementation   Microphones play a relevant role in the development of the rotating measuring system. The integration of the microphones within the air turbine represents a technical challenge due to the limited space available for their installation. As illustrated by the zoom area B in Fig. 4.7(a), the region between the carrier plate and the outer microphone ring is very narrow, with a vertical distance measured at the center point of the plate of 20 mm. As a consequence, the microphone selection is confined to sensors having this maximal length including measuring microphone, preamplifier and cable. Based on this restriction, high quality and compact pre-assembled condenser type microphones were chosen. These microphones integrate a measurement capsule and a preamplifier as a unit, ensuring the best possible sensor response characteristics as well as a common sensitivity (Frederiksen et al. 1979).

The chosen sensors are 1/4"–high temperature prepolarized pressure field microphones sets Type 46BD from the manufacturer G.R.A.S. Sound and Vibration$^{©}$. The Type 46BD microphone set consists of a 1/4" high-frequency pressure microphone cartridge Type 40BD and a 1/4 preamplifier Type 26CB-S10, a special version of the Type 26CB. The preamplifier was electrically modified by the manufacturer through an aging process in an attempt to reach an operating temperature of at least 120°C (the operating temperature of the device is restricted to 100°C). Representative diagrams as well as photographs regarding the described measurement microphone set are displayed in Fig. 4.8.
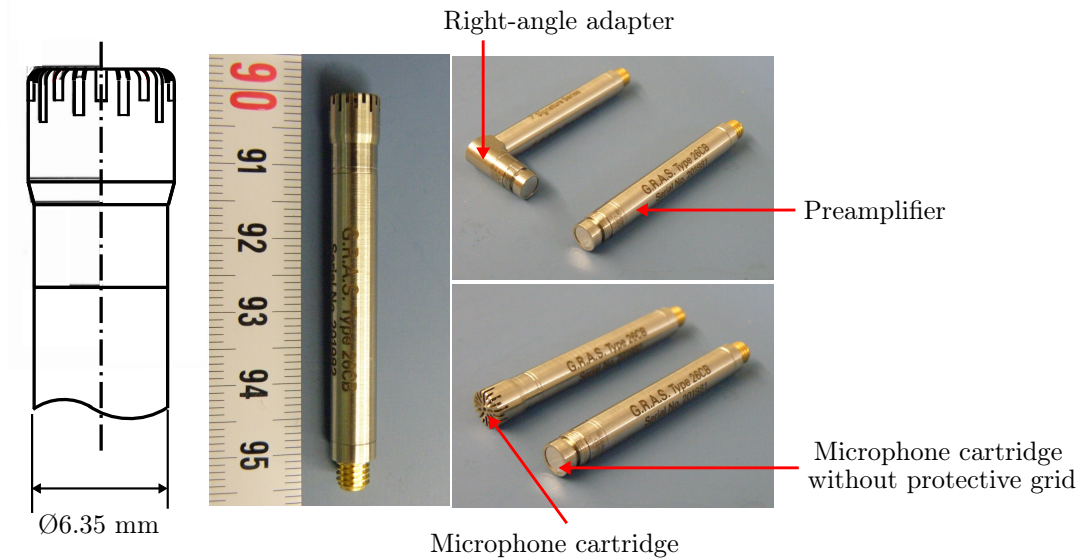
Figure 4.8: Measurement microphone set Typ 46BD

The microphones are horizontally placed and axially flush mounted on one of the interchangeable aluminum carrier plates by means of a right-angle adapter (cf. Figs. 4.7 and 4.8), thus not altering the in-duct prevailing flow field. A constant axial spacing of 20 mm between each acoustic sensor is chosen. This selection is based on a restricted maximum plate carrier width and an optimization study which evaluated the sensor arrangement dependence on the results of the Singular Value Decomposition (cf. Section 3.2). The optimization determined an optimal axial positioning range of 16 to 21 mm between microphones for chosen acoustical modes (Ioannou 2012).

The acoustical sensor selection is not solely based on dimensional issues but also on performance specifications. Regarding this point, a broad frequency operating range is considered appropriate (4 Hz to 70 kHz), since the highest expected multiple of the f_{BPF} amounts to 18250 Hz (cf. Fig. 4.4). A further item defining a suitable acoustic performance is related to the microphone linear dynamic range. For the chosen microphone, a dynamic range varying between 44 dBA and 165 dBA is specified. The stated dynamic range covers the expected sound pressure levels based on previous measurements performed on radial (Rautenberg and Kassens 1970) and axial (Hellmich 2008) turbomachinery.

A summary of performance specifications of the employed microphone sets is shown in Tab. 4.4. Having defined the appropriate measurement instruments based on either spatial and technical performance restrictions, a further aspect is shortly discussed in the next section, namely, the microphone ring external transmission mechanism.

Table 4.4: Microphone set specifications

Nominal sensitivity mV/Pa	Frequency response Hz	Dynamic range dBA (re. 20 μPa)	Temperature range °C	Length mm	Weight g
1.6	4 - 70 k	44 to 165	-30 to +120	54	10

Microphone ring external transmission mechanism   As required by the general design concept of the microphone ring, external control as well as rotation during turbine operation are required. To accomplish both tasks, an external transmission mechanism was designed, constructed and documented by Trenke (2012). Fig. 4.9 shows the final construction of the transmission mechanism. The transmission mechanism is driven by a two-phase ISEL$^{©}$ step motor model MS 300-HT connected to a worm drive by means of a bellows coupling (cf. Fig. 4.9). The step motor is in turn driven by an external programmable controller, the ISEL$^{©}$ iMC-S8 multi-axis controller. The controller converts and subsequently transfers all the commands programmed by the user in a LabVIEW$^{©}$ software driver into angular displacement and rotation direction signals for the connected step motor.
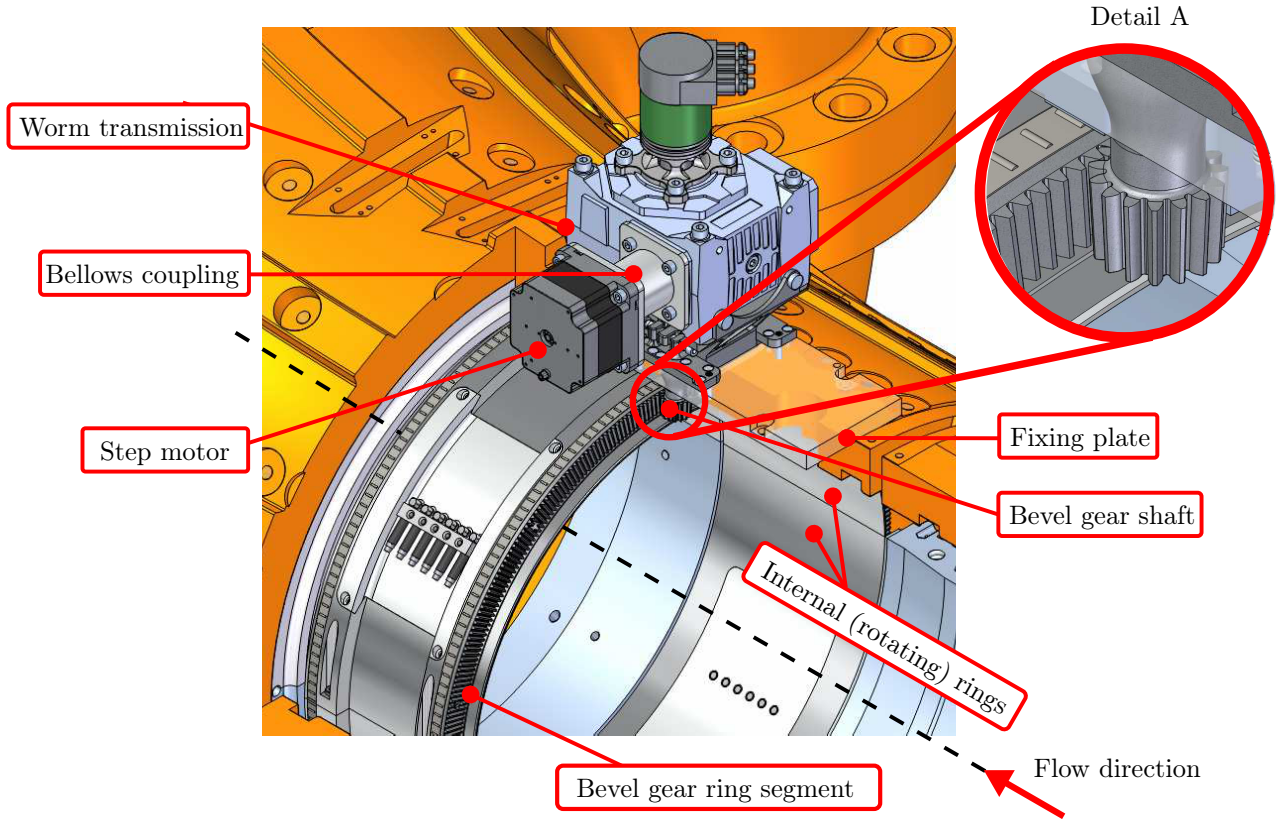
Figure 4.9: Microphone ring transmission mechanism

In this way, the desired motor motion is first evaluated, executed and finally transmitted via the step motor directly to the worm drive. The worm transmission is in turn equipped with a hollow shaft into which the designed bevel gear shaft is inserted. The pinion shaft teeth are in turn coupled to two 180° - bevel gear segments integrated in the microphone ring. This mechanism enables a complete ring rotation with a resolution of 1°.

In this way, a total of 179 circumferential modes can be measured (cf. Sec. 3.2), representing a total of 2160 measurement points (360 circumferential measurement positions and six axially distributed microphones). Additionally, the measurement system is able to decompose radial mode orders up to $n = 2$ (considering upstream and downstream propagating modes) or $n = 5$ (including only downstream modes).

Having covered all the details related to the microphone ring installation and operation, the section to follow handles a key aspect of the performed aeroacoustical experiments, namely, the general measurement scheme. Included in this section are aspects related to the data acquisition devices and required instrumentation for the determination of the turbine flow parameters and a general overview of the control and measurement programs employed for the operation of the microphone ring.

4.2.2 Measurement scheme

After concluding the hardware implementation process, represented in the microphone ring design along with various related topics including positioning, instrumentation and rotation, a further aspect is yet to be discussed, namely, the measurement process. The data acquisition process contemplates the recording of the turbine flow operating parameters and the propagating in-duct sound field. Accordingly, the measurement process is split into two different tasks. The first measurement task deals with the acquisition and recording of sound pressure signals and turbine operating variables. The second one is closely related to the external transmission control for the microphone ring rotation. Both tasks are briefly handled in the sections to follow.

Data acquisition and recording

As stated before, sound pressure signals as well as turbine flow operating variables, including pressure, temperature and angular velocity are required to be measured. To accomplish this task, a modular data acquisition system based on the PXI platform from National Instruments$^{©}$ is chosen. The PXI architecture defines a PC platform for measurement and automation tasks (Starkloff et al. 2003). A PXI system is basically composed of four elements, a chassis with integrated timing and synchronization capabilities, a system controller, a variety of peripheral modules, and a software which enables the user interface with the data acquisition hardware. An overview of a typical PIX data acquisition system is shown in Fig. 4.10.
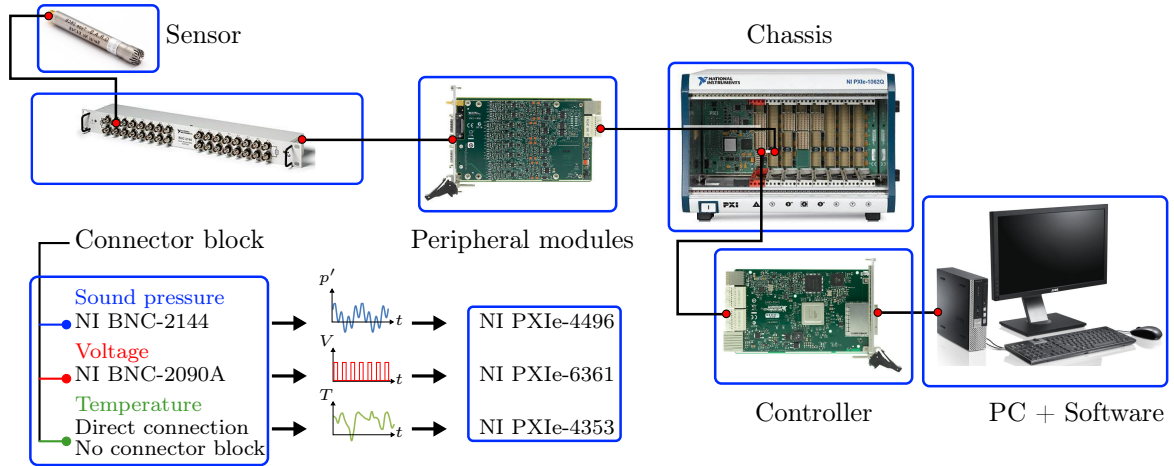
Figure 4.10: Data acquisition scheme

For the present research, three peripheral modules are chosen. The selected modules are specified in Fig. 4.10. On the one hand, a NI PXIe-4496 module is regarded as the right choice for the intended acoustical measurements, as it offers high channel sample rates and constant current signal conditioning for microphone power supply. On the other hand, a NI PXIe-6361 module is chosen for the acquisition of voltage signals. The device handles high sample rates as well and provides analog output channels. Finally, a NI PXIe-4353 module is selected for temperature measurements via thermocouples.

Further technical information of the peripheral modules is presented in Tab. 4.5. All modules are integrated into a NI PXIe-1062Q chassis, a device which physically links the personal computer with the measurement modules enabling the subsequently collection, analysis, presentation and storing of measurement data (cf. Fig. 4.10).

Table 4.5: Peripheral devices technical specifications

Technical feature	NI PXIe-4496	NI PXIe-6361	NI PXIe-4353
Analog input channels	16	16	32
Sample rate (Hz)	204.8k	$1M^3$ and $2M^4$	90
Resolution (bits)	24	16	24

The general measurement and data acquisition set-up for the sound propagation experiments is shown in Fig. 4.11. As indicated by the diagram, the data acquisition is performed by two desktop computers, each one associated with a PXI system. The system labeled Acoustic PC records all sound pressure signals and the varying output voltage of a Hall sensor for the quantification of the rotor angular velocity. The output voltage arises as a result of the passing by of a disc equipped with a rectangular notch at its circumference and coupled to the rotor. Additionally, the external transmission mechanism is controlled by the aforementioned computer via RS 232 serial port.
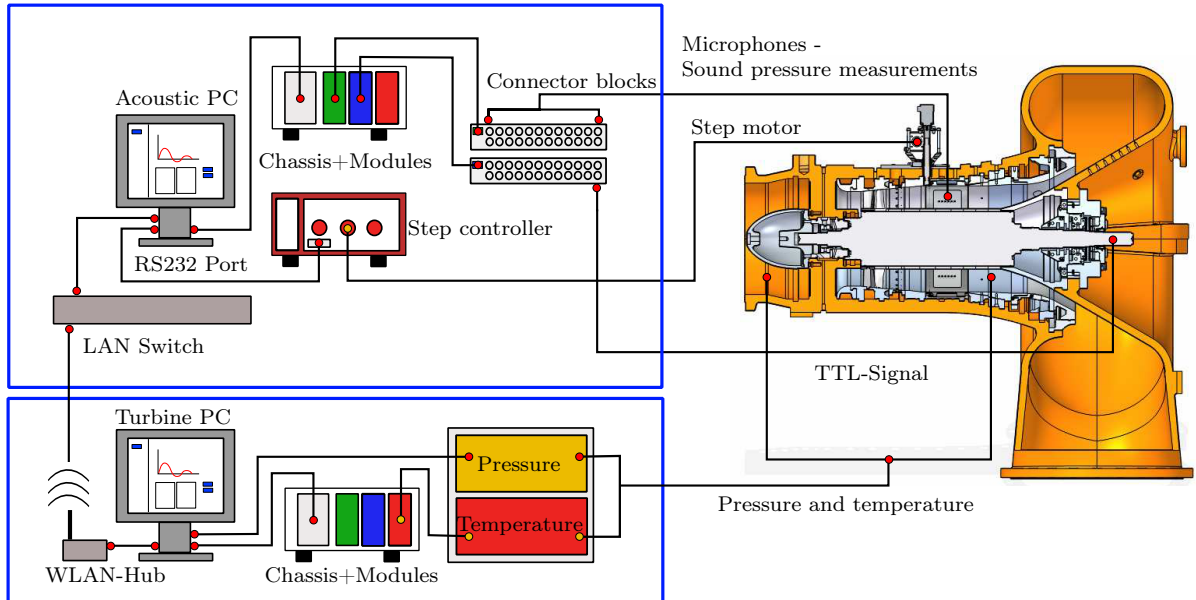
Figure 4.11: General measurement set-up

---

[3]Single channel measurement sample rate
[4]Multi-channel measurement sample rate

The second computer, labeled Turbine PC is, however, used for the acquisition of the single-stage turbine operating parameters. In this respect, the air turbine test facility disposes of permanently installed instrumentation outside the test stand itself. The referred external instrumentation serves to determine the ambient air conditions (pressure, temperature, and relative humidity in front of the screw compressors inlet) as well as to quantify the mass flow by means of the venturi nozzle placed ahead of the turbine inlet.

Turbine in-duct flow measurements are performed to determine the inlet and outlet operating parameters. To this end, stationary measuring probes are employed. Directly ahead of the turbine inlet, a pitot-static tube is installed in order to determine the total and static pressure at this location. The total air temperature is measured as well at this position with a standard temperature probe from the company United Sensors©. The total pressure in the turbine downstream region is measured with a five-hole pneumatic probe equipped also with a total temperature sensor (Binner 2011, Herzog 2008, Kang 2006). Both the pitot-tube and the five-hole probe data are sampled by rack-mounted piezo-resistive pressure scanners Model 9816 from Measurement Specialties©.

The PXI system connected to the host Turbine PC acquires only the temperature data. The in-duct pressure data and the atmospheric pressure ahead the screw compressors (cf. Fig. 4.3), however, are sampled by the rack-mounted pressure scanners and a precision barometer from the company Mensor©, respectively. As seen on Fig. 4.11, a desktop switch transfers the measurement data from the pressure scanners and the high accuracy barometer to the Turbine PC host, which sends this data including temperature readings to the Acoustic PC host. In this way, the operating status of the turbine is known during the performed experiments. Complementing the turbine data acquisition and recording information, the corresponding measurement range and uncertainty of the previously listed instrumentation is summarized in Tab. 4.6:

Table 4.6: Measurement range and uncertainty of the data acquisition devices

Measuring device	Variable	Instrument range	Measurement uncertainty
PSI Scanner 9816	Pressure	2.5 to 520 kPa	$\pm$ 0.15 to $\pm$ 0.05 % FSO[5]
NI PXIe-4353	Temperature	-100 to +1100°C	$\pm$ 0.36°C
Mensor Series 6000	Pressure	80 to 120 kPa	$\pm$ 0.02 % FSO
Microphone 46BD	Sound pressure	44 to 165 dB	$\pm$ 2 dB

After treating the associated measurement scheme for the sound propagation studies in the context of this research, this section is concluded by presenting a general overview of the experimental measurement assembly. Figure 4.12(a) shows a schematic diagram of the turbine test rig along with the integrated microphone ring and the positioned pressure and temperature probes. All measurement planes are labeled in ascending order left to right in flow direction. Associated with each plane are the corresponding measured variables. Shown are the variables P (pressure), T (temperature), p' (sound pressure), and Ω (angular velocity).

---

[5]FSO: **F**ull **S**cale **O**utput
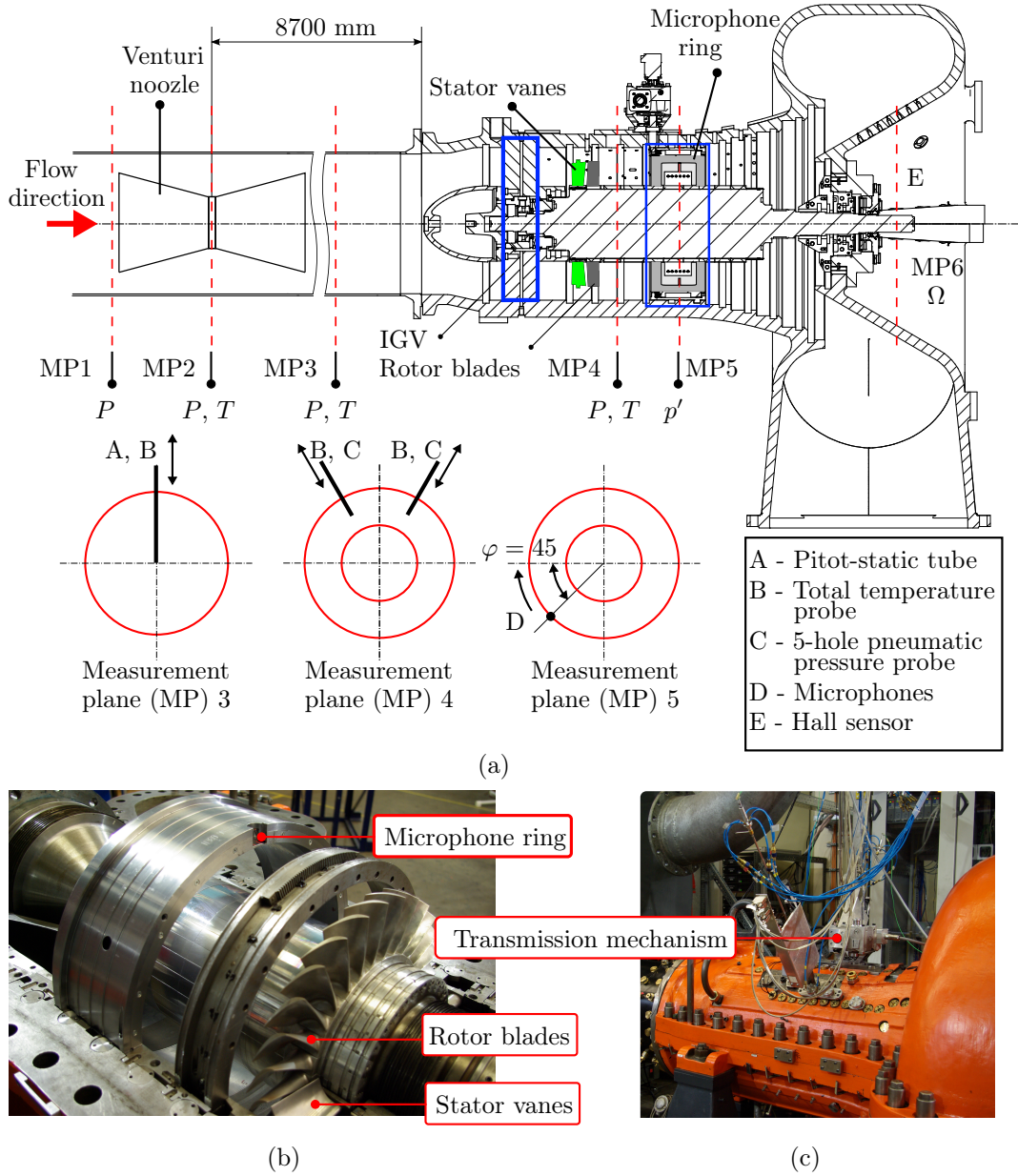
Figure 4.12: Overview of the instrumentation of the single-stage TFD air turbine (based on Zehner (1980)). (a) Schematic representation, (b) integrated microphone ring behind the rotor blades, and (c) assembled test facility

A cross section of three measurement planes at the bottom of Fig. 4.12(a) schematically illustrates the angular orientation of the temperature and pressure probes within the test facility flow channel. The initial position of the microphone ring instrumented plate when integrated into the turbine flow channel is also presented (cross section of the measurement plane 5). As seen in the associated view, the microphones are located at an angle of 45° with respect to the parting line separating both turbine outer housing segments. Complementing the schematic diagram, Figs. 4.12(b) and (c) show the actual assembled experimental set-up. Both the integrated microphone ring as well as the external transmission mechanism can be recognized.

Measurement and control program general overview

Having established the foundations of the data acquisition process in the context of the current experiments, the data acquisition process as well as the step motor control are briefly discussed below. Both data acquisition and motor control are required to be adequately synchronized in order to guarantee satisfactory experimental results. Accordingly, an integrated data acquisition and control program is developed in LabVIEW$^©$. The program consists of two separate modules that nevertheless run simultaneously. The first module, the data acquisition module, records all sound pressure data, the rotor TTL signal and receives the transferred turbine operating data via Ethernet from the "Turbine PC" host. The second module, the control one, is in charge of the microphone ring rotation through the step motor and the external transmission mechanism. In this way, the data acquisition as well as motion control is guaranteed for the proper execution of the intended aeroacoustical experiments.

4.3 Concluding remarks

The current chapter has concentrated so far in the development of a rotating ring as a measurement concept for the subsequent application of an in-duct modal analysis method for sound propagation studies, specifically the RMA. In respect thereof, the rotating ring technical requirements and limitations as well as its construction, implementation and installation in the TFD low-pressure turbine test rig were discussed.

Complementing this discussion, operating aspects of the test rig were presented along with the sensors and data acquisition systems required for the intended aeroacoustical studies. The latter was complemented by a general overview of the measurement setup. Based on the aforementioned aspects, the following concluding remarks can be established:

1. The developed rotating ring enables the measurement and subsequent analysis in high resolution of the in-duct propagating sound structure within a low-pressure air turbine. The measurement system is appropriate for the application of the RMA to aeroacoustical studies in full-scale axial turbomachinery. This is possible as a result of the accurate circumferential positioning of the measurement system executed by an external transmission mechanism.

2. The implemented instrumentation for the measurement of the flow field and turbine operating parameters (inlet and outlet pressure and temperature, and rotor angular velocity) guarantees an accurate estimation of the expected in-duct propagating structure. This acoustical field is defined in terms of the modes Cut-Off frequencies as well as in terms of the propagating mode combinations (m, n) (cf. Section 2.3.5).

3. With the measurement system implemented in the turbine outlet, a systematic sensitivity study of the RMA output variation as a consequence of changing data acquisition and turbine related flow parameters can be performed. The results derived from this analysis are useful to develop a careful experimental design leading low uncertainty results derived from the RMA output. Further details regarding the performed sensitivity analysis are presented and discussed in Chapter 6.

Having described the general experimental setup for the intended aeroacoustical measurements in the context of this work, the resulting sound field is first analyzed in Chapter 5 by means of the RMA for a specific operating point. As such, the propagating acoustical field is quantified in terms of circumferential and radial mode amplitudes for the one-stage TFD low pressure air turbine configuration. This analysis is followed by a sensitivity study of the RMA output to specific data acquisition and turbine operating parameters. The focus is set on the variation of the circumferential mode amplitude to alterations in the aforementioned parameters. The latter is covered in Chapter 6 of the present document.

5 Sound propagation measurements at the TFD low-pressure turbine

The previous chapter presented the experimental set-up for the intended sound propagation studies on the TFD model air turbine. Additional to the test rig itself, an overview of the instrumentation required for the application of the **R**adial **M**ode **A**nalysis (RMA) was provided. The latter represents the starting point of the acoustical field analysis performed with the aid of this method. As such, the current chapter presents the results derived from sound pressure measurements with wall-flush mounted microphones evaluated via RMA. In this way, the spatial structure of the sound pressure distribution in selected cross sections of the model air turbine is quantified in terms of circumferential and radial mode amplitudes. Previous to the presentation of this results, the machine operating parameters corresponding to the performed acoustical experiments are first established. Afterwards, and based on the turbine flow parameters, the in-duct sound pressure structure within the model turbine is defined in terms of the acoustical mode combinations (m, n) and the corresponding Cut-On frequencies. The chapter is concluded with a discussion related to measurement uncertainty sources when performing in-duct noise studies and evaluating derived results with the RMA.

5.1 Experimental design - Experiments execution

The sound propagation experiments were performed at the model air turbine of the TFD. The experiments were conducted under diverse operating conditions. These are directly related to the machine operating point, which is characterized by the mass flow, the rotor angular velocity and the pressure and temperature within the test section. The turbine configuration chosen for the experimental measurements was a single-stage (rotor/stator) arrangement including a row of 29 stationary vanes and a row of 30 rotating blades (cf. Sec. 4.1). The performed measurements were systematically carried out according to the test scheme shown in Tab. 5.1. The operating points are displayed in terms of the mass flow and the angular velocity normalized with respect to the nominal parameters of the turbine one-stage configuration (cf. Tab. 4.1), both defined as

$$\dot{m}_{rel} = \frac{\dot{m}}{\dot{m}_{nom}} \tag{5.1}$$

and

$$\Omega_{rel} = \frac{\Omega}{\Omega_{nom}} \tag{5.2}$$

Table 5.1: Operating points of the experiments on the one-stage turbine

$\dot{m}_{rel}$		
0.64	0.90	Ω_{rel}
x	-	0.23
x	-	0.47
x	x	0.93

A single operating point was chosen for the execution of the sensitivity study on the output of the RMA. The chosen operating point corresponds to that with a relative mass flow $\dot{m}_{rel} = 0.64$ ($\dot{m} = 5$ kg s^{-1}) and a relative angular speed $\Omega_{rel} = 0.47$ ($\Omega = 3500$ min^{-1}). The mass flow ($\dot{m}$) as well as the turbine inlet and outlet total pressure ($P_{\text{tot-in}}$ and $P_{\text{tot-out}}$) were recorded. Additionally, the inlet and outlet total temperature ($T_{\text{tot-in}}$ and $T_{\text{tot-out}}$) along with the ambient pressure and temperature (P_{amb} and T_{amb}) were acquired. The aforementioned operating parameters were complemented by the measured rotor angular velocity for every shaft rotation.

As previously stated in Sec. 4.2.2, the flow variables were simultaneously recorded along with the acoustical measurements. In regard to the latter, a sample rate $f_{\text{s}} = 60000$ Hz was selected for the acquisition of the sound pressure data. A total of $N = 60000$ samples were registered, leading to a measurement period $T = 1$ s. In relation to the acquisition of the flow parameters, for each circumferential measuring position swept by the microphone ring, two samples of the aforementioned flow variables were recorded over the same time period and afterwards averaged. The data acquisition process performed at one specific operating point implied a complete rotation of the microphone ring. The rotation was carried out in 1° steps, resulting in a total of 360 circumferential measurement positions and 2160 measurement points (6 microphones circumferentially displaced over 360 circumferential positions).

5.2 In-duct steady flow field measurements

An overview of the resulting flow parameters is illustrated in Fig. 5.1. The flow variables are shown in terms of a measurement cycle, which is equivalent to the circumferential measurement position of the microphone ring. As a general remark, it can be noticed that both the magnitude of the total temperature and total pressure decrease from the inlet to the outlet of the turbine. Figure 5.1(a) shows the turbine inlet and outlet total pressure as well as the ambient pressure variation with the microphone ring circumferential measurement position. The corresponding pressure values slightly vary with the measuring cycle, i.e., with the circumferential measuring position, indicating the steadiness of the flow field during the whole measurement time. A variation of 0.1% of the maximum value with respect to the mean value is quantified for the inlet total pressure, whereas the outlet and ambient pressure exhibit a maximum magnitude variation in the order of 0.001% when compared to their mean values.
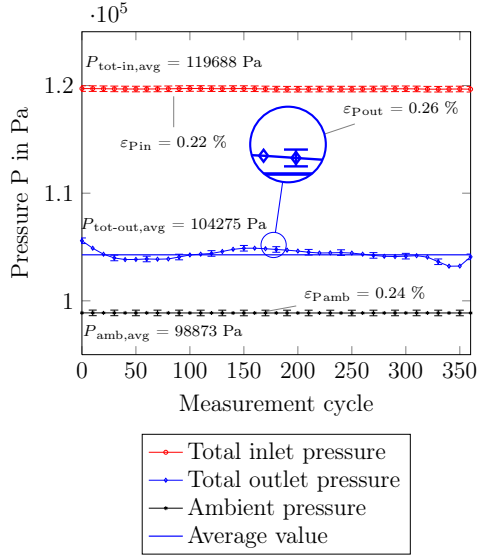
(a) Total and ambient pressure
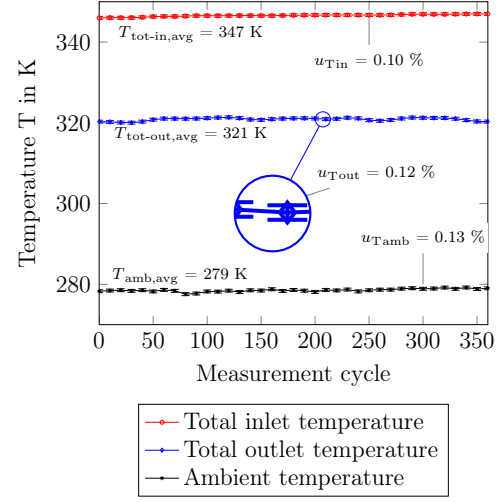
(b) Total and ambient temperature
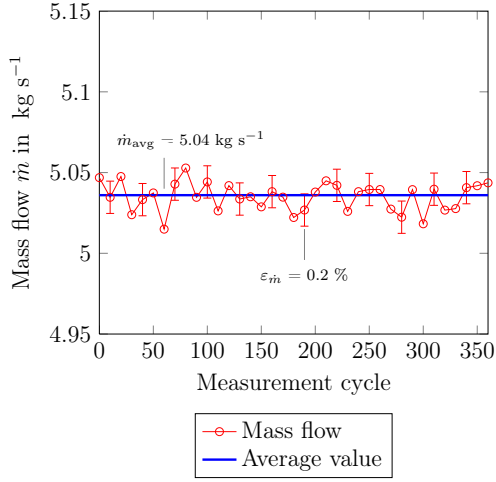
(c) Mass flow
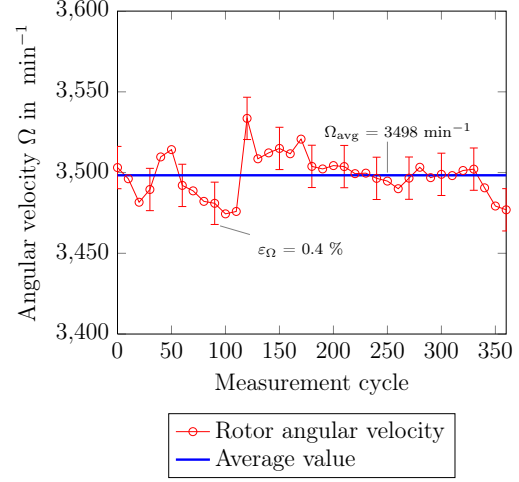
(d) Rotor angular velocity

Figure 5.1: Flow parameters of the operating point $\dot{m} = 5$ kg s^{-1}, $\Omega = 3500$ min^{-1}

A similar diagram is displayed for the turbine temperature variation (cf. Fig. 5.1(b)). A slight rise in the inlet total temperature can be recognized, resulting in a maximum variation of 0.1% in its magnitude with respect to its mean value. In contrast to this trend, the outlet temperature continuously fluctuates around the mean value of 321 K, exhibiting a maximal variation of 0.14% compared to this value. This temperature fluctuation behind the blading region is attributed to the heating of the rotor as a result of the contact with the incoming hot fluid (Binner 2011). This initial heating is afterwards transferred to the subsequent stator vanes and rotor blades as a result of the higher thermal conductivity between the rotor and the blading material than that between the rotor and the moving fluid. Once the fluid leaves the blading region, heat is then again transferred to it, leading to a temperature variation behind the rotor blades, which in this case is just noticeable.
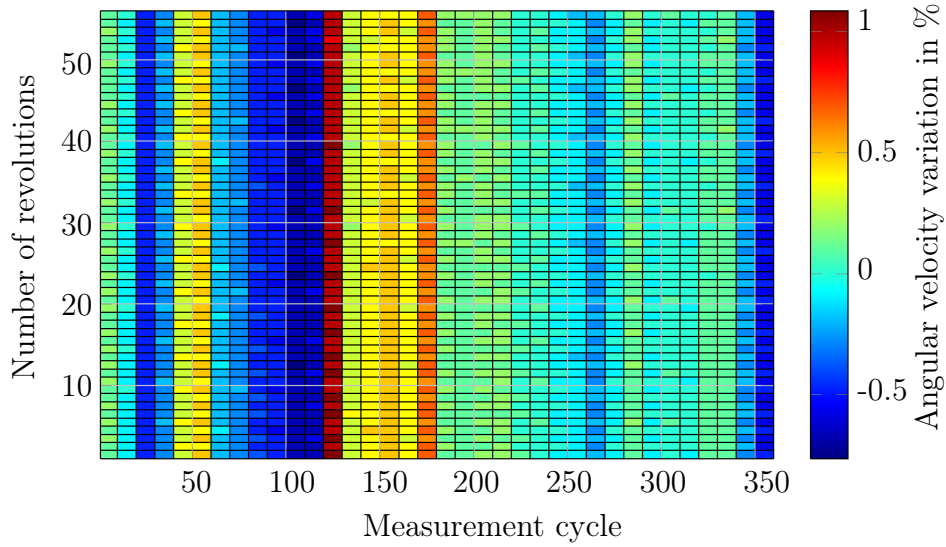
Figure 5.2: Deviation of the rotor angular velocity from its average value

Regarding the mass flow, its time variation is shown in Fig. 5.1(c). A stable pattern is identified, giving rise to a maximal variation of 1.1% in the magnitude of this flow variable. The rotor angular velocity variation is presented in Fig. 5.1(d). This diagram corresponds to the mean value fluctuation of this parameter with the circumferential position of the microphone ring. The absolute difference between the lowest and highest recorded angular velocity amounts to 64 min^{-1}, equivalent to a relative value of 1.8% when compared with the mean value ($\Omega_{avg} = 3498$ min^{-1}). Complementing the rotor angular velocity mean value diagram, Fig. 5.2 displays the deviation in percentage of the rotational speed from the averaged angular velocity calculated for the whole measurement time. As noticed, the ordinate displays the number of rotor revolutions. For the chosen operating point, a maximal of 58 revolutions in a time interval of one second could be recorded ($\Omega = 3500$ min$^{-1} = 58$ s$^{-1} = 58$ Hz). However, only 56 revolutions were finally considered as a consequence of a previous synchronization procedure performed for the application of the RMA. This process implied data reduction in order to establish a common starting point for the acoustical measurements. According to the diagram, deviations of the angular velocity between -0.9% and 1.1% took place during the measurement time.

As a way to complement the previously presented operating parameters, the absolute velocity components along the turbine flow channel are displayed below in Fig. 5.3. Both the axial (c_x) and circumferential (c_u) components of the absolute flow velocity c are shown for five different planes. The determination of the absolute velocity in Plane 0 is based on the measured data delivered by the pitot-static tube and the total temperature probe located ahead of the turbine inlet (cf. Fig. 4.12). At this position (Plane 0), the air flow is assumed to be homogenous, axial and fully developed. As a consequence, no absolute circumferential velocity component is expected. The magnitude of the axial and circumferential velocity magnitudes of the subsequent plane (Plane 1) is computed based on the measurement parameters (total pressure and temperature) recorded at the turbine inlet as well as on the rotor angular velocity.
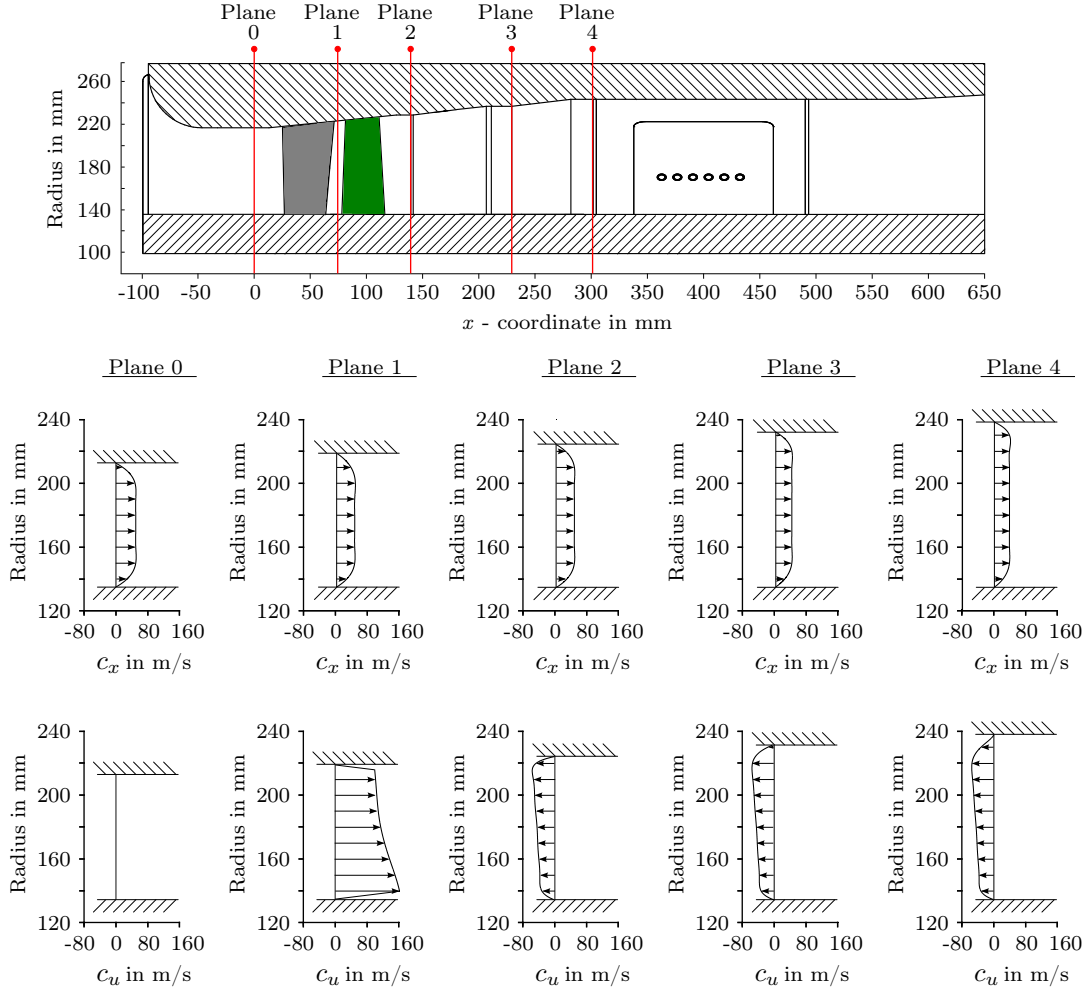
Figure 5.3: Turbine in-duct flow profiles

The calculation in Plane 1 is performed by means of a velocity diagram, an approach which in turn rest upon the incidence and exit angles of the stator vanes and rotor blades, α and β, respectively. The incidence and exit angles distribution along the vane and blade height are schematically presented in Fig. 5.4(a) (Sandstede 1974). Regarding the remaining planes, a similar approach based on velocity diagrams is undertaken. As opposed to planes 0 and 1, the Cartesian components of the absolute velocity corresponding to planes 2, 3 and 4 (cf. Fig. 5.3) are determined based on the operating data recorded by the five hole pressure probe located in Plane 3. To validate this procedure, the results of c_x and c_u in Plane 3 are compared with the outcome of the data measured by the pressure probe. The latter requires the usage of the recorded pressures in parallel with the calibration coefficients of the probe to determine the total and static pressure as well as the total temperature at the measurement location. The absolute velocity vector angle γ has to be determined as well by means of an iterative procedure. The mentioned parameters of the pressure probe are shown for clarity in Fig. 5.4(b). With these parameters, the absolute velocity and its axial and circumferential components can be quantified. The exact procedure and further details are summarized in Evers (1985).

63
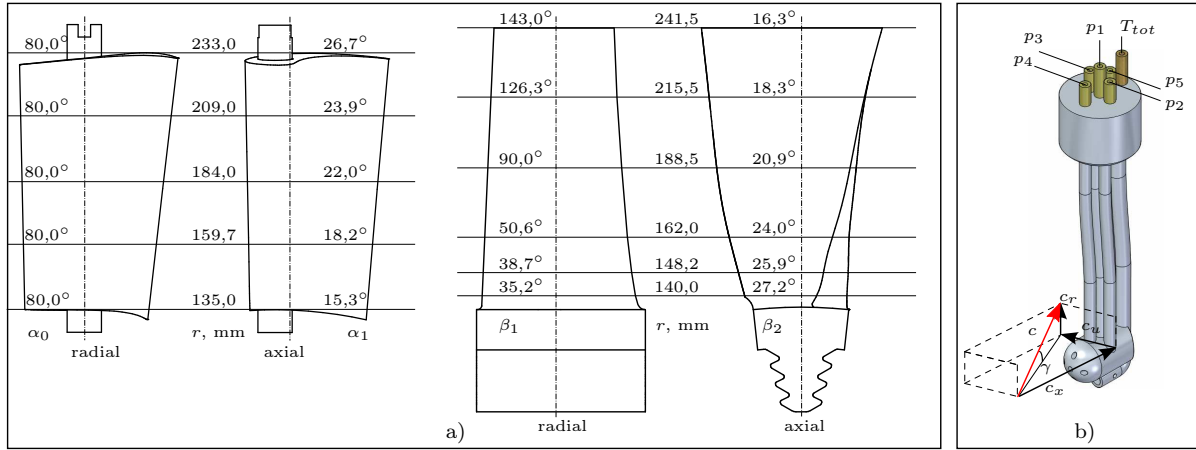
Figure 5.4: Distribution of the incidence and exit angles along the vane and blade height according to Sandstede (1974) (a) and, (b) five-hole pressure probe accompanied by the definition of the absolute velocity components and the corresponding flow angles

The previously mentioned comparison is performed in this position (Plane 3) since it corresponds to the location of the pressure probe (cf. Fig. 4.12). The outcome of the comparison is presented in Fig. 5.5(a). The results of the pressure probe are shown as discrete data points, since only a finite number of measurements were recorded along the radial direction of the flow channel. A good agreement between both data sets is revealed by superposing the evaluated information. Variations in the order of magnitude of 1.9% and 5.4% for the absolute axial and circumferential velocities, respectively, are quantified. This variation is calculated by considering the difference between both data sets and by further comparison with the mean value of the resulting measurements from the pressure probe. This fact confirms the validity of the undertaken approach based on velocity diagrams.

Once the rectangular components of the absolute velocity vector are quantified, the Mach number for both Cartesian components can be determined, namely, the axial and circumferential Mach numbers, Ma_x and Ma_φ, respectively. The magnitudes corresponding to both Mach numbers in Plane 4 (ahead of the microphone ring, cf. Fig. 4.12 and 5.3) are shown in Figs. 5.5(b). Both play a prominent role in the determination of the sound field within the turbine. These directly influence the Cut-On frequency, $f_{\mathrm{Cut\text{-}On}}$, and therefore the propagating acoustical structure. On the one hand, and according to Eq. 2.65, an increasing Ma_x derives in a decreasing value of $f_{\mathrm{Cut\text{-}On}}$. This is reflected in lower excitation frequencies required to prompt the propagation of specific acoustical modes. On the other hand, according to the direction of rotation of the circumferential flow and therefore, depending on the algebraic sign accompanying Ma_φ, $f_{\mathrm{Cut\text{-}On}}$ may be reached with lower or higher excitation frequencies. For the evaluated operating point of the turbine, Ma_x averages 0.1, meanwhile Ma_φ varies between -0.1 and -0.16. Once all the parameters characterizing the flow-regime within the air turbine are known, the dominating propagating acoustical structure can be predicted. The procedures and results related to the sound field determination are presented in the following section.
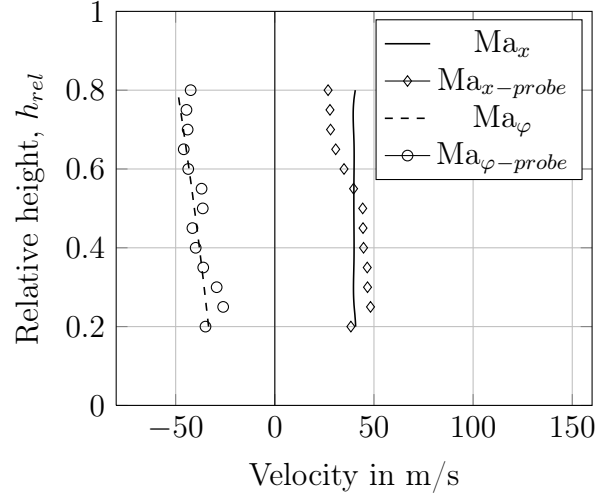
(a)
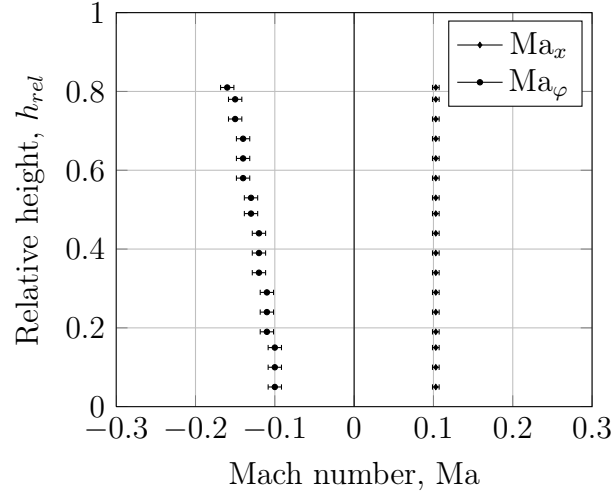
(b)

Figure 5.5: Comparison of the calculated circumferential and axial velocity profiles (a), and (b) circumferential and axial Mach number

5.3 Identification of propagating acoustical modes

Having quantified the flow parameters within the turbine flow channel, the in-duct sound pressure structure is defined in the sections to follow in terms of the propagating acoustical modes. The analyzed modes are generated by two processes involving the interaction of the moving blades with the stator and with the inlet guide vanes (cf. Fig. 2.16). The modes are first identified based on the calculation of the Cut-Off frequency. This is reflected in a propagation diagram, in which all modes are displayed within a specific frequency range. Considering that only the discrete tones are of interest in this work, the blade-passing frequency and one of its associated multiples are solely considered.

In this section, the acoustical mode combinations (m, n) resulting from the analysis of the mathematical expression of the Cut-Off frequency, Eq. (2.65), are presented. As aforementioned, the results are displayed in a propagation diagram, which exhibits an overview of Cut-On mode orders as a function of the excitation frequency. This representation is ideal, since it clearly establishes the constitution of the sound field for specific frequencies, namely, for the blade-passing frequency f_{BPF} and its harmonic multiples. The effect of the swirling flow on the propagation is considered as well. Its effect is quantified in terms of the magnitude of the circumferential Mach number, Ma_{φ}.

The results are based on the previously presented operating parameters of the air turbine. The considered parameters are the mean values of the static temperature (required for the calculation of the speed of sound) and those of the axial and circumferential Mach numbers at Plane 4 (cf. Fig. 5.3). These parameters represent the input values required to determine the Cut-On frequency $f_{\mathrm{Cut\text{-}On}}$ and therefore the propagating sound field within the air turbine. The mean values are calculated over the whole measurement cycle (360 cycles, cf. Sec. 5.1). For the determination of the blade-passing frequency, the average of the angular velocity of the rotor over the whole measurement cycle is considered as well. The values are summarized in Tab. 5.2.

Table 5.2: Averaged operating parameters of the TFD single-stage LPT for the propagating sound field calculations

Parameter	Value
Static temperature in K	$319 \pm 0.03\%$
Axial Mach number	$0.1 \pm 0.04\%$
Circumferential Mach number	$-0.13 \pm 0.06\%$
Rotational speed in $\min^{-1}$	$3498^{+1.1\%}_{-0.8\%}$

For the present operating point, the analyzed frequencies correspond to the f_{BPF} and its first harmonic, i.e., 1750, and 3500 Hz. These values represent the frequencies where the discrete tonal noise components are expected to emerge as a result of the in-duct sound propagation and the rotor/stator interaction. The resulting acoustical modes corresponding to the given flow condition and for the selected frequency components are graphically shown in Fig. 5.6. Each color frame represents a specific radial mode-order. In this way, the diagram can be divided into two regions; a first region indicating no propagation - blank region - and a second zone pointing out the presence of several in-duct propagating modes. The non-propagating modes are a result of the lower magnitude of the excitation frequency when compared with the Cut-Off frequency. Once the excitation frequency exceeds the Cut-Off frequency, the resulting acoustical modes contribute to the dominating sound field structure within the turbomachine. In this respect, and in general, low-order as well as high-order radial modes are associated with a broad spectrum of azimuthal mode orders and excitation frequencies.
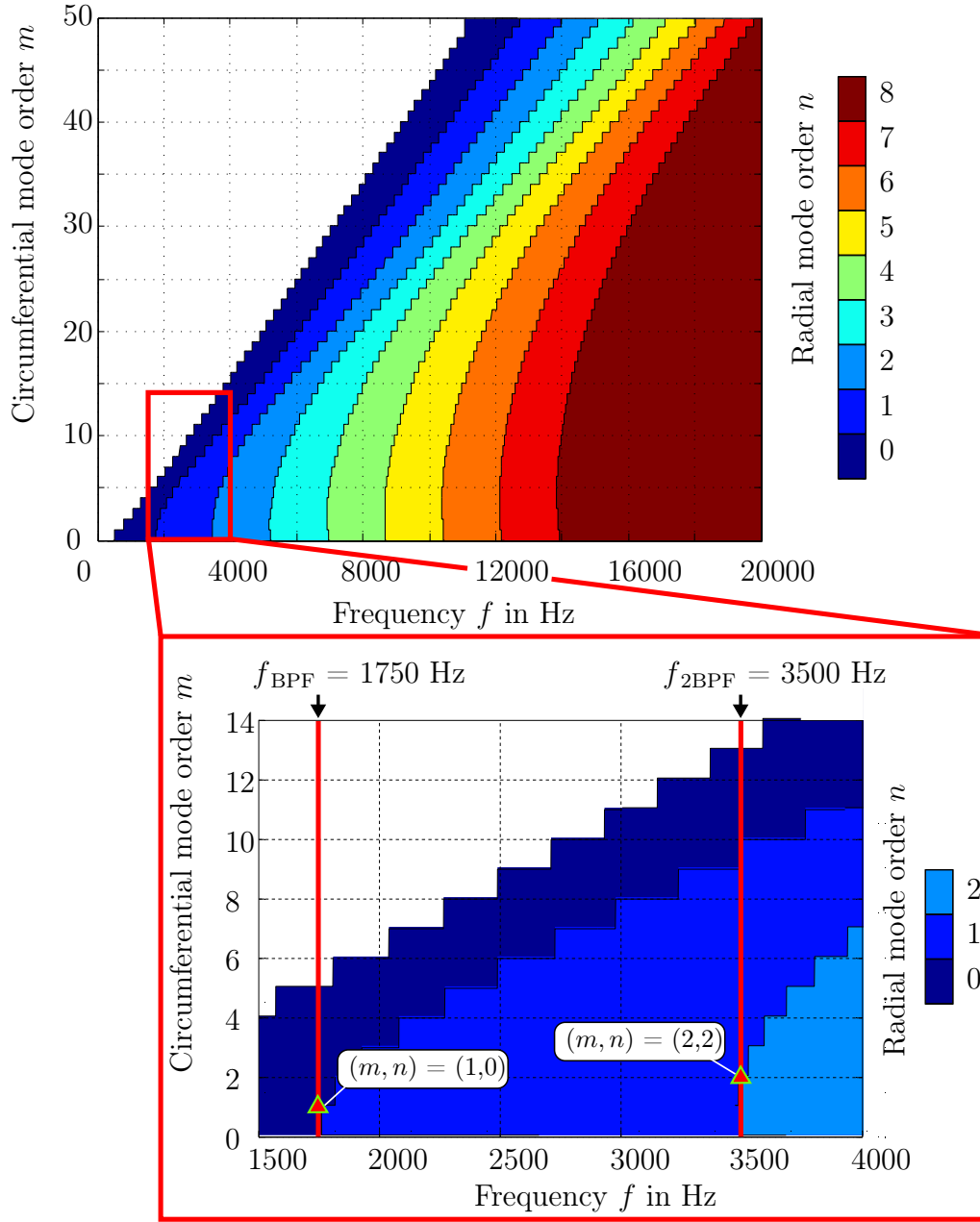
Figure 5.6: Propagating acoustical, operating point $\dot{m} = 5$ kg s^{-1}, $\Omega = 3500$ min^{-1}

It can be observed from Fig. 5.6 that theoretically, every acoustical mode lying over the vertical line indicating the tonal frequency is able to propagate. However, this propagation in turbomachinery-related flows is limited by the rotor/stator interaction, which gives rise to specific circumferential mode orders according to the Tyler and Sofrin equation (cf. Eq. 2.67). In accordance with this fact, the resulting mode orders m based on the moving and fixed blade configurations shown in Tab. 5.3 are unveiled in Tab. 5.4. The arising mode orders m are arranged according to the harmonic multiple h. This outcome is valid for several integers s and a fixed number of blades, vanes and inlet guide vanes. By comparing Tab. 5.4 and the detailed view of Fig. 5.6, it is inferred that only low order modes are cut-on in the measurement duct section of the turbine rig.

67

Table 5.3: Moving and fixed blading configurations

Configuration	Interacting blade row	Number of blades, B	Number of vanes, V
1	R1/S1	30	29
2	R1/IGV	30	6

Table 5.4: Circumferential mode orders m derived from the Taylor & Sofrin equation

Interaction	s	-5	-4	-3	-2	-1	0	1	2	3	4	5
R1/S1	$h = 1$	-115	-86	-57	-28	1	30	59	88	117	146	175
	$h = 2$	-85	-56	-27	2	31	60	89	118	147	176	205
	$h = 3$	-55	-26	3	32	61	90	119	148	177	206	235
	$h = 4$	-25	4	33	62	91	120	149	178	207	236	265
	$h = 5$	5	34	63	92	121	150	179	208	237	266	295
R1/IGV	$h = 1$	0	6	12	18	24	30	36	42	48	54	60
	$h = 2$	30	36	42	48	54	60	66	72	78	84	90
	$h = 3$	60	66	72	78	84	90	96	102	108	114	120
	$h = 4$	90	96	102	108	114	120	126	132	138	144	150
	$h = 5$	120	126	132	138	144	150	156	162	168	174	180

The Cut-On modes are expected to originate only from the rotor/stator interaction. The Cut-On modes as well as its corresponding Cut-On frequencies are summarized in Tab. 5.5 below. The associated uncertainty is determined based on the method of propagation of error. The method quantifies the global measurement uncertainty associated with a physical quantity which is a function of several other variables. The magnitude of the associated error is calculated by following the procedures corresponding to the propagation of uncertainty for multivariable functions (Beckwith et al. 2006).

Table 5.5: Propagating (m, n) modes for selected tonal frequency components

	f_{BPF}	f_{2BPF}	f_{2BPF}	f_{2BPF}
$(m, n)_{\text{Cut-On}}$	(1,0)	(2,0)	(2,1)	(2,2)
$f_{\text{Cut-On}}$	$276 \pm 0.27\%$[1] Hz	$549 \pm 0.28\%$ Hz	$1817 \pm 0.26\%$ Hz	$3487 \pm 0.26\%$ Hz

The acoustical modes resulting from the pressure field and wake interactions between the rotating blades and the IGV also contribute to the sound field inside the LPT. Among them, the plane mode $(0, 0)$ is present for the f_{BPF}. Further acoustical mode combinations are the co-rotating modes $(6, 1)$ and $(12, 0)$, both at f_{2BPF}, and both for values of $s = $ -9 and $s = $ -8, respectively (values not shown in Tab. 5.4).

---

[1] Measurement inaccuracy in percentage of the indicated Cut-On frequency.
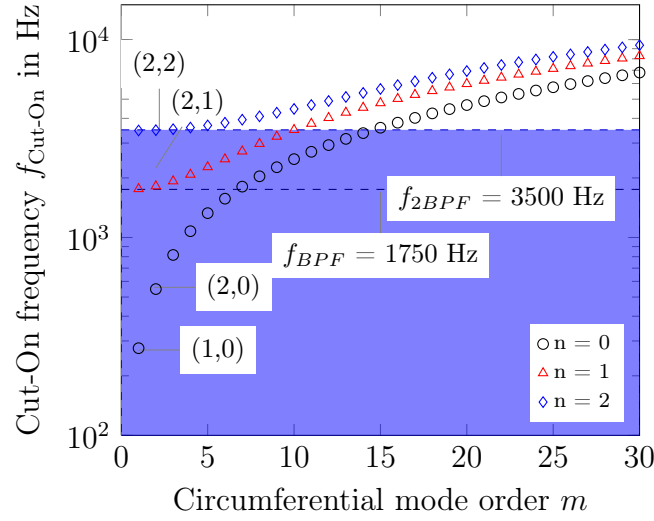
Figure 5.7: Cut-On frequencies for selected mode orders

In order to complement the information presented before regarding the propagating acoustical modes, Fig. 5.7 depicts a limited number of modes with radial orders varying from $n = 0$ to $n = 2$ and circumferential orders $m = 1...30$. The shaded area below the first harmonic component of the $f_{2\text{BPF}}$ (3500 Hz) represents the modes which are capable of propagating. The region above this frequency encloses non-propagating modes. Included within the shaded area are all the circumferential mode orders m generated by the rotor/stator arrangement (cf. Tab. 5.5) and by the rotor/IGV set-up and predicted by the Tyler and Sofrin equation (cf. Tab. 5.4). Knowing the expected acoustical mode combinations propagating through the LPT, the data analysis procedure to determine the circumferential and radial mode amplitudes is presented in the sections to follow. The procedure requires in first place the determination of the circumferential mode amplitudes, A_m. Based on these magnitudes, the radial mode amplitudes $A_{[mn]}^{\pm}$ are subsequently computed. Both are necessary to provide a clear picture of the sound pressure structure within the turbine flow channel.

5.4 Analysis method and proccesing

5.4.1 Unsteady sound pressure data processing prior to RMA

The circumferential as well as the radial amplitudes of the in-duct propagating modes are determined by means of the Radial Mode Analysis (cf. Chapter 3). Accordingly, the sound pressure is measured at several circumferential and axial measurement positions. In the present work, this task is performed by a turbine-integrated rotating-ring. Before the amplitudes of the in-duct acoustical modes are established, a data reduction procedure is carried out. The former is necessary to ensure a proper analysis of the recorded unsteady sound pressure data sets. In respect thereof, unsteady signals recorded by measurement microphones are constituted by deterministic and stochastic components. The deterministic part of the signal comprises a steady-state average value and periodically fluctuating components, while the stochastic fraction of it exhibits random noise (Gostelow 1977). Mathematically, the signal is thus defined as follows

$$y(t) = \underbrace{\bar{y} + y(t)_p}_{y(t)_{det}} + \underbrace{y'(t)}_{y(t)_{stc}} \tag{5.3}$$

where $\bar{y}$ represents the steady-state average value, $y(t)_p$ is the periodically varying component and $y'(t)$ stands for the random fraction of the time signal. For the current data analysis, it is of great interest to retain the periodicity of the recorded signal, specially knowing in advance that the nature of the in-duct pressure field in many turbomachinery applications exhibit such cyclic behavior (Moore 1972, Tyler and Sofrin 1962). Provided that the signal displays such periodicity, it can be recovered from the background random noise by extracting the fluctuating as well as the steady-state components from the raw data. This procedure is accomplished by suitable filtering and averaging methods.

A well-known method is the *phase-locked ensemble average*, short PLEA, developed by Gostelow (1977) in order to reduce the noise of raw data aided by the periodic passing of a rotor blade as a phase reference. This technique is used in the present work in order to isolate the tonal noise components of interest from the broadband turbine noise (cf. Sec. 2.4.1). The suppression of such noise components takes place by a process of waveform averaging. Unsteady sound pressure signals, each one revolution period long, are successively averaged with each other resulting in a broadband noise-reduced waveform phase locked to the turbine rotor.

The data analysis based on the *phase-locked ensemble average* is accomplished in a series of steps once the unsteady sound pressure data has been recorded. The general procedure consists of first properly storing all recorded data sets and subsequently filtering them. A data synchronization routine is implemented afterwards. This routine guarantees that all data sets are referenced to an appropriate phase and a common data acquisition starting point. The phase reference is given by a trigger signal, represented in a voltage pulse generated by the passing of a specific turbine blade. Once the data is phase and time synchronized, a number or ensemble of data samples, each of one cycle long, is taken.

Due to variations of the rotor angular speed, several ensembles may not display a constant quantity of data samples. The ensemble averaging requires, however, ensembles of equal length in order to avoid signal phase shift. As a result of this, the varying length of the ensembles is set to a common sample size, specifically to that representing the largest data sample size (i.e., that corresponding to the lowest rotor angular speed). This is accomplished by a resampling routine, in which the data is interpolated by an specific factor, which results in a variation of the original sampling frequency to match the new data length requirement. Following the data resampling, all ensembles are successively averaged with each other, thus concluding the unsteady data analysis procedure. The averaging is accomplished solely by taking the instantaneous value of each ensemble for every time t, summing the values, and dividing by the number of ensembles, in this case represented by the number of considered rotor revolutions. Before the relevant steps of the data evaluation routine are discussed into more detail, a graphical scheme of the analysis procedure is shown in Fig. 5.8.
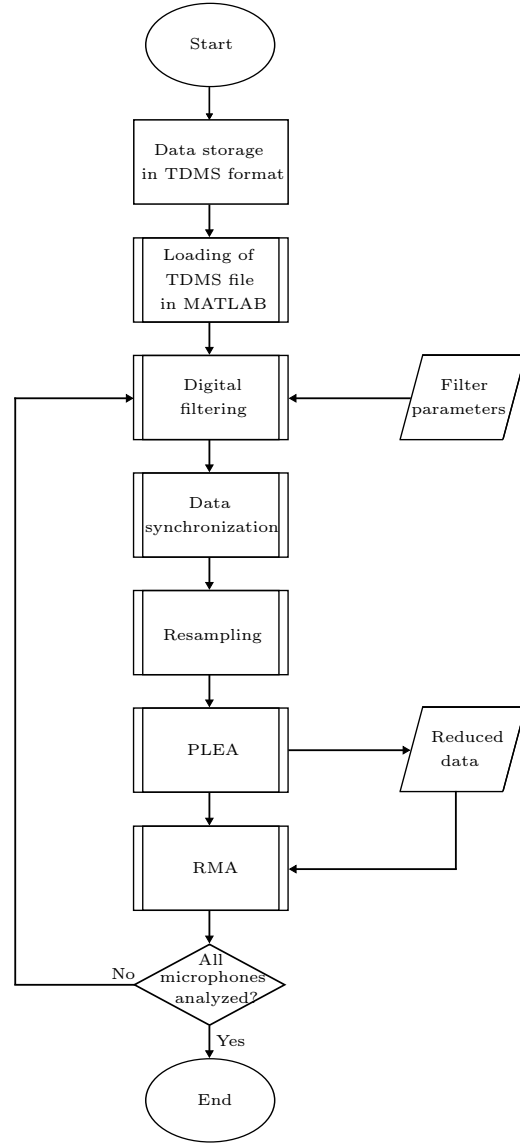
Figure 5.8: Graphical scheme of the data analysis procedure

5.4.2 Phase-locked ensemble average, PLEA

The constituting steps for the unsteady sound pressure data processing prior to the implementation of the RMA are discussed in detail in the present section. Special emphasis is placed on the PLEA routine and the steps for its execution. The first step involves the organization of the recorded data in a **T**echnical **D**ata **M**anagement **S**treaming (TDMS) file format. This binary file format enables a structured and organized management of experimental data (Georgi and Metin 2012). Accordingly, the measured sound pressure data is organized in an array of dimension (N x M x N_φ). N corresponds to the data samples (N=60000 samples), M represents the number of measurement microphones (M=6) and N_φ stands for an specific circumferential measurement position, N_φ=1...360. In this way, the binary file comprises the acquired sound pressure data for one complete rotation of the microphone ring with a resolution of 1°.

The second step related to the data analysis procedure comprises the digital filtering of the previously recorded data. Each sound pressure signal is digitally processed with a Butterworth band-pass filter tuned to the blade-passing frequency and to the first of its harmonic multiples. This procedure enables a convenient spectral analysis of the recorded signal, as only the tonal components of the sound pressure remain after filtering the raw sound pressure signal. According to Gostelow (1977), the filtered spectral components correspond to background random noise. The technical specifications and parameters of the digital filter employed to process the sound pressure data are exposed in Sec. 5.5 of the present document.

Continuing with the analysis procedure, a data synchronization process is performed in third place. Based on this procedure, every recorded sound pressure signal is referenced to a common starting point. The former guarantees that the beginning of the data acquisition is synchronized with a common starting angular position of the rotor blading for every recorded revolution of the shaft. Figure 5.9 schematically exemplifies the data synchronization approach. As such, the synchronization task is accomplished by means of a trigger signal delivered by a magnetic sensor emitting a voltage pulse generated by the passing of one blade (Hall sensor, cf. Figs. 4.11 and 4.12). The result is a "one-pulse-per-revolution" signal of the rotor shaft (red continuous line) simultaneously recorded with the sound pressure data (blue continuous line). Displayed in the left side of Fig. 5.9 are a few representative time signals - each constituting a circumferential position of the microphone instrumentation arrangement. All time signals are shown for a common starting data acquisition time. As noted, none of the signals is time synchronized with the passing of the rotor blade through the common angular reference point (labeled with a red triangle). As a consequence, each data record is phase shifted with reference to the beginning of the data acquisition process.
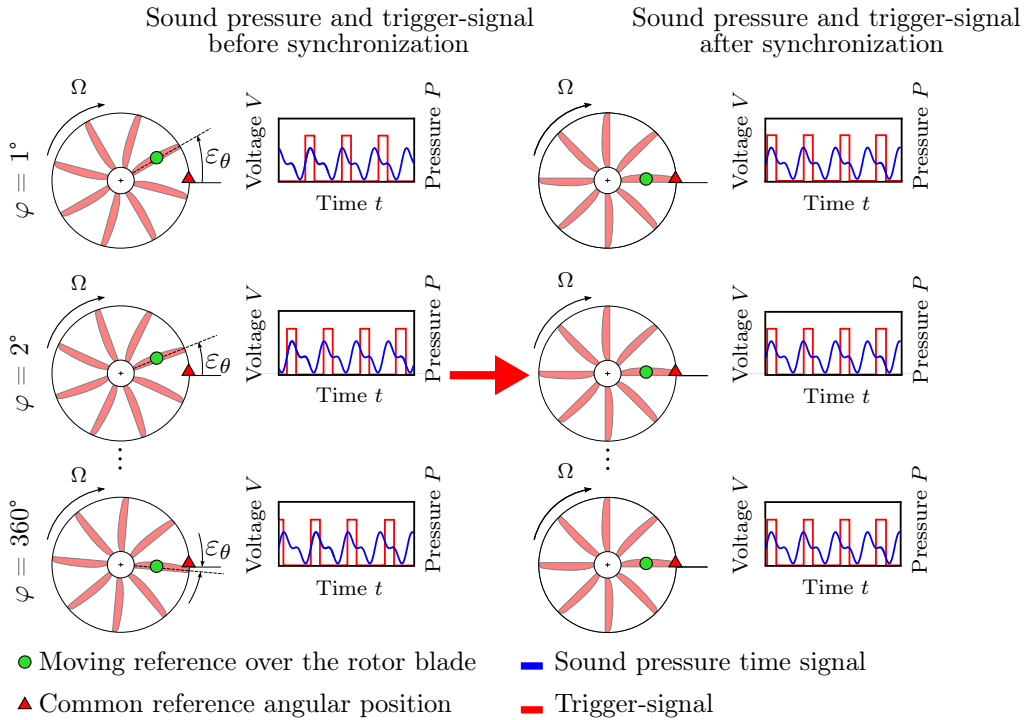
Figure 5.9: Schematic representation of the data synchronization process

An accurate management of the phase shift problem consists of identifying the exact time instant corresponding to the start of the first rotor revolution. This is accomplished by means of the rising edges of the trigger signal. The first voltage pulse and the corresponding rising edge of the trigger signal denote the appointed time instant. Once identified, the recorded sound pressure data is time shifted to match the beginning of the first rotor revolution. As such, the sound pressure samples recorded before the first trigger pulse are discarded. As a result, the trigger as well as the pressure-time signals are synchronized as shown in the right side of Fig. 5.9. The aforementioned procedure is carried out for each sound pressure signal recorded at every circumferential measuring position sampled by the turbine-integrated rotating-ring.

Following the exposed data-synchronization procedure, the recorded sound pressure samples are afterwards divided with the aid of the trigger signal. In this way, data samples corresponding to the length of a rotor revolution are generated. The number of data samples per rotor revolution varies depending on the machine rotational speed. For the present operating point ($\Omega = 3500$ min^{-1} = 58 s^{-1}) about 1034 data samples per revolution are expected. The number of data samples is derived in conjunction with the corresponding sample rate (60000 Hz/58 s^{-1} $\backsim$ 1034 samples). This quantity actually fluctuates around the nominal value of 1034 samples. This fluctuation is due to the variable rotational speed of the rotor and is reflected in the deviation of the rotor angular velocity from its average nominal value. The magnitude of the deviation is exemplified in Fig. 5.10(a). The ensemble size remains stable in the short run, i.e., for just one circumferential measurement position. In contrast, once a whole measurement routine is considered, higher fluctuations are expected despite the stable flow field. In respect thereof ensemble sizes between 1018 and 1038 samples were effectively measured as shown in Fig. 5.10(b) below.
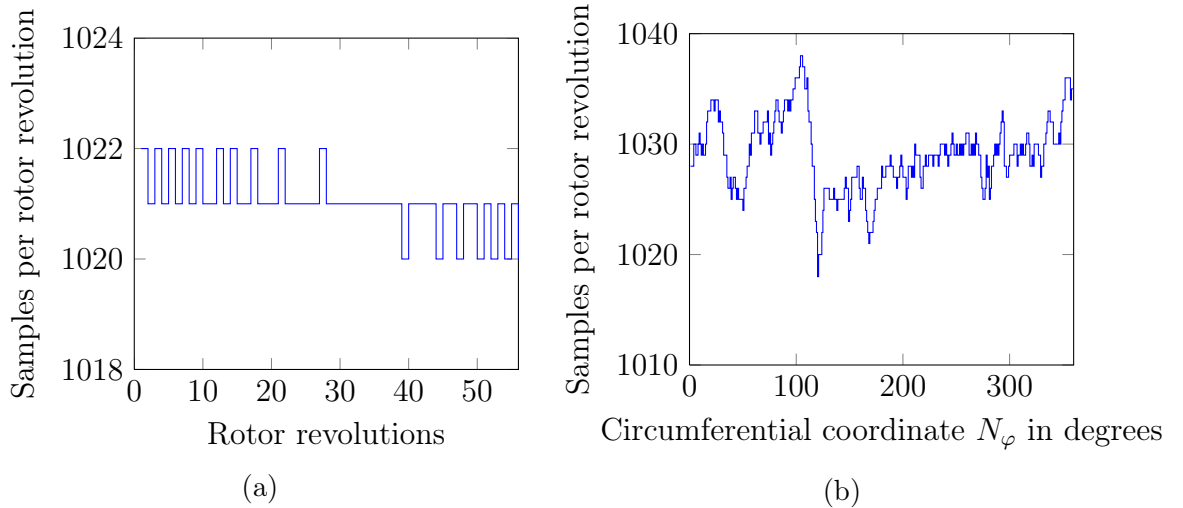
Figure 5.10: Variation of the ensemble size as a function of the recorded rotor revolutions (a), and (b) samples per shaft revolution as a function of the circumferential measurement position
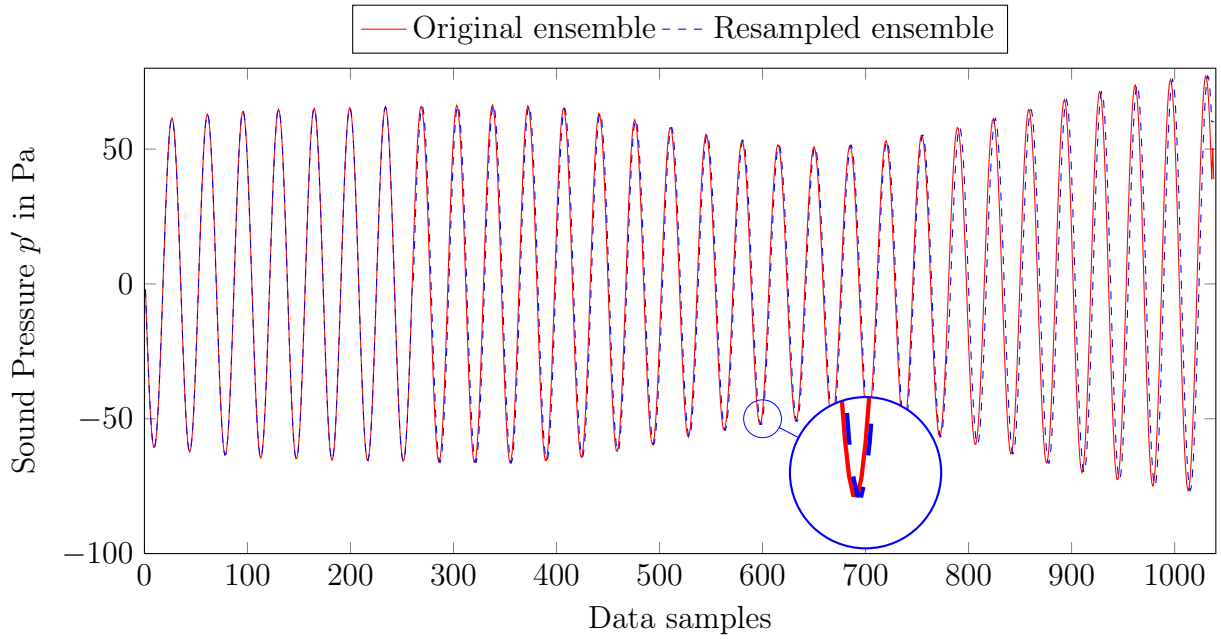
Figure 5.11: Comparison between an original and a re-sampled data ensemble

As mentioned before in Sec. 5.4.1, the implementation of the *phase-locked ensemble average* requires data ensembles of equal length. For this purpose, the variable length of the ensembles is set to a standard sample size by means of a resampling algorithm. The data ensembles are thus processed with MATLAB using the `resample` function of the *Signal Processing Toolbox*. The data ensembles are interpolated by a rational factor, defined as the ratio of the output sample rate to the input sample rate. This is done in order to interface two different data sets with two different sample rates - the original data samples and those with the desired common length. The MATLAB `resample` function uses a FIR (Finite Impulse Response) filter to accomplish this task. The filter is required to compensate the effects of the interpolation and in this way to match as close as possible the original input signal (Kroese and Chan 2014). Figure 5.11 above displays the effect of the resampling routine on the input data. A single recorded data ensemble (before resampling) of one rotor revolution is shown together with the resulting data set after resampling. The magnification reveals a good approximation of the processed data with the original one. The presented data sets correspond to filtered sound pressure data sets.

After all data ensembles have been set to a common sample length, all digital values are summed over all recorded rotor revolutions resulting in an average value for the ensemble. Figure 5.12 schematically illustrates and summarizes the procedure regarding the programmatic implementation of the *phase-locked ensemble average*, PLEA. A recorded data series is shown in top of the diagram, each square representing a sample value x_j^i, where the index j outlines the recorded rotor revolution, and i stands for the sample position within the ensemble. The desired periodic signal $y(t)_{det}$, free of random variations after the execution of the PLEA-routine is mathematically defined as

$$\bar{y}_i = \frac{1}{N_\Omega} \sum_{j=1}^{N_\Omega} x_j^i \qquad (5.4)$$

with N_Ω representing the number of averaged rotor revolutions. The data reduction process carried out on the raw sound pressure signals by means of the *PLEA* is a prerequisite for the subsequent data analysis procedure, namely, the RMA. As such, the data sets generated by the *PLEA* are afterwards used as input data sets in order to conduct the in-duct sound pressure study by means of the RMA.
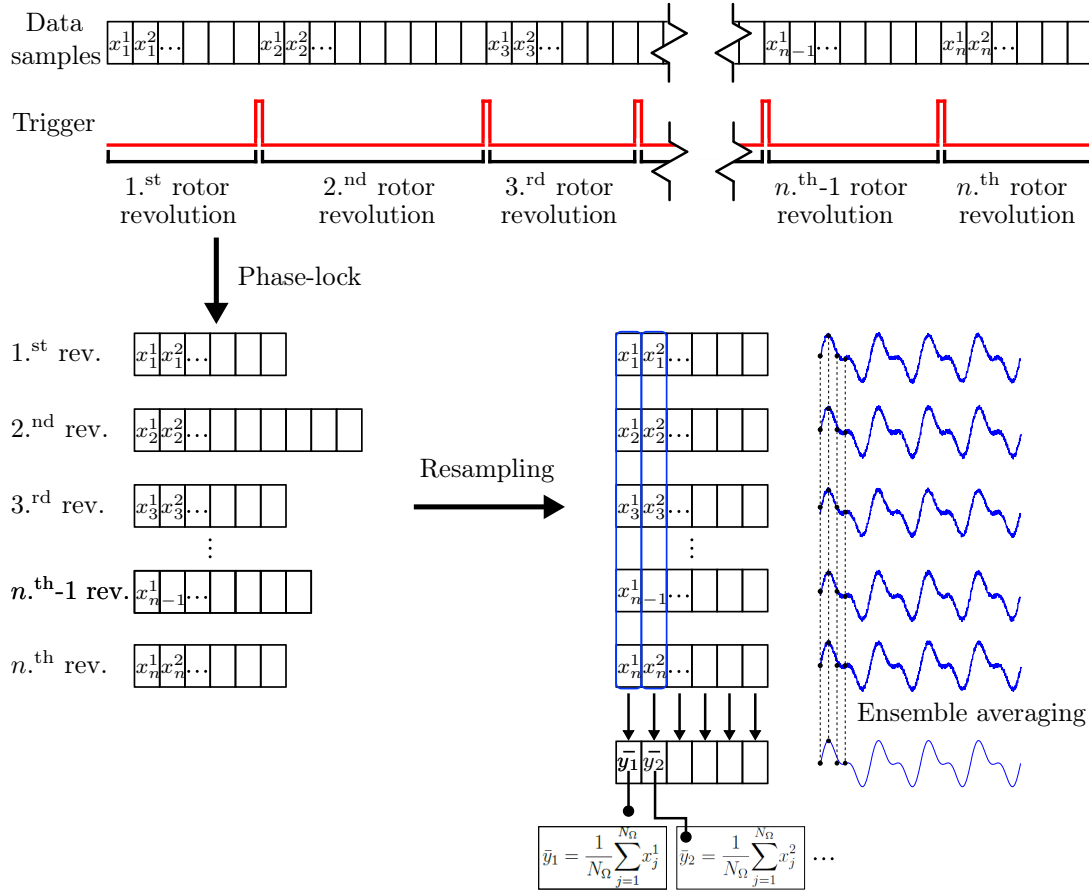
Figure 5.12: Schematic representation of the phase locked-ensemble average, PLEA

5.5 Circumferential acoustical modes

According to the theoretical concepts on the subject of the RMA discussed in Sec. 3.2, the main objective of the evaluation method is to quantify the acoustical structure within rotating machinery. This structure is constituted by circumferential and radial sound pressure distributions - acoustical modes -, which in turn mathematically represent a solution to the acoustic wave equation (cf. Eq. 2.17). Once the above-mentioned sound pressure distributions have been quantified, a clear picture of the in-duct acoustical structure can be established.

Accordingly, the magnitude of the circumferential acoustical modes corresponding to the analyzed operating point of the LPT are shown in this section. Previous to the presentation of these results, the outcome of the filter analysis preceding the data reduction procedure is discussed. In respect thereof, the filter analysis turns out to be of significant importance, since only the tonal noise components associated with the blade passing-frequency and its subsequent multiples are considered within the scope of the current work.

5.5.1 Filter analysis

As aforementioned in Sec. 5.4.2, digital filtering is conveniently done by means of an adjustable Butterworth band-pass filter. In this way, the recorded sound pressure time series are passed through a filter tuned to the desired harmonic blade-passing frequency. This procedure ensures that only the tonal noise components of the recorded sound pressure remain for further signal analysis. An essential requirement of the digital filtering procedure is primarily concerned with keeping the original magnitude as well as accounting for the phase shift of the tonal noise components. It should be assured that the amplitude of those frequency components after filtering the raw signal is exactly the same as the one shown by the signal frequency spectrum before filtering.

The way to guarantee a constant amplitude response is by means of a filter analysis. Consequently, each microphone signal is separately evaluated. As already stated, each microphone records 360 signals, each resulting from a measuring point located at the turbine in-duct circumference. A **F**ast **F**ourier **T**ransformation (FFT) is carried out for all measurement positions. Subsequently, all signals are analyzed with a Butterworth band-pass filter. The analysis consists in varying the filter order, n_F, and its frequency specifications, including the lower and the upper limit frequencies, f_l and f_u, respectively. Once the time varying sound pressure signals have been filtered, a FFT is carried out again over these signals. The dominant frequencies are identified and organized in an array. As a result, a single dominant frequency is identified for each circumferential measurement position and for each measurement microphone. The identified dominant frequency should match the blade-passing frequency or one of its harmonic multiples. Complementary to each dominant frequency, the corresponding amplitude is also identified. The dominant amplitudes correspond also to the blade-passing frequency or one of its multiples.

The results of the filter analysis are displayed in Fig. 5.13, in which the dominant nominal frequencies ($f_{BPF} = 1750$ Hz and $f_{2BPF} = 3500$ Hz) are organized in a diagram as a function of the circumferential measurement position. Both dominant frequencies resulting from the original and from the filtered sound pressure signals are presented and subsequently compared. The comparison is carried out by simply determining the difference between the dominant frequencies before and after filtering. A similar diagram is also shown in Fig. 5.14, which in contrast exhibits the sound pressure amplitude corresponding to the dominant frequency before and after filtering takes place. The displayed values are also function of the microphone circumferential measurement position.
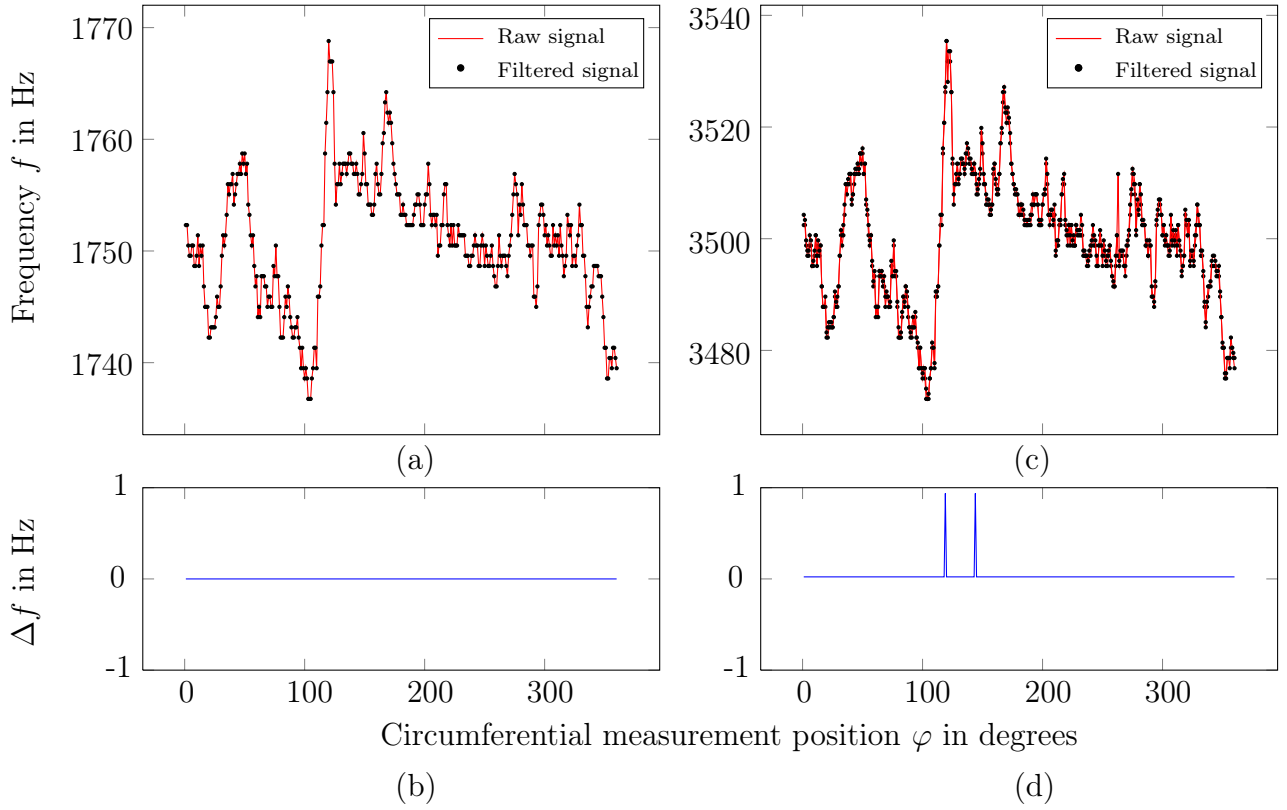
Figure 5.13: Dominant frequencies as a function of the circumferential measuring position before and after signal filtering (a), and (b) comparison of both signals. Results correspond to $f_{\text{BPF}} = 1750$ Hz and one measurement microphone. Dominant frequencies as a function of the circumferential measuring position before and after signal filtering (c), and (d) comparison of both signals. Results correspond to $f_{\text{2BPF}} = 3500$ Hz and one measurement microphone

The results shown correspond to the best possible combination of parameters (filter order and upper and lower limiting frequencies). The best combination is a result of an iterative process in which all three parameters were varied until establishing the lowest minimal frequency and sound pressure amplitude difference between the original and the filtered signals, Δf and $\Delta p'$, respectively. As noted, no relevant frequency shift is expected after filtering both tonal noise components, Figs. 5.13(b) and 5.13(d). Minor frequency variations are identified for two circumferential measurement positions associated with the f_{2BPF}, fluctuations which are below 1 Hz. Regarding the amplitude response, the sound pressure magnitude corresponding to the analyzed tonal noise components is minimally affected by the filtering process. Consequently, only minor variations in the order of 0.4% (for f_{BPF}, cf. Fig. 5.14(b)) and 1.1% (for f_{2BPF}, cf. Fig. 5.14(d)) were established in the amplitude response of the tonal noise components of the sound pressure signals. The percentage variations result from the ratio of the highest sound pressure difference Δp to the highest absolute sound pressure p found over all circumferential measurement positions φ.
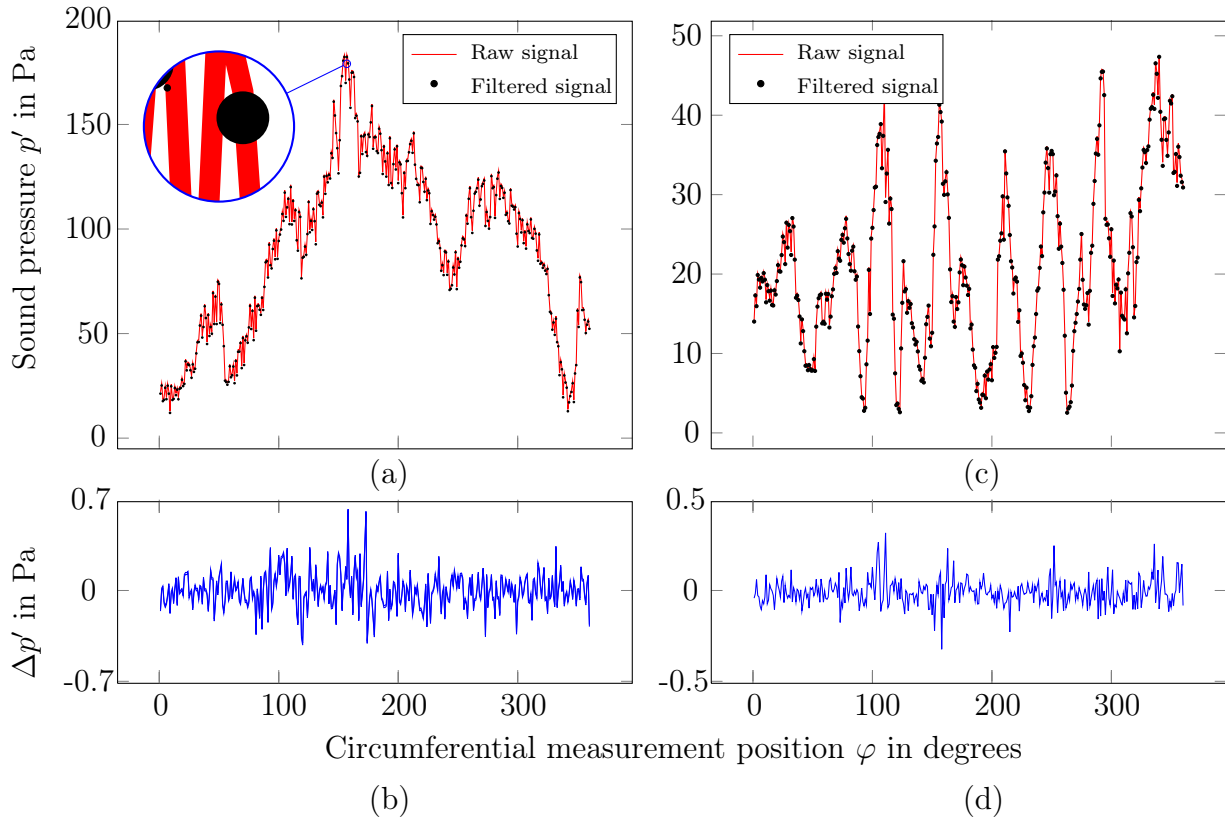
Figure 5.14: Dominant sound pressure amplitudes as a function of the circumferential measuring position before and after signal filtering (a), and (b) comparison of both signals. Results correspond to $f_{\text{BPF}} = 1750$ Hz and one measurement microphone. Dominant sound pressure amplitudes as a function of the circumferential measuring position before and after signal filtering (c), and (d) comparison of both signals - non filtered and filtered. Results correspond to $f_{\text{2BPF}} = 3500$ Hz and one measurement microphone

The sound pressure variations $\Delta p'$ shown by Figs. 5.14(b) and 5.14(d) are a consequence of the filter magnitude response. In this respect, the magnitude and phase response of the band-pass filter is shown in Fig. 5.15. The diagram corresponds specifically to the filter centered about the blade-passing frequency $f_{\text{BPF}} = 1750$ Hz. Associated with the frequency response, an ideal constant gain (0 dB) takes place in a narrow frequency range. Within the frequency range $1750 \leq f \leq 1765$ Hz, the magnitude response is ideal, since the original signal is neither amplified nor damped and all frequency components lying inside this interval are uniformly handled by the designed filter. Frequency components outside this interval are slightly damped and yield marginal variations in the sound pressure magnitude associated with the filtered tonal noise components. This section is concluded by presenting in Tab. 5.6 a summary of the filter parameters used for the further signal analysis, both for f_{BPF} and f_{2BPF}. As a closing remark, the undertaken filter analysis proved to be useful to ensure the original magnitude of the examined tonal noise components, which as aforementioned, turns out to be of vital importance for further signal analysis and for the determination of the circumferential mode amplitudes.
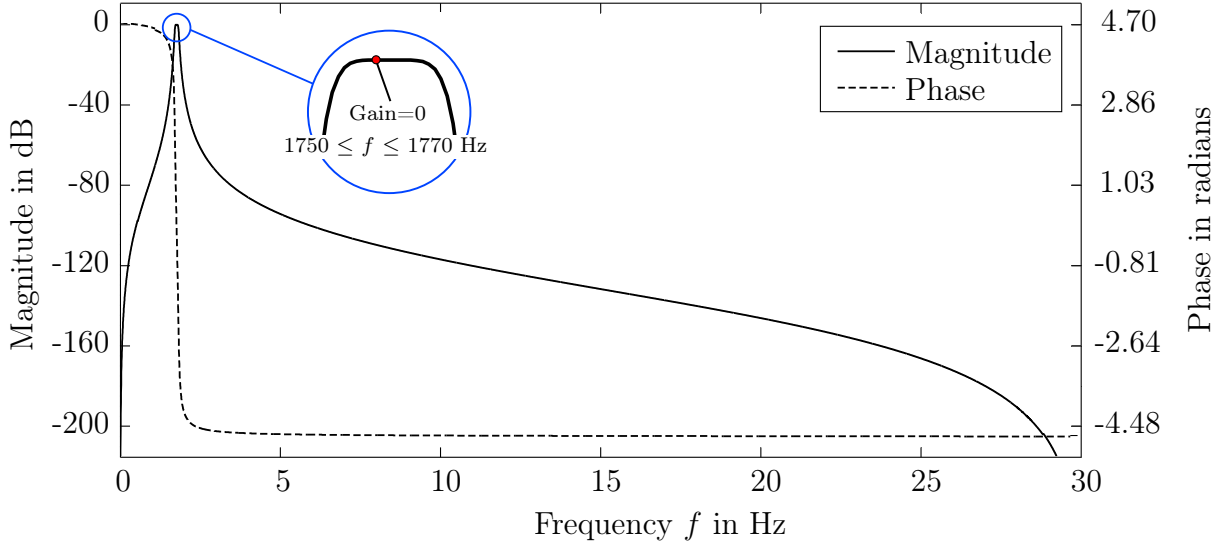
Figure 5.15: Magnitude and phase response of the designed Butterworth band-pass filter

Table 5.6: Butterworth band-pass filter parameters

Parameter	f_{BPF}	f_{2BPF}
Filter order, n_F	6	8
Lower limit frequency f_l in Hz	1700	3450
Upper limit frequency f_u in Hz	1820	3550

5.5.2 Results of the phase-locked ensemble average, PLEA

Having determined the optimal parameters for the digital filtering of the sound pressure signals, the data processing analysis is followed by the data synchronization and the phase-locked ensemble average procedures as previously stated in Sec. 5.4.2. In this respect, Fig. 5.16(a) shows a signal recorded by one microphone at the angular position labelled by **D** in Fig. 4.12(a). This circumferential measurement position represents the starting point for every data recording procedure carried out within the scope of the present work. It is located 45° in counterclockwise direction when referenced to the turbine cross-section center line. The signal amplitude is normalized by the root mean square (RMS) of the recorded time signal. The time signal is composed of a series of periodic waves representing the tonal noise components generated within the turbine in-duct and broadband noise associated with all pressure fluctuations past the blade surfaces. Figure 5.16(b) displays the result of digital filtering over the raw signal about the f_{BPF}. Several peak amplitudes have been suppressed, however, a clear signal periodicity cannot be explicitly recognized. This effect is a consequence of the filter frequency response. The frequency components within a range of $\pm$ 20 Hz about the blade-passing frequency f_{BPF} are not suppressed (cf. Fig. 5.15), giving rise to a complex time signal with more than a single tonal component.
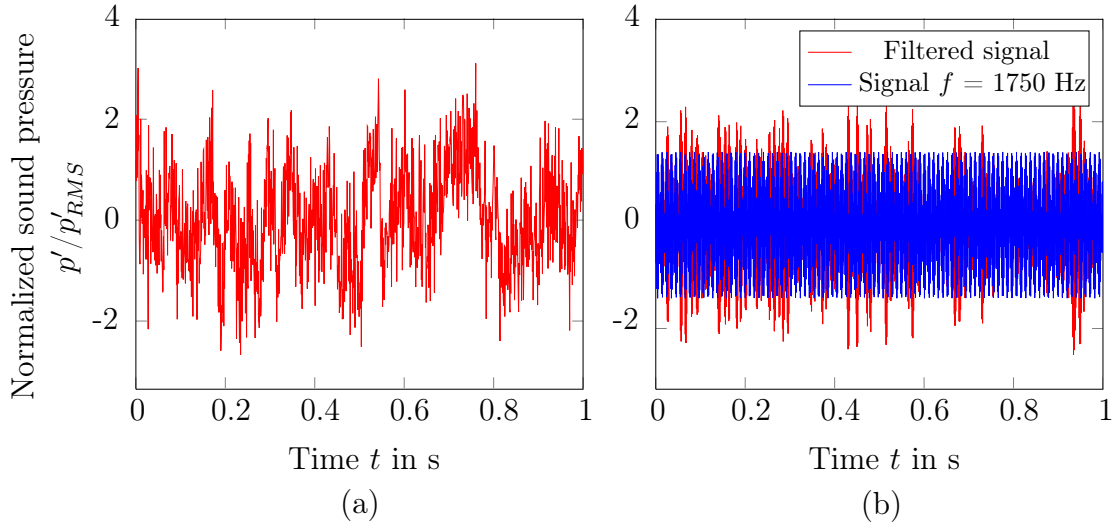
Figure 5.16: Recorded time variable sound pressure signals, examined before filtering (a), and after filtering (b). Results correspond to the data recorded by one microphone at the circumferential measurement position $\varphi = 1°$. Sound pressure data is normalized to RMS value

The tonal noise component corresponding to the f_{BPF} have been superposed to the diagram (cf. 5.16(b)) to emphasize the original periodic nature of the filtered signal. A clearer picture is given though by the frequency spectrum of both time signals previously presented in Fig. 5.16. Accordingly, a FFT with an associated Hanning window is carried out over both signals. The result of the performed frequency analysis is shown in Figs. 5.17(a) and (b).
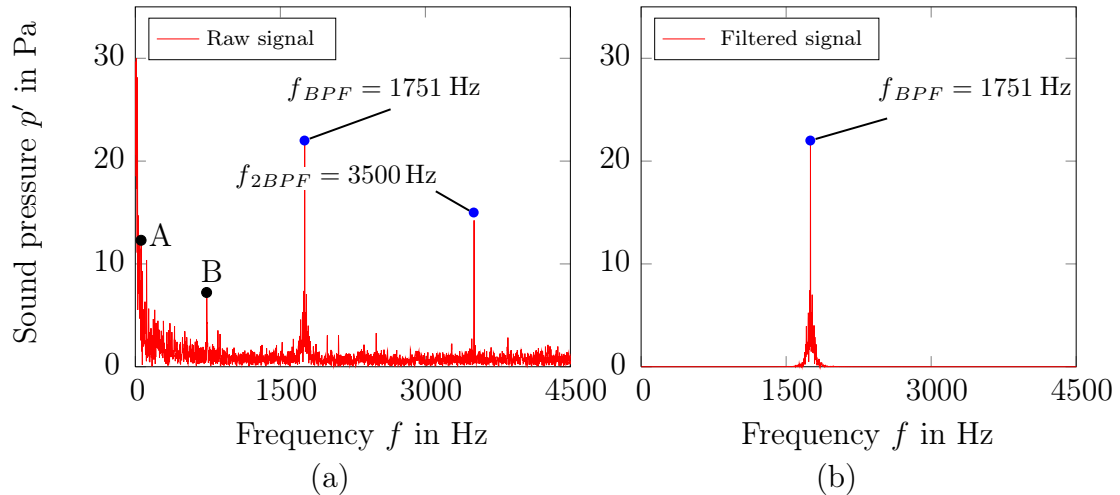
Figure 5.17: Frequency spectrum of the recorded sound pressure signal, (a) before filtering, after filtering (b). Results correspond to the data recorded by one microphone at the circumferential measurement position $\varphi = 1°$

Dominant peaks corresponding to the tonal noise components acting at the f_{BPF} and its associated harmonics are identified. Complementary to this, the frequency spectrum of the filtered signal displays a single dominant component, demonstrating the effective action of the filter by suppressing all other harmonic multiples of the f_{BPF}. A few noticeable peaks between 60 Hz (denoted by $\boldsymbol{A}$) and 740 Hz (denoted by $\boldsymbol{B}$) are also present in the frequency spectrum of the non-filtered signal, Fig. 5.17(a). A sharper impression of the mentioned peaks is shown in Fig. 5.18 below, which displays the frequency spectrum of the sound pressure signal recorded by one microphone within a wider frequency range extending up to 10 kHz.
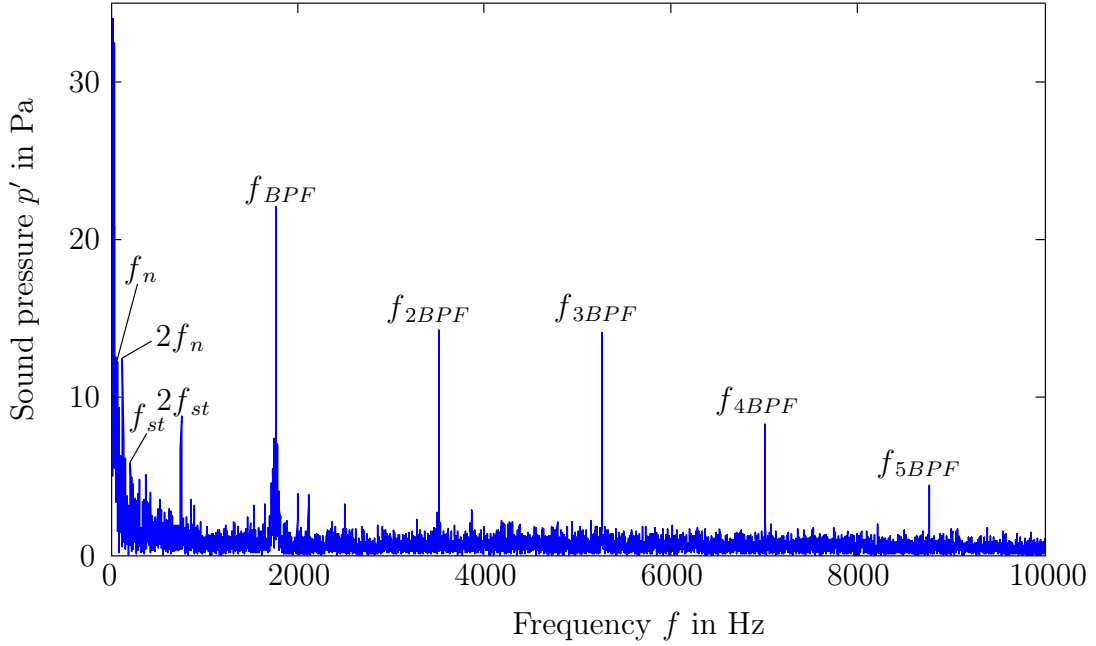
Figure 5.18: Frequency spectrum of the sound pressure time series recorded by one microphone at the circumferential measurement position $\varphi = 1°$

As shown in Fig. 5.18, the frequency spectrum is dominated by tonal noise components. As a result, it can be noticed that the amplitude associated with these frequency components decreases once the order of the harmonic multiples $h \cdot f_{\mathrm{BPF}}$ increases. Additional peaks are identified particularly at low frequencies, starting about 60 Hz. This specific frequency is associated with the shaft rotatory frequency, f_n. The first harmonic multiple of the shaft rotatory frequency, f_{2n}, can also be identified around 120 Hz. At a frequency of approximately 370 Hz an additional peak is present. The described frequency component is linked to tonal noise originated as a result of the flow interaction with the turbine inlet guide vanes, IGV, which amounts to a total number of six vanes, V (cf. Tab. 5.3). The frequency is denoted by f_{st} in Fig. 5.18. The value of this tonal noise component is determined based on the mathematical expression for the f_{BPF}, with the number of turbine blades B replaced by the number of inlet guide vanes V and subsequently multiplied by the rotor angular velocity Ω:

$$f_{st} = hV\Omega \tag{5.5}$$

The magnitude for f_{st} predicted by Eq. 5.5 differs indeed by 20 Hz from the value found in the frequency spectrum. According to Eq. 5.5, f_{st} amounts to 350 Hz. This difference originates as a result of the varying rotor angular velocity, which was shown to fluctuate with the time or measurement cycle as previously displayed in Fig. 5.2. A harmonic multiple of this tonal frequency of 740 Hz, denoted by f_{2st}, is also present in the frequency spectrum. The information regarding the turbine in-duct frequency structure is complemented by presenting an overall averaged frequency spectrum composed of all individual spectra, each representing a measurement cycle. Figure 5.19(a) displays the respective result and simultaneously illustrates the strong amplitude variation of single frequency components. Figure 5.19(b) supports the previous observation by illustrating the same frequency spectra in terms of the sound pressure level (SPL) in dB. Variations as low as 80 dB and as high as 140 dB can be identified for the f_{BPF}, this as a result of fast varying flow and turbine-operating related conditions.

(a)

(b)
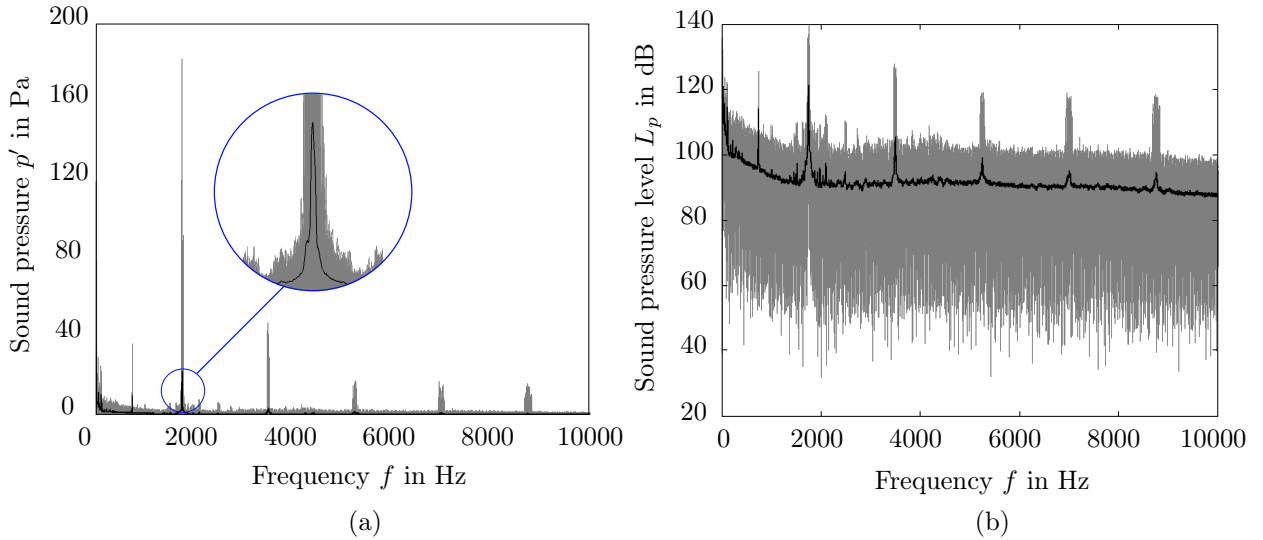
Figure 5.19: Frequency spectrum of the sound pressure time series recorded by the microphone ring (a), and (b), frequency spectrum displayed in terms of the sound pressure level L_p. Black bold line corresponds to the averaged frequency spectrum from 360 circumferential measurement positions. Shaded area is associated with the fluctuating individual measuring cycles

Having identified the expected tonal noise components by means of the previously presented frequency spectra, the PLEA algorithm is implemented. As stated in Sec. 5.4.2, all time signals recorded at selected circumferential measurement positions around the turbine channel are filtered about f_{BPF} and its first harmonic multiple and subsequently rotor-synchronized before being averaged for further analysis. The results of the application of the PLEA are exemplary shown in Fig. 5.20. Shown is the average of 56 time series, each one rotor revolution long for one microphone and one angular position, in this case, for $\varphi = 1°$. The sound pressure data was filtered about $f_{\mathrm{BPF}} = 1750$ Hz.
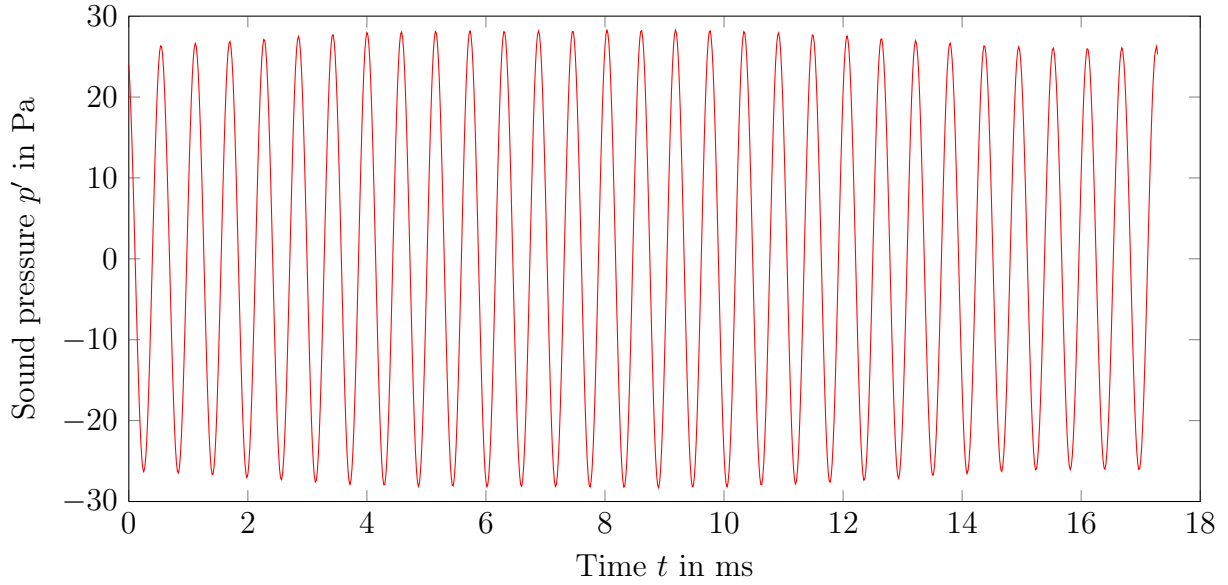
Figure 5.20: Sound pressure time series after filtering (about $f_{\mathrm{BPF}} = 1750$ Hz) and after implementation of the phase-locked ensemble average algorithm. 56 successive samples, each one cycle or rotor revolution long were averaged with each other. Results correspond to the data recorded by one microphone at the circumferential measurement position $\varphi = 1°$
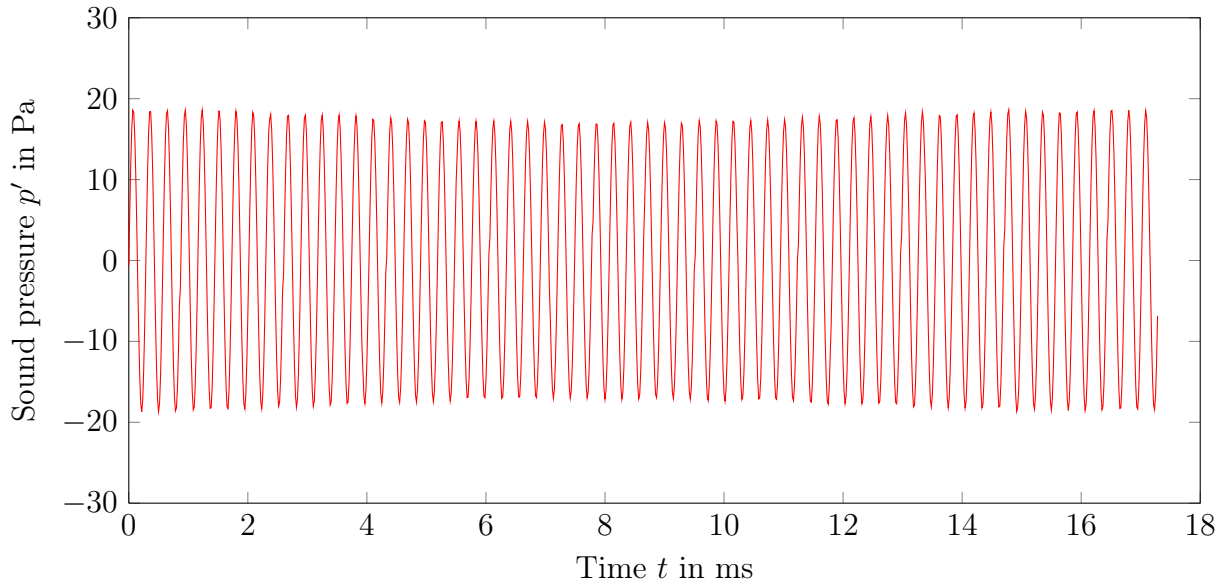
Figure 5.21: Sound pressure time series after filtering (about $f_{\mathrm{2BPF}} = 3500$ Hz) and after implementation of the phase-locked ensemble average algorithm. 56 successive samples, each one cycle or rotor revolution long were averaged with each other. Results correspond to the data recorded by one microphone at the circumferential measurement position $\varphi = 1°$

The application of the PLEA algorithm to the original recorded sound pressure data effectively isolated the tonal noise components from the broadband turbine noise, resulting in a clearly recognizable periodical signal with frequency f_{BPF}. A similar result for the same data set is shown in Fig. 5.21, however, the signal is filtered about the first harmonic multiple f_{2BPF}. The amplitude of both averaged signals is consistent with the amplitudes of the original signal previously displayed in the frequency spectrum (cf. Fig. 5.18). To facilitate the comparison of the signal amplitudes, the frequency spectrum of both averaged time signals is shown in Fig. 5.22. The fact that both signal amplitudes, before and after synchronizing and averaging are consistent in magnitude is relevant, as it should be ensured that the amplitude of the tonal noise frequency components remain the same after the PLEA for the succeeding determination of the circumferential mode amplitudes. In order to complement the previously presented information, Fig. 5.23 presents the signal averaging process for the f_{BPF} tonal noise component carried out exemplary with only four successive rotor revolutions. The amplitude of the averaged signal, Fig. 5.23(e), exceeds the amplitude of the averaged signal with 56 rotor revolutions also corresponding to f_{BPF} (cf. Fig. 5.20). This observation implies that the number of analyzed rotor revolutions affects the outcome of the acoustical mode analysis, as the RMA requires as input the averaged signals. The sensitivity of the RMA to the number of averaged rotor revolutions is therefore discussed in more extent in the chapter to follow, being this a central part of the present work.
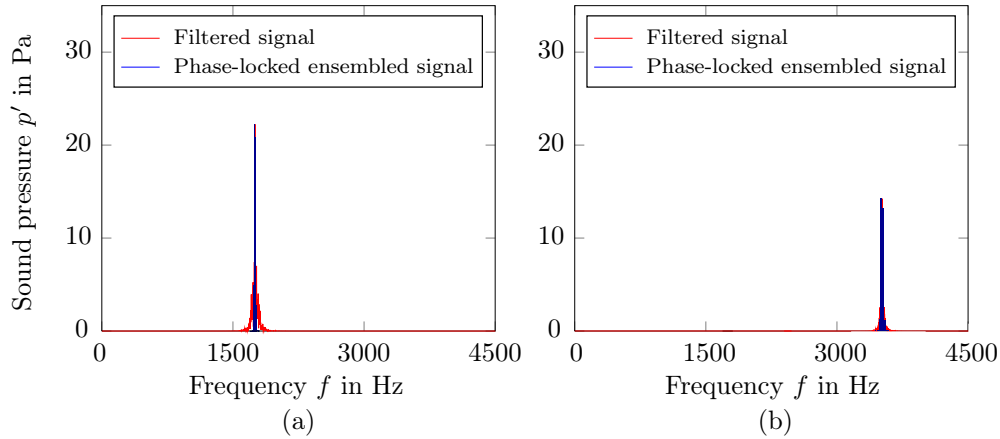
Figure 5.22: Comparison between the frequency spectra of the filtered signal derived from the original recorded data and that after implementation of the PLEA. Signal filtered about (a) $f_{\mathrm{BPF}} = 1750$ Hz and, (b) $f_{\mathrm{2BPF}} = 3500$ Hz

5.5.3 Circumferential mode amplitudes

The result of the implementation of the PLEA algorithm is a synchronized and time averaged sound pressure signal for each circumferential position sampled by the microphone ring (cf. Fig. 5.20). Once this procedure has been concluded, the further determination of the circumferential modes amplitudes can take place. As a consequence, a circumferential sound pressure signal is reconstructed for an specific time instant t_i. The new signal is thus constituted by the corresponding amplitude of each one of the 360 previously acquired time sound pressure signals, for the previously mentioned time instant.
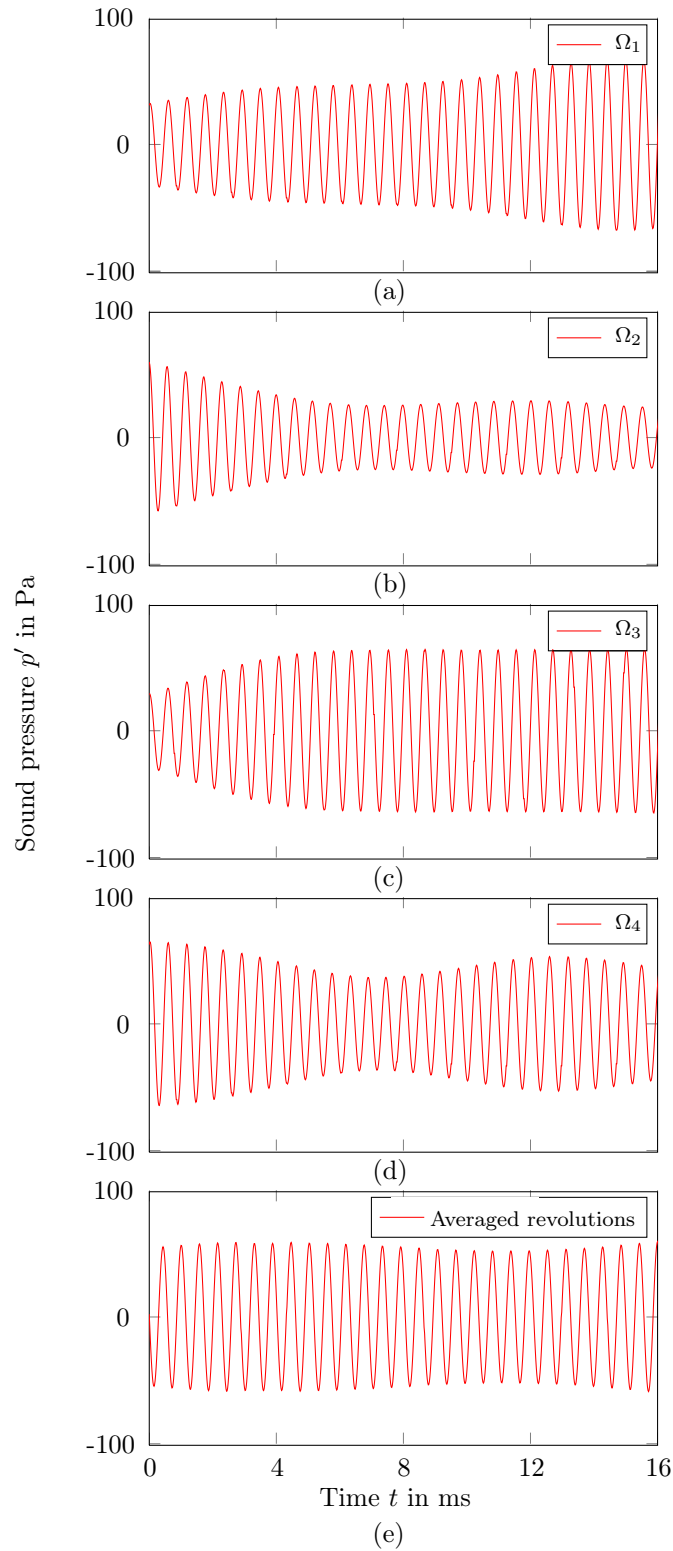
Figure 5.23: Results derived from the application of the PLEA routine (e) to four successive waveforms, each corresponding to a rotor revolution, (a) first, (b) second, (c) third, and (d) fourth rotor revolution. Results correspond to the data recorded by one microphone at the circumferential measurement position $\varphi = 1°$ and filtered about $f_{\mathrm{BPF}} = 1750$ Hz

An instantaneous picture of such circumferential pressure pattern $p'(\varphi, t_i)$ for the blade-passing frequency $f_{\mathrm{BPF}} = 1750$ Hz is shown in Fig. 5.24(a). Each point represents the sound pressure associated with an specific circumferential measurement position. The random-like pattern of the reconstructed signal is expected, since higher-order modes other than the propagating circumferential mode $mn_{[1,0]}$ and its respective amplitude $A_{m=1}$ at the f_{BPF} have been generated (cf. Figs. 5.6 and 5.7). The information pertaining Fig. 5.24(a) is complemented in Fig. 5.24(b) by the superposition of several instantaneous circumferential pressure patterns. The signals are shown solely for the interval $\varphi = 0...30°$, this for visualization purposes. The additional circumferential pressure signals correspond to subsequent time instants. A total of 25 succeeding time points t_i covering a time interval of approximately 0.4 ms are depicted. The signal previously presented in 5.24(a) is depicted in Fig. 5.24(b) as well in blue.
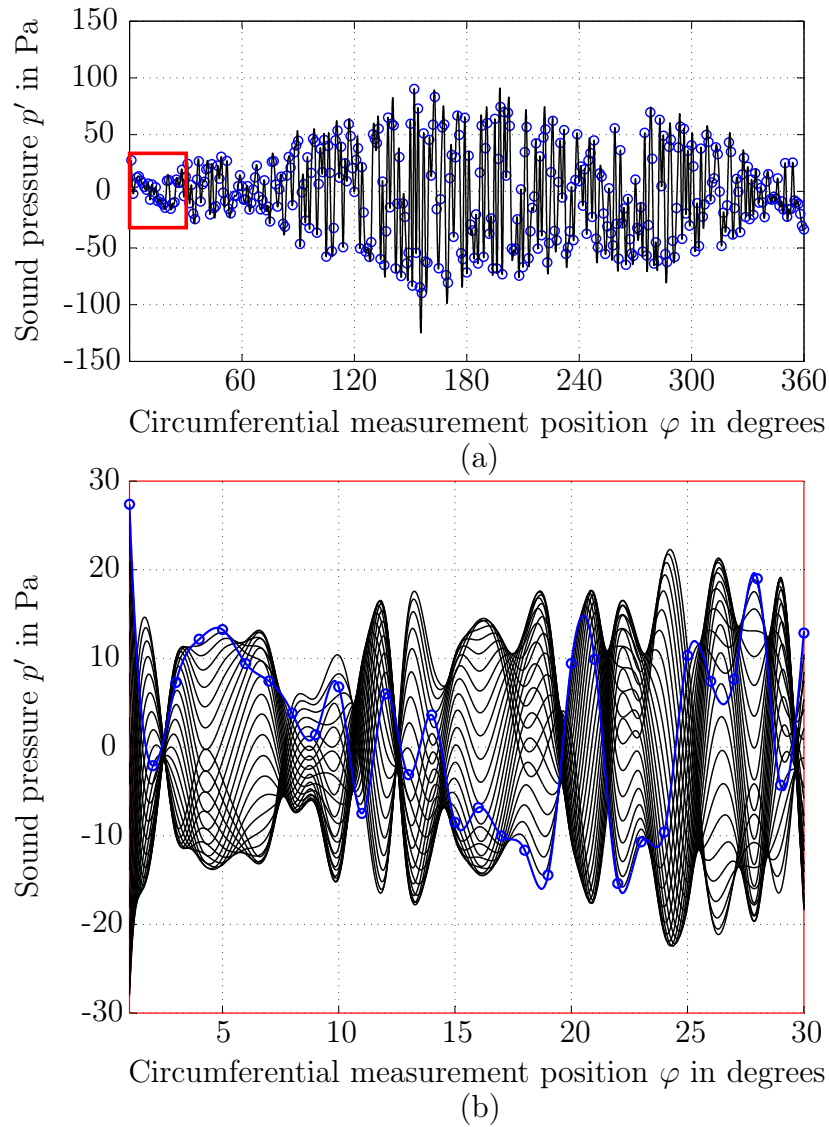
Figure 5.24: Reconstructed circumferential sound pressure signal for (a) one specific time instant, and (b) for several time instants

Noticeable is the variable nature of the amplitude associated with the circumferential pressure distribution $p'(\varphi, t_i)$ for each displayed time instant t_i. In respect thereof, it is expected that the circumferential mode amplitudes A_m vary as well according to the analyzed time instant. In other words, no constant A_m is anticipated for the whole recorded sound pressure data. This fact is enhanced by Fig. 5.25, which replicates the information previously displayed in Fig. 5.24(b) in form of a contour plot. The reconstructed circumferential sound pressure signals are shown as a function of the azimuthal position φ and for an extended time step range, $t_i = 1...200$, from a total of 1038 time steps (representing the duration of one rotor revolution, approximately 17 ms).

The periodicity of single time signals for specific values of φ can be recognized in the contour plot. The magnitude of p' varies periodically with a frequency corresponding to f_{BPF}. The variation takes place at different levels. The region corresponding to $\varphi = 0...60°$ features variations in p' below 60 Pa, whereas the domain $\varphi = 120...240°$ reveals variations above 160 Pa. The latter circumferential region evidences also the highest magnitudes corresponding to p'. Both observations stay in accordance to the results anticipated. Being the azimuthal mode order $m = 1$ the only expected propagating mode, the resulting circumferential pressure distribution should indicate a single maxima as well a single minima region. This feature is certainly not perfectly reproduced, i.e., a one cycle sine or cosine signal. This is a result of the complex in-duct sound pressure distribution, which encloses not only the expected propagating modes but also additional decaying modes.

Bearing resemblance to a variable time signal, a space-variable signal can also be analyzed by means of a Fourier Transformation. The sound pressure distribution in azimuthal direction is composed of a series of superposed harmonic signals, each representing a sound pressure pattern varying in the aforementioned direction (cf. Eq. 2.63 and Fig. 2.9). Accordingly, an instant circumferential pressure signal - taken at an specific time - will vary its amplitude along its circumference. The spectral analysis delivers analogous results, but in contrast, the modal content of the signal is extracted after such analysis. This procedure thus enables the identification of the dominant circumferential mode orders m from the previously presented reconstructed azimuthal sound pressure signals. The output of the spatial FFT yields the amplitudes of the circumferential modes A_m and its respective mode order m. This procedure is carried out for all time steps and representative shown in Fig. 5.26(a) for the first 100 time instants.

Depicted are solely the absolute values for A_m resulting from the spatial FFT analysis. The diagram confirms the variable magnitude of A_m and additionally reveals its periodical behavior. The results indicate as well the presence of a dominant mode order $m=1$. Additional modes are identified, however these are not dominant and are considered not to contribute to the propagating field. Additionally, the circumferential modes amplitudes A_m are quantified in Figs. 5.26(b) and (c). Both diagrams display the normalized value of A_m in respect to its maximal absolute value for all time steps. Figure 5.26(b) represents the time step corresponding to the maximal amplitude of A_m. As a result, the normalized value for the mode order $m = 1$ is equal to unity. Figure 5.26(c) on the other side shows the average value of A_m over all time steps.
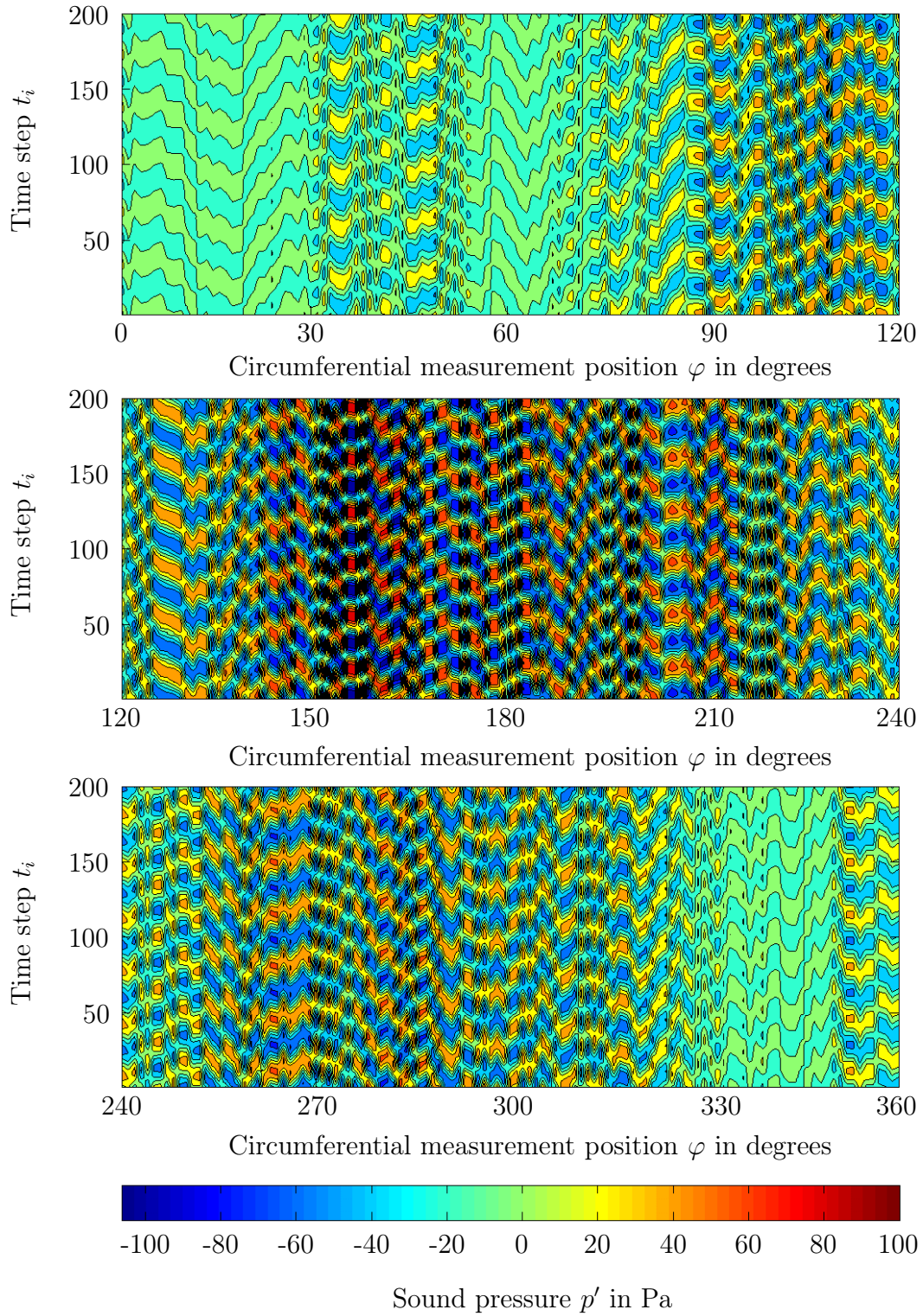
Figure 5.25: Circumferential sound pressure distribution $p'(\varphi, t_i)$ for several time steps t_i. Results correspond to the data recorded by one microphone at the circumferential measurement positions $\varphi = 1...360°$ and filtered about $f_{\mathrm{BPF}} = 1750$ Hz
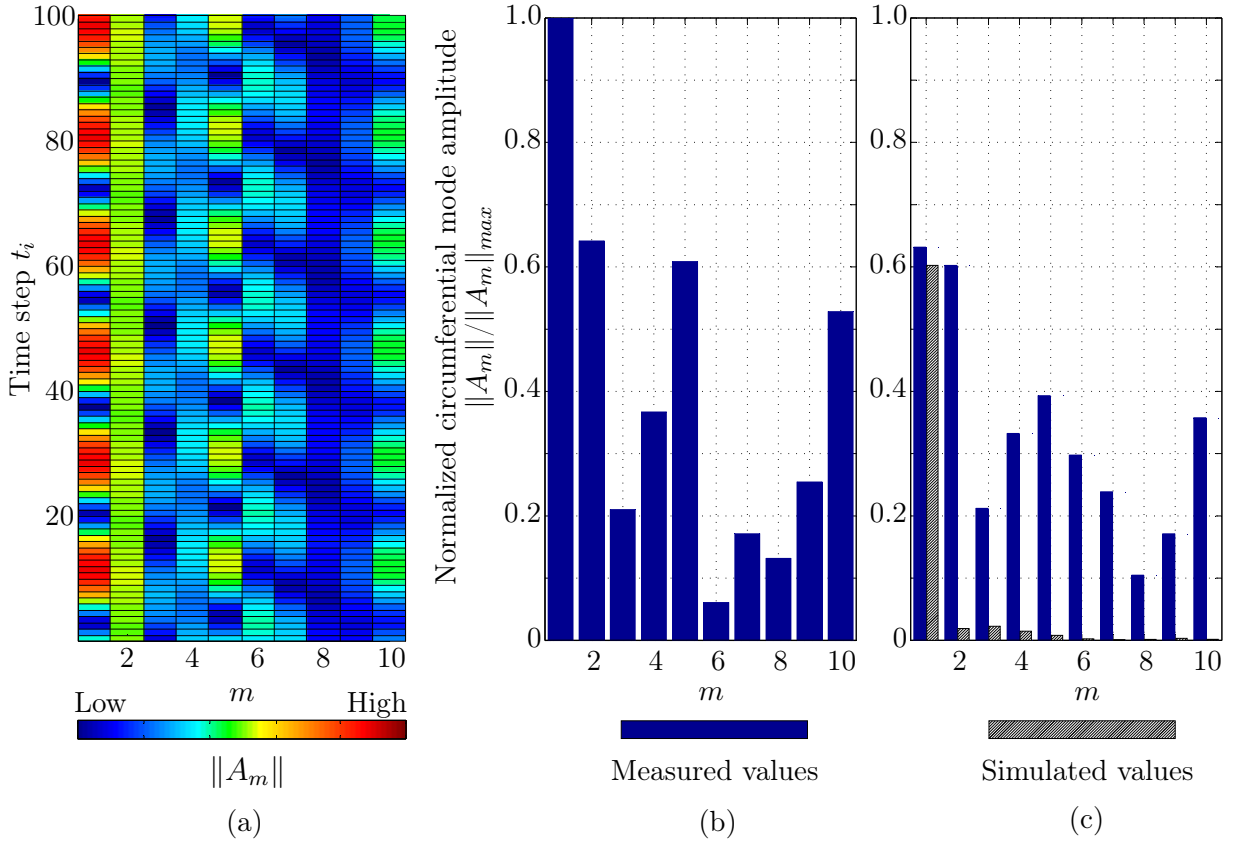
Figure 5.26: Time variation of the circumferential mode amplitudes $\|A_m\|$ for selected time steps and mode orders (a). Normalized circumferential mode amplitudes $\|A_m\|$ with respect to $\|A_m\|_{max}$ for (b) maximal $\|A_m\|$, and (c) average $\|A_m\|$ over all time steps. Results correspond to the data recorded by one microphone about $f_{\mathrm{BPF}} = 1750$ Hz

    The results correspond to the sound field recorded by a single microphone. Similar diagrams for the five remaining sensors are shown in App. A. Figure 5.26(c) shows the results of a numerical simulation in which modal structures were generated based upon real turbine operating data (cf. Tab. 5.2). The numerically based results are used for validation purposes as well as to evaluate the achieved quality of the obtained experimental results. The simulation routine rests on the analytical solution of the acoustic wave equation (cf. Eq. 2.63) and on the description of the specific modes produced as a result of the rotor-stator interaction. The generation of the modal structure is described in detail by Laguna et al. (2013b). In general, the procedure requires the determination of the highest propagating circumferential mode order m as well as the corresponding radial mode orders n and associated flow, operating and acoustic parameters such as the axial wave number (cf. Eq. 2.64). The calculation of numerically generated circumferential mode amplitudes as well as the whole in-duct sound field requires the magnitude of the radial mode amplitudes $A_{[mn]}^{\pm}$ (cf. Eqs. 3.1 and 3.2). As indicated in Chapter 3, these amplitudes are determined through the RMA, but in this case, these are instead generated by means of a mathematical model (Laguna et al. 2013b).
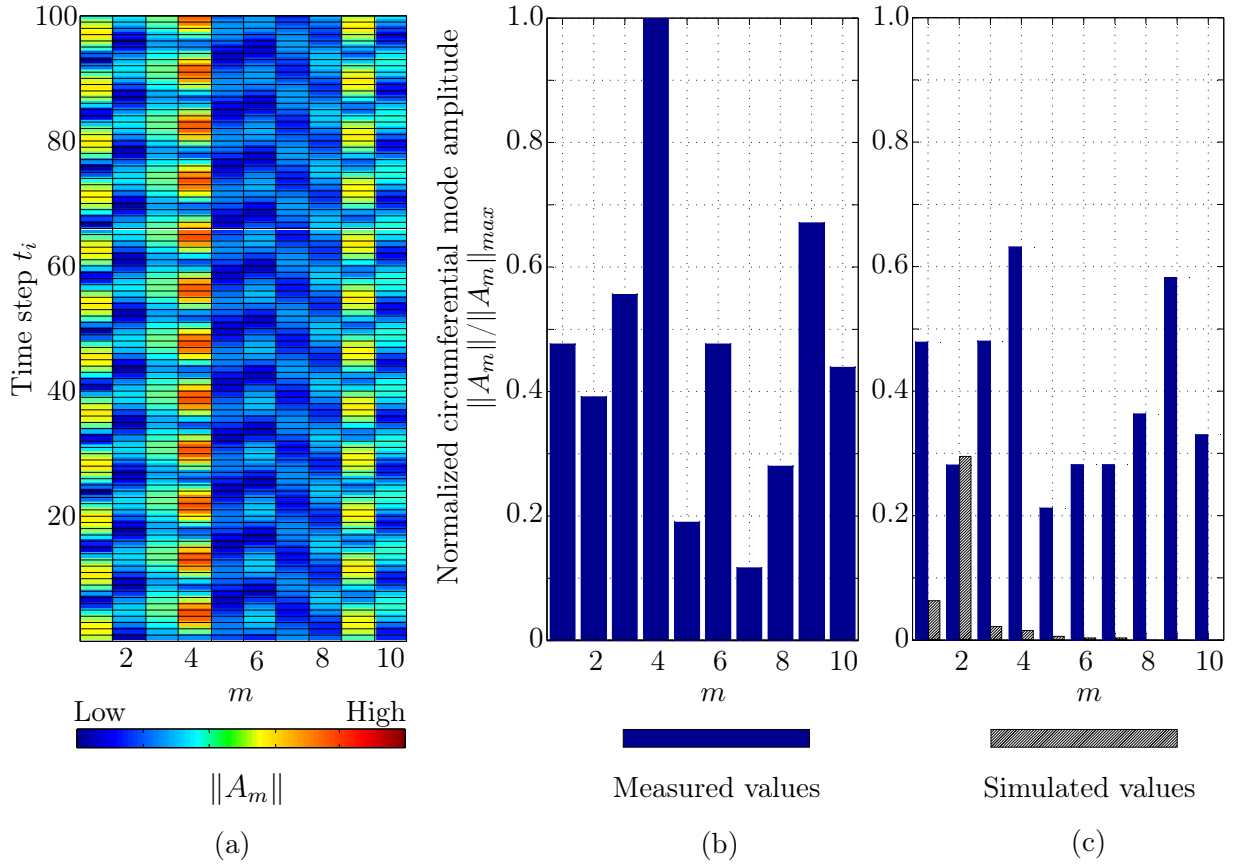
Figure 5.27: Time variation of the circumferential mode amplitudes $\|A_m\|$ for selected time steps and mode orders (a). Normalized circumferential mode amplitudes $\|A_m\|$ with respect to $\|A_m\|_{max}$ for (b) maximal $\|A_m\|$, and (c) average $\|A_m\|$ over all time steps. Results correspond to the data recorded by one microphone about $f_{2\text{BPF}} = 3500$ Hz

The numerically based simulation results are placed beside the experimentally obtained values of $\|A_m\|/\|A_m\|_{max}$ in order to directly compare both outcomes. The dominant circumferential mode amplitude associated with the mode order $m = 1$ is well replicated by the numerical simulation. However, the ascending mode orders are marginally well represented and do not match the results experimentally obtained. This is a result of the numerical model itself. As previously explained and according to Laguna et al. (2013b), the resulting in-duct acoustic sound field is exclusively composed of the theoretically propagating mode combinations (m, n). In this way, for the blade-passing frequency f_{BPF} only the mode $mn_{[1,0]}$ is present. For the second frequency considered within the analysis ($f_{2\text{BPF}}$), the mode combination $mn_{[2,2]}$ is also expected to propagate. The normalized circumferential mode amplitudes associated with mode orders above $m = 1$ are a result of the stochastic modal composition included in the numerical model. The stochastic component of the simulation is conferred by a Gamma probability distribution with an arithmetical mean of 1, added to an exponential decay of modes generated by harmonic orders h of the f_{BPF}.

The results derived from the spatial Fourier Transformation for the first multiple of the blade-passing frequency are also considered. Figure 5.27(a) displays again the absolute value of A_m for several time steps. Noticeable is the dominance of the circumferential mode orders $m = 1$ and $m = 4$. This result deviates from the expected propagating mode, which was calculated to have an order $m = 2$ (cf. Tab. 5.5). A possible reason for this outcome is that low order modes have already been excited by the examined frequency ($f_{2\mathrm{BPF}}$). The same situation is valid for the high-order modes $m = 3$ and $m = 4$. The normalized amplitudes of the maximal and average values of A_m are also quantified in Figs. 5.27(b) and (c), respectively. As already indicated, $m = 4$ turns out to be the dominant mode, reason why its value in Fig. 5.27(b) is unity. The numerical simulation exhibits a good agreement with the expected propagating mode order. On the other hand and based on the arguments exposed before, the dominant modes $m = 1$ and $m = 4$ are not validated to a good extent.

5.6 Radial acoustical modes

As previously discussed in Sec. 3.2, the determination of the acoustical propagating structure inside the turbine requires the magnitude of the radial mode amplitudes $A_{[mn]}^{\pm}$. These amplitudes are mathematically expressed in terms of the circumferential mode amplitudes A_m (cf. Eq. 3.2). With A_m known for the specific operating point $\dot{m} = 5$ kg s^{-1}, $\Omega = 3500$ min^{-1}, the corresponding radial mode amplitudes are calculated. As a reminder, the radial mode amplitudes $A_{[mn]}^{\pm}$ are determined by grouping together the radial and axial terms of the general solution to the homogeneous acoustic wave (cf. Eq. 2.63). This results in a linear system of equations for one specific circumferential mode order m including the previously established circumferential mode amplitudes A_m for different axial positions.

Analog to the circumferential mode amplitudes, the downstream and upstream radial mode amplitudes $A_{[mn]}^{\pm}$ were determined for all six microphones, but shown are only those corresponding to a single one. Figures 5.28(a) and (c) present the aforementioned amplitudes for the tonal frequencies $f_{\mathrm{BPF}} = 1750$ Hz and $f_{2\mathrm{BPF}} = 3500$ Hz, respectively. Both diagrams exhibit a maximal radial mode order $n = 2$ (cf. Sec. 3.2). Again, and for validation purposes, the results derived from the numerical simulation regarding the absolute magnitudes associated only to the upstream radial modes $A_{[mn]}^{+}$ are shown ($\|A_{[1,n]}^{+}\|_{sim}$ and $\|A_{[2,n]}^{+}\|_{sim}$). It follows that the upstream propagating modes are as significant as the downstream propagating ones, this due to the similar amplitude of both variables obtained for almost all mode combinations shown in both figures. In this way, the acoustical modes present in the in-duct field structure do propagate but also reflect in the direction of the turbine blading. This effect is especially pronounced for the mode $mn_{[1,0]}$. The numerical simulation exhibits a reasonable agreement with the results obtained for the propagating modes $mn_{[1,0]}$ and $mn_{[2,2]}$. The values associated with the remaining modes are considered to be negligible, since these are below the inherent noise level of a measurement microphone (below 6.5 dBA). Complementary to the absolute radial mode amplitudes, the in-duct sound field structure is shown in Fig. 5.28(b) and (d). The acoustical structure is exhibited for both considered tonal frequencies.

(a)

(b)

(c)

(d)
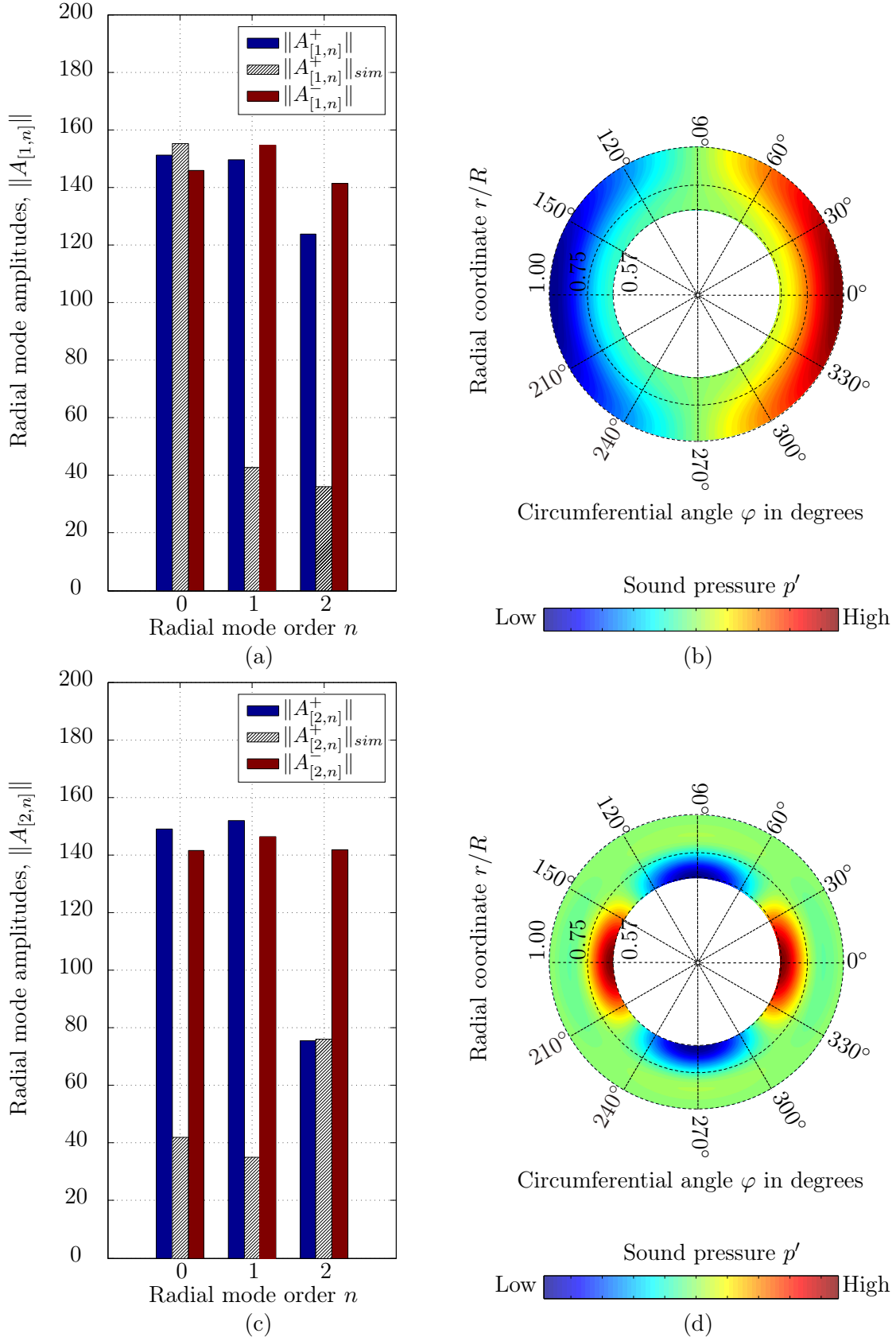
Figure 5.28: Absolute radial mode amplitudes for (a) $m = 1$ and $f_{\mathrm{BPF}} = 1750$ Hz, (c) $m = 2$ and $f_{\mathrm{2BPF}} = 3500$ Hz. In-duct sound pressure for (b) f_{BPF}, and (d) f_{2BPF}

5.7 Concluding remarks

The current chapter presented the results derived from the application of the **R**adial **M**ode **A**nalysis (RMA) to the in-duct sound field recorded by a rotating microphone ring. Accordingly, the turbine operating parameters corresponding to the performed acoustical measurements were first presented. The respective in-duct steady flow field measurements were as well established along with the corresponding instrumentation. Once the flow parameters were quantified, the propagating in-duct acoustical structure was identified. Accordingly, the rotor-stator as well as the rotor-inlet guide vane interactions were evaluated and as a result, a series of acoustical mode combinations were established for specific tonal noise frequencies associated with the low-pressure turbine. Prior to the implementation of the RMA, the data processing associated to it was discussed in detail. In this respect, aspects related to digital filtering, data synchronization, resampling and phase-locked ensemble average were introduced. Following the aforementioned topics, the in-duct acoustical structure in terms of the circumferential and radial mode amplitudes associated with two tonal frequencies was quantified. A series of concluding remarks derived from the aforementioned aspects are mentioned as follows:

1. An accurate evaluation of the turbine in-duct acoustical structure demands a detailed knowledge of the dominating flow field as well as of the machine operating parameters. This was possible due to the implemented instrumentation for the measurement of such variables (inlet and outlet pressure and temperature, and rotor angular velocity), which guaranteed an accurate estimation of the expected in-duct propagating structure.

2. First results derived from the application of the RMA to recorded in-duct acoustic data were obtained. The gained results constitute a confirmation of the validity of the analysis method, in particular when compared with the numerical simulation carried out parallel to the experimental measurements. Associated results of the circumferential and radial mode amplitudes are consistent with the theoretical predictions of the propagating sound field specially for the blade-passing frequency ($f_{\mathrm{BPF}} = 1750$ Hz). Results associated with the first multiple of the blade-passing frequency ($f_{\mathrm{2BPF}} = 3500$ Hz) featured, however, significant differences between the expected and the actually measured mode structure. These deviations are attributed to the excitation of low as well as high order modes by frequencies below f_{2BPF} which are part of the existing sound field for the mentioned frequency.

3. Prior results indicating the effect of the number of analyzed rotor revolutions on the outcome of the acoustical mode analysis were established. This result stresses the necessity of carrying out a systematic sensitivity study of the RMA output variation as a result of variable data acquisition parameters.

Having discussed in detail the procedure associated with the application of the RMA to a set of recorded acoustical data in the present chapter, Chapter 6 concentrates on the sensitivity of the RMA output to data acquisition parameters. The focus is set on the study of the variation of the circumferential mode amplitude to alterations of such parameters.

6 Sensitivity analysis

Having presented the results of the implementation of the RMA on recorded sound pressure data, the current chapter focuses on studying the sensitivity of this method to chosen data acquisition parameters. The considered parameters are: (1) the circumferential spacing of the the measuring positions, and (2) the number of rotor-triggered revolutions. Both parameters are varied while the impact of the performed changes are quantified in terms of the variation on the magnitude of the circumferential mode amplitude A_m. Before these results are presented, previous findings in form of a test case derived from a numerical simulation are shown. The numerical simulation is based on the generation of modal structures under turbine-like operating conditions. This approach enables a direct comparison between the experimental and the numerically obtained results while simultaneously providing a reasonable procedure to validate the results derived from the sensitivity analysis. The sensitivity analysis provides a detailed insight into the measurement error associated with the application of the RMA. This knowledge is used to define the requirements for high fidelity measurements by allowing the selection of optimum ranges for the data acquisition parameters previously listed.

6.1 Test case on the sensitivity of the RMA

The quantification of the influence of data acquisition and turbine-related operating parameters on the acoustic decomposition of sound fields is a important requirement in the development of a high-quality testing environment for aeroacoustic studies in turbomachinery (Laguna et al. 2013b). The purpose of this section is to provide an insight into the influence of data acquisition parameters on the amplitude of the azimuthal modes determined through the RMA. This is accomplished by means of a numerical simulation. This computational routine was already described in Sec. 5.5.3. As previously indicated, the simulation generates a in-duct acoustical field based on real turbine operating parameters. In this way, it is possible to execute virtual measurements, in which the data recording with a microphone array located inside the turbine can be simulated. The resulting acoustical signals are subsequently processed by the RMA routine.

A test case is presented as follows. The operating point corresponds to the nominal operating parameters of the LPT. As already stated in Chapter 4, the chosen configuration of the turbine features a cylindrical section downstream of the stage, followed by an annular diffusor which further downstream discharges the flow vertically downward into a pipe. The operating parameters of the turbine used for the sensitivity analysis carried out for this specific test case are shown in Tab. 6.1.

Table 6.1: Test case nominal operating parameters of the TFD air turbine

Parameter	Value
Inlet Mach number, Ma_x	0.215
Circumferential Mach number, Ma_u	0.4
Inlet total temperature, $T_{\text{tot-in}}$	100°C
Rotor blades, B	30
Stator vanes, V	29
Nominal angular speed, Ω	7500 min^{-1}
Blade-Passing Frequency, f_{BPF}	3750 Hz

The resulting acoustical mode combinations (m, n) based on the nominal operating parameters of the LPT are presented in Tab. 6.2. Noticeable is the inclusion of swirling flow, which results in a different in-duct acoustical structure as that before presented in Fig. 4.4. The numerical calculations are executed for the blade-passing frequency f_{BPF} and its first two harmonic multiples, i.e., 3750, 7500 and 11250 Hz. The listed values represent the frequencies where the discrete tonal noise components are expected to emerge as a result of the in-duct sound propagation.

Table 6.2: Propagating (m, n) modes for selected tonal frequency components

	Cut-on modes
f_{BPF}	(1,3)
f_{2BPF}	(-27,4)/(2,6)/(31,3)
f_{3BPF}	(-55,2)/(-26,9)/(3,10)/(32,7)/(61,1)

The sensitivity analysis is performed only for selected modes at each tonal noise frequency. This is done in this way as a result of the number of available axial measurement positions (N_x) on the microphone ring. A maximum number of radial mode orders can be resolved depending on the number of axial measuring positions (cf. Eq. 3.2). As a consequence, radial mode orders up to $n = 2$ (considering upstream and downstream propagating modes, $n = N_x \backslash 2$) or $n = 5$ (including only downstream modes, $n = N_x - 1$) can be determined. Radial orders exceeding the specified limits lead to a undetermined system of equations (cf. Eq. 3.11).

Accordingly, the analyzed propagating mode combinations for the f_{BPF} and the remaining harmonic multiples are the following: for the blade-passing frequency the mode $mn_{[1,3]}$ is analyzed, followed by the mode $mn_{[31,3]}$ for f_{2BPF}. Finally, for the second harmonic of the blade-passing frequency, the acoustical mode $mn_{[-55,2]}$ is examined. The chosen acoustical modes are representative for low as well as for high circumferential and radial-mode orders.

Knowing beforehand the expected acoustical modes, the variation range of the data acquisition parameters for the sensitivity analysis are shown in Tab. 6.3. Additional to the number of triggered revolutions and the spacing of the circumferential measuring positions, a trigger delay and the signal-to-noise ratio (SNR) of the microphones are also included. The latter are only considered within the scope of the numerical simulation and are not taken into account for the experimental results presented in the following section of this chapter. In regard to the remaining simulation parameters, the axial and circumferential Mach number as well as the total inlet temperature are kept constant. Within this operating temperature, the examined mode combinations (m, n) are cut-on. The angular resolution is maintained below 3° to assure that the number of circumferential data acquisition points is at least twice the corresponding mode order m for a proper spatial FFT analysis. The presented range for the SNR ratio is typical for condenser type measurement microphones. The data acquisition parameters are varied in such a way that the RMA results are influenced without modifying the in-duct acoustical structure.

Table 6.3: Ranges of the data acquisition parameters

Parameter	Value
Circumferential spacing, $\Delta\varphi$	1°...3°
Number of triggered revolutions, N	1...150
SNR	5...60 dB
Trigger delay, Δt	0...10

6.1.1 Circumferential spacing - Test case

The influence of the angular resolution on the accuracy of the RMA results was analyzed for a SNR value of 60 dB. The sensor circumferential spacing was varied in steps of 1, 2 and 3°, resulting in 360, 180 and 120 circumferential measuring positions, respectively. The measurement time was restricted to one triggered revolution and the sampling rate was established at 100 kHz. The results for the analyzed mode combinations are presented in Fig. 6.1. The relative error slightly increases with decreasing angular resolution. The low-order azimuthal mode $mn_{[1,3]}$ exhibits relative errors below 1% despite the reduced spatial measurement resolution. As opposed to this, for the high-order azimuthal mode combinations ($mn_{[31,3]}$ and $mn_{[-55,2]}$) variations up to 1% are ascertained for a reduced number of circumferential measuring positions. In this way, high-order modes may be measured without requiring a high circumferential measurement resolution, this as a result of low measurement errors for low angular resolution. The consequence is that the time required to complete a measurement campaign may be reduced by a factor of 3, from the initial 360 to a final quantity of 120 measuring positions.
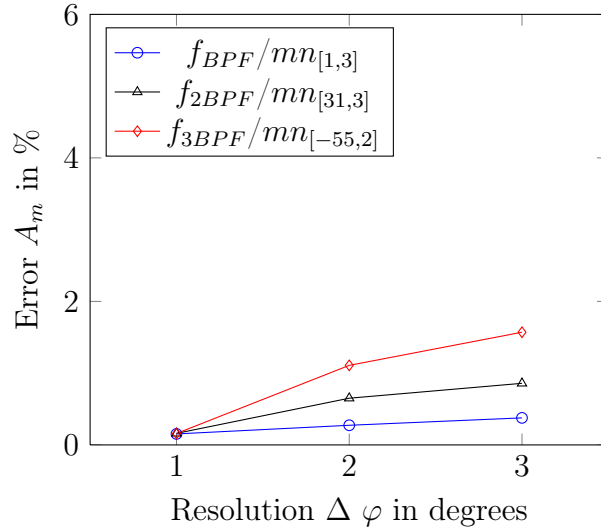
Figure 6.1: Relative error as a function of the angular resolution $\Delta \varphi$ for SNR = 60 dB, based on the results of Laguna et al. (2013b)

As a complementary comment and following Laguna et al. (2013b), the relative error arising as a result of the influence of the circumferential spacing on the RMA is based on the relative difference between the so-called calculated and simulated circumferential mode amplitudes, $(A_m)_s$ and $(A_m)_c$, respectively. Both amplitudes are determined based on the analytical solution of the wave equation in a hard-walled annular duct, Eq. 2.63, and the description of all possible excitable circumferential modes, Eq. 2.67. The relative error calculation is accomplished based on a simulation which generates a modal structure in the duct behind the last stage of the LTP. The modal structure is generated by rearranging the Cut-On frequency expression (cf. Eq. 2.65) for the highest possible eigenvalue $s_{[mn]}$ at the f_{BPF} or any of its harmonic multiples. In this case, with the f_{BPF} being a known quantity, the maximum order of the acoustical modes (m, n) is indirectly limited. By means of a root finding algorithm, the highest propagating mode order m, with radial mode order 0 is determined. This is done by increasing the order m of the radial function $g(r)$ (cf. Eq. 2.45) in each iteration and searching for the first root of its derivative, i.e, the eigenvalue $s_{[m,0]}$.

Subsequently, the Tyler and Sofrin expression (cf. Eq. 2.67) is used to determine the excitable circumferential modes for each harmonic multiple of the f_{BPF}. In this way, all propagating mode combinations (m, n) are established. With this information, the axial wave numbers and further parameters are calculated for all modes present in the simulated acoustical structure. This derives in an almost complete representation of the analytical solution (cf. Eq. 2.63), with the limitation, that the radial-mode amplitudes $A_{[mn]}^{\pm}$ are missing. These amplitudes, which are normally determined by means of the RMA, are instead generated based on a simple mathematical model. This model considers an exponential decay of modes generated by the harmonic multiples h of the f_{BPF} as well as for the radial-mode orders n. With the radial-mode amplitudes calculated by means of the mathematical model, any acoustical signal, which could be measured at any given point inside the duct, can be analytically determined by means of the expression:

$$p(x, r, \varphi, t) = \sum_{m=-\infty}^{\infty} (A_m)_s \, \mathrm{e}^{im\varphi} \mathrm{e}^{i\omega t} \tag{6.1}$$

As previously indicated, this expression allows the generation of sound pressure signals. These signals resemble measurements performed by a microphone array. The generated signals are then analyzed by means of the RMA, resulting thus on the calculated circumferential mode amplitudes. Finally, both amplitudes - simulated and calculated - are directly compared in Eq. 6.2 by the calculation of the relative error. Therefore, the magnitude of this relative error represents the influence that the data acquisition and the LPT operating parameters have on an actual measurement campaign. The procedure to calculate the relative error is not only applicable to the influence of the circumferential spacing, but also to the influence on the RMA of further measurement parameters such as those summarized in Tab. 6.3.

$$Error \ A_m[\%] = \left| \frac{(A_m)_s - (A_m)_c}{(A_m)_s} \right| \tag{6.2}$$

6.1.2 Triggered revolutions - Test case

The variation of the number of rotor-triggered revolutions is possible as a result of the performed synchronized sound pressure measurements, both with the numerical simulation and actual recorded data (cf. Sec. 5.4.1 and 5.4.2). Accordingly, the current section studies the influence of a specific number of rotor revolutions on the outcome of the RMA. A range of measurement periods varying between 1 and 150 revolutions with a SNR = 60 dB were evaluated while maintaining an angular resolution of 1°. The results for the low as well as for the high-order acoustical modes are presented in Fig. 6.2. For all acoustical modes the relative error decreases as more triggered revolutions are evaluated for signal averaging. All modal orders present errors below 1%. For the associated SNR value, an improvement in the measurement error is noticed for data acquisition periods above one rotor revolution. Above 10 rotor revolutions, the error stabilizes and remains practically unaltered for further data acquisition periods. This is due to the waveform averaging and the *phase-locked ensemble average*, in which non-stationary tones and broad-band noise are separated from the tonal components, resulting in a noise reduction of the raw data (cf. Sec. 5.4.1).

6.1.3 Microphone signal-to-noise-ratio - Test case

Additional to the circumferential spacing and the number of triggered revolutions, the influence of the SNR on the accuracy of the RMA results was as well examined. High quality sensors are expected to have a high SNR, therefore, this parameter is varied between 5 and 60 dB. The evaluated values of the SNR started at 5 dB and were followed by the values 8, 10, 12 and 15 dB. Afterwards, 10 dB intervals starting from 20 dB up to 60 dB were analyzed while keeping an angular resolution of 1°. The measurement time was limited to one triggered revolution and a sample rate of 100 kHz.
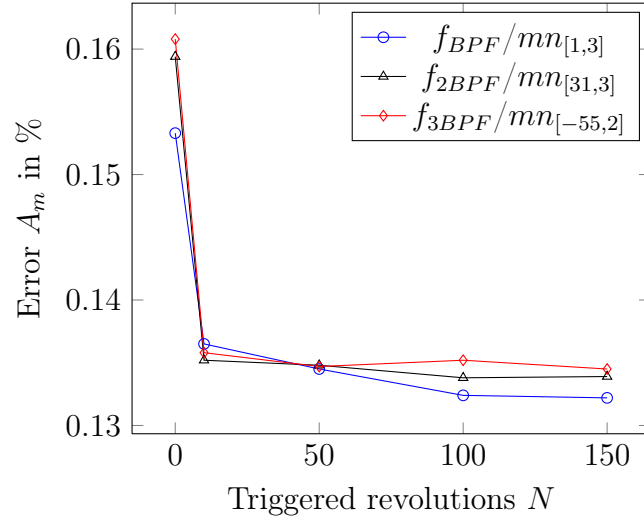
Figure 6.2: Relative error as a function of the number of triggered revolutions, based on the results of Laguna et al. (2013b)
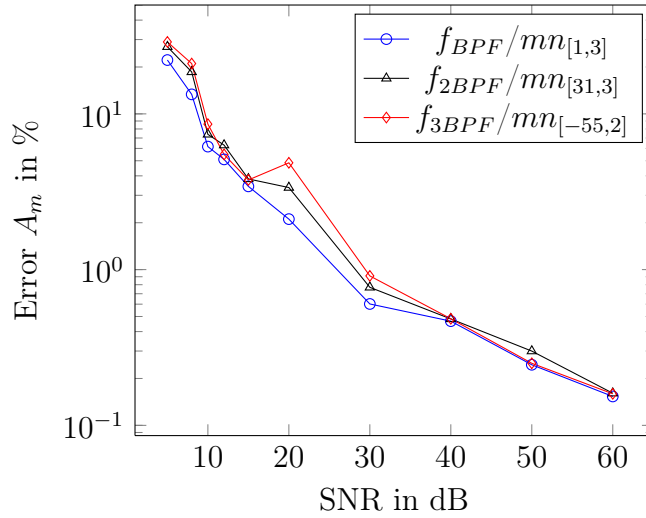
Figure 6.3: Relative error as a function of the SNR, based on the results of Laguna et al. (2013b)

The results for the evaluated acoustical modes are presented in Fig. 6.3. For all analyzed modes the relative error decreases with increasing SNR. Within the studied SNR range, the error reduction is of two orders of magnitude, from 25-28% for SNR = 5 dB to approximately 0.1% for SNR = 60 dB. SNR values below 10 dB exhibit high errors (over 10%) independent of the considered acoustical mode. In contrast to this, the error tends to stabilize about a value of 4% for values of SNR above 15 dB. This observation indicates that acoustic sensors affected by background noise (low SNR sensors) still can obtain trustable measurements in turbomachinery dominated-environments. As a final remark, the error tends to stabilize for SNR greater than 30 dB.

6.1.4 Trigger delay - Test case

As previously exposed in Sec. 5.4.2, acoustical measurements in turbomachinery require data acquisition once per rotor revolution. This is accomplished by triggered with a "one-pulse-per-revolution" signal to avoid a phase mismatch between the in-duct placed microphones and the propagating sound pressure waves. The simulations and hence the results previously presented were based on the assumption that the measurement was triggered without any delay. However, as shown in this section, such inadequate triggering has consequences on the output of the RMA. To quantify its influence, a maximum trigger delay in milliseconds was defined and the relative error in the amplitude of the circumferential modes was afterwards computed. Following trigger delays were evaluated: no delay, 1, and 10 ms time delay. The analysis was performed with 10 triggered revolutions. This value was considered, because additional triggered revolutions do not represent a significant decrease in the relative error (cf. Sec. 6.1.2). Representative results are shown in Fig. 6.4. It is observed that a trigger delay influences the relative error, with values close to 30%. A time delay leads to a signal phase mismatch, which results in wave superposition or cancellation and in loss of acquired information.

Figure 6.4: Relative error as a function of a trigger delay, based on the results of Laguna et al. (2013b)

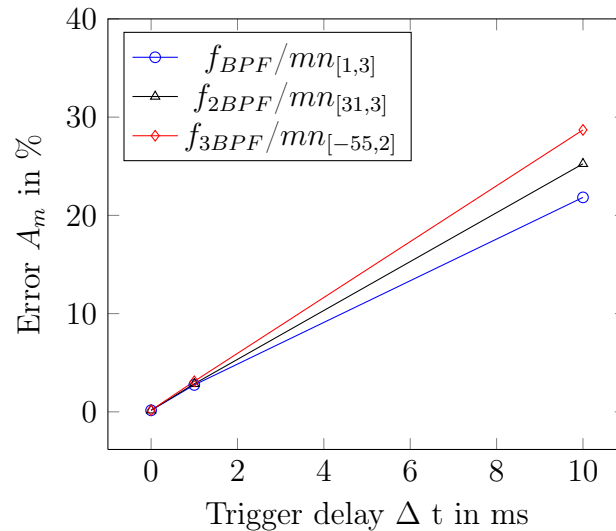The before presented results constitute a confirmation of the optimization potential of the RMA if the measurement parameters are carefully chosen. In respect thereof, the section to follow, examines the effect on the output of the RMA of data acquisition parameters under realistic measurement conditions.

6.2 Sensitivity analysis – Turbine measurements

As already mentioned, the current section focuses on studying the sensitivity of the RMA output to (a) the circumferential spacing of measurement microphones and (b) the number of triggered revolutions. The study is carried out for a single turbine operating point, $\Omega = 3500$ min^{-1} and $\dot{m} = 5$ kg s^{-1}, with the associated flow parameters previously shown in Tab. 5.2. The circumferential mode amplitudes are determined as in Chapter 5 for two tonal frequencies, $f_{BPF} = 1750$ Hz and $f_{2BPF} = 3500$ Hz. The associated propagating modes are $mn_{[1,0]}$ for the f_{BPF} and $mn_{[2,2]}$ for the first harmonic multiple of the blade-passing frequency (cf. Tab. 5.5). The influence of the variation of the data acquisition parameters on the output of the RMA is quantified in terms of the amplitude of the circumferential mode amplitudes A_m. In this way, the results corresponding to the maximal circumferential resolution ($\Delta\varphi = 1°$) and to the maximal number of rotor-triggered revolutions ($N = 56$, cf. Sec. 5.4.2) are taken as a reference value with which the examined parameter variations are compared. Thus, the variation of the data acquisition parameters on the output of the RMA is quantified as a relative error in the form:

$$\text{Error } A_m[\%] = \left| \frac{(A_\mathrm{m})_\mathrm{ref} - (A_\mathrm{m})_\mathrm{var}}{(A_\mathrm{m})_\mathrm{var}} \right| \tag{6.3}$$

where $(A_\mathrm{m})_\mathrm{ref}$ represents the reference circumferential mode amplitude and $(A_\mathrm{m})_\mathrm{var}$ the azimuthal mode amplitude resulting from the modified data recording parameter. The relative error is based on the maximal value of the circumferential mode amplitudes, both for the reference value ($\Delta\varphi = 1°$ and $N = 56$ revolutions) as well as for the modified ones. Considering that the propagating acoustical modes are low order (the maximal circumferential mode order m equals 2), a maximal circumferential spacing of $\Delta\varphi = 90°$ can be examined within the scope of the sensitivity analysis. In this case, data is recorded in a total of four circumferential positions. According to the Nyquist-Shannon sampling theorem (cf. Eq. 3.6), the quantity of circumferential measuring positions N_φ should be at least twice the azimuthal mode order m. This guarantees a proper execution of the spatial Fourier analysis and therefore, proper results for the circumferential mode amplitudes A_m. As a result, a range varying between $\Delta\varphi = 1°$ and $\Delta\varphi = 90°$ is analyzed. However, the resolution of the variation range of the circumferential spacing is not 1°. This is due to the fact, that the resulting angular spacing has to be a whole number. The considered circumferential spacing values along with the corresponding number of azimuthal positions are summarized in Tab. 6.4. The number of rotor-triggered revolutions is varied in steps of 5 revolutions, starting with a single revolution up to the maximum allowed number for the analyzed operating point ($N = 56$ revolutions).

As a final remark before proceeding to the results of the sensitivity analysis, the influence of the trigger delay and the sensor signal-to-noise ratio on the RMA is not experimentally studied. In regard to the latter, a condenser microphone is rated with a unique SNR value, resulting in the impossibility to arbitrarily modify its value. Concerning the trigger delay, no trustworthy value could be established for the mentioned variable.

Table 6.4: Circumferential spacing data acquisition values

$\Delta\varphi$	N_φ	$\Delta\varphi$	N_φ
1°	360	15°	24
2°	180	18°	20
3°	120	20°	18
4°	90	24°	15
5°	72	30°	12
6°	60	36°	10
8°	45	40°	9
9°	40	45°	8
10°	36	60°	6
12°	30	90°	4

6.2.1 Triggered revolutions for constant angular resolution

The influence of the number of triggered revolutions on the output of the RMA is first studied. Therefore, a data set for one microphone with the maximal possible circumferential resolution ($\Delta\varphi = 1°$) is taken as reference. The data set is processed as usual, i.e., it is filtered, synchronized, re-sampled and finally time averaged according to the procedure shown in Fig. 5.12. Prior to the re-sampling process, a specific number of rotor revolutions can be selected in order to continue with the *phase-locked ensemble average* before proceeding to the RMA evaluation routine. In this way, any number of rotor revolutions can be chosen as input for the data averaging process. A first result of the influence of these parameters on the output of the RMA was presented in Sec. 5.5.2. It was noticed that the number of rotor revolutions affected the frequency spectrum of a set of sound pressure time series. The amplitude of the signal evaluated with only four successive rotor revolutions laid above that corresponding to the data evaluated with 56 revolutions (cf. Figs. 5.20 and 5.23). With the purpose of quantifying the order of magnitude of these variations, the number of rotor-triggered revolutions is varied, as aforementioned, by keeping a constant angular resolution of $\Delta\varphi = 1°$. The results are displayed in Figs. 6.5 and 6.6 for the acoustical modes $mn_{[1,0]}$ and $mn_{[2,2]}$, respectively. Both graphs are complemented by the results of the numerical simulation for purposes of comparison.
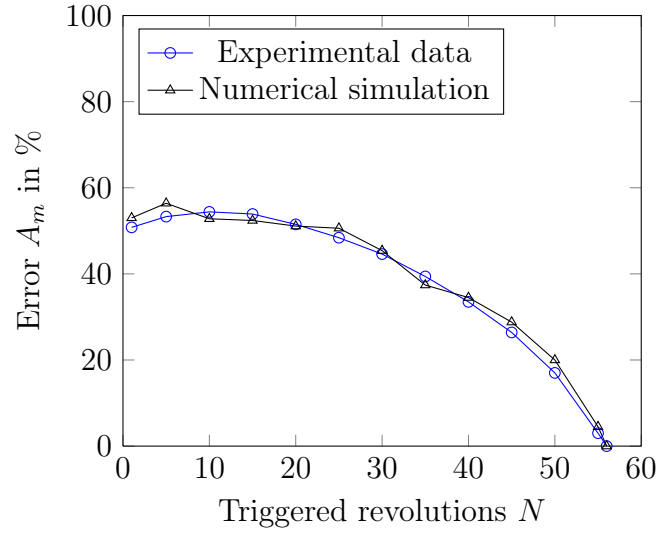
Figure 6.5: Relative error as a function of the number of triggered revolutions for the acoustical mode $mn_{[1,0]}$. Results correspond to the data recorded by one microphone with an angular resolution of $\Delta\varphi = 1°$
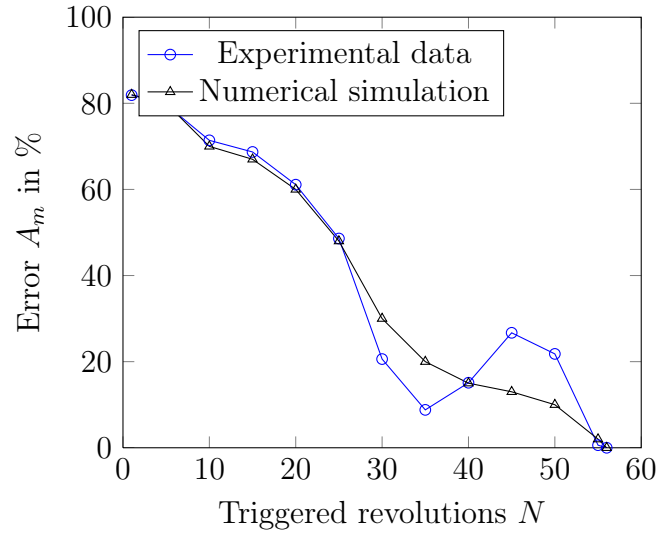
Figure 6.6: Relative error as a function of the number of triggered revolutions for the acoustical mode $mn_{[2,2]}$. Results correspond to the data recorded by one microphone with an angular resolution of $\Delta\varphi = 1°$

For both analyzed acoustical modes, the relative error decreases once the number of rotor-triggered revolutions increases. A similar behavior was previously established in Sec. 6.1.2. The relative error for $N = 56$ is in both cases 0%, which doesn't mean any error is associated with this value, it is solely a result of the definition conferred to the relative error, cf. Eq. 6.3. To clarify this observation, the consideration of a number of revolutions above the reference value $N = 56$ would result in a low relative error different from zero. Nevertheless, the tendency is positive and indicates that a higher number of recorded revolutions can significantly reduce the error associated with the amplitude of the circumferential modes A_m. As before, the cause of this tendency is attributed to the process of waveform averaging performed once the PLEA is implemented. Regarding the data validation through the numerical simulation, a good data fit is evidenced for mode $mn_{[1,0]}$.

6.2.2 Angular spacing for a constant number of triggered revolutions

Knowing beforehand the influence of the number of triggered revolutions on the output of the RMA, the sensitivity analysis is continued by examining the effect of the measurement angular resolution. Based on the results of Sec. 6.2.1, it is presumed that the best parameter to carry out the proposed study is that based on a maximal number of triggered revolutions. As a consequence, this parameter is kept constant at $N = 56$ while the angular resolution is varied according to Tab. 6.4. The results for the acoustical mode $mn_{[1,0]}$ propagating at the f_{BPF} are shown in Fig. 6.7 below. The results derived for the mode $mn_{[2,2]}$ are presented in Fig. 6.8.

Figure 6.7: Relative error as a function of the number of the angular resolution Δ_φ for the acoustical mode $mn_{[1,0]}$. Results correspond to the data recorded by one microphone with a number of triggered resolutions of $N = 56$

Figure 6.8: Relative error as a function of the number of the angular resolution Δ_φ for the acoustical mode $mn_{[2,2]}$. Results correspond to the data recorded by one microphone with a number of triggered resolutions of $N = 56$

For both analyzed modes the relative error steadily increases with decreasing angular resolution. High resolution values of the circumferential angular spacing ($\Delta\varphi = 1...5°$) lead to relative errors below 5%. This observation is valid for both analyzed acoustical modes. The magnitude of the relative error is more pronounced for the higher mode order $mn_{[2,2]}$. This is caused by the amplitude difference existing between the propagating modes for the analyzed tonal frequencies. Although not explicitly shown in terms of absolute values in Figs. 5.26 and 5.27, the maximum circumferential mode amplitude $A_{m=1}$ lies two orders of magnitude above that corresponding to the mode $mn_{[2,2]}$, $A_{m=2}$. Accordingly, the values associated with $A_{m=1}$ tend to remain stable almost independent of the angular spacing starting at $\Delta\varphi = 20°$. In the case of $A_{m=2}$, a slight change in amplitude results in a marked variation in the relative error. In spite of this situation, relative errors about 10% are evidenced for high angular resolution values for the mode $mn_{[2,2]}$. The numerical simulation follows the curve tendency in both cases, however it overestimates the results with a range lying between 5% and 10% above the experimental results. This is attributed to the inability of the numerical model to match the in-duct time varying flow field conditions, leading to the exposed differences in the relative error.

In order to complement the presented information regarding the influence of the angular spacing on the output of the RMA, a similar analysis is carried out with a reduced number of triggered revolutions, in this case, $N = 5$. This is done to emphasize the importance of the selection of this parameter in association with a varying angular resolution. The results of the analysis are shown in Fig. 6.9 for the acoustical modes $mn_{[1,0]}$ and $mn_{[2,2]}$, respectively. As noted, the relative error increases significantly for both cases once the number of triggered revolutions is reduced. This outcome was expected, because as already seen, a relative error increase is associated with a decrease of the number of time averaged data grouped in rotor-triggered revolutions.
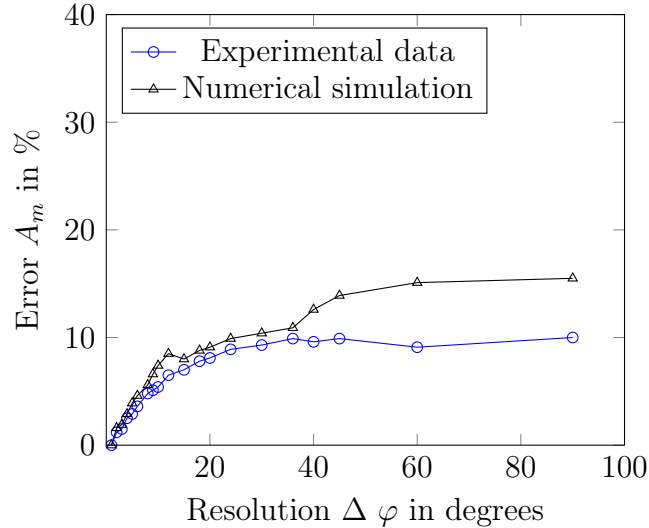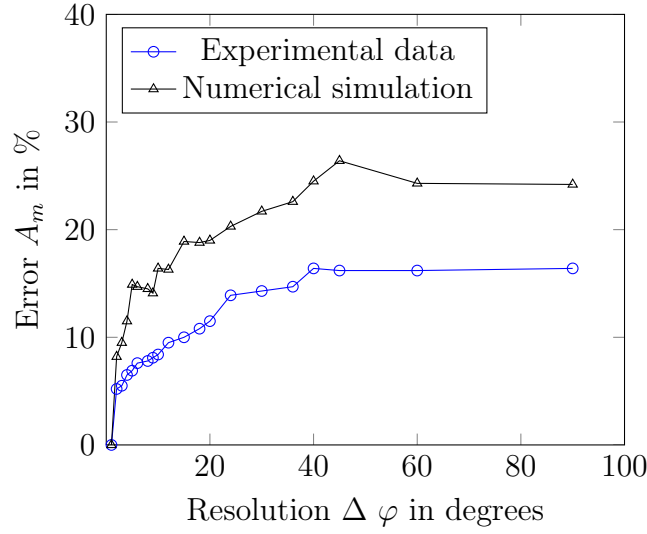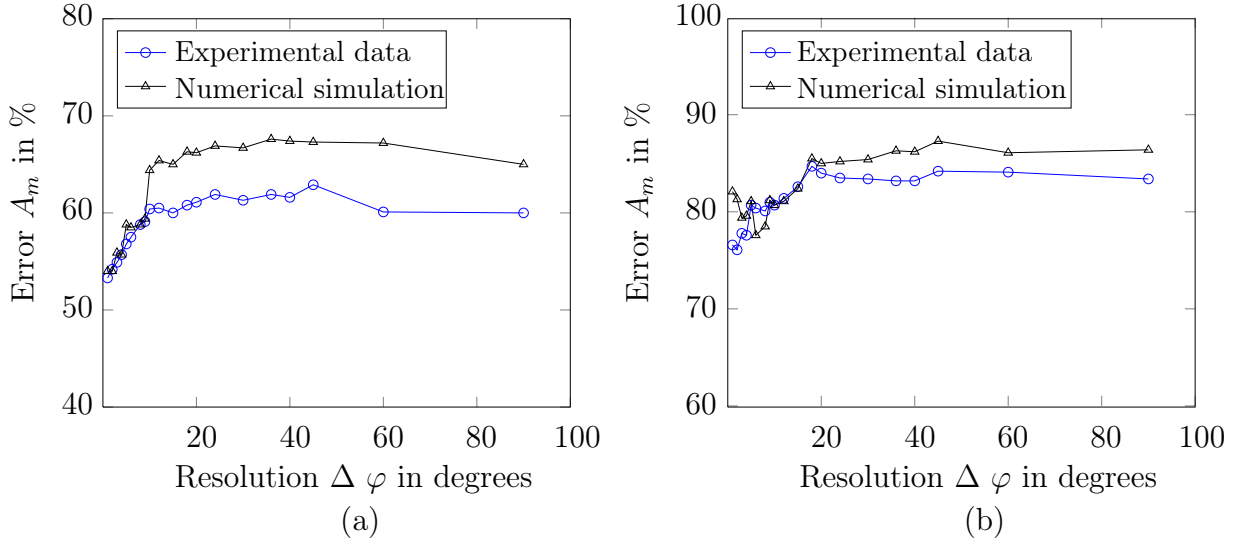
Figure 6.9: Relative error as a function of the number of the angular resolution Δ_φ for the acoustical modes $mn_{[1,0]}$ (a), and (b) $mn_{[2,2]}$. Results correspond to the data recorded by one microphone with a number of triggered resolutions of $N = 5$

Recalling the already presented results, and as a conclusion, it can be stated that low-order as well as high order modes may be measured without requiring a high circumferential spacing resolution. This is a result of the low relative error for angular resolutions below $\Delta\varphi = 1°$. Angular resolutions up to $\Delta\varphi = 5°$ result in relative errors below 10% in the worst case, specifically, for the acoustical mode $mn_{[2,2]}$. The result of this is that the time required to complete a in-duct measurement with the microphone ring may be reduced by a factor of 5. In other words, from the initial 360 circumferential measurement positions, a total of 72 angular positions are required to still obtain results with acceptable relative error. This reduction in angular measurement positions is possible if a significant number of rotor-triggered revolutions is also recorded and subsequently analyzed. Otherwise, the use of a reduced number of triggered revolutions can lead to relative errors as high as 50%, even for a high angular resolution (cf. Fig. 6.9).

6.3 Concluding remarks

This chapter focused on the sensitivity of the output of the RMA to specific data acquisition parameters. The chapter began with a test case based on numerical simulations. The acoustical in-duct field for the analyzed test case was simulated with the nominal operating parameters of the TFD low pressure air turbine. The test case was implemented with the purpose of giving an insight into the order of magnitude of the associated error on the circumferential mode amplitudes. This error emerged as a consequence of varying data acquisition parameters. Four parameters were considered for the test case, these were (a) the sensor circumferential spacing, (b) the number of triggered revolutions, (c) the sensor signal-to-noise ratio, and (d) a trigger delay.

The obtained results were quantified in terms of a relative error. Following the test case, a sensitivity analysis based on recorded acoustical data sets under realistic test conditions was performed. The influence of the number of triggered revolutions by keeping the circumferential spacing was first assessed. Subsequently, the influence on the output of the RMA was determined. In this case, a series of angular spacing data ranges were selected. The influence of both data acquisition parameters was again quantified in terms of a relative error on the amplitude of the resulting circumferential mode amplitudes. In regard to the aforementioned observations, following remarks are listed:

1. The influence of data acquisition parameters on the output of the RMA constitutes the first step to assess the magnitude of the measurement uncertainty derived from its implementation.

2. A realistic measurement setting for future experiments should be ideally performed with high signal-to-noise ratio sensors and under a maximum circumferential resolution ($\Delta\varphi = 1°$). At least 50 triggered revolutions are recommended for proper results, namely, a relative error below 10%. This setup is proposed under the premise that each triggered revolution is properly acquired, i.e., no trigger delay is present.

Having exposed the results of the sensitivity analysis performed over the RMA routine, this work is finalized by presenting the general conclusions associated with it as well as a series of recommendations and ideas for future work. Both sections are presented in Chapter 7 to follow.

7 Conclusions and Outlook

7.1 Conclusions

The current work concentrates on the enhancement of existing experimental analysis methods for the quantification of the sound propagation within axial turbomachinery, specifically within a LPT. In this way, the recorded acoustical data is processed by means of the RMA. In respect thereof, previous investigations have shown that the RMA is susceptible to errors. The latter are reflected on the resulting amplitude of the circumferential modes and are to a great extent generated by the instrumentation arrangement, i.e., by the location of the microphones within the test section.

The previously mentioned error sources have been established by means of numerical simulations based on synthetic sound pressure fields. In order to complement the findings related to the above mentioned sources of error, an experimental analysis of the influence of selected data acquisition parameters on the RMA is carried out. Specifically, the effect of the recorded number of triggered revolutions as well as the circumferential spacing of measurement microphones on the output of the RMA is examined. This approach is useful to quantify the sensitivity of the analysis method to variations on the aforementioned data acquisition parameters. In this way, a minimal measurement uncertainty derived from the application of the RMA can be guaranteed through the specification of optimum ranges for the analyzed measurement variables. In this regard, the main contributions of this work are the development of a measuring unit for the practical implementation of the sensitivity study and the results derived from the aforementioned analysis. Both contributions are discussed in the sections to follow.

7.1.1 Design integration of the acoustical instrumentation

A detailed measurement concept was developed to perform the sensitivity study of the RMA. This was accomplished by an instrumented rotating ring. The benefit of this instrumentation is due to its integration within the LPT. The sound pressure measurements were performed within the turbine flow channel and not upstream or downstream of the turbine casing, the latter being a a common practice for sound propagation studies in the last decades. The implemented measurement approach allows the data acquisition behind the turbine blades, offering a realistic picture of the sound field. A further particularity of the ring construction is the low number of implemented microphones. The extended circumferential range of motion provided by the external rotation control allowed a detailed recording of the acoustical field. By contrast, measurement set-ups previous to this study used several microphones as a result of space and displacement limitations, leading to high costs and low flexibility.

7.1.2 Results of the RMA

The sound pressure measurements were performed for a single operating point ($\dot{m} = 5 \, \text{kg s}^{-1}$, $\Omega = 3500 \, \text{min}^{-1}$). The results are specific to the TFD low-pressure turbine. Generally valid is, however, the data analysis procedure which comprises the pre-processing of the acoustical data and the application of the RMA routine itself. Based on the in-duct measured flow parameters, the Cut-On modes were estimated analytically based on the simplifying assumption that only co-rotating and downstream acoustical modes were propagating. This procedure was performed for each tonal noise frequency and resulted in the following acoustical modes: The mode $m_{[1,0]}$ propagated at f_{BPF}, the Cut-On modes $m_{[2,0]}$, $m_{[2,1]}$ and $m_{[2,2]}$ at f_{2BPF}.

The circumferential mode order associated with f_{BPF} was identified from the spatial spectral analysis. However, significant differences between the expected and the actually measured mode structure for f_{2BPF} were established. This is attributed to the excitation of low and high order modes by frequencies below f_{2BPF}, others than $m_{[2,2]}$. Regarding the radial mode amplitudes, the expected mode orders n were identified for both examined tonal frequencies. Both sets of results, circumferential and radial mode amplitudes, were compared with the output of a numerical simulation. The numerical simulation was performed based on a mathematical model which considered the exponential decay of modes generated by the harmonic tonal frequencies and a stochastic modal composition by means of amplitudes randomly generated by a Γ distribution. The expected mode orders were well reproduced by the numerical model and consistent with the theoretical predictions of the propagating sound field.

7.1.3 Scientific contribution

Within the scope of this work, two important data acquisition parameters affecting the output of the RMA were investigated. The effect of both the number of recorded rotor revolutions and the circumferential sensor positioning was studied. The aforementioned data acquisition parameters had, as already mentioned, an influence on the output of the RMA. Regarding the effect of the circumferential angular spacing $\Delta\varphi$, the relative error steadily increased with decreasing $\Delta\varphi$. Relative errors up to 5% were established by high values of $\Delta\varphi$, varying between $\Delta\varphi = 1...5°$. As such, a sufficient number of circumferential measurement positions assured a low relative error of the circumferential amplitude, provided that the number of triggered revolutions N is high enough - in this case - $N = 56$. The relative error stabilized around 10% starting from a angular resolution of 20°. Similar results were obtained for f_{2BPF}, however, the magnitude of the relative error is slightly higher.

Complementing the sensitivity analysis, only a high number of triggered revolutions ensured optimal results independent of the circumferential mode order. The relative error is in turn coupled to the circumferential angular resolution, i.e., the relative error of the analyzed modes decreased once the number of rotor-triggered revolutions increased. However, even for a high circumferential resolution (i.e., $\Delta\varphi = 1°$), the relative error exceeded 50% for a low number of revolutions.

The circumferential sensor spacing and the number of recorded rotor-triggered revolutions play an important role in any measurement set-up. A realistic measurement setting for future experiments should ideally be performed with maximal circumferential resolution ($\Delta\varphi = 1°$) and at least $N = 50$ triggered revolutions for proper results, with an expected relative error below 10%. Values below $N = 50$ revolutions lead to significant errors even for high angular resolutions. As inferred from the previously presented results, the quantification of the influence of the data acquisition parameters on the RMA is a first step towards establishing the magnitude of the uncertainty of the method itself. As applied here, the sensitivity analysis performed within the scope of this work provides a useful tool for a detailed experimental design for future sound propagation experiments within the TFD low-pressure turbine.

7.2 Outlook

Future work should concentrate on the experimental evaluation of the signal-to-noise ratio (SNR). As a consequence, the SNR value for each used condenser microphone should be first established before each measuring campaign. A systematic study could be carried out by placing a different microphone in a reference axial position for every measurement iteration. This procedure would quantify the influence of an inherent metrological parameter associated with the whole test set-up.

A final observation is related to the quantity of rotor-triggered revolutions, a potential for improvement was also identified. The measuring time for all performed acoustical measurements within the scope of this work amounted to one second. A extended recording time permits the acquisition of a higher number of rotor-triggered revolutions. As a consequence, and based on the simulated as well as experimental results derived from the variation of the triggered revolutions, a extended data acquisition period is recommended, at least two seconds. For the analyzed operating point, this would mean a maximum of 116 triggered revolutions, which according to the numerical model, would result in relative errors below 1% specially for high SNR sensors. This is precisely the case of the condenser microphones used in this work.

7 Conclusions and Outlook

Bibliography

Abramowitz, M. and Stegun, I. (2007): Handbook of Mathematical Functions With Formulas, Graphs, and Mathematical Tables. Dover Publications, Inc., New York, USA.

Airbus (2013): Global Market Forecast: Future Journeys 2013–2032. Blagnac Cedex, France.

ASEB (1968): Civil Aviation Research and Development – An Assessment of Federal Government Involvement – Aircraft Noise. Technical Report, Aeronautical and Space Enginnering Board – National Academy of Enginnering, Washington, D.C., USA.

Bartelt, M. (2014): Schalltransport durch eine Niederdruckturbine. Ph.D. Thesis, Institut für Turbomaschinen und Fluid-Dynamik, Leibniz Universität Hannover, Hannover, Germany.

Bartelt, M.; Laguna, J. and Seume, J. (2013): Synthetic Sound Source Generation for Acoustical Measurements in Turbomachines. In: Proceedings of ASME Turbo Expo 2013. San Antonio, Texas, USA, GT2013-95045.

Bartelt, M. and Seume, J. (2011): Auslegung und Optimierung eines Aeroakustik-Kanals für Turbomaschinenanwendungen unter Verwendung numerischer Methoden. In: Deutscher Luft- und Raumfahrtkongress 2011. Bremen, Germany.

Bartlett, P.; Humphreys, N.; Phillpson, P.; Lan, J.; Nesbitt, E. and Premo, J. (2004): The Joint Rolls-Royce/Boeing Quiet Technology Demonstrator Programme. In: 10th AIAA/CEAS Aeroacoustics Conference.

Beckwith, T.; Marangoni, R. and Lienhard, J. (2006): Mechanical Measurements. Prentice Hall, 6. Edition.

Beranek, L. (1969): Aircraft Noise. In: Proceedings of the Conference Noise as a Public Health Hazard. Washington, D.C., USA.

Binner, M. (2011): Experimentelle Untersuchung von Teil- und Schwachlastzuständen in Hochdruckdampfturbinen. Ph.D. Thesis, Institut für Turbomaschinen und Fluid-Dynamik, Leibniz Universität Hannover, Hannover, Germany.

Binner, M. and Seume, J. (2014): Flow Patterns in High Pressure Steam Turbines During Low-Load Operation. In: Journal of Turbomachinery, 136(6).

Boeing (2013): Current Market Outlook 2013–2032. Seattle, WA, USA.

Bibliography

Bolleter, U. and Crocker, M. (1971): Theory and Measurement of Modal Spectra in Hard-Walled Cylindrical Ducts. In: Journal of the Acoustical Society of America, 50(137): 1439–1447.

Brüel&Kjaer (1996): Microphone Handbook - Vol. 1: Theory. Naerum, Denmark.

Bräuling, W. J. G. (2009): Flugzeugtriebwerke. Springer Verlag, Berlin, Germany, 3rd Edition.

Carolus, T. (2013): Ventilatoren - Aerodynamischer Entwurf, Schallvorhersage, Konstruktion. Springer Vieweg, Wiesbaden, Germany.

Cohen, A. (1969): Effects of Noise on Psychological State. In: Proceedings of the Conference Noise as a Public Health Hazard. Washington, D.C., USA.

Delfs, J. (2011): Vorlesungsskript - Grundlagen der Aeroakustik. Institut für Aerodynamik und Strömungsmechanik, Technische Universität Braunschweig, Braunschweig, Germany.

Ehrenfried, K. (2004): Skript zur Vorlesung Strömungsakustik. Mensch & Buch Verlag, Berlin, Germany.

Enghardt, L.; Holewa, A. and Tapken, U. (2007): Comparison of Different Analysis Techniques to Decompose a Broadband Ducted Sound Field in its Mode Constituents. In: Proceedings of 13th AIAA/CEAS Aeroacoustic Conference, Rome, Italy.

Enghardt, L.; Raitor, T.; Tapken, U. and Giebmanns, A. (2009): Neuartige aktive/passive Systeme zur Geräuschminderung an Triebwerken. Technical Report Nr. 20T0310C, Deutsches Zentrum für Luft- und Raumfahrt - DLR.

Enghardt, L.; Tapken, U.; Neise, W.; Kennepohl, F. and Heinig, K. (2001): Turbine Blade/Vane Interaction Noise: Acoustic Mode Analysis using In-Duct Sensor Rakes. In: Proceedings of 7th AIAA/CEAS Aeroacoustic Conference, Maastricht, Netherlands.

Enghardt, L.; Zhang, Y. and Neise, W. (1999): Experimental Verification of a Radial Mode Analysis Technique using Wall-Flush Mounted Sensors. In: 137th Regular Meeting of the Acoustical Society of America, 2nd Convention of the EAA: Forum Acusticum - Integrating the 25th German Acoustics DAGA Conference.

EPA (1971): Community Noise. Technical Report Contract 68-04-0046, Wyle Laboratories, Washington, D.C., USA.

Evers, H. B. (1985): Strömungsformen im Ventilationsbetrieb einer ein-und mehrstufig beschaufelten Modellturbine. Ph.D. Thesis, Institut für Strömungsmaschinen, Universität Hannover, Hannover, Germany.

Fisher, M. and Self, R. (2002): Aeroacoustics Research in Europa: The CEAS-ASC Report on 2001 Highlights. In: Journal of Sound and Vibration, 258(1): 1–30.

Franssen, E. A. M.; van Wichen, N. D.; Nagelkerke, N. J. D. and Lebret, E. (2004): Aircraft Noise Around a Large International Airport and its Impact on General Health and Medication Use. In: Occupational and Environmental Medicine, 61(5): 405–413.

Frederiksen, E.; Eirby, N. and Mathiasen, H. (1979): Prepolarized Condenser Microphones for Measurement Purposes. Technical Review 4, Brüel & Kjaer.

Galloway, W. J. and Von Gierke, H. E. (1966): Individual and Community Reaction to Aircraft Noise: Present Status and Standardization Efforts. In: International Conference on the Reduction of Noise and Disturbance Caused by Civil Aircraft. London, United Kingdom.

Georgi, W. and Metin, E. (2012): Einführung in LabVIEW. Carl Hanser Verlag, Munich, Germany, 5th Edition.

Goldstein, M. (1976): Aeroacoustics. McGraw-Hill International Book Company, USA, 1st Edition.

Golubev, V. and Atassi, H. (1996): Sound Propagation in an Annular Duct with Mean Potential Swirling Flow. In: Journal of Sound and Vibration, 198(5): 601–616.

Gostelow, J. (1977): A New Approach to the Experimental Study of Turbomachinery Flow Phenomena. In: Journal of Engineering for Power, 99(1): 97–105.

G.R.A.S (2014): Calibration Chart Pressure-Field Microphone Set. Holte, Denmark.

Hanson, D. (1973): Unified Analysis of Fan Stator Noise. In: Journal of the Acoustical Society of America, 54(6): 1571–1591.

Hanson, D. (1994): Coupled 2-Dimensional Cascade Theory for Noise and Unsteady Aerodynamics of Blade Row Interaction in Turbofans - Volume 1-Theory Development and Parametric Studies. NASA Contractor Report NAS3-25952, NASA - National Aeronautics and Space Administration, Lewis Research Center, Cleveland, Ohio, USA.

Hellmich, B. (2008): Acoustic Resonance in a High-Speed Axial Compressor. Ph.D. Thesis, Institut für Turbomaschinen und Fluid-Dynamik, Universität Hannover, Hannover, Germany.

Henke, M.; Biester, M.; Gündogdu, Y.; Lippl, F.; Mass, E. and Seume, J. (2012): Numerical Assisted Design of a Variable Rotating Vane Carrier Device for Turbine Test Rings with Split Housing Structures using a Segmented Half-Ring Bearing Concept. In: Proceedings of the 53rd AIAA/ASME/ASCE/AHS/ASC Structures, Structural Dynamics, and Materials Conference. Honolulu, Hawaii, USA, AIAA 2012-1660.

Herzog, N. (2008): Numerische Untersuchung von Schwachlastströmungen in mehrstufigen Axialturbinen. Ph.D. Thesis, Institut für Turbomaschinen und Fluid-Dynamik, Leibniz Universität Hannover, Hannover, Germany.

Bibliography

Herzog, N.; Gündogdu, Y.; Kang, G. and Seume, J. (2005): Part Load Operation of a Four-Stage Turbine. In: Proceedings of ASME Turbo Expo 2005. Reno-Tahoe, Nevada, USA, GT2005-68700.

Holste, F. (1995): Ermittlung der aerodynamischen Lärmquellen und Berechnung des abgestrahlten Schallfeldes mittels der im Nahfeld gemessenen Druckschwankungen am Beispiel eines Triebwerkmodells. Ph.D. Thesis, Technische Universität Berlin, Berlin, Germany.

Holste, F. and Neise, W. (1992): Experimental Determination of the Main Noise Sources in a Propfan Model by Analysis of the Acoustic Spinning Modes in the Exit Plane. In: Proceedings of 14th DLRG/AIAA Aeroacoustic Conference, Aachen, Germany.

Holste, F. and Neise, W. (1997): Noise Source Identification in a Propfan Model by Means of Acoustical Near Field Measurements. In: Journal of Sound and Vibration, 203(4): 641–655.

Hummel, D. (2012): Der Campus Forschungsflughafen: Luftfahrtforschung und-lehre in Braunschweig - Rückblick und Ausblick. Technical Report, Technische Universität Braunschweig, Braunschweig, Germany.

ICAO (2008): Annex 16 to the Convention on International Civil Aviation: Environmental Protection – Volume I: Aircraft Noise. International Civil Aviation Organization, Montréal, Canada, 5th Edition.

Ioannou, E. (2012): Singular Value Decomposition (SVD) for the Optimization of Microphone Measurement Positions for Sound Propagation Studies. Master Thesis, Institut of Turbomaschinery and Fluid Dynamics, Leibniz Universität Hannover, Hannover, Germany.

Jansen, G. (1969): Effect of Noise on Physiological State. In: Proceedings of the Conference Noise as a Public Health Hazard. Washington, D.C., USA.

Kang, G. (2006): Strömungsmechanische Untersuchungen in einer Axialturbine im Ventilations- und Leerlaufbetrieb. Ph.D. Thesis, Institut für Turbomaschinen und Fluid-Dynamik, Leibniz Universität Hannover, Hannover, Deutschland.

Klingelnberg, J. (2008): Kegelräder. Springer-Verlag, Berlin, Germany, 1st Edition.

Költzsch, P. (1984): Geräusche von Strömungsmaschinen - Ein Beitrag zur Lärmbekämpfung an Maschinen und Anlagen. Deutscher Verlag für Grundstoffindustrie, Leipzig, Germany.

Kousen, K. (1996): Pressure Modes in Ducted Flows with Swirl. In: Proceedings of 2nd AIAA/CEAS Aeroacoustics Conference, State College, Pennsylvania, USA.

Kousen, K. (1999): Eigenmodes of Ducted Flows With Radially-Dependent Axial and Swirl Velocity Components. Final Contractor Report 1999-208881, NASA - National Aeronautics and Space Administration, Glenn Research Center, Cleveland, Ohio, USA.

Kroese, D. and Chan, J. (2014): Statistical Modeling and Computation. Springer, New York, USA.

Kryter, K. (1960): The Meaning and Measurement of Perceived Noise Level. In: Noise Control, 6(5): 12–27.

Laguna, J.; Bartelt, M.; Drechsel, B. and Seume, J. (2012): Entwicklung einer variablen Messeinheit für Schallfeldanalysen in Turbomaschinen. In: 38. Jahrestagung für Akustik - DAGA 2012. Darmstadt, Germany.

Laguna, J.; Bartelt, M.; Keller, C. and Seume, J. (2013a): Sensitivity and Uncertainty of the Radial Mode Analysis for Turbomachinery Applications. In: Proceedings of the ETC 10. Lappeenranta, Finland.

Laguna, J.; Bartelt, M. and Seume, J. (2013b): Impact of Swirl on the Sensitivity of the Radial Mode Analysis in Turbomachinery. In: Proceedings of the ASME Turbo Expo 2013. San Antonio, Texas, USA, GT2013-95460.

Lohmann, D. (1977): Zur Schallausbreitung in Zylinderkanälen mit helikalen Einbauten. Ph.D. Thesis, Technische Universität Braunschweig, Braunschweig, Germany.

Lowis, C. and Joseph, P. (2006): Determining the Strength of Rotating Broadband Sources in Ducts by Inverse Methods. In: Journal of Sound and Vibration, 295(3-5): 614–632.

Martens, S. (2002): Jet Noise Reduction Technology Development at GE Aircraft Engines. In: ICAS 2002 - 23rd International Congress of Aeronautical Sciences. Toronto, Canada.

Mason, V. (1969): Some Experiments on the Propagation of Sound Along a Cylindrical Duct Containing Flowing Air. In: Journal of Sound and Vibration, 10(2): 208–226.

Mensen, H. (2003): Handbuch der Luftfahrt. Springer Vieweg, Berlin, Deutschland, 2nd Edition.

Michalke, A. (1989): On the Propagation of Sound Generated in a Pipe of Circular Cross-Section with Uniform Mean Flow. In: Journal of Sound and Vibration, 134(2): 203–234.

Michalke, A. (1990): On Experimental Sound Power Determination in a Circular Pipe with Uniform Mean Flow. In: Journal of Sound and Vibration, 142(2): 311–341.

Bibliography

Mongenau, L.; Thompson, D. and McLaughlin, D. (1993): Sound Generation By Rotating Stall in Centrifugal Turbomachines. In: Journal of Sound and Vibration, 163(1): 1–30.

Moore, C. (1972): In-Duct Investigation of Subsonic Fan Rotor Alone Noise. In: Journal of the Acoustical Society of America, 51(5): 1471–1482.

Moore, C. (1979): Measurement of Radial and Circumferential Modes in Annular and Circular Fan Ducts. In: Journal of Sound and Vibration, 62(2): 235–256.

Morfey, C. (1964): Rotating Pressure Patterns in Ducts: Their Generation and Transmission. In: Journal of Sound and Vibration, 1(1): 60–87.

Mugridge, B. (1969): The Measurement of Spinning Acoustic Modes Generated in an Axial Flow Fan. In: Journal of Sound and Vibration, 10(2): 227–246.

Neise, W. and Enghardt, L. (2003): Technology Approach to Aero Engine Noise Reduction. In: Aerospace Science and Technology, 7(5): 352–363.

Nelson, P. and Yoon, H. (2000): Estimation of Acoustic Source Strength by Inverse Methods: Part I, Conditioning of the Inverse Problem. In: Journal of Sound and Vibration, 233(4): 643–668.

Nijboer, R. (2001): Eigenvalues and Eigenfunctions of Ducted Swirling Flows. In: Proceedings of 7th AIAA/CEAS Aeroacoustics Conference, Maastricht, Netherlands.

Peake, N. and Parry, A. (2012): Modern Challenges Facing Turbomachinery Aeroacoustics. In: Annual Review of Fluid Mechanics, 44: 227–248.

Press, W.; Teukolsky, S.; Vetterling, W. and Flannery, B. (2007): Numerical Recipes: The Art of Scientific Computing. Cambridge University Press, New York, NY, USA, 3rd Edition.

Price, A. (1967): The Boeing 707. Profile Publications, Leatherhead, Surrey, England.

Rademaker, E.; Sijtsma, P. and Tester, B. (2001): Mode Detection with Optimised Array in a Model Turbofan Engine Intake at Varying Shaft Speeds. Technical Report No. 2001-132, National Aerospace Laboratory NLR, Amsterdam, The Netherlands.

Rautenberg, M. and Kassens, K. (1970): Strömungsschall-Messungen im Diffusor eines Radialverdichters und Entwicklung einer Messmethode zur Erfassung des instationären Strömungszustandes nach dem Laufrad. Technical Report 233/70, Institut für Strömungsmaschinen - Technische Universität Hannover, Hannover, Germany.

Reed, D.; Herkes, W. and Shivashankara, B. (2006): The Boeing Quiet Technology Demonstrator Program. In: 25th International Congress of the Aeronautical Sciences.

Rossing, T. (2007): Springer Handbook of Acoustics. Springer Science+Business Media, LLC., New York, USA.

Salant, R. (1967): Symmetric Normal Modes in Uniformly Rotating Fluid. In: The Journal of the Acoustical Society of America, 43(6): 1302–1305.

Salikuddin, M. and Ramakrishnan, R. (1987): Acoustic Power Measurement for Single and Annular Duct-Noozle Systems utilizing a Modal Decomposition Scheme. In: Journal of Sound and Vibration, 113(3): 441–472.

Sandstede, H. (1974): Der Einfluß der Oberflächenrauhigkeit von Schaufelprofilen auf das strömungstechnische Verhalten einer Turbine. Ph.D. Thesis, Institut für Strömungsmaschinen, Technische Universität Hannover, Hannover, Germany.

Schiffer, H. (1976): Ausbreitung des Schalles von Turbomaschinen in Rohrleitungen mit Diskontinuitäten. Ph.D. Thesis, Rheinische-Westfälische Technische Hochschule Aachen, Aachen, Germany.

Schimming, P. (2003): Counter Rotating Fans - An Aircraft Propulsion for the Future? In: Journal of Thermal Science, 12(2): 97–103.

Sijtsma, P. and Zillmann, J. (2007): In-Duct and Far-Field Mode Detection Techniques for Engine Exhaust Noise Measurements. Technical Report No. 2007-347, National Aerospace Laboratory NLR, Amsterdam, The Netherlands.

Smith, M. (1989): Aircraft Noise. Cambridge University Press, USA, 1st Edition.

Spurk, J. and Aksel, N. (2010): Strömungslehre - Einführung in die Theorie der Strömungen. Springer Verlag, Berlin, Germany, 8. Edition.

Starkloff, E.; Fountain, T. and Black, G. (2003): The PXI Modular Instrumentation Architecture. In: 2003 IEEE International Test Conference (ITC). 2, 21–30.

Taddei, F.; De Lucia, M.; Cinelli, C. and Schipani, C. (2009): Experimental Investigations of Low Pressure Turbine Noise: Radial Mode Analysis for Swirling Flows. In: Proceedings of the 12th International Symposium on Unsteady Aerodynamics, Aeroacoustics and Aeroelasticity of Turbomachines ISUAAAT12, London, UK.

Tapken, U.; Bauers, R.; Arnold, F. and Zillmann, J. (2008): Turbomachinery Exhaust Noise Radiation Experiments–Part 2: In- Duct and Far-Field Mode Analysis. In: 14th AIAA/CEAS Aeroacoustics Conference. Vancouver, British Columbia, Canada, AIAA-2008-2858.

Tapken, U.; Bauers, R.; Neuhaus, L.; Humphreys, N.; Wilson, A.; Stöhr, C. and Beutke, M. (2011): A New Modular Fan Rig Noise Test and Radial Mode Detection Capability. In: 17th AIAA/CEAS Aeroacoustics Conference. Portland, Oregon, USA, AIAA-2011-2897.

Tapken, U. and Enghardt, L. (2006): Optimisation of Sensor Arrays for Radial Mode Analysis in Flow Ducts. In: Proceedings of the 12th AIAA/CEAS-Aeroacoustics Conference, Cambridge, Massachussets, USA.

Bibliography

Tapken, U.; Enghardt, L.; Neise, W. and Schimming, P. (2001): Active Noise Control of Noise from Turbomachines - Results of Radial Mode Analysis. In: INTERNOISE 2001, 30th International Congress on Noise Control Enginnering. The Hague, Netherlands.

Trenke, M. (2012): Auslegung und Konstruktion einer Verstelleinheit für rotierende Leitschaufelträger. Master Thesis, Institut für Turbomaschinen und Fluid-Dynamik, Leibniz Universität Hannover, Hannover, Deutschland.

Tyler, J. M. and Sofrin, T. (1962): Axial Flow Compressor Noise Studies. In: Society of Automotive Engineers Transactions, 70: 309–332.

WHO (2011): Burden of Disease from Environmental Noise – Quantification of Healthy Life Years Lost in Europe. World Health Organization (WHO) Regional Office for Europe, Copenhagen, Denmark.

Wilson, D. and Korakianitis, T. (1998): The Design of High-Efficiency Turbomachinery and Gas Turbines. Prentice Hall, Berlin, Germany, 2nd Edition.

Wittel, H.; Muhs, D.; Jannasch, D. and Voßiek, J. (2013): Roloff/Matek Maschinenelemente-Normung, Berechnung, Gestaltung. Springer Vieweg, Wiesbaden, Deutschland, 21. Edition.

Wright, S. (1975): The Acoustic Spectrum of Axial Flow Machines. Technical Report Technical Report No. 69, Institute of Sound and Vibration Research - University of Southampton, Southampton, United Kingdom.

Yardley, P. (1974): Measurement of Noise and Turbulence Generated by Rotating Machinery. Ph.D. Thesis, Institute of Sound and Vibration - University of Southampton, Southampton, United Kingdom.

Yoon, H. and Nelson, P. (2000): Estimation of Acoustic Source Strength by Inverse Methods: Part II, Experimental Investigation of Methods for choosing Regularization Parameters. In: Journal of Sound and Vibration, 233(4): 669–705.

Zehner, P. (1980): Vier-Quadranten-Charakteristiken mehrstufiger axialer Turbinen. Fortschrittberichte der VDI Zeitschriften. VDI-Verlag GmbH, Düsseldorf, Germany.

Zorumski, W. and Lester, H. (1974): Unified Analysis of Ducted Turbomachinery Noise. NASA Technical Memorandum TM X-72633, NASA - National Aeronautics and Space Administration, Langley Research Center, Hampton, Virginia, USA.

A Appendix

A.1 Circumferential mode amplitudes A_m for $f_{BPF} =$ 1750 Hz

Figure A.1: Time variation of the circumferential mode amplitudes $\|A_m\|$ for selected time steps and mode orders (a). Normalized circumferential mode amplitudes $\|A_m\|$ with respect to $\|A_m\|_{max}$ for (b) maximal $\|A_m\|$, and (c) average $\|A_m\|$ over all time steps. Results correspond to the data recorded by microphone 2 about $f_{\mathrm{BPF}} = 1750$ Hz

Figure A.2: Time variation of the circumferential mode amplitudes $\|A_m\|$ for selected time steps and mode orders (a). Normalized circumferential mode amplitudes $\|A_m\|$ with respect to $\|A_m\|_{max}$ for (b) maximal $\|A_m\|$, and (c) average $\|A_m\|$ over all time steps. Results correspond to the data recorded by microphone 3 about $f_{\mathrm{BPF}} = 1750$ Hz
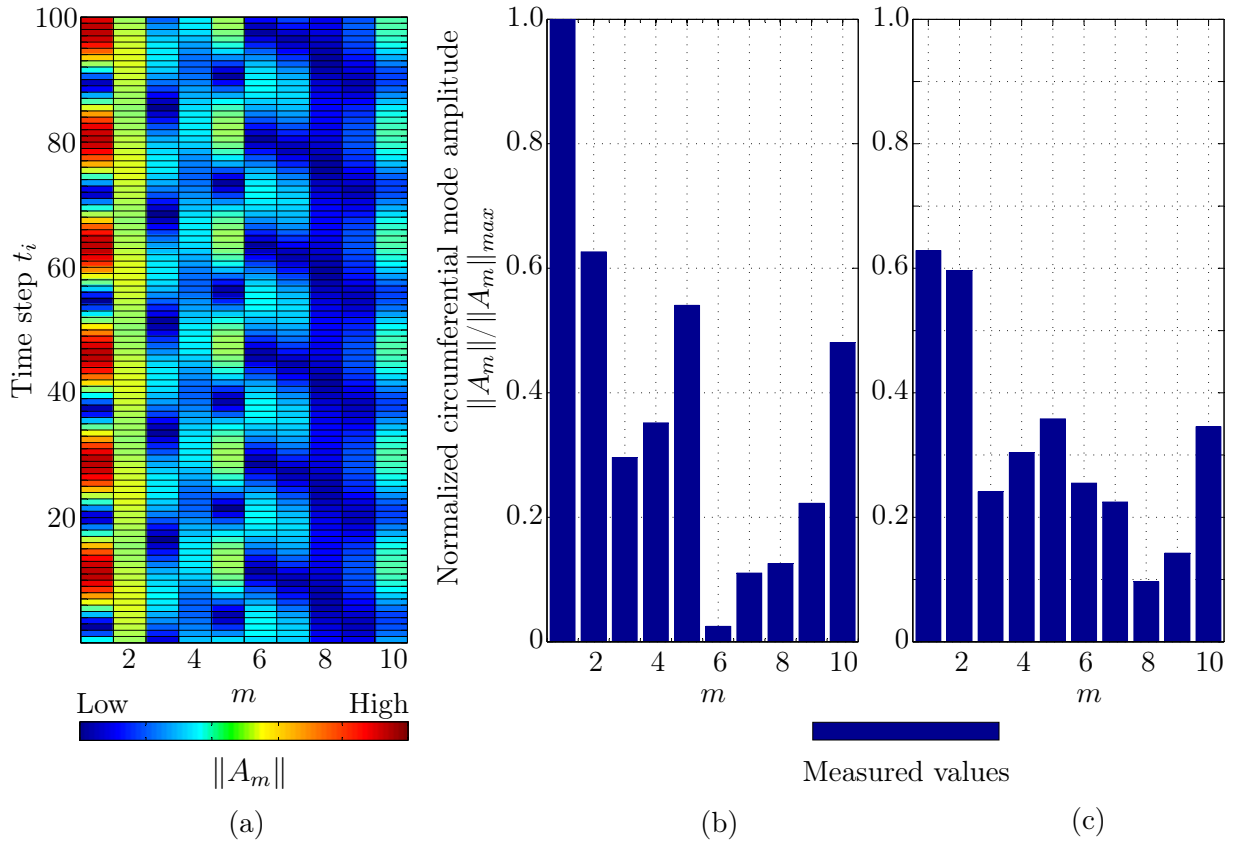
Figure A.3: Time variation of the circumferential mode amplitudes $\|A_m\|$ for selected time steps and mode orders (a). Normalized circumferential mode amplitudes $\|A_m\|$ with respect to $\|A_m\|_{max}$ for (b) maximal $\|A_m\|$, and (c) average $\|A_m\|$ over all time steps. Results correspond to the data recorded by microphone 4 about $f_{\mathrm{BPF}} = 1750$ Hz

Figure A.4: Time variation of the circumferential mode amplitudes $\|A_m\|$ for selected time steps and mode orders (a). Normalized circumferential mode amplitudes $\|A_m\|$ with respect to $\|A_m\|_{max}$ for (b) maximal $\|A_m\|$, and (c) average $\|A_m\|$ over all time steps. Results correspond to the data recorded by microphone 5 about $f_{\mathrm{BPF}} = 1750$ Hz
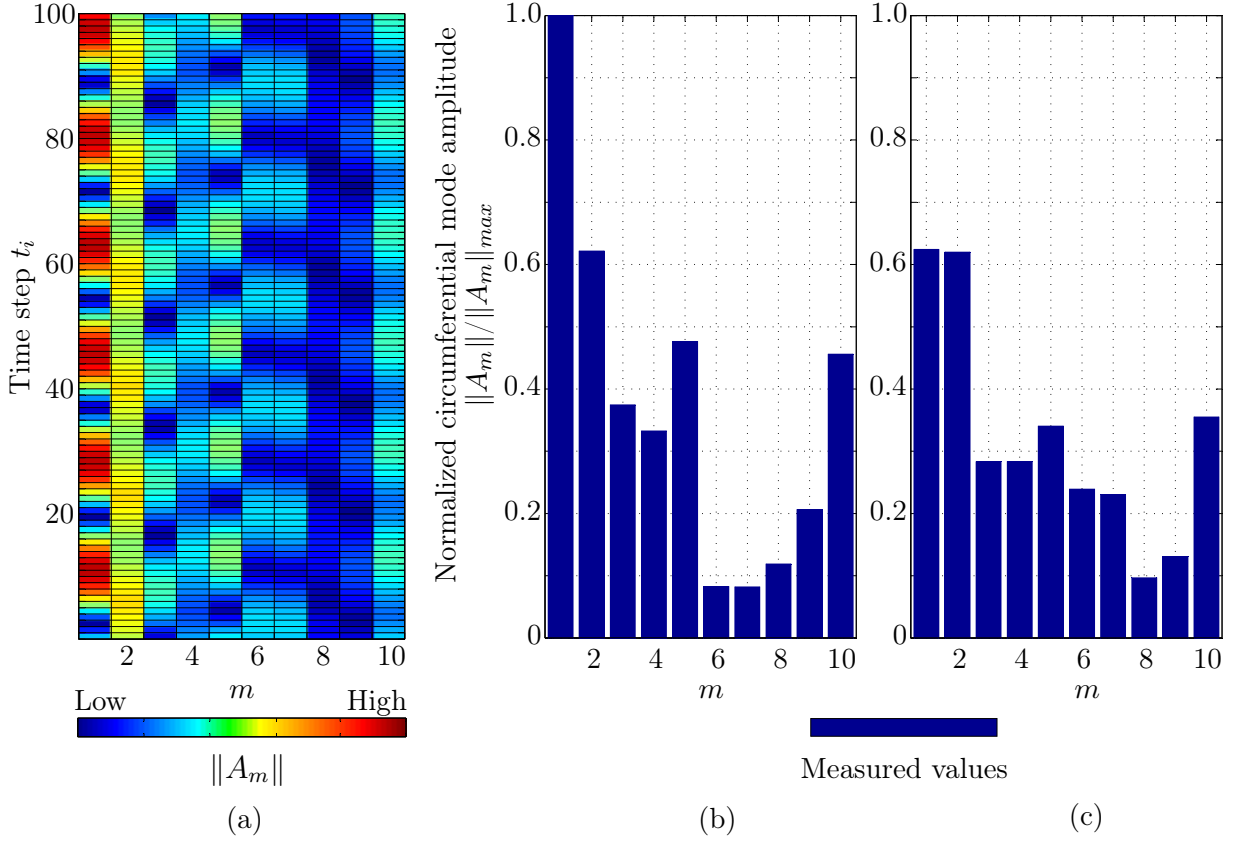
Figure A.5: Time variation of the circumferential mode amplitudes $\|A_m\|$ for selected time steps and mode orders (a). Normalized circumferential mode amplitudes $\|A_m\|$ with respect to $\|A_m\|_{max}$ for (b) maximal $\|A_m\|$, and (c) average $\|A_m\|$ over all time steps. Results correspond to the data recorded by microphone 6 about $f_{\mathrm{BPF}} = 1750$ Hz

A.2 Circumferential mode amplitudes A_m for $f_{2BPF} =$ 3500 Hz
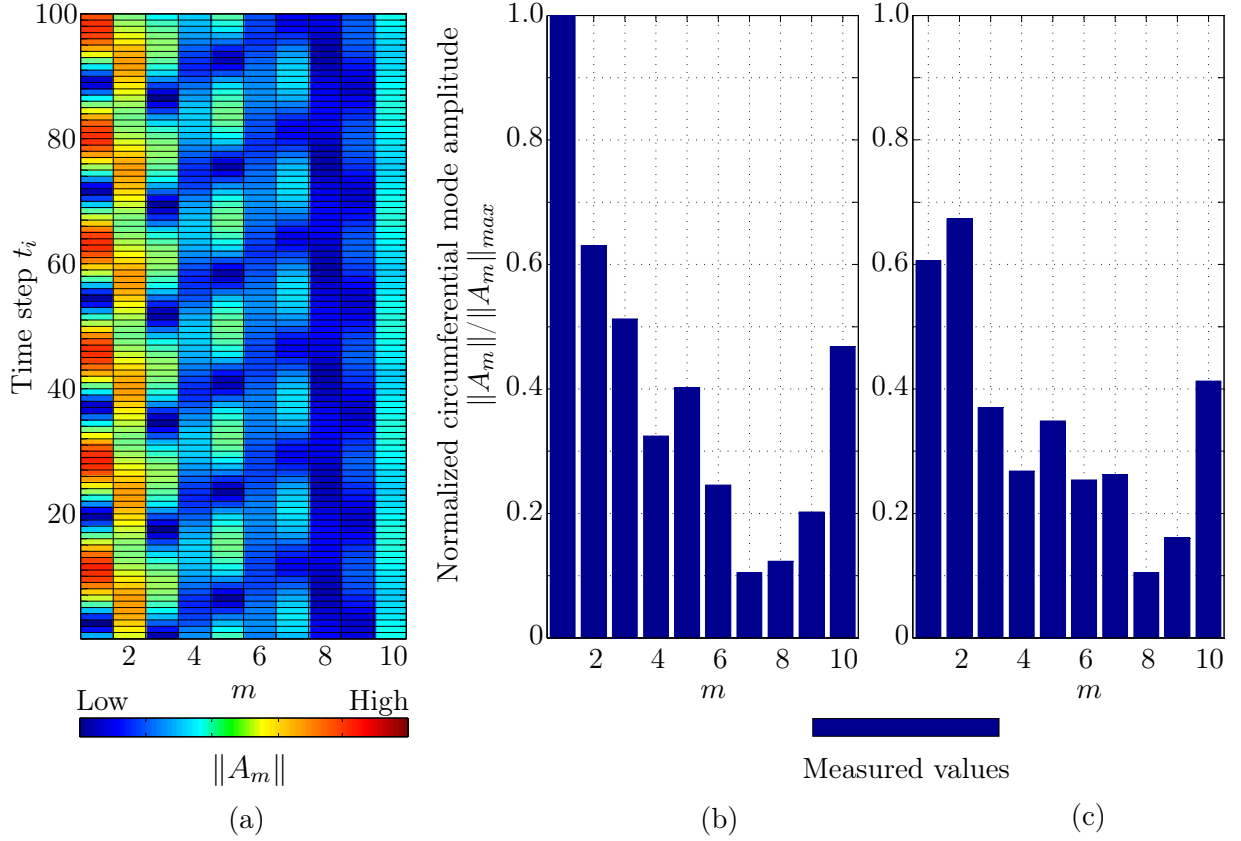

Figure A.6: Time variation of the circumferential mode amplitudes $\|A_m\|$ for selected time steps and mode orders (a). Normalized circumferential mode amplitudes $\|A_m\|$ with respect to $\|A_m\|_{max}$ for (b) maximal $\|A_m\|$, and (c) average $\|A_m\|$ over all time steps. Results correspond to the data recorded by microphone 2 about $f_{2\text{BPF}} = 3500$ Hz
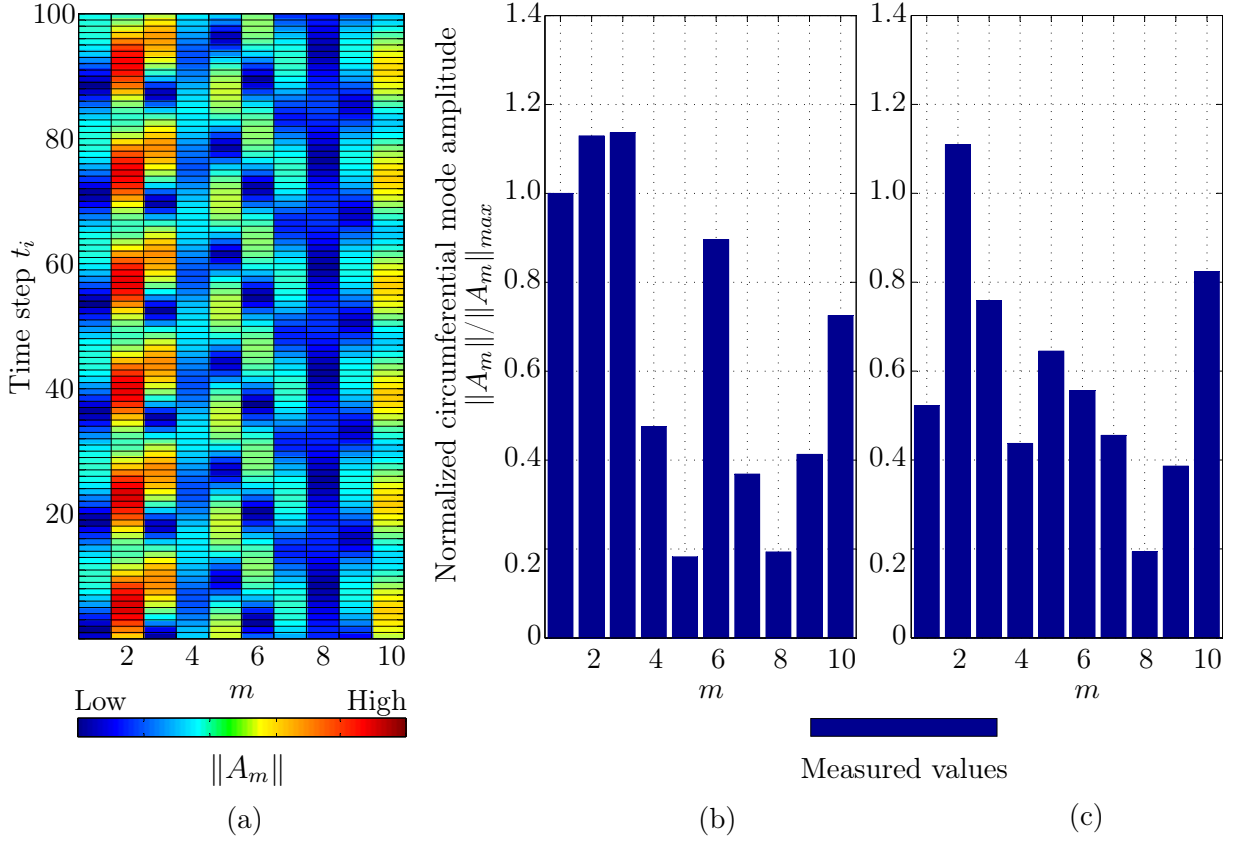
Figure A.7: Time variation of the circumferential mode amplitudes $\|A_m\|$ for selected time steps and mode orders (a). Normalized circumferential mode amplitudes $\|A_m\|$ with respect to $\|A_m\|_{max}$ for (b) maximal $\|A_m\|$, and (c) average $\|A_m\|$ over all time steps. Results correspond to the data recorded by microphone 3 about $f_{2\mathrm{BPF}} = 3500$ Hz
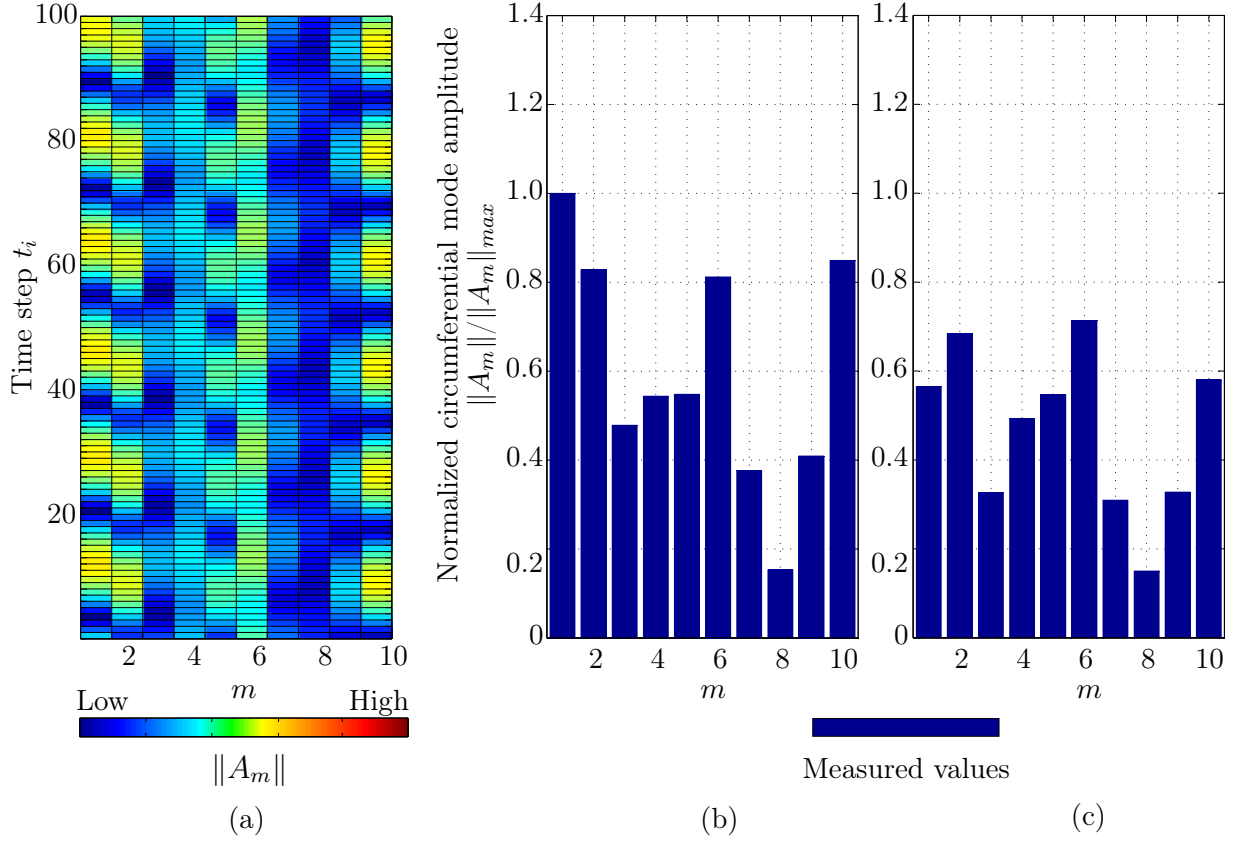
(a) (b) (c)

Figure A.8: Time variation of the circumferential mode amplitudes $\|A_m\|$ for selected time steps and mode orders (a). Normalized circumferential mode amplitudes $\|A_m\|$ with respect to $\|A_m\|_{max}$ for (b) maximal $\|A_m\|$, and (c) average $\|A_m\|$ over all time steps. Results correspond to the data recorded by microphone 4 about $f_{2\mathrm{BPF}} = 3500$ Hz

Figure A.9: Time variation of the circumferential mode amplitudes $\|A_m\|$ for selected time steps and mode orders (a). Normalized circumferential mode amplitudes $\|A_m\|$ with respect to $\|A_m\|_{max}$ for (b) maximal $\|A_m\|$, and (c) average $\|A_m\|$ over all time steps. Results correspond to the data recorded by microphone 5 about $f_{2\text{BPF}} = 3500$ Hz
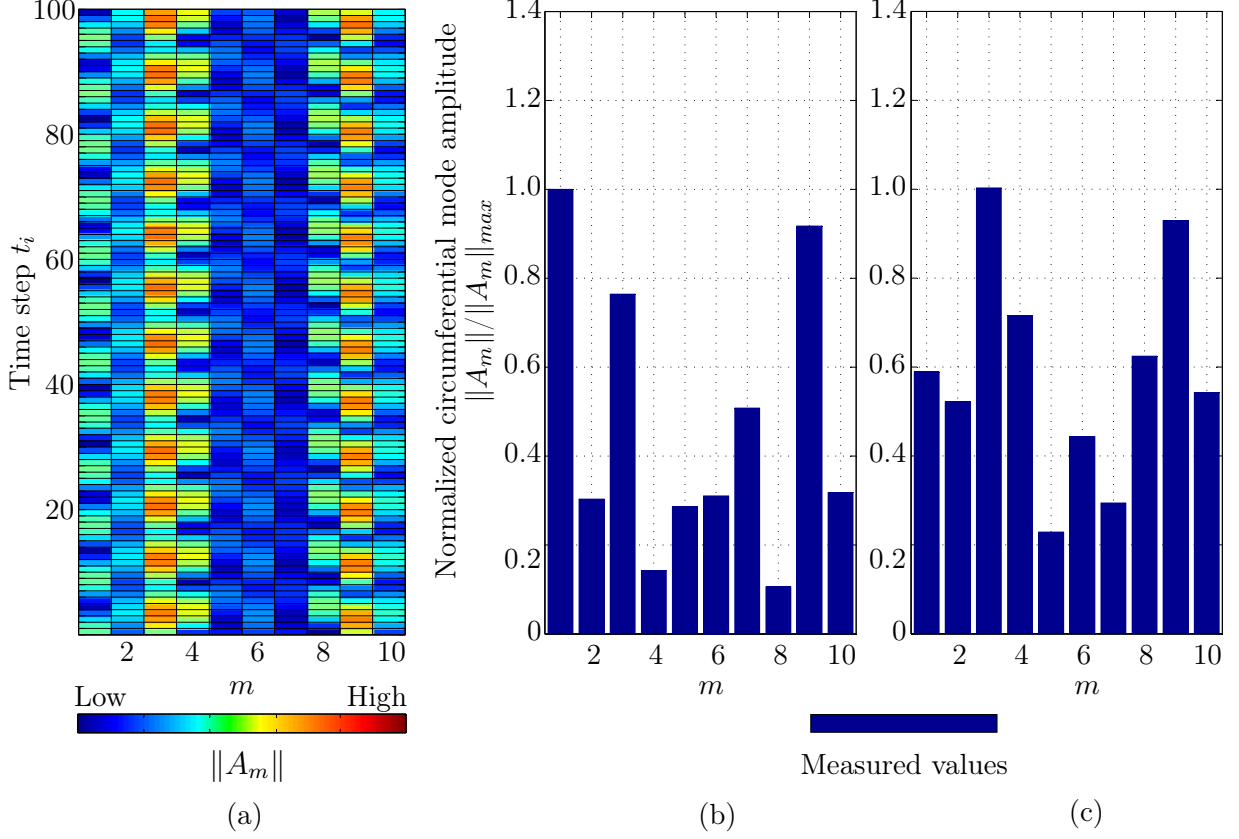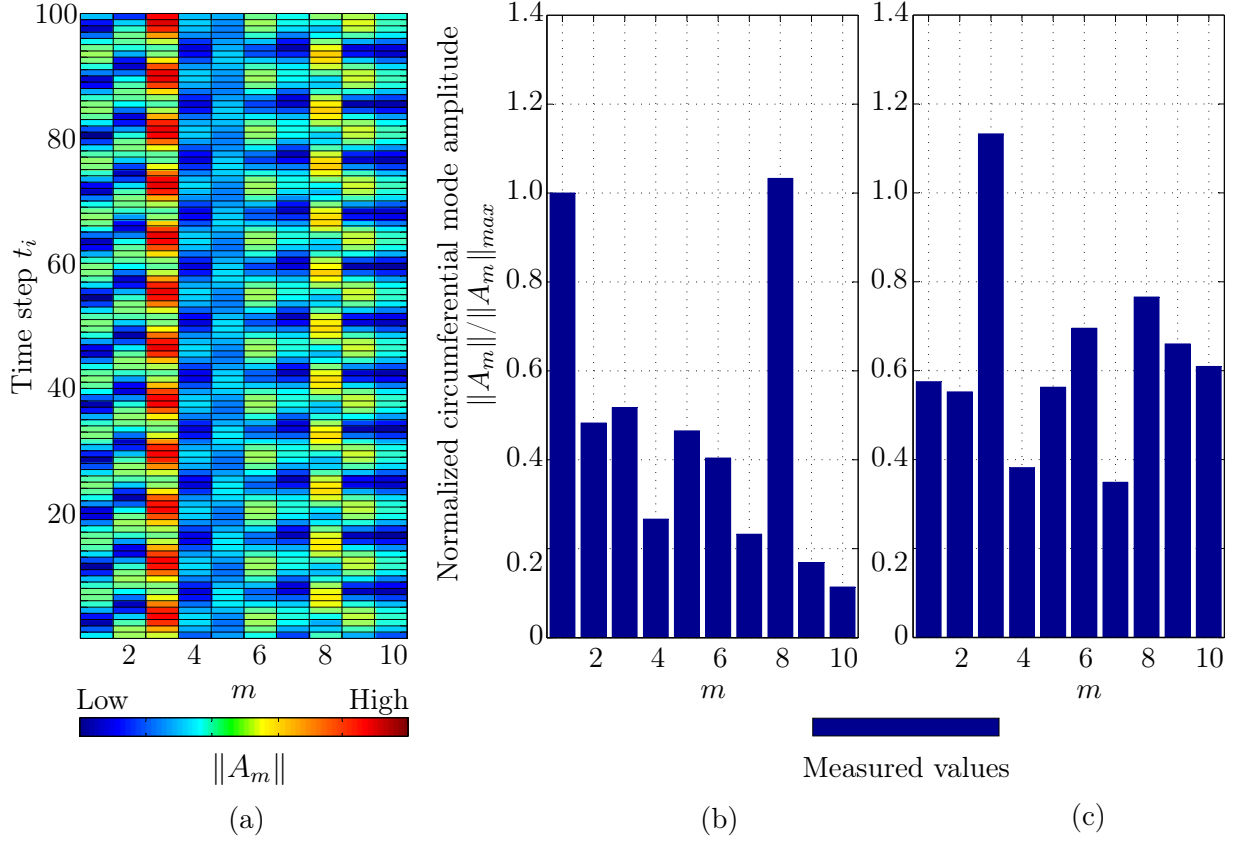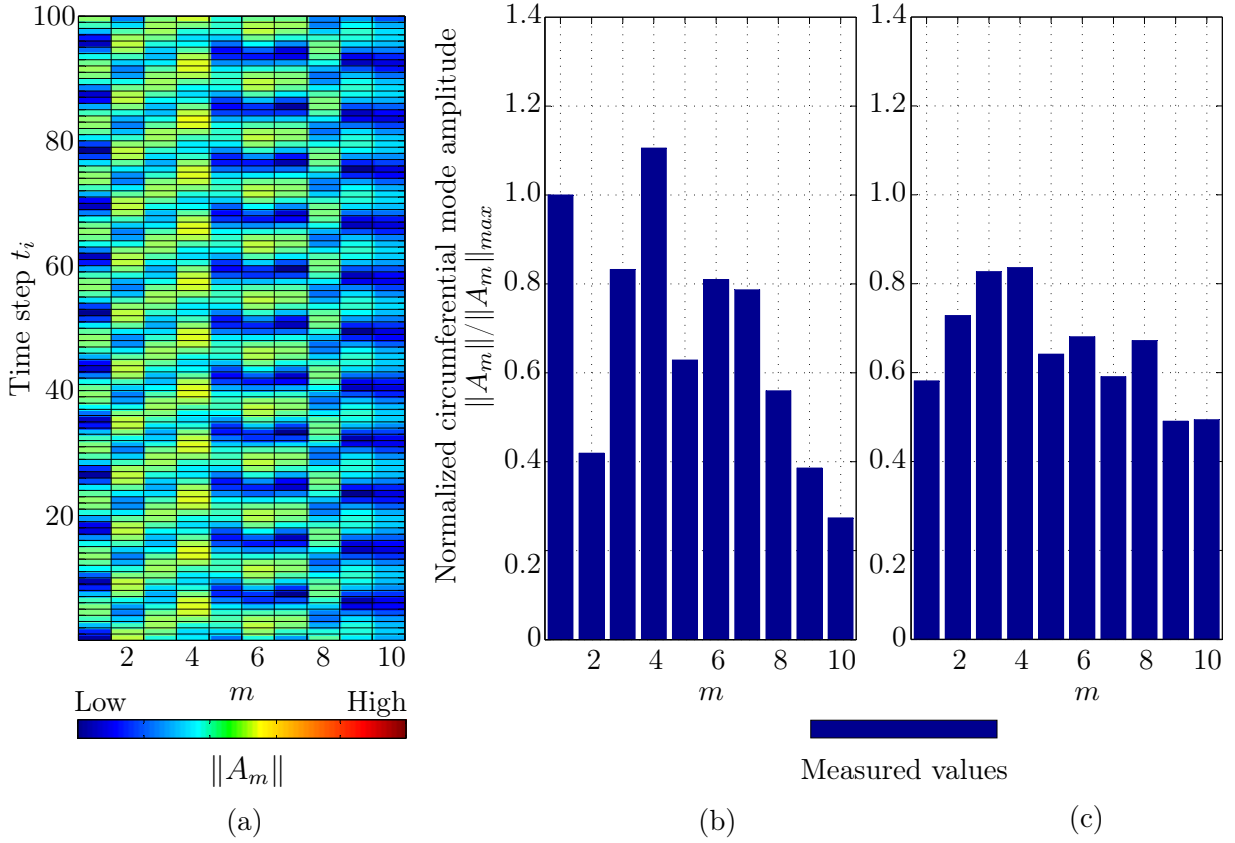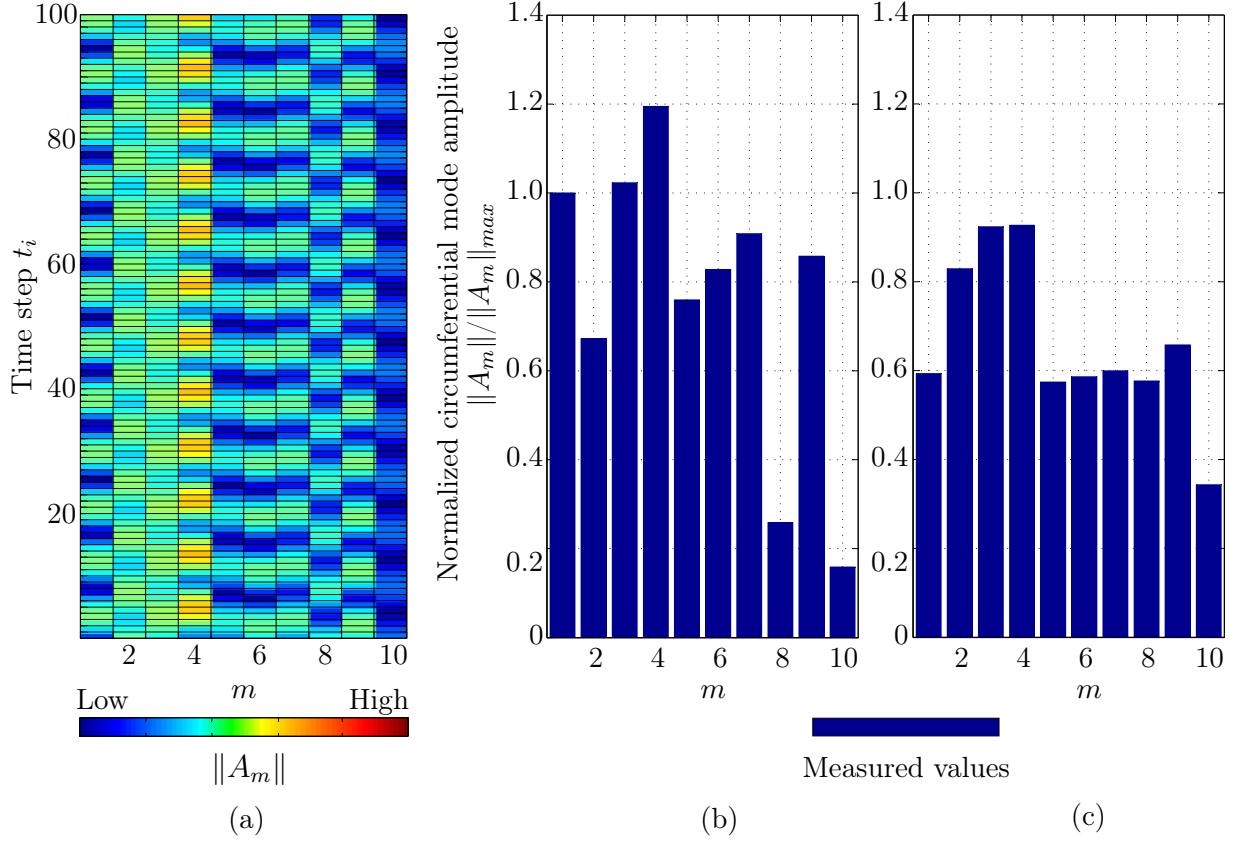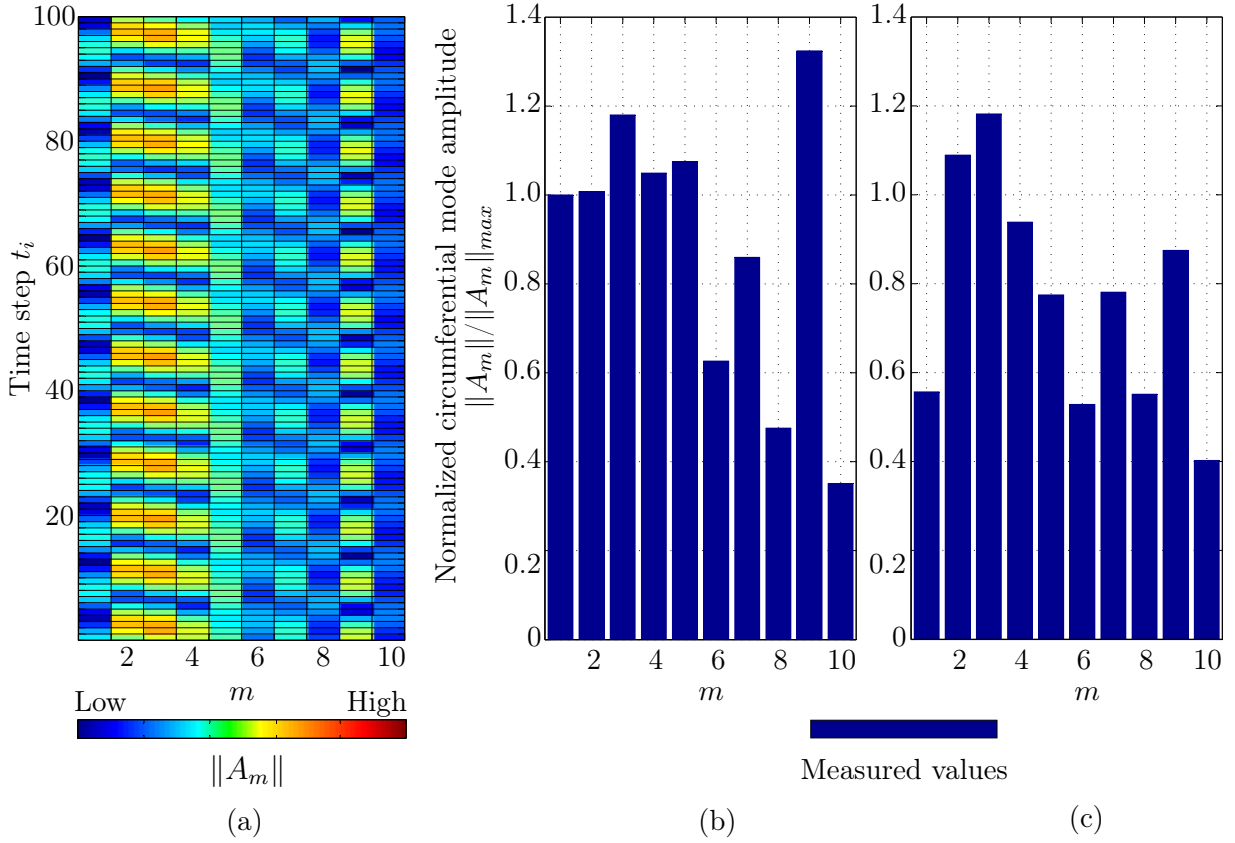
Figure A.10: Time variation of the circumferential mode amplitudes $\|A_m\|$ for selected time steps and mode orders (a). Normalized circumferential mode amplitudes $\|A_m\|$ with respect to $\|A_m\|_{max}$ for (b) maximal $\|A_m\|$, and (c) average $\|A_m\|$ over all time steps. Results correspond to the data recorded by microphone 6 about $f_{2\text{BPF}} = 3500$ Hz

A.3 Microphone ring - Design details

The study of sound transport in a LPT required within the frame of this work the development of a measurement concept. As such, a measurement unit, integrated into the LPT flow channel was designed and constructed, this being one of the main objectives of the current work. General details related to the measurement unit were already presented in Chapter 4. In this regard, the current section complements the information presented in Chapter 4 by going further into the engineering design of the measurement system.

Following (Laguna et al. 2012) and as already indicated in Sec. 4.2.1, an important aspect defining the development process of the microphone ring was related to the air turbine type of design. The TFD air turbine test-rig is constituted by two half segments, one fixed and one movable, and a rotor manufactured as a single steel component. Based on the aforementioned design characteristics and for easiness of installation and assembly, the microphone ring was designed and subsequently manufactured in two half segments, as shown in Fig. A.11.

Each half section of the designed microphone ring is constituted by an internal half annular segment coupled to an external ring, as illustrated by Fig. A.11. As can be seen, the external ring is fixed to the turbine housing, while the internal ring is free to rotate within the flow channel. In order to ensure this free rotation, flat single-row bearing cages with bearing rollers from the company Schäffer Technologies & Co were used (model reference FF2010). The needle roller bearings were placed within two parallel rectangular grooves with a cross section of 20 mm x 3 mm, milled around the inner ring sides (cf Fig. A.11(a)). Detail A clarifies the position and function of the needle roller bearings. As required, the system was rotated during turbine operation by means of an external system located outside of the turbine flow channel. The rotation was accomplished by a transmission mechanism constituted by a bevel gear wheel fastened to the inner ring front side and a drive shaft guided through the turbine housing to the outside. The external ring had a width of 193 mm and precisely fitted between the outer ring blade and vane carriers, as also shown in Fig. A.11(a). The internal section of this ring was constituted by a hollow segment of 163 mm in width and 10.5 mm in depth, allowing the movable inner ring to fit in. The internal ring was in turn equipped with four interchangeable aluminum carrier plates, allowing the installation of acoustic instrumentation, as shown in Figs. A.11(b) and A.11(c).

As previously indicated in Sec. 4.2.1, the installation and operation of the microphone ring inside the turbine flow passage derived in a number of complex technical requirements. These technical requirements included the design and operation of an external transmission mechanism, the selection and installation of measurement microphones as well as issues related to the electrical supply and cable leading-out of the microphones. Each one of the listed items will be now separately treated in detail, starting with the implementation of the measurement microphones.
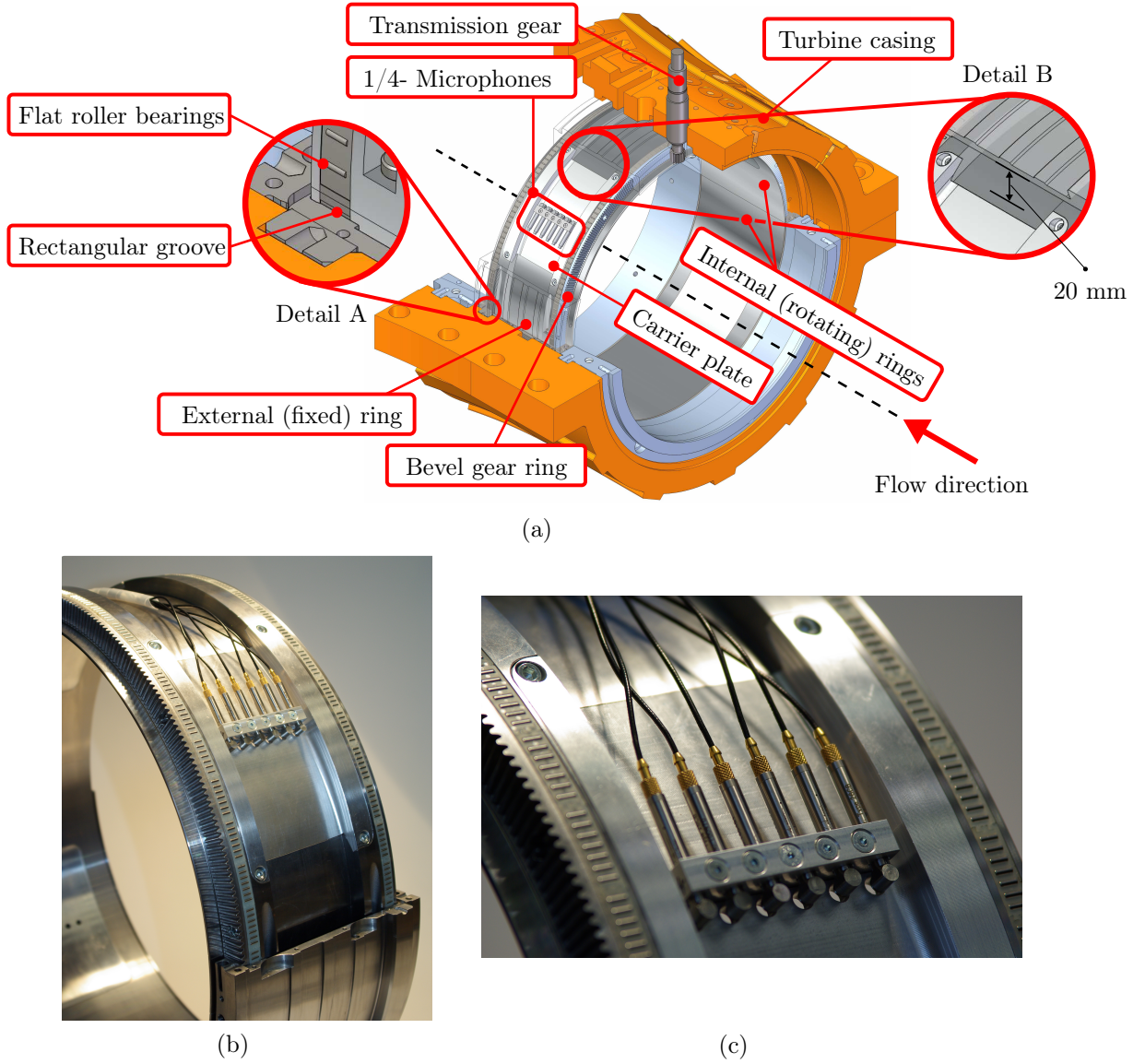
Figure A.11: Microphone ring, (a) microphone ring set-up, (b) assembled set-up, and (c) detailed view of the instrumented plate, adapted from Sec. 4.2.1

Implementation of the measurement microphones   The microphones were an essential part of the measurement ring. Its integration within the air turbine was complex due to the limited space available for their installation, as illustrated by the cross-sectional area shown in the Detail B of Fig. A.11(a). In this regard, the region between the carrier plate and the outer microphone ring was very narrow, with a vertical distance measured at the center point of the plate of 20 mm. In this way, the microphone selection was constrained to sensors having a maximal length of 20 mm including all required components, i.e., measuring microphone, preamplifier and cable. Before presenting the selected microphone that conformed to the technical requirements demanded for installation within the turbine, some general aspects regarding measurement microphones are discussed.

High quality acoustical measurements are performed with condenser type microphones, leading to the choice of this sensor type for the intended acoustical studies. Condenser microphones consist of two parallel plates, featuring a tensioned metal membrane and a rigid metal backplate (cf. Fig. A.12). The parallel plates act as a capacitor, with the backplate being electrically charged either externally by means of a power supply (externally polarized) or internally through a charge-holding electret material on the back plate (prepolarized). Once the membrane vibrates as a result of a change in the surrounding sound pressure field, the capacitance varies resulting in an output voltage. In this way, the condenser microphone acts as a transducer, converting the pressure variations acting on the tensioned membrane in an electrical signal, represented by a voltage variation sensed on a platted terminal attached to the microphone backplate. Once the electrical signal is generated by the transduction process, it needs to be acquired and then recorded in a computer, which is normally placed away from the microphone. Due to the microphone high electrical impedance, the necessary load made up by the sensor and the cable connecting it to the data acquisition system cannot be resisted by the microphone itself. As a consequence, a preamplifier is required, a device which besides minimizing the microphone and cable combined load, allows the use of long cables.
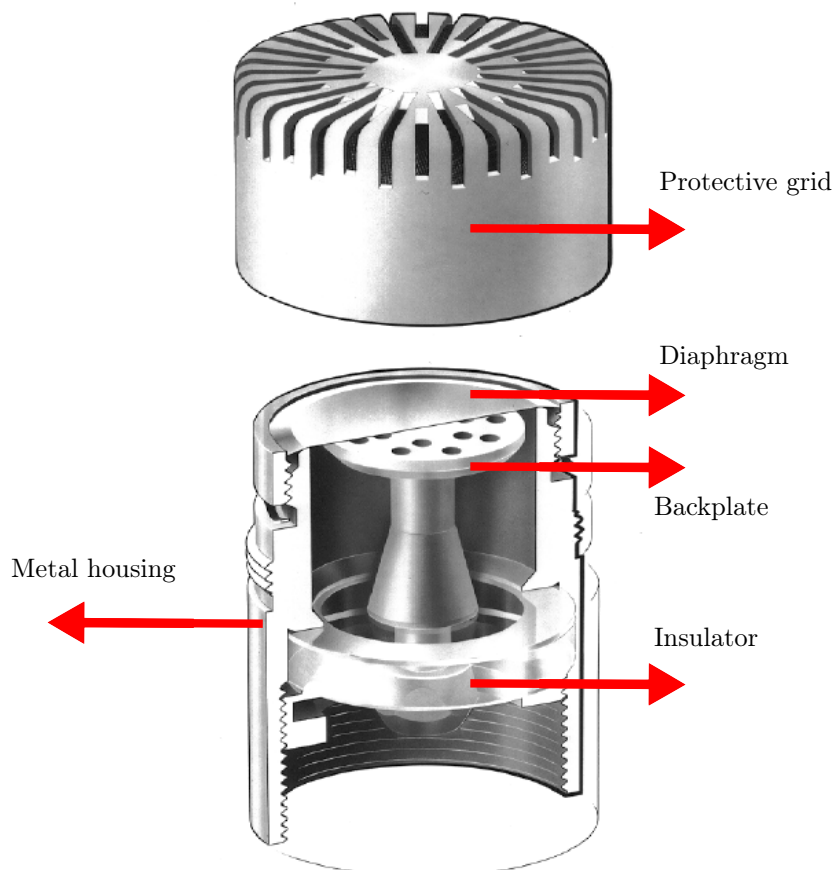

Figure A.12: Classic design of a condenser measurement microphone, adapted from Brüel&Kjaer (1996)

A Appendix

The preamplifier converts the microphone high output impedance into low impedance, allowing the transduced sound pressure signal to be recorded via a data acquisition system. Measurement microphones are actually delivered in pre-assembled sets, in which the microphone capsule and preamplifier are integrated as a unit. This combination ensures the best possible sensor response characteristics as well as a common sensitivity, normally expressed in units of millivolt per Pascal (mV/Pa). Microphone sets are designed to respond to different sound fields. Accordingly, they are further classified in free-field, pressure and random-incidence microphones. Free-field microphones respond best to an acoustic field in which waves freely propagate, away from reflecting or disturbing surfaces. Pressure-field microphones are mainly employed for measurements of the sound pressure within closed geometries and at boundaries or walls. On the other hand, for diffuse acoustical fields, in which sound waves do not have a defined direction of propagation but instead simultaneously arrive from several directions as a result of hard reflecting walls, random-incidence microphones are used. The physical size of the microphone is in turn associated with the type of acoustic field. As a consequence, microphones may also be grouped according to the size of the external diameter of the microphone capsule, with sizes as small as 1/8" (3.175 mm) and 1/4" (6.35 mm) up to 1/2" (12.70 mm) and 1" (25.40 mm). Small microphone dimensions represent a particular advantage for measurement in confined spaces. Based on this argument, six 1/4"–high temperature prepolarized pressure field microphones sets Type 46BD from the manufacturer G.R.A.S. Sound and Vibration© were chosen. The Type 46BD microphone set consists of a 1/4" high-frequency pressure microphone cartridge Type 40BD and a 1/4" preamplifier Type 26CB-S10, a special version of the Type 26CB. The preamplifier was electrically modified through an aging process in an attempt to reach an operating temperature of at least 120°C (the nominal operating temperature of the device is restricted to 60°C according to the manufacturer). Representative diagrams as well as photographs regarding the described measurement microphone set are displayed in Fig. A.13.
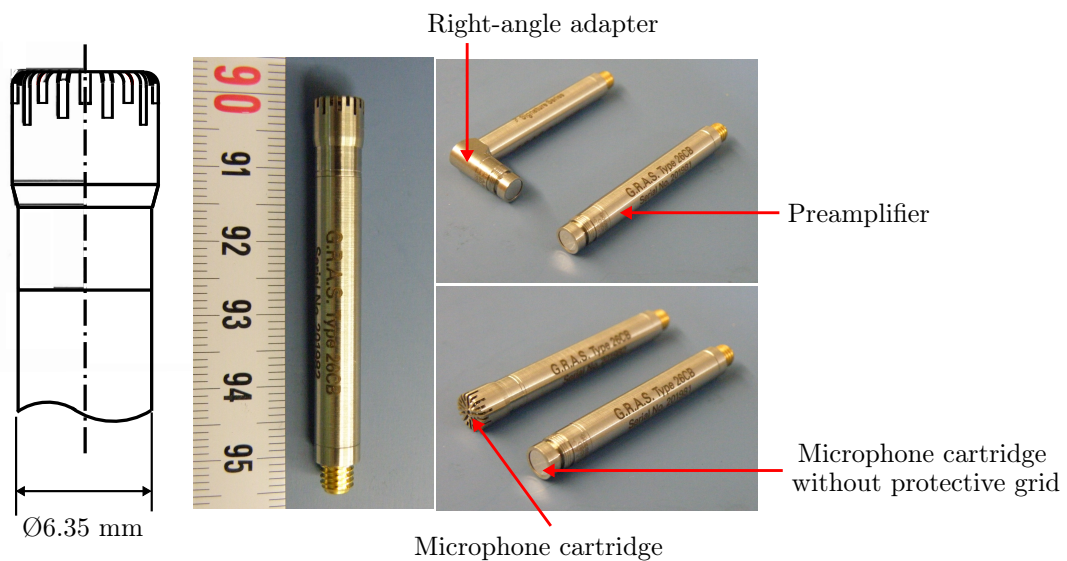

Figure A.13: Measurement microphone set Typ 46BD, adapted from Sec. 4.2.1

The microphones were axially flush mounted on one of the interchangeable aluminum carrier plates, thus not altering the in-duct prevailing flow field. Although the microphone set length exceeded the 20 mm vertical distance between the plate and the outer ring (with a overall length of 54.5 mm including microphone capsule and preamplifier), the microphone set was horizontally placed and flush mounted on the plate wall by means of a right-angle adapter, cf. Fig. A.13. The acoustical sensor selection was not solely based on dimensional issues but also on performance specifications. Regarding this point, several considerations were taken into account and are detailed below:

1. Acoustic and electrical performance

   a) Frequency response

      A wide as well as a flat frequency response was preferred. The chosen microphone has a broad frequency operating range, from 4 Hz to 70 kHz, with an almost flat response (0 dB) up to 20 kHz as shown in Fig. A.14. The frequency response was appropriate for the in-duct sound propagation studies of the tonal noise components, since the expected f_{BPF} amounts to 3750 Hz (rotational speed of 7500 min^{-1} and 30 rotor blades). Higher harmonics of the f_{BPF} were also of particular interest, however, these f_{BPF} multiples generally exhibit low tonal noise amplitudes. As a result, tonal noise components of maximal 18750 Hz are contemplated (4th harmonic of the f_{BPF}).
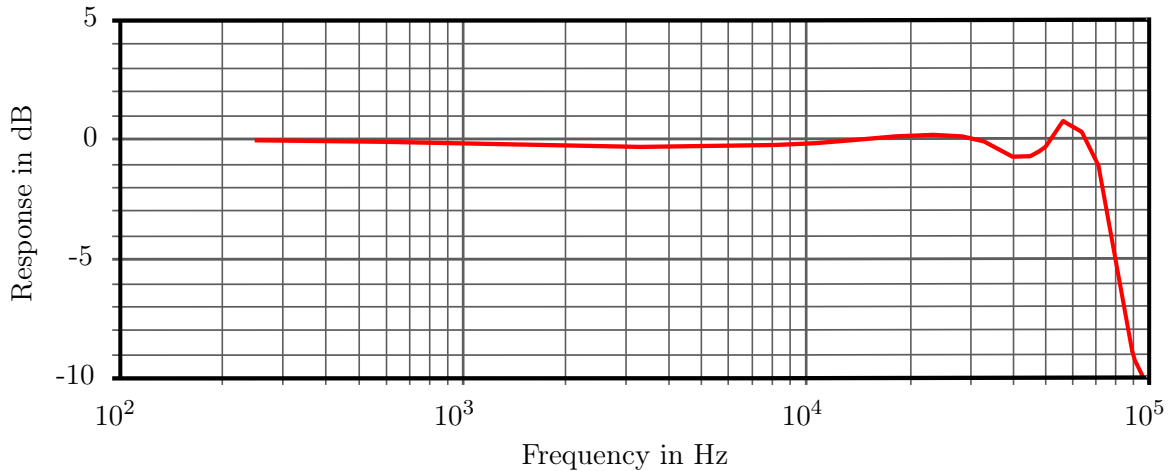
Figure A.14: Frequency response from a G.R.A.S. 46BD microphone set, adapted from G.R.A.S (2014)

   b) Linear dynamic range

      A further item defining a suitable acoustic performance is related to the microphone linear dynamic range. The dynamic range is specified by the difference between the highest and lowest measurable sound pressure levels that the microphone is able to detect. For the chosen microphone, a dynamic range varying between 44 dBA and 165 dBA was specified.

The upper limit of the dynamic range was considered to be important for the sensor selection, since sound pressure levels within the air turbine were expected to exceed 90 dB. To verify this assumption, a Brüel & Kjaer microphone Type 4189 was flush mounted 450 mm away from the turbine inlet. The sensor recorded the varying sound pressure during 10 s for three different rotational speeds, 2100, 3500 and 3650 min^{-1}. Afterwards, the Root Mean Square (RMS) of the time signal was determined, value finally used to compute the corresponding sound pressure level. The results are presented in Fig. A.15. Sound pressure levels up to 115 dB were measured, justifying the microphone selection. Unfortunately, higher rotational speeds were not achieved once the described measurement was performed, hindering a thorough study of the awaited turbine noise levels. Nevertheless, noise levels beyond 140 dB are not anticipated, based on previous studies.
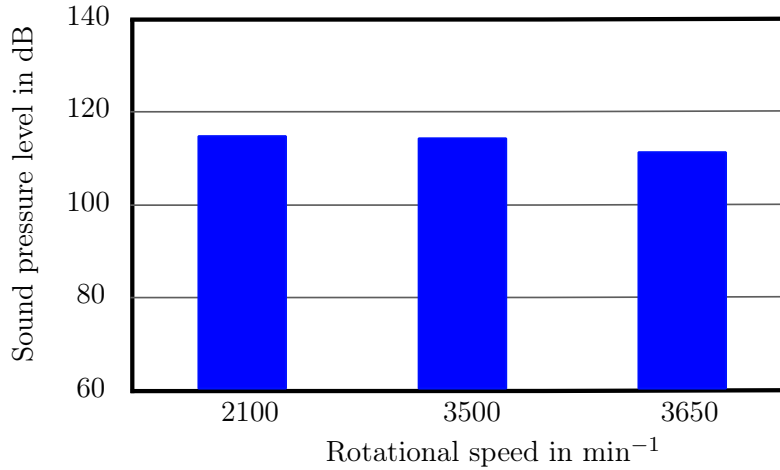
Figure A.15: Sound pressure level detected by the measurement microphone at different rotational speeds

2. Measurement environment influence

   a) Temperature influence

   The original microphone set is able to withstand temperatures up to 60°C as claimed by the manufacturer. This temperature restriction is imposed by an integrated memory circuit built into the preamplifier, the **T**ransducer **E**lectronic **D**ata **S**heet, abbreviated TEDS. The circuit stores the transducer characteristics, including manufacturer name, sensor type, model number, serial number, and calibration data, however, it is limited to operate up to 60°. Recalling that the microphone ring was installed behind the turbine blades, a flow temperature below 180°C was expected at this location (cf. Tab. 4.1). The turbine outlet temperature reaches a maximum value of 120°C at the nominal operating point, preventing however the adequate usage of the microphone sets. As such, the preamplifiers had to be modified in order to be able to operate within this environment.

According to G.R.A.S, the microphone manufacturer, besides damaging the TEDS chip, the microphones would gradually lose some of its sensitivity when continuously operated or stored at 120°C. To corroborate this statement, and after electrically modifying the amplifier, a series of tests were carried out at the company headquarters in Denmark. Six new microphone sets Type 46BD were initially calibrated and then exposed to cyclic temperature variations. The microphones were placed in a temperature-controlled chamber and subjected to 10 cycles of temperature variations from 23°C to 120°C. The temperature increase and decrease rate was set to 4 °C/min. After reaching 120°C, this temperature was maintained for one hour. Down to 23°C, the temperature was kept constant at this value for 20 min before beginning a new cycle. Once the ten temperature cycles were completed, the sensitivity of each microphone was determined (Test A). Ten additional cycles were performed and the sensitivities were measured again (Test B). The reported results are shown below in Fig. A.16.
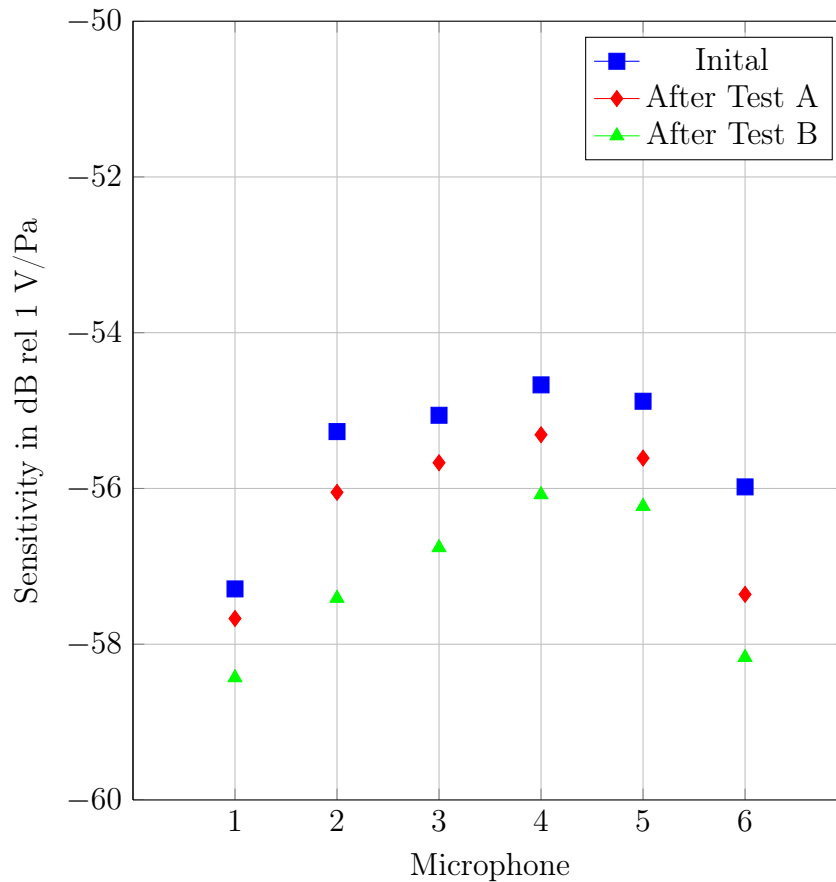

Figure A.16: Sensitivity change after two cycles of temperature exposure of 120°C of the microphone set G.R.A.S 40BD

The exposure of the microphones to cyclic temperature variations and prolonged periods of time at 120°C results in a change of sensitivity of less than 1 dB. As a result, the measurement under high temperature conditions is considered to be well performed by the chosen microphones.

b) Pressure influence

According to Tab. 4.1, a maximum pressure ratio of 1.3 was expected to prevail within the turbine inner housing during operation. Such pressure levels are excessive for a condenser microphone due to the fairly small static pressure difference that can be withstood between the front and the rear side of its membrane. For this reason, condenser microphones are equipped with rear or side vented static pressure equalization channels located on the preamplifier or at the microphone housing side, respectively. The latter variant was preferred for the chosen microphones (cf. Fig.A.17). Wall flush mounted sensors, as in this case, are typically subjected to large static pressure differences existing between the inside and the outside of the turbine flow channel.

Pressure equalization
vent
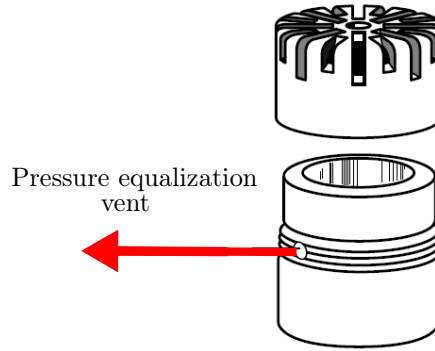
Figure A.17: Static pressure equalization - Side vented microphone

Having discussed various technical features related to the microphone selection, a summary of performance specifications of the employed microphone sets is shown in Tab. A.1. Figure A.18, directly below Tab. A.1, displays the microphone distribution on the aluminum plate. Two aspects of the Fig. A.18 and Tab. A.1 are highlighted. The first one is related to the microphone separation. A constant axial spacing of 20 mm between each acoustic sensor was chosen. This choice was based on two reasons. In the first place, only a limited number of microphones - six, to be more exact - could be equidistantly positioned over the plate, due to a prescribed maximum plate width of 100 mm. Second, the 20 mm gap resulted from an optimization study which evaluated the sensor arrangement dependence on the results of the Singular Value Decomposition (SVD). As previously stated in Chapter 3, the SVD is the factorization of a real or complex matrix (Press et al. 2007). The pseudoinverse of the factorized matrix computed by means of the SVD can be used to analytically determine the radial mode amplitudes A_{mn} of the turbine propagating sound field (Tapken and Enghardt 2006).

The optimization determined an optimal positioning range of 16 to 21 mm between microphones for chosen acoustical modes (Ioannou 2012). Further details related to the SVD algorithm for the optimization of microphone measurement positions are found in Nelson and Yoon (2000) and Yoon and Nelson (2000). Additionally, the role played by the SVD in the Radial Mode Analysis was further analyzed in Chapter 3 of the present document.

Table A.1: Technical characteristics of the measurement microphone sets

Microphone set number	Sensitivity in mV/Pa	Frequency range	Temperature range
1	1.08	4 Hz - 70 kHz	-30 to 60°C
2	1.01	4 Hz - 70 kHz	-30 to 60°C
3	1.00	4 Hz - 70 kHz	-30 to 60°C
4	1.26	4 Hz - 70 kHz	-30 to 60°C
5	1.13	4 Hz - 70 kHz	-30 to 60°C
6	1.40	4 Hz - 70 kHz	-30 to 60°C
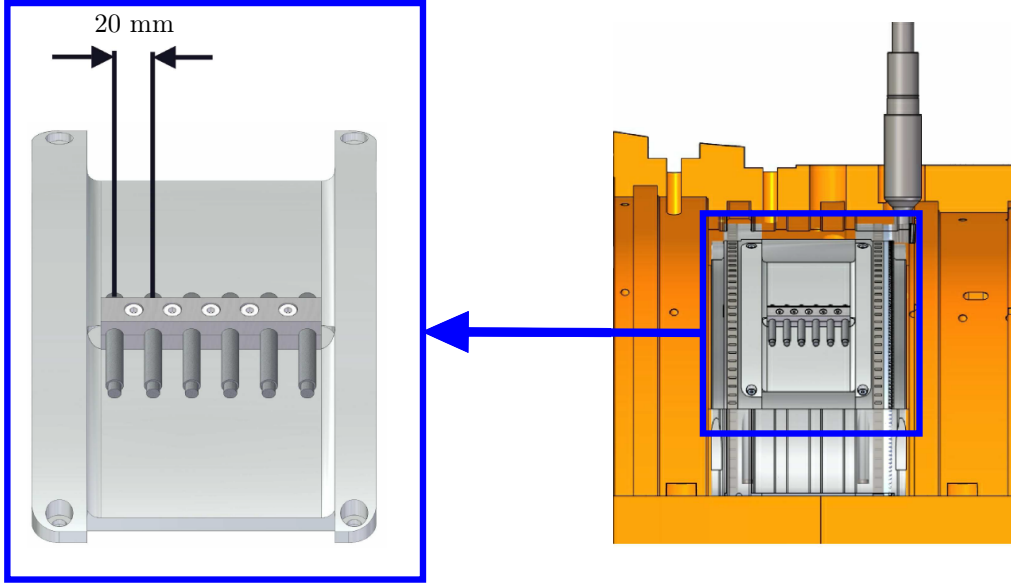
Figure A.18: Technical characteristics of the measurement microphone sets

The second noticeable aspect of Tab. A.1 is associated with the microphones calibration. Displayed are the actual instrument sensitivities. Before being installed in the aluminum plate, each microphone was calibrated with a sound pressure calibrator. The calibrator generated a sound pressure of 94 dB at a single tone frequency of 1000 Hz. The sound pressure output of the microphone was compared

to that generated by the calibrator and correspondingly corrected. The process was performed with the portable calibrator Type 4231 from the company Brüel & Kjaer. In general, the chosen microphones sensitivities are relatively low, varying between 1 mV/Pa and 1.3 mV/Pa, thus allowing higher sound pressure levels to be measured.

Closing with the microphones calibration procedure and having previously defined the appropriate measurement instruments based on either spatial and technical performance restrictions, a further aspect is discussed, namely, the microphone ring external transmission mechanism. Regarding this point, details related to the design of the system are presented in the section to follow.

Microphone ring external transmission mechanism   As demanded by the general design concepts of the microphone ring, external control as well as rotation during turbine operation are required. To accomplish both tasks, an external transmission mechanism was designed, constructed and documented by Trenke (2012) in the context of the project Unsteady Work Optimized Turbine, UWOTurb, (Henke et al. 2012). The transmission was originally conceived to circumferentially displace a blade ring carrier installed within the turbine in order to study the influence of the stator blades flow wakes on the machine overall performance. The mechanism is conceived as a bevel gear transmission, allowing to tilt the rotation axes of the individual gear components perpendicular to each other (Wittel et al. 2013, Klingelnberg 2008). The driven bevel gear was fastened to the microphone ring itself, while being coupled and driven by the bevel gear shaft as shown in Fig. A.20. This arrangement turned to be advantageous for the current application, as the power required for the microphone ring angular adjustment was perpendicularly supplied through the turbine housing by the driving bevel gear.

The transmission mechanism was flexibly designed taking into account the following technical restrictions:

a) Compact design with a number of components as low as possible

b) The turbine must be sealed to prevent air flow leakage through the material removed from the outer housing to allow the installation of the external transmission components

c) As far as possible no modification of existing pneumatic probe holes or traversing grooves on the outer turbine housing, i.e., surrounding surfaces must remain undamaged due to mechanical treatment

d) Adjustable flank clearance, i.e., the whole external transmission must be able to be axially displaced in order to ensure a perfect gear coupling

e) The range of angular adjustment should cover a complete rotation, i.e., the microphone ring should be able to be rotated 360°
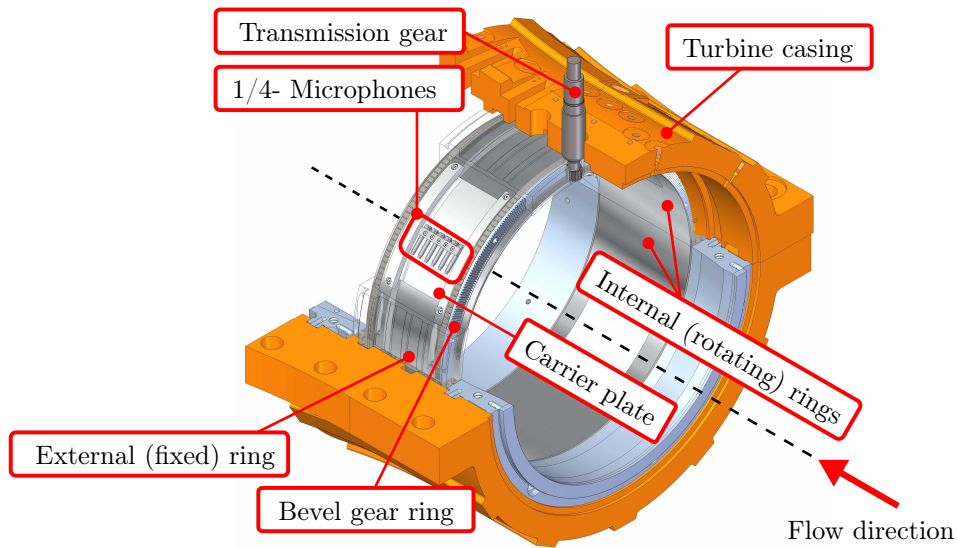
Figure A.19: Microphone ring transmission, adapted from Sec. 4.2.1

Complying with the aforementioned requirements, the result was a versatile mechanism, not only usable for the original UWOTurb project but also for the current research. Figure A.20 shows the design of the transmission mechanism mounted on the turbine housing. The transmission was fixed to a base plate located between the pneumatic probe holes and the traversing grooves.
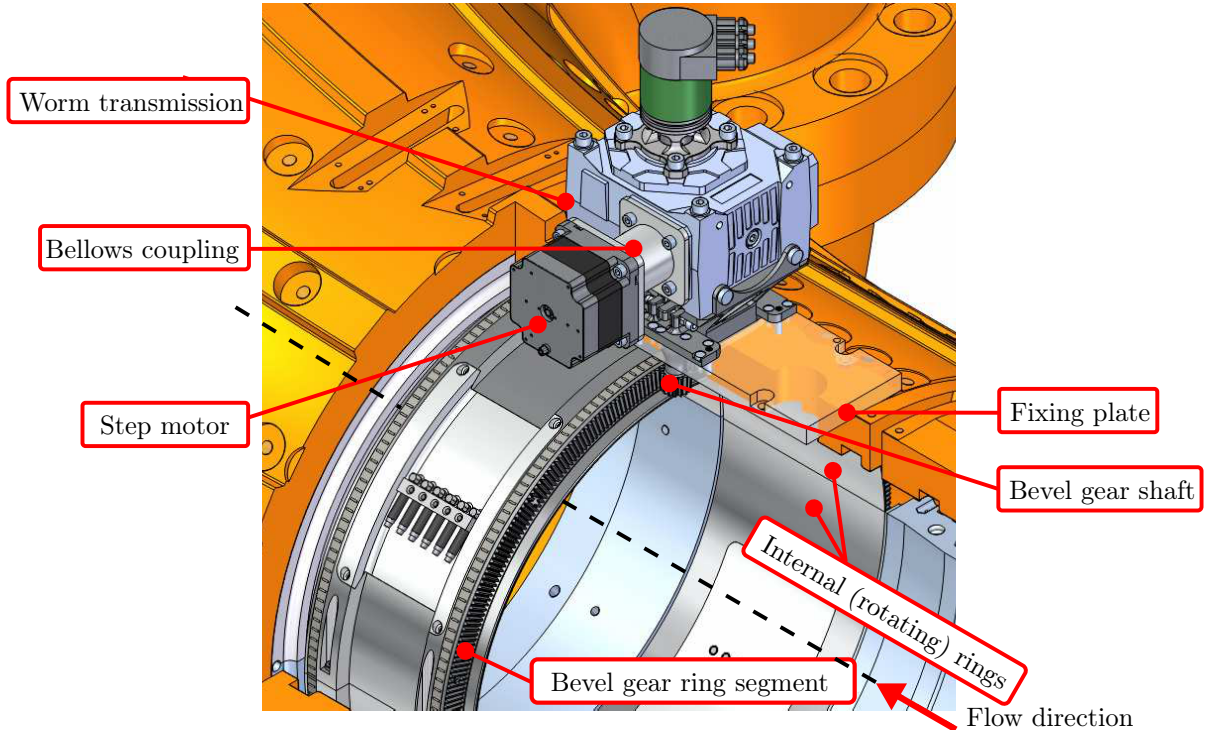
Figure A.20: External transmission mechanism, adapted from Sec. 4.2.1

The transmission mechanism was driven by a two-phase ISEL step motor model MS 300-HT connected to a worm drive by means of a bellows coupling, both components from the company Flohr Industrietechnik GmbH. The step motor was in turn driven by an external programmable controller, the ISEL iMC-S8 multi-axis controller. The controller converted and subsequently transferred all the commands programmed by the user in a LabVIEW$^{©}$ software driver into angular displacement and rotation direction signals for the connected step motor. In this way, the desired motor motion was first evaluated, executed and finally transmitted via the step motor directly to the worm drive. The worm transmission was in turn equipped with a hollow shaft into which the designed bevel gear shaft was inserted. The pinion shaft teeth were in turn coupled to two 180° bevel gear segments connected via M6 bolts to the in-duct integrated carrier system inner ring. In the remainder of this section, the main components of the transmission unit are presented along with brief technical specifications.

a) Driven bevel gear

The manufacturing of a single-piece, 360° bevel gear, was not feasible because of fabrication reasons. On the one hand, the available space in the inner microphone ring for the installation of the bevel gear could not be exceeded. The available room was restricted to a cross section of 20 mm x 20 mm, resulting in a relative slender gear transverse profile prone to bending during the manufacturing process. On the other hand, because of those possible deformations, an adequate placement of the whole segment into the inner ring side could not be guaranteed. To avoid possible complications resulting from the aforementioned situations, the driven bevel gear was manufactured in two 180° segments. Each segment was manufactured with the quenched and tempered alloy steel 42CrMo4 and was fastened via five M6 bolts to the inner microphone ring side. The positioning of the half-segments was performed as well with the M6 bolts. The screw holes were located on a circle of 500 mm diameter.

b) Bevel gear shaft

The bevel gear shaft transmitted the necessary power for the microphone ring rotation once coupled to the driven bevel gear. As indicated before, this was done by fitting the bevel gear pinion into a hollow shaft in the worm transmission. The shaft had a diameter of 25H7 and a total length of 267 mm. It was manufactured in steel 31CrMoV9 and was nitrated after the machining process.

c) Two-phase step motor

The microphone ring angular positioning required a controlled power transmission. A step motor was therefore appropriate for several reasons. Step motors, on the one hand, can be programmed to turn by very precise angles, resulting in accurately positioning and repeatability of movement. On the other hand, they are able to provide high torque at low speeds, are easy to control and highly reliable.

The step motor chosen for the present application was the ISEL MS HT-300 (Trenke 2012). It rotated at 1.8° step angles, thus performing a complete revolution in 200 steps. The step motor choice was based on two reasons. First of all, due to the precise positioning provided by the step motor, a fine circumferential traversing resolution was achieved. For the current research, the microphone ring was traversed with an angular resolution of 1°. A second argument supporting the selection of the step motor is its ability to overcome a starting torque of 1.25 Nm required to rotate a blade ring carrier, being this the reason for which the transmission was originally conceived (cf. Trenke (2012)). However, as the microphone ring was not subjected to any incident flow, no aerodynamic moments needed to be overcome by the transmission, except for the moment generated by the friction as a result of the contact of the outer microphone ring with the needle roller bearings installed on the inner ring. Nevertheless, the specified starting torque of the step motor was sufficient for the current application. The step motor is shown in Fig. A.20 along with further associated technical data.

d) Worm-gear transmission

In order to guarantee a precise and reliable power transmission for the angular positioning of the microphone ring, a large gear reduction was needed. For this purpose, a worm drive was used. The selected unit corresponded to the frame size model 045 manufactured by the company Flohr Industritechnik GmbH. The transmission was delivered as a compact unit with a gear ratio $i = 30{:}1$ and a turning precision inferior to one arc minute (one sixtieth of a degree). The worm drive was fixed to a structural carrier, which was in turn secured to the base plate mounted directly on the turbine housing. The worm transmission is shown in Fig. A.20.

Having presented and detailed to some extent the external transmission mechanism for the microphone ring rotation, it can be pointed out, that the measurement concept including both systems allowed the detection of higher propagating acoustical modes with a minimum number of spatially distributed microphones. By accomplishing a complete ring rotation with a resolution of 1° and simultaneously acquiring the sound pressure variation with six flush mounted microphones, a total of 179 circumferential modes can be measured. Additionally, the measurement system is able to decompose radial mode orders up to $n = 2$ (considering upstream and downstream propagating modes) or $n = 5$ (including only downstream modes). Radial orders exceeding the specified limits lead to a undetermined system of equations (cf. Chapter 3). Since six axial measurement positions are available (cf. Fig. A.18), one azimuthal mode amplitude $A_m(x_i, r)$ per axial position can be calculated through the RMA. This allows the determination of the upstream and downstream radial modes $A^{\pm}_{[m,0]}$, $A^{\pm}_{[m,1]}$ and $A^{\pm}_{[m,2]}$ or the downstream radial modes $A^{+}_{[m,n]}$ with $n = 0...5$.

Before proceeding with the specification of the general measurement scheme employed in the context of the performed acoustical measurements in the TFD multi-stage air turbine, some issues regarding the microphones electrical supply as well as the cable leading-out from the microphone ring are briefly discussed in the following section.

Microphones electrical supply and cable leading-out   As aforementioned, only one of the four aluminum plates attached to the microphone ring was instrumented. The initial angular position of the instrumented plate when integrated into the turbine flow channel is shown in Fig. A.21. As seen on the associated detail view, the microphones were located at a 45° angle with respect to the parting line separating both turbine outer housing segments. Starting from this position, the inner microphone ring and consequently, the instrumented plate, rotated clockwise. The ring clockwise rotation implied a simultaneous angular translation of the microphones and the cable needed to supply power to them as well as to acquire the measured data.
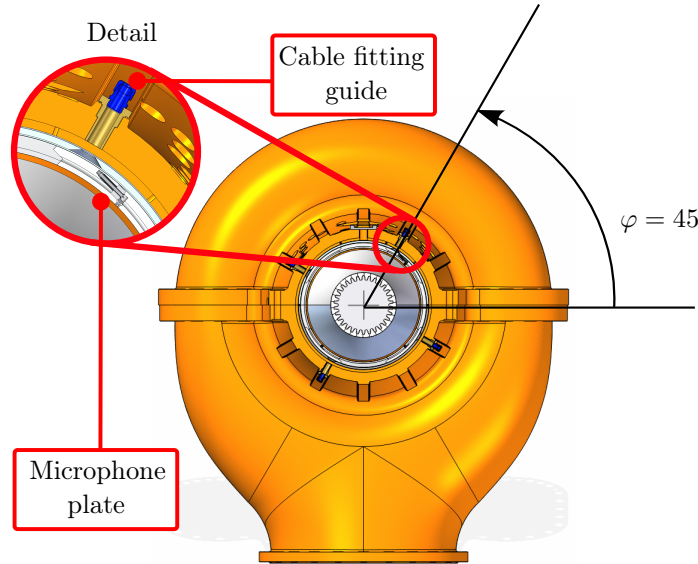
Figure A.21: Position of the instrumented plate and cable fitting guide

The position of the cable during the rotation of the inner microphone ring segment was a matter of great concern, because if not properly controlled, could have resulted in its breaking due to exceedingly high tension or excessive kinking. To avoid this potential situation, the condenser microphones were supplied with flexible Microdot-BNC 10 m cable. A cable segment of 800 mm was inserted between the inner and outer microphone ring segments. One end was connected to the microphones while the other end was attached and secured to the lower turbine casing by means of a cable fitting as shown in Fig. A.21. Once the rotation began, the microphones pulled the cable out, but with enough cable length inside the inner ring groove, no tension was exerted by the moving microphones during the whole system rotation.

Having covered all the details related to the microphone ring installation and operation, the section to follow handles a key aspect of the performed aeroacoustical experiments, namely, the general measurement scheme.

Included in this section are aspects related to the data acquisition devices, the instrumentation required for the determination of the turbine flow parameters during the experiments and a general overview of the control and measurement programs employed for the operation of the microphone ring.

A.3.1 Measurement scheme

After concluding the hardware implementation process, represented in the microphone ring design along with various related topics including positioning, instrumentation and rotation, a further and key topic is yet to be discussed, namely, the measurement process.

This refers to the conceived measurement plan, i.e, the set of actions carried out to enable an appropriate data acquisition and control during the performance of the aeroacoustic experiments. Accordingly, the measurement process was separated in two different tasks which nevertheless needed to be simultaneously executed and perfectly synchronized.

The first measurement task dealt with the acquisition and recording of sound pressure signals and turbine operating variables. The second one was closely related to the external transmission control for the microphone ring rotation. Both tasks are (separately) handled in the sections to follow.

Data acquisition and recording

As stated in Sec. 5.2, sound pressure signals as well as turbine flow operating variables, including pressure, temperature and angular velocity were measured with a modular data acquisition system based on the PXI platform from National Instruments$^{©}$. This PC-based platform offered a high degree of performance and flexibility when it comes to the acquisition of analog signals.

High performance is achieved as a result of the integration of internal signal conditioning, high sampling rates and very high resolution; flexibility is attained as a consequence of the modular capabilities of the PXI system, capabilities represented in a broad spectrum of devices for the acquisition of specific physical variables.

A PXI system is composed of four elements, a chassis, a system controller, peripheral modules, and a software. An overview of a typical PIX data acquisition system is shown in Fig. A.22.
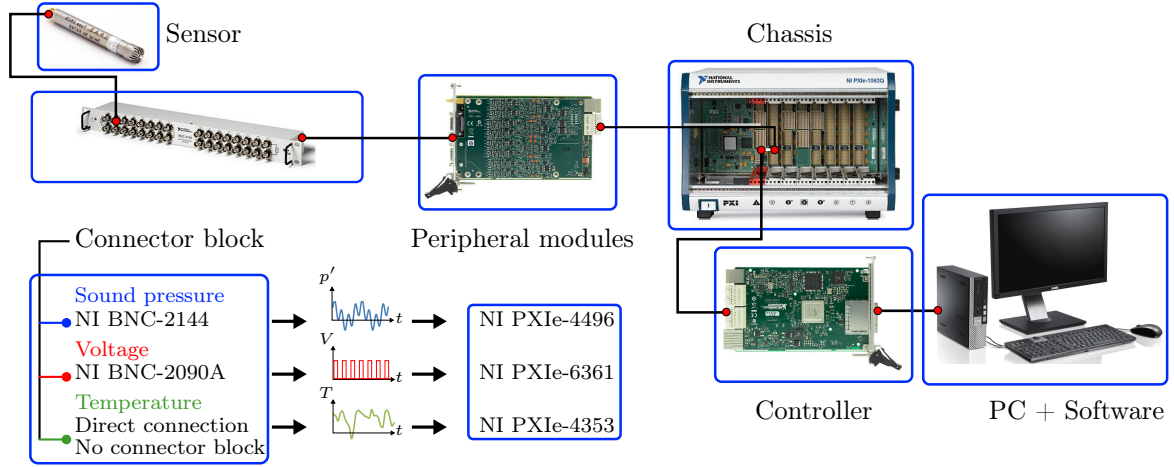
Figure A.22: PXI data acquisition system scheme, adapted from Sec. 4.2.2

The specification of the appropriate PXI system begins by knowing in advance the physical variables to be measured. For the present research, this specification resulted in the selection of three peripheral devices. On the one hand, a NI PXIe-4496 was chosen for the acoustic measurements. The device offers 16 analog input channels, sample rates per channel up to 204.8 kS/s, constant current signal conditioning for microphone power supply, a maximum working voltage of $\pm$ 10 V, and 24-bit resolution, accounting for signal voltage changes as low as 1.2 μV. On the the other hand, a NI PXIe-6361 module was chosen for the acquisition of voltage signals. The module has 16 analog input channels with a maximum sample rate of 2 Ms/s or 1 Ms/s when measuring with a single channel or more than one channel, respectively. The analog input is complemented by 2 analog output channels with an associated sample rate of 2.86 Ms/s, further 24 digital inputs/outputs and a 32-bit counter are provided. Both analog inputs and outputs support up to $\pm$ 10 V signals with a maximum 16-bit resolution. Finally, a NI PXIe-4353 module was chosen for temperature measurements via thermocouples. The module supports 32 thermocouple input channels with a maximum sample rate of 90 S/s pro channel.

Both analog/digital conversion (ADC) and data conditioning tasks were undertaken by the peripheral modules. But technically, the modules require a housing platform to fulfill both mentioned functions. Accordingly, each module is integrated into a chassis with separate slots and a backplane, which manages the PXI system's data, timing and triggering buses. The chosen chassis was the NI PXIe-1062Q, having eight slots in total. Four are intended to accommodate PXI-only architecture modules, one houses a PXI Express device and two are arranged for the insertion of PCI (technology preceding the PXI architecture), PXI or PXI Express modules, the so-called PXI Express hybrid slots. The remaining slot was reserved for the controller, a device which physically links the personal computer with the chassis, enabling the direct control of the integrated PXI modules.

The link was materialized by connecting a NI PCIe-8372 board in the PC with a NI PXIe-8370 module in slot 1 of the chassis. Furthermore, the practical PC-PXI module's interface was established by the software LabVIEW$^{©}$, which aside from providing an easy integration with the PXI hardware, also allowed the collection, analysis, presentation and storing of measurement data. An additional consideration before a measurement can actually be performed is hereafter discussed. Since the measurement instruments do not have a direct signal connectivity to the measurements modules, a connector block is required to act as an interface between both components. As such, three connector blocks were selected to comply with this requirement: the NI BNC-2144, which provided BNC connectivity up to 32 analog acoustical input signals and the BNC-2090A, a desktop/rack-mountable device with 22 BNC input jacks for connecting analog, digital, and timing signals. Additionally, the NI TB-4353 isothermal terminal block for direct connectivity with the NI PXIe-4353 module was also implemented.

The general measurement and data acquisition set-up for the sound propagation experiments is shown in Fig. A.23. The data acquisition and recording was effected by means of two desktop computers, each one associated with a PXI system. The system labeled "Acoustic PC" was in charge of recording all sound pressure signals. It also generated output digital signals for individually controlled excitation acoustic units via two 8-channel FPGA cards driven by a NI PXI-7854R multifunction module (c.f. Bartelt et al. (2013)) and recorded the varying output voltage of a Hall sensor for the quantification of the rotor angular velocity. The specific data acquisition devices and channel count are detailed in Fig. A.23. Additionally, the external transmission mechanism was controlled by the aforementioned computer via RS 232 serial port. This was accomplished by the iMC-S8 step controller from ISEL, a freely programmable controller for circular axes driven by 2-phase step motors. Further details regarding the step motor control are discussed in the following section.

The second computer, labeled "Turbine PC", was used for the acquisition of the turbine operating parameters. In this respect, the multi-stage air turbine test facility disposed of permanently installed and mounting-independent instrumentation outside the test stand itself. As shown in Fig. A.23, the referred instrumentation served to determine the ambient air conditions (pressure and temperature in front of the screw compressors inlet) as well as to quantify the mass flow by means of the venturi nozzle placed ahead of the turbine inlet, where static pressure and pressure difference were determined at the inlet and at the narrowest cross section of the nozzle, respectively. Turbine in-duct flow measurements were also performed in order to determine the inlet and outlet operating parameters. Both measurements were executed with 5-hole pneumatic probes equipped with a thermocouple, allowing the total pressure and total temperature quantification at the mentioned measurement positions (Binner 2011, Herzog 2008, Kang 2006).

The PXI system connected to "Turbine PC" acquired only the temperature data. The pressure data, however, was sampled by a series of rack-mounted pressure
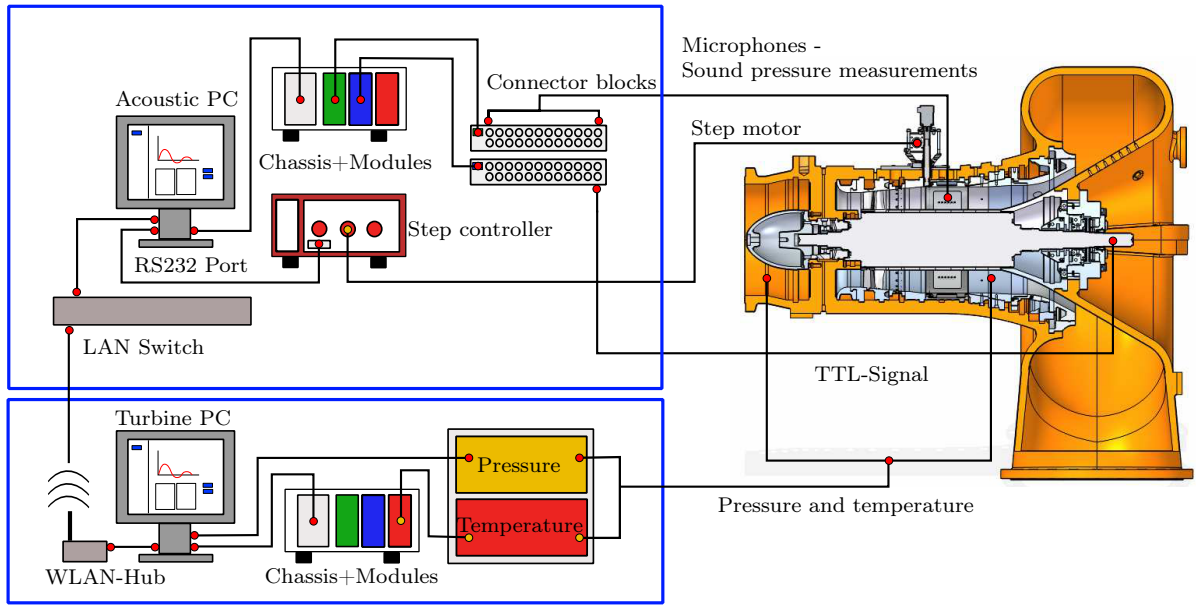
Figure A.23: General measurement and data acquisition set-up, adapted from Sec. 4.2.2

scanners from the company Measurement Specialties. The measurement system consisted of the interface rack model 98RK-1 housing up to eight pressure scanners model 9816, each which in turn integrated up to 16 silicon piezoresistive pressure sensors specified for several pressure ranges and able to reach sample rates up to 100 S/s. The interface rack enabled the pressure sensors to communicate with the host computer via 10/100/1G Ethernet protocol, a global standard for wired local networks. That implies, that in contrast to the PXI systems, the pressure scanners were no directly connected to the host computer, but rather transferred all measurement data via broadband transmission network. The same data transfer method applied for the measurement of the atmospheric pressure (measured ahead the screw compressors), which was performed by the CPG 2500 barometer from the company Mensor©, a high accuracy barometer with a range of 55 to 117 kPa.

The acquired operating data of the turbine was sent to the "Turbine PC" host via Ethernet. This task was performed by a desktop switch model GS116 from Netgear, a device which integrated all connected computers and instruments and facilitates the mutual sending and receiving of information via Ethernet10/100/1G protocol. As seen on Fig. A.23, the desktop switch allowed the data transfer from the pressure scanners and the high accuracy barometer to the "Turbine PC" host, which in turn, sent this data complemented with temperature readings to the "Acoustic PC" host. In this way, the operating status of the turbine was known during the performed sound propagation experiments.

Having established the foundations of the data acquisition process in the context of the current experiments, the data acquisition program structure as well as the step motor control are briefly discussed in the section to follow.

Measurement and control program general overview

As already mentioned, both data acquisition and motor control are required to be adequately synchronized in order to guarantee satisfactory experimental results. In these order of ideas, an integrated data acquisition and control program was developed in LabVIEW©. As such, the program consisted of two separate modules that nevertheless ran simultaneously. The first module, the data acquisition module, recorded all sound pressure data, the rotor TTL signal and received the transferred turbine operating data via Ethernet from the "Turbine PC" host. The second module, the control one, was in charge of the microphone ring rotation through the step motor and the external transmission mechanism.

The functional principle of the program was based on the requirements of the experiments to be performed. As stated before, the determination of the in-duct propagating acoustical structure demanded measurements at several positions, imposition fulfilled by the high circumferential measurement resolution offered by the rotating microphone ring. Considering also one of the main objectives of the present work, which was to analyze the sensitivity of the results of the RMA to the measurement circumferential resolution, implies that the ring had to be positioned inside the duct with variable circumferential distance.

In this respect, and in order to guarantee an optimal execution of all measurement and control procedures, the main program was organized into subprograms, each assigned to a tab. In the first subroutine, the measurement channels for the microphone as well as for the voltage analog data were selected along with a text file including the calibration data of the microphones. Once this information was loaded, the second and third subprograms were executed, the ones corresponding to the second (acoustic signals) and third tab (voltage signals) in the main program, respectively.

The fourth tab had an interface assigned for the display of the machine operating data which was transferred from the turbine host PC to the acoustic host PC. Finally, the last tab of the main program exhibited a user interface with several fill-in fields, in which specific information related to the actual measurement was prompted to be registered. Additionally, the data saving location and measurement file name were specified. Furthermore, a box for the step motor control was included. Only two inputs were required: the angular range to be covered by the microphone ring and the circumferential resolution.

As already mentioned, the step motor control was performed through the iMC-S8 controller, a freely programmable controller which integrated all the necessary components including internal step motor power supply, a core processor or module programmed via a serial interface (RS232) and according to the controller version, connection up to four linear or circular axes. While being permanently connected to (with) a host computer, the controller's core module transformed and afterwards processed the parameters set by the user in the form of programmed commands into clocking and direction signals for the connected step motors.

The command lines were directly transferred and executed by the controller, a initialization procedure was required. The initialization was conducted by the inclusion of the @ sign, followed by the specification of the device number (0 = default) and the number of axes to be traversed. Once the initialization was completed, the controller expects the specification of the type of motion (absolute or relative motion of the axis), the number of motor steps and velocity (steps per second, Steps/s), information specified also as a command line. Once this was done, the command was transmitted to the controller, subsequently decoded and finally executed. Right after this, a corresponding confirmation was generated, indicating that correct execution of the command line, or conversely, reporting an occurring error. As mentioned before, only the circumferential range and angular resolution were specified by the user. Once this is done, a measurement procedure can be executed.

The input parameters are collected (measurement channels, calibration coefficients, circumferential range and resolution), immediately after the sound pressure and TTL signals are recorded for the microphone ring initial angular position. During this recording time, the turbine operating variables were transferred to the acoustic host PC. Once the recording time has been reached, the measurement was finalized and the step motor displaced the microphone ring to the following measurement position, where the whole procedure was repeated again. Once the measurement data has been recorded at the last ring azimuthal position, the step motor displaced the ring to its original start position, thus allowing the beginning of a new measurement.

Wissenschaftlicher Werdegang

Persönliche Daten

Name   Juan David Laguna Trujillo

Geburtsdatum   8. Januar 1985

Geburtsort   Bogota

Familienstand   ledig

Schulausbildung

1991 - 1996   Gimnasio Británico, Grundschule

1996 - 2001   Gimnasio Británico, Gymnasium

Studium

2001 - 2006   Universidad de los Andes, Kolumbien
                    Abschluss: Bachelor Maschinenbau

2006 - 2007   Universidad de los Andes, Kolumbien
                    Abschluss: Master Maschinenbau

seit 2010   Leibniz Universität Hannover
                    Promotionsstudium Maschinenbau

Berufstätigkeit

seit 2010   Stipendiat am Institut für Turbomaschinen und Fluid-Dynamik
                    der Leibniz Universität Hannover

Hannover, im Oktober 2015